# Quasiparticles in a diffusive conductor: Interaction and pairing
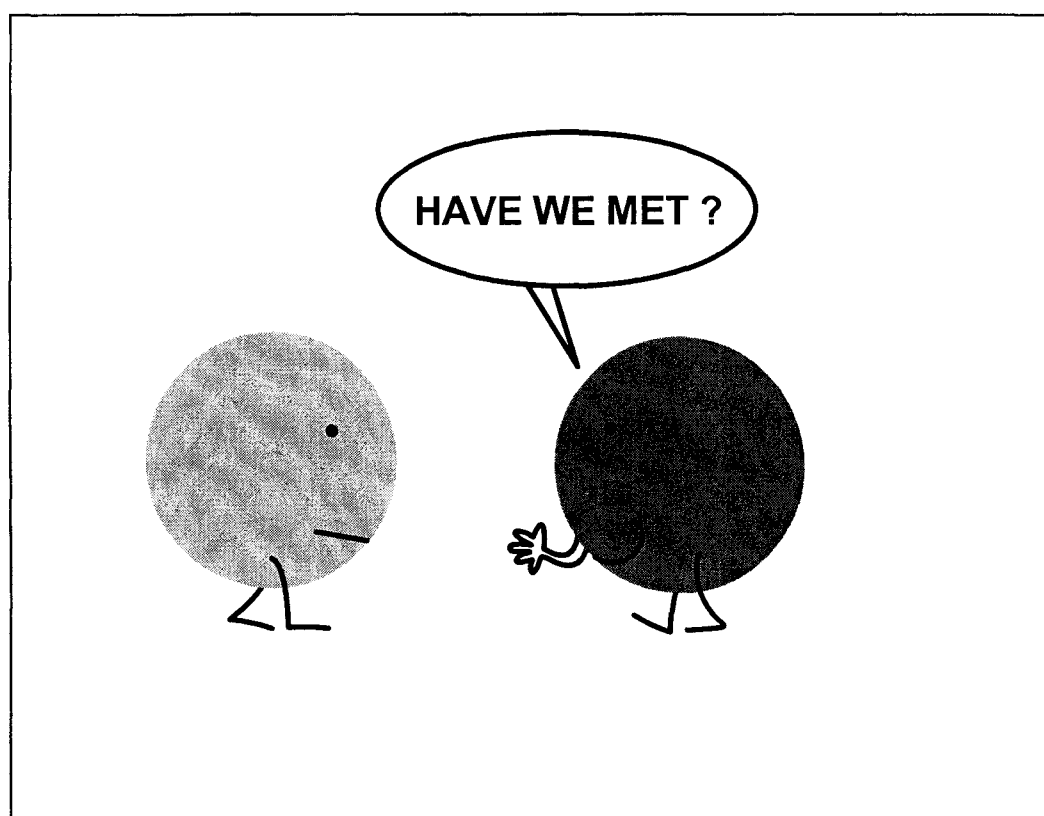
Sophie Guéron
Quantronics Group
CEA Saclay

THESE DE DOCTORAT DE L'UNIVERSITE PARIS 6

Quasiparticules dans un conducteur diffusif : interactions et appariement

spécialité :
Physique des solides

Présentée par :
Sophie Guéron
pour obtenir le grade de docteur de l'Université Paris 6

Soutenue le 17 octobre 1997
Amphithéâtre Claude Bloch,
Orme des merisiers,
CEA-Saclay.

devant le jury composé de
Président :   J. Bok
Rapporteurs :   T. Klapwijk
                            B. Pannetier
Examinateurs :   H. Bouchiat
                            M. Devoret
                            G. Montambaux

A mes grand-parents
Geneviève Bernheim, Jules Guéron, Anna Kostokovsky, Louis Tabachnick,
A mes parents,
A Claire,
A Benoît.

Errors in some formulas of Chapter 5 in the first edition of this thesis were pointed out to us by John Martinis. The definition of H_0 on p. 101, formulas (5.52) to (5.54), formula (5.59), formulas (5.61) to (5.67), and the corresponding formulas on pages 141 and 142, have been edited and corrected in this second edition.

Hugues Pothier and Sophie Guéron,
Saclay, December 1998

Remerciements

Mes remerciements s'adressent tout d'abord au Groupe de quantronique, au sein duquel j'ai effectué ce travail. Faire partie du groupe a signifié pour moi être contaminée par la conviction que tous les phénomènes peuvent être compris en termes intuitifs, et décrits par une image qui, si elle est correcte, doit pouvoir être illustrée par une expérience simple et claire. L'idée d'une expérience née d'heures de discussions au tableau d'une salle informatique exiguë illustre le petit miracle qui s'accomplit lorsque s'allient curiosité, réflexion, écoute, créativité et enthousiasme. Au sein du groupe, j'ai eu l'impression de grandir en même temps que progressaient les expériences et leur compréhension.

Je remercie Michel Devoret, mon directeur de thèse, pour l'attention constante qu'il m'a prodiguée, le soin avec lequel il m'a expliqué les concepts qu'il jugeait fondamental de comprendre, au cours de nombreuses discussions dans lesquelles j'admirais la combinaison de la rigueur de raisonnement et de la présentation claire des concepts. Daniel Estève, en directeur de thèse dual, m'a enseigné aussi bien les techniques expérimentales, nanométriques et macroscopiques, que la façon de considérer une théorie de plusieurs points de vue différents. Son dynamisme et son efficacité époustouflants rendent sa gentillesse et l'importance qu'il apporte aux relations personnelles d'autant plus émouvantes. Hugues Pothier complète le trio : aucune des expériences présentées dans cette thèse n'aurait pu être réalisée sans lui. Ses idées astucieuses ont permis la fabrication d'échantillons complexes, et son irrévérence a grandement contribué à désacraliser les théories, étape essentielle dans la compréhension de concepts qui me sont ensuite devenus familiers. Ses encouragements, moqueries bienveillantes, jeux de mots toujours subtils lors de son suivi permanent de mon travail, ont fait de cette thèse un bonheur quotidien. Je remercie tous trois de l'aide extrême et permanente qu'ils m'ont apportée durant la rédaction du manuscrit.

J'ai eu grand plaisir à travailler avec Norman Birge durant sa visite au laboratoire, durant laquelle ont été réalisées les expériences sur la mesure de la densité d'états et l'interaction entre quasiparticules. Il m'a fait partager ses connaissances, m'initiant aux charmes de la détection synchrone Lock-in, à la rigueur expérimentale en général, sans parler de la tarte au potiron. C'est dans ces conditions de travail exceptionnelles, qui ont pu rappeler à certains le BTP chilien, que j'ai découvert la richesse des expériences sur les systèmes alliant nature quantique et classique.

Dans un mois, dans un an, comment souffrirons- nous,
Seigneur, que tant de mers me séparent de vous?
Que le jour recommence et que le jour finisse
Sans que jamais Titus puisse voir Bérénice?

Table of Contents

Chapter 1
Introduction

1.1 Quasiparticles in a disordered metal

Although electrons in a metal constitute a many-body system of particles interacting strongly through the Coulomb repulsion, the independent electron model, pioneered by Drude and Sommerfeld, has proven very successful in explaining practically all properties of metals. The theoretical justification of this simplification is due to Landau, who showed that any system of interacting fermions maps onto a system of independent fermionic particles, the "quasiparticles", which are the real particles with their quantum correlations [1]. In metals, a quasiparticle can be pictured as the charged electron (or hole) surrounded by its screening cloud. The many-body aspect of the system almost completely disappears, except for a residual interaction between quasiparticles. This residual interaction explains for instance how quasiparticles can thermalize to a higher temperature than the phonon temperature when power is injected into a metallic film. The aim of the first part of this thesis is to provide direct evidence for this interaction by measuring the energy exchange rate between quasiparticles in the case of thin metallic diffusive films. In such films, quasiparticles are strongly scattered by the surface of the sample and its impurities, so that interactions between quasiparticles are predicted to be stronger than in a perfect metal. The experimental results agree qualitatively with these predictions, but are not explained quantitatively by the existing theories.

If many-body correlations between electrons in metals are difficult to reveal, in some metals the correlations are exclusively two-body correlations: in the presence of a sufficiently large

electron-phonon coupling, a metal becomes superconducting at low temperature, *i.e.* is in a quantum state characterized by correlations between pairs of electrons with opposite spin [2]. The second part of this thesis deals with the propagation of these pair correlations in a normal (*i.e.* non superconducting) metal when it is placed in contact with a superconductor. This "proximity effect" was investigated in the sixties, and the understanding reached then was that superconductivity penetrates a finite, temperature-dependent length $L_T = \sqrt{\hbar D/k_B T}$ into the normal metal, where T is the temperature and D the normal metal diffusion constant [3]. In the last decade, demonstrations of coherent transport in normal metals have revived interest in this effect [4], because a superconductor placed next to a normal metal reveals the coherence of the electrons in this metal. For instance, the current which flows across the normal/superconducting interface is due to pairs of time-reversed electrons of the normal metal entering the superconductor. Consequently, the longer the phase coherence time in the normal metal, the greater the current. The aim of the experiments presented in the second part of this thesis is to specify in what sense a normal metal in proximity with a superconductor develops a superconducting character. These experiments constitute a test of the present theoretical framework of the proximity effect. We have on the one hand measured the quasiparticle density of states in the normal metal, close to a good contact with a superconductor, to test the predictions of the theory for this fundamental quantity. On the other hand, we have devised an interference experiment in order to probe the quantum coherence in a normal metal in proximity with a superconductor.

We present in the following the main results of the three experiments mentioned above.

1.2   Interaction between quasiparticles in a diffusive wire

To access the interaction between quasiparticles in a diffusive metal, we have implemented an out-of-equilibrium situation, by placing a diffusive metallic wire between two thick metal pads biased at different electrochemical potentials. Since the energy exchange between quasiparticles tends to establish a local equilibrium, the quasiparticle energy distribution function along the wire should be sensitive to interaction. The practical set-up is sketched in Fig. 1.1. A wire of length L is connected to two thick pads which act as reservoirs of quasiparticles: they inject in the wire quasiparticles distributed in energy according to a Fermi function at the tem-
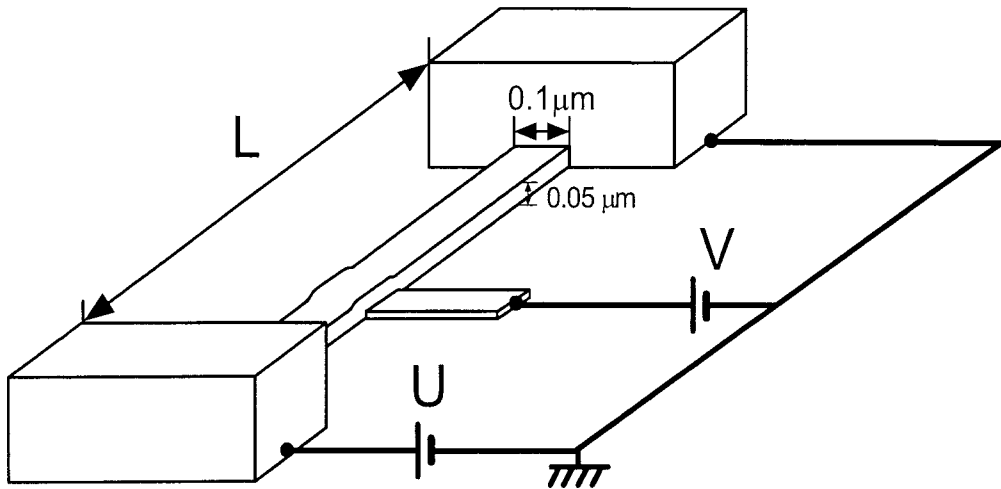
Fig. 1.1. Schematics of the experimental layout: a metallic wire of length L is connected to two thick pads at electrochemical potentials differing by eU. The energy distribution function in the wire is deduced from the differential conductance of the tunnel junction formed between the wire and a superconducting electrode placed underneath.

perature of the crystal and with an electrochemical potential given by the voltage of the pad. These quasiparticles diffuse from one pad to the other in a typical diffusion time $\tau_D = L^2/D$. The experiment is based on the strong dependence of the shape of the quasiparticle energy distribution function upon the amount of energy exchanged between the quasiparticles during the diffusion time. The experiment is performed at low temperature, so that the only mechanism leading to a redistribution of the quasiparticle energy is quasiparticle-quasiparticle interaction. The distribution function is measured at a given position by a superconducting tunnel probe. The differential conductance of this tunnel junction, deconvolved by the superconducting density of states, yields the energy distribution function.

We have determined in this way the distribution function in the middle of three diffusive wires, differing by their length or the value of their diffusion constant. The functions, measured at a temperature of 30 mK and with a potential difference $U = 0.2$ mV applied between the pads, are plotted as continuous lines in figure 1.2. The three curves differ distinctly. The distribution function in the middle of a 1.5 μm−long wire (top panel) is close to a step function (dotted curve), which corresponds to the half sum of the boundary distributions. Such a step function is expected if the energy of the quasiparticles is entirely conserved over the duration of their diffusion across the wire. The slight rounding of the measured distribution is a sign that some interaction has occurred. The distribution plotted in the central panel corresponds

- 13 -
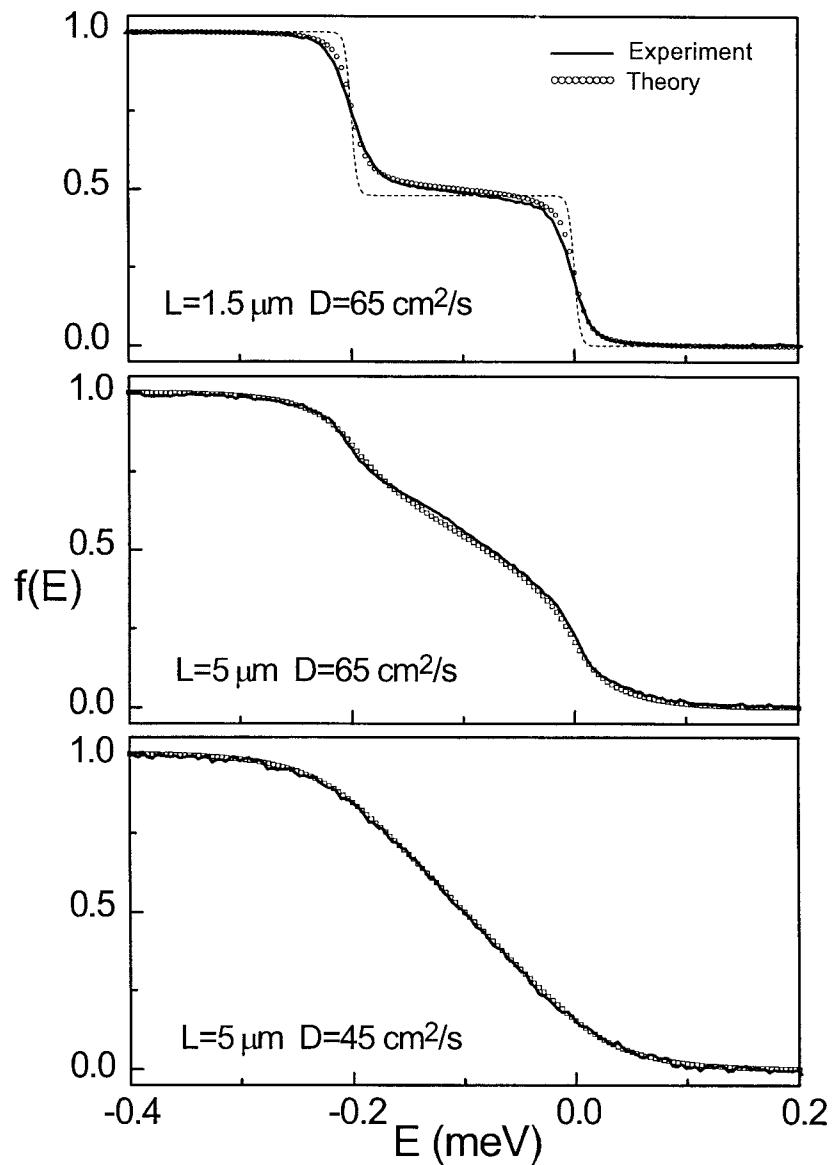
Fig. 1.2. Continuous curves: energy distribution function in the center of three different copper wires. Top panel: 1.5 μm−long wire of diffusion constant $D = 65$ cm^2/s. Middle panel: $L = 5$ μm, $D = 65$ cm^2/s. Lower panel: $L = 5$ μm, $D = 45$ cm^2/s. All three wires were 45 nm thick and 110 nm wide. The potential difference applied between the two reservoirs is $U = 0.2$ mV. Measurements were performed at $T = 30$ mK. Symbols: distributions computed using $\tau_0 = 1$ ns (wires with $D = 65$ cm^2/s) and $\tau_0 = 0.5$ ns (wire with $D = 45$ cm^2/s). Dotted curve in top panel: distribution expected if the quasiparticles do not interact during the entire time of their diffusion across the wire.

to a 5 μm-long wire fabricated simultaneously. Its diffusion constant should thus be identical to the one of the previous wire, so that electrons take roughly ten times longer to diffuse from one end of the wire to the other. Indeed this curve is more rounded than the previous one, a sign that interaction has caused some redistribution of the electronic energy. The last curve was measured in the middle of a 5 μm-long wire as well, but with a diffusion constant 40% smaller. This distribution can be fitted by a Fermi-Dirac distribution at a temperature $T = 665$ mK, within 5% of the temperature expected if electrons thermalize in each point of the wire.

These results demonstrate the interaction between quasiparticles, and provide the energy relaxation rate, which is of the order of the inverse diffusion time across the second wire $1/\tau_{D_2} \simeq 1$ ns^{-1}. As we shall see, they also give the energy dependence of the interaction law: we find an interaction rate inversely proportional to the square of the energy exchanged between quasiparticles. The proportionality coefficient can be interpreted as a typical interaction rate τ_0^{-1}. We determine this rate by fitting the distributions computed with such an interaction law to the measured curves. The symbols plotted in Fig. 1.2 are distributions computed with times τ_0 of respectively 1 and 0.5 ns.

These results indicate that interaction is quite sensitive to the diffusion constant of the metal. In addition, the energy dependence of the exchange rate given by the experiment is not the one predicted by the standard theoretical calculations. This rate would imply a finite quasiparticle lifetime of approximately τ_0, even at low energy. To account for this result, we present a model in which the diffusive wire is decomposed into an array of small resistors. Each elementary resistor is the source of a fluctuating current, function of the local quasiparticle distribution. The interaction corresponds to the absorption by a second resistor of part of the power emitted by the first.

1.3   Density of states in a normal metal in contact with a superconductor

The single particle density of states, *i.e.* the number of states per unit energy and unit volume of a system, is possibly the physical property which best exhibits the correlations in a metal. Any deviation from a constant density of states as a function of energy (for energies small compared to the Fermi level) is the sign of correlations between two or more quasiparticles. For instance, there are no states below a threshold energy (the gap) in a superconductor, whose ground state consists of paired quasiparticle states at low energy. In
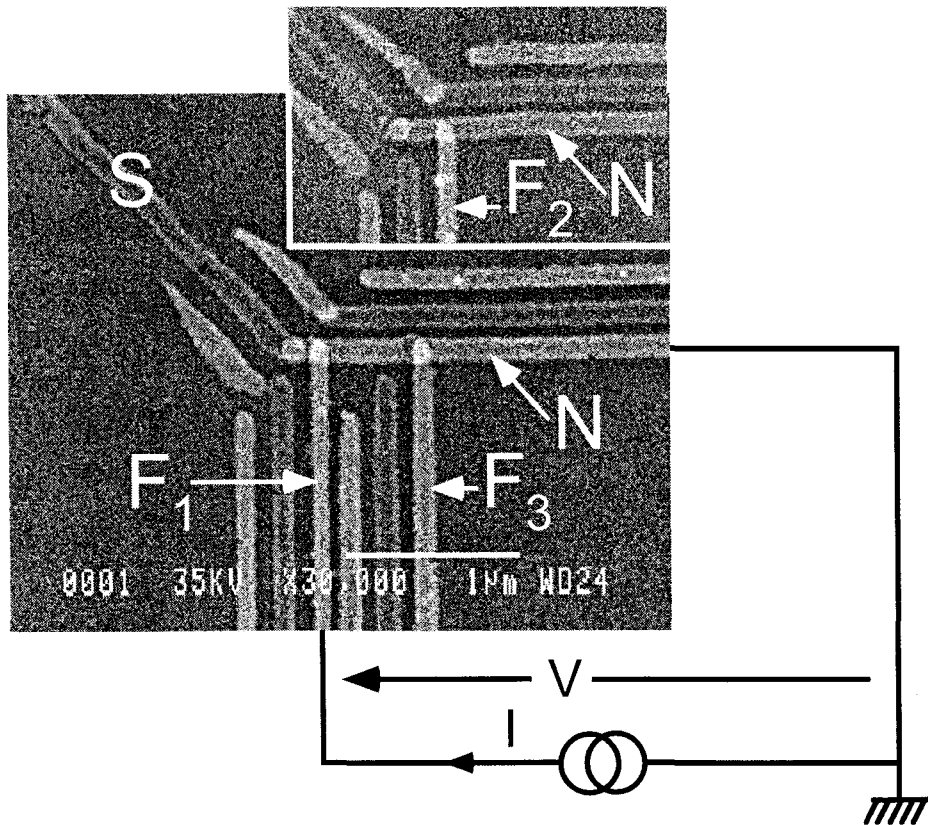
Fig. 1.3. Scanning electron micrograph of the proximity sample, made of two similar circuits. In each circuit, a normal copper wire (N, horizontal) is in good contact with a superconducting aluminum wire (S, diagonal wire on the left). The contact area is the bright region of the NS overlap. The density of states in the normal wires of both circuits is given by the differential conductance of the junctions formed between the normal wires and three normal probes (vertical), labeled F_1, F_2 and F_3. The bright areas are the junction regions.

order to determine the magnitude and energy and space dependence of the pair correlations induced in a normal metal connected to a superconductor, we have measured the single particle

density of states in a normal metal wire in good contact with a superconducting wire, at different distances from the contact. The density of states is proportional to the differential conductance of a tunnel junction between the wire and a normal metal tunnel probe (see scanning electron micrograph of the structure in Fig. 1.3). We present in Fig. 1.4 the conductances of three tunnel junctions, positioned respectively 100, 200 and 700 nm away from the normal/superconductor interface. For comparison, the differential conductance of a tunnel junction between a BCS superconductor and a normal probe is shown in the inset. It is clear from the comparison that the three densities of states in the normal metal do not resemble those of a BCS superconductor: the proximity spectra contain neither an excitation gap nor a strong singularity. Rather, the proximity effect is characterized by a depletion of single particle states at low energy and an excess density of states somewhere below the superconducting gap energy. A constant density of states is recovered at large energy. Not surprisingly, the curve with the strongest deviations from a normal density of states is that of junction F_1, the closest to the interface. It is depleted at the Fermi level to 55% of the normal value. The densities of states measured by junctions F_2 and F_3 are depleted to 65% and 95% of the normal value at the Fermi energy. If one defines as a typical pair correlation energy the energy corresponding to the maximal density of states, one finds that this typical energy decreases as the distance to the interface increases. This can be understood in the following way: when a Cooper pair enters the normal metal, the phase difference between the doubly occupied quasiparticle state and the doubly empty state, which is constant in the superconductor, evolves in the normal metal with time t as $2Et/\hbar$, where $2E$ is the energy difference between the two states. Since the pair correlations at a given position in the normal metal are determined by the contributions of all diffusive trajectories originating in the superconductor and reaching that position, they will be averaged out at distances of the order of $\sqrt{\hbar D/E}$. Conversely, the typical energy scale at a distance x from the NS interface is the Thouless energy $E_C = \hbar D/x^2$. This behavior is well accounted for by the theory of the proximity effect (see lower panel of Fig. 1.4).
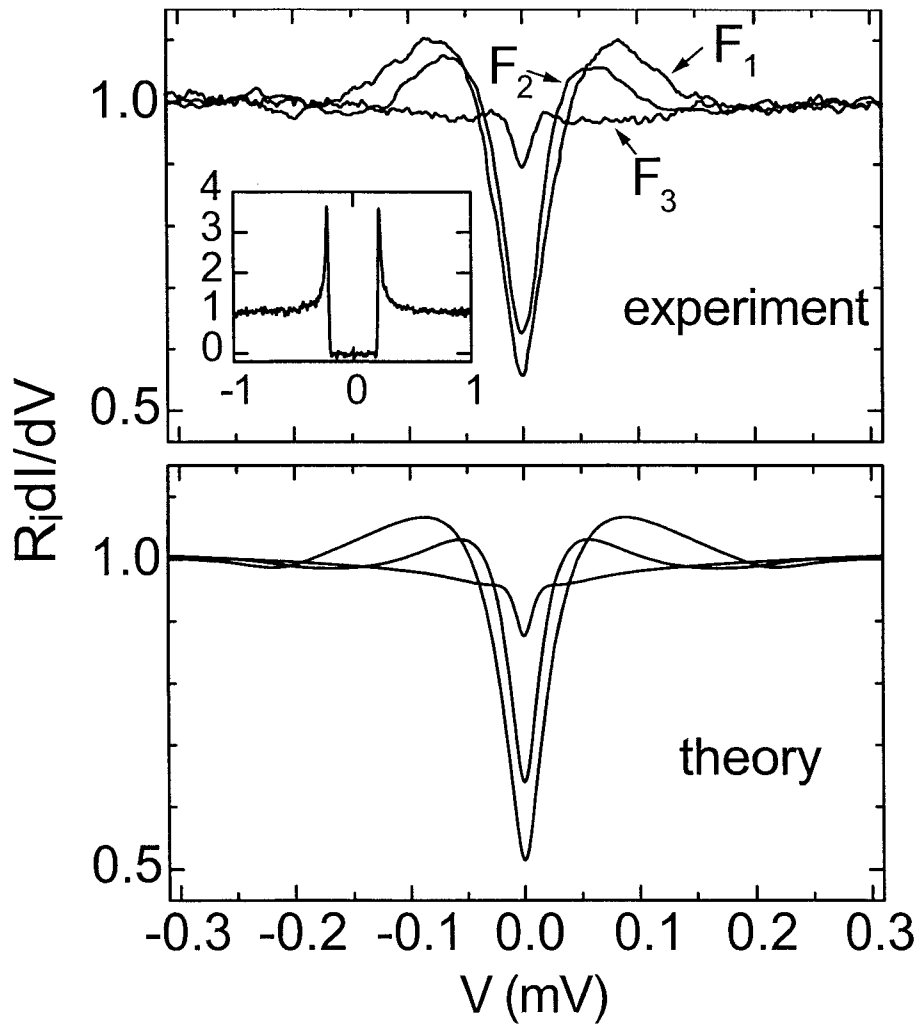
Fig. 1.4. Top panel: Conductance of tunnel junctions F_1, F_2 and F_3, placed respectively 100, 200 and 800 nm away from the NS interface, normalized by the junction conductance at voltage $V = 0.3$ mV. The conductance is proportionnal to the DOS in the copper wire in good contact with the aluminum wire. Inset: normalized differential conductance of a tunnel junction between a normal probe and a superconducting aluminum wire. All measurements were performed at $T = 30$ mK. Bottom panel: predicted DOS using the theory of the proximity effect, calculated with a spin-flip scattering time of $\tau_{sf} = 65$ ps.

1.4   Coherent transport at an NS boundary: the NS-QUID

The subgap (or Andreev) current through a normal metal/superconductor tunnel junction is another indicator of the pair correlations in the normal metal. Indeed, this current is exclusively due to pairs of normal electrons tunneling into the superconductor. Since this tunneling of a pair is a second order process in barrier transmission, the current across opaque barriers should be negligible. However, tunneling attempts by pairs of electrons in *time-reversed* states add up coherently, in contrast with the incoherent tunneling attempts of a single electron (see Fig. 1.5). Therefore the Andreev current should be enhanced in a metal where impurities or boundaries confine the electronic trajectories near the NS interface, and all the more so as the coherence time in the normal metal is long.
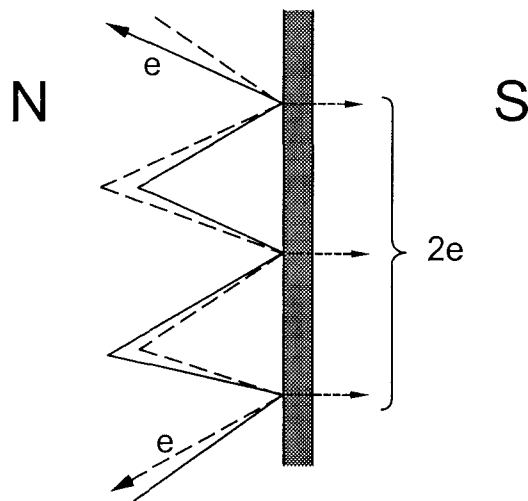
Fig. 1.5. Semiclassical representation of the mechanism responsible for constructive interference in the tunneling of pairs of normal electrons. Two weakly localized electrons in the normal electrode with nearly time-reversed wave functions tunnel through the barrier at different points with the same total phase. If the order parameter of the superconductor is uniform, the tunnel amplitudes at these different points contribute constructively to the total current.

In order to probe the quantum coherence of electrons in the normal metal, we have devised an interference experiment with two superconducting/normal tunnel junctions in parallel. The relative phase of the two superconducting electrodes is controlled by applying a magnetic field perpendicular to the plane of the loop they form (see Fig. 1.6 for the electron micrograph of three such NS-QUIDs, which differ only by the length of normal wire separating the two tunnel

junctions). The interference pattern is the conductance of the structure, which is sinusoidally modulated by the field. Figure 1.7 shows the IV characteristics of three NS-QUIDs, measured
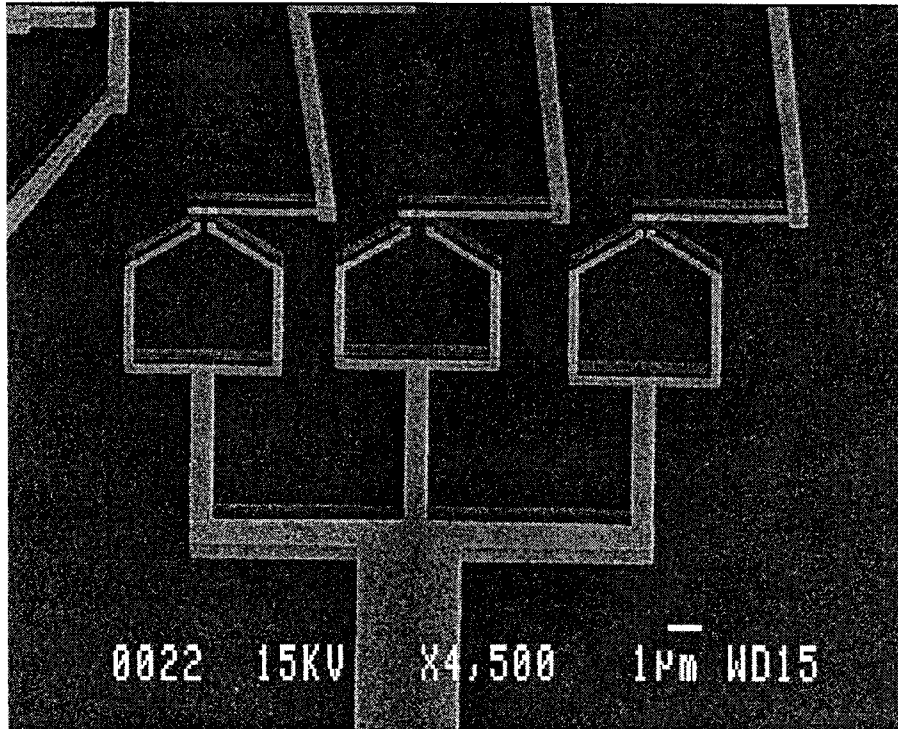
Fig. 1.6. Scanning electron micrograph of a sample containing three NSQUIDs: each device is made of an open superconducting aluminum loop (upper shadow of the loop), oxidized to form two tunnel junctions with the normal copper wire (lower grey shadow of horizontal wire). The three devices differ only by the distance between the two tunnel junctions.

respectively with no magnetic flux (maximal subgap current), and one flux quantum (minimum subgap current) in the loop.

The modulation of the current by the magnetic field, measured at one point of the IV curve of one NS-QUID, is shown in the panel below. The modulation is perfectly sinusoidal. In addition, in all three NS-QUIDs, the magnitude of the modulated current (difference between the current with a superconducting phase difference of 0 and π) is of the order of the total current through the structure. The intensity of the modulated current as a function of voltage is shown in the right panel of Fig. 1.7. The maximal current at low voltages, and the decrease in current modulation at high voltage illustrate the loss of coherence between electron pairs with non negligible energy difference. The difference in modulation intensity between the three NS-QUIDs at low energy demonstrates the existence of inelastic processes, such as scattering
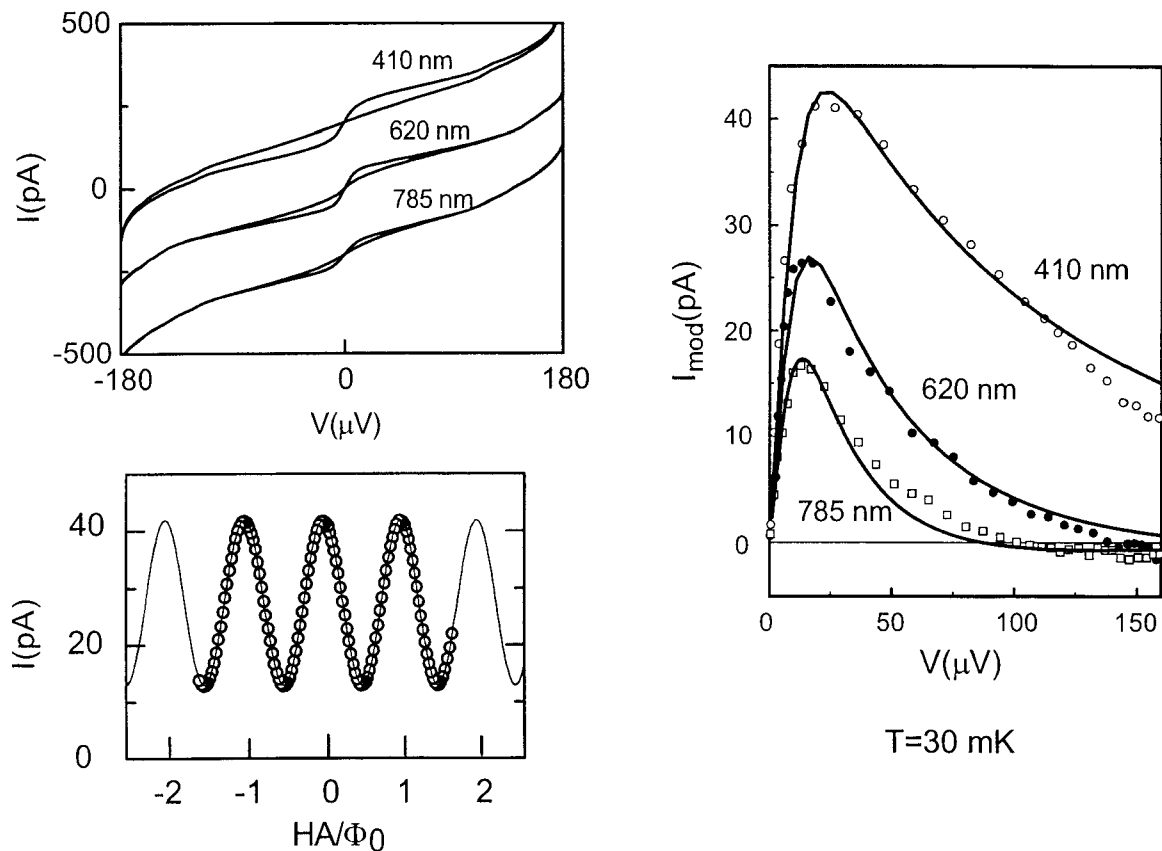
Fig. 1.7. Top panel: IV curves of three interferometers with tunnel junctions separated by 410, 620 and 785 nm respectively; with zero magnetic field (maximal subgap current) and one half flux quantum (minimal current) in the loop. The three sets of curves have been offset vertically for clarity. Lower panel: modulation of the current through an interferometer, for a given voltage, by a magnetic field H applied perpendicularly to the loop of surface A (symbols). The continuous curve is a cosine fit to the data. Right pannel: measured modulated current (symbols) compared to the current computed from the semi-classical probability to diffuse from one junction to the other (continuous lines). All measured curves were taken at T=30 mK.

by magnetic impurities, which limit the coherence of electron pairs in the normal metal. From the measured curves, a coherence time of about 100 ps, corresponding to a coherence length of about 1 μm, is inferred. The specific shape of the modulated current of all three devices can be deduced from an Andreev rate given by the Fermi golden rule. This current can also be calculated with the theory of the proximity effect. In that framework, the current is due to the existence of pair correlations induced in the normal metal by the presence of the superconductor. This experiment illustrates how Andreev reflection and the proximity effect are two aspects of the same phenomenon.

REFERENCES

[1] D. Pines, P. Nozières, *The theory of quantum liquids* (W.A. Benjamin, New York, 1966).

[2] M. Tinkham, *Introduction to Superconductivity* (Mc Graw Hill, New York, 1985), chapter 3.

[3] P. G. de Gennes, *Superconductivity of metals and alloys* (W. A. Benjamin, New York, 1966).

[4] V. T. Petrashov, V. N. Antonov, P. Delsing, and T. Claeson, Phys. Rev. Lett. **70**, 347 (1993); See also *Procedings of the NATO Advanced Research Workshop on Mesoscopic Superconductivity*, F. W. J. Hekking, G. Schön, and D. V. Averin, Editors (Elsevier, Amsterdam, 1994).

Chapter 2
Experimental techniques

2.1 Sample fabrication

In the following we describe the different steps leading to a sample in its final form before measurement. Most of these steps use by now standard nanofabrication techniques. The basic principle is to fabricate a mask with carefully designed openings overhanging above a substrate, and to deposit the metals composing the circuit through this mask. By depositing the various metals at different angles, and possibly allowing for an oxidation step, one can implement on the substrate a complex circuit which includes contacts and tunnel junctions between different metals.

The typical fabrication scheme is outlined in Fig. 2.3. The process begins with the coating of a 2-inch oxidized silicon wafer with two layers of electrosensitive polymers (bilayer process), which can be separated by an intermediate germanium layer (trilayer process). The coated wafer is then cut into small chips, which are processed individually. A chip is first exposed to the electron beam of a scanning electron microscope, scanned according to a predefined pattern. The polymer chains exposed to the beam are broken, so that when the chip is developed after exposure only the non exposed regions of the top layer remain. If the chip is made from a wafer coated with a bilayer, the developed top polymer layer constitutes a suspended mask. In the trilayer process, the pattern in the top layer is transferred to the germanium layer through etching. The etched germanium layer then constitutes the mask. In both techniques, the bottom polymer layer acts as a ballast which sustains the mask. The

next step is the deposition of metals through the mask at different angles, and oxidation in between if necessary. The undercut under the mask, due to the greater electrosensitivity of the bottom layer, determines which projections of the mask openings fall onto the substrate and which are projected on the edges of the ballast layer. After deposition, both the mask and the ballast are lifted off in acetone, leaving the circuit deposited on the substrate.

Although the trilayer technique involves a greater number of steps, it is preferred when long, fine structures are needed. Indeed, because of its rigidity, the germanium mask can be suspended over greater lengths than a polymer mask. In addition, the details obtained with a trilayer are usually finer because the electrons backscattered in the thin germanium layer do not widen the exposed areas, and because the electrons backscattered in the ballast and in the silicon substrate are prevented from reaching the top layer by the germanium.

2.1.1   Wafer preparation

We now detail the fabrication process.

2.1.1.1   Bilayer coating

In the bilayer technique, the substrate is first coated with a "ballast" layer, whose role is to sustain the second layer, which will constitute the mask, as well as enable an undercut under the openings in the mask. To that end, the bottom layer is a copolymer, whose chains are more easily broken by exposure to the electron beam than those of the top polymer layer. The thickness of the bottom layer is determined by the height at which the mask should hang over the substrate. We have used the following coating procedure:
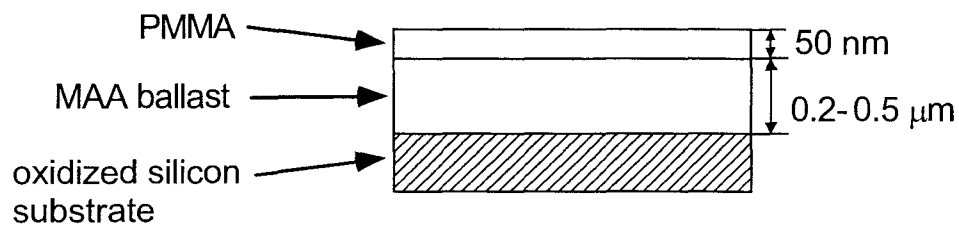
Fig. 2.1.

Bottom layer: copolymer polymethyl-meta-acrylate/meta-acrylate acid (PMMA /MAA) diluted at 70 g/l in 2-ethoxyethanol, filtered with 0.2 μm filters. Spun at 850 rpm for about 50 s, and baked on a hot plate at 180 °C for 10 mn; thickness $\sim$ 0.5 μm. We use PMMA of

PMMA

Ge

MAA ballast

oxidized silicon
substrate

50 nm
50 nm

0.8-1 μm
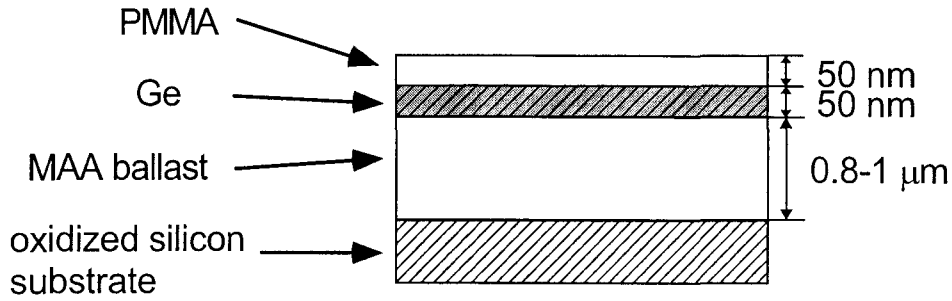
Fig. 2.2.

molecular weight 950K in all cases.

Top layer: PMMA diluted at 15 g/l in methyl isobutyl butyl ketone (MIBK), filtered with 0.2 μm filters. Spun at 850 rpm for about 50 s, and baked on a hot plate at 170 °C for 25 mn.

2.1.1.2 Trilayer coating

In the trilayer technique, the mask is made of a germanium layer sandwiched between the same two resists as those used in the bilayer technique. Thin germanium layers are required when large deposition angles are desired. On the contrary, in some designs (such as the sample for the experiment on the quasiparticle energy relaxation), one of the projections is not wanted. The germanium layer will therefore be made thick so that selected openings of the mask clog up before the last deposition. The thickness of the germanium mask typically varies between 10 and 50 nm.

We have used the following procedure:

Bottom layer: PMMA/MAA diluted at 90 g/l in 2-ethoxyethanol, filtered with 0.2 μm filters. Spun at 850 rpm for about 50 s, and baked on a hot plate at 160 °C for 15 mn. This produces a ballast layer of thickness $\sim$ 900 nm.

Middle layer: 10 − 50 nm of thermally evaporated germanium, at a rate of 0.1 nm/s in a vacuum of $5 \ 10^{-6}$ mbar.

Top layer: PMMA diluted at 15 g/l in MIBK, filtered with 0.2 μm filters. Spun at 850 rpm for about 50 s, and baked on a hot plate at 150 °C for 15 mn. As described in [1] , this layer should be baked at a temperature slightly inferior to the baking temperature of the first layer, in order to limit the stress between layers. Without this precaution, characteristic circular cracks may appear in the thin germanium layer.

2.1.2   Processing of a single chip

The coated wafers are diced into 8×8 mm^2 chipswith a diamond-tip scriber, and each chip is then processed separately.

2.1.2.1   Exposure to electron beam

The patterning of each chip is done with the beam of a JEOL 840A scanning electron microscope. The exposure pattern, dose and blanking of the electron beam are commanded by the Proxy-writer system from Raith GmbH. We currently use a beam acceleration voltage of 35 kV, for which the standard exposure dose is about 2 pC/μm^2.

Principle of electron beam lithography

The principle of the lithography of a multilayer chip with an electron beam is straightforward. Electrons focused onto the sample penetrate both the polymer and copolymer layers (and the Ge layer when there is one). Their energy is released in the resin, breaking the PMMA and MAA into fragments of smaller molecular weight, which are dissolved in the developer in a subsequent development step. As pictured in Fig. 2.3, a broader region in the MAA layer is fragmented by the beam for two reasons. First, the copolymer chains are more easily broken than the PMMA chains. Second, electrons scattering in the MAA layer as well as those backscattered from the substrate contribute to the profile. Thus a lower dose is sufficient to break chains in the MAA layer without damaging the PMMA layer, thereby enabling the realization of a mask with fine openings on top of a sustaining layer with large undercuts. Below we explain how the undercut can be precisely patterned, thereby enabling the fabrication of more elaborate circuits than previously.

Accurate control of the undercut through a two-step exposure sequence

All the samples measured in the course of this thesis were fabricated by depositing through a suspended mask materials at different angles. When the materials are deposited at more than two different angles, undesired contacts or junctions in parallel with the structure to be measured almost unavoidably are produced. This happens because the undercut is symmetric around the openings of the mask, and has an extension which is not controlled. In order to prevent parasitic images, we have developed a two-step exposure sequence which enables an asymmetric undercut of controlled extension, thereby allowing the deposition on the substrate
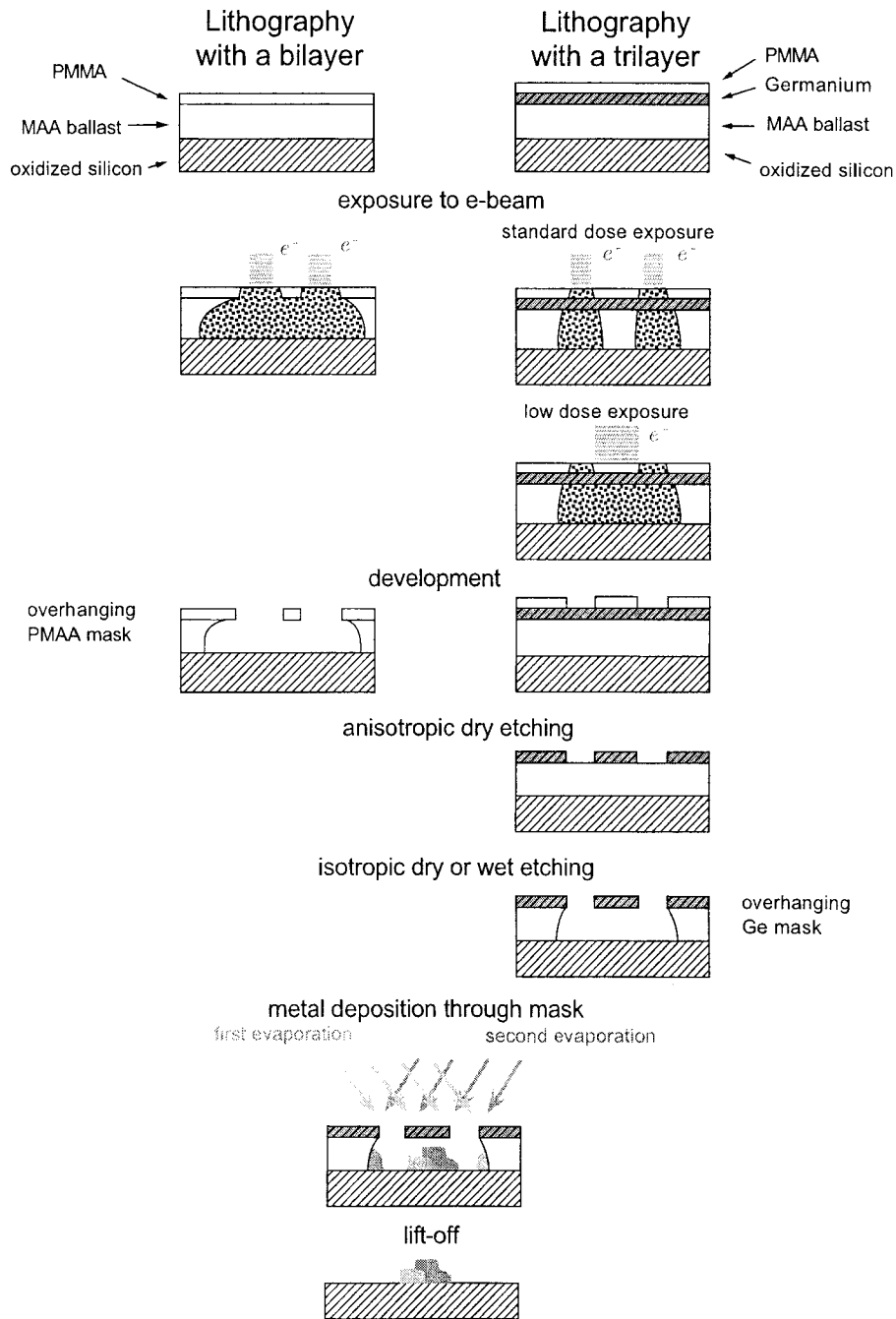
Fig. 2.3. Sequence of steps leading to the fabrication of circuits with the technique of deposition through a suspended mask of PMMA (bilayer technique) or germanium (trilayer technique). The exposure stage of the trilayer process comprises a first standard dose exposure which draws the fine patterns of the mask. A second exposure at low dose patterns the undercut regions.

of certain mask openings while sending other projections into the ballast layer. The first step is the usual patterning of the finer outlines of the mask, with standard exposure dose. This delimits a small, limited undercut region. The second step patterns the undercut region to the exact desired extension. To that end, the regions delimiting the desired undercut are exposed with a low dose (typically 25% of the standard dose). This suffices to break the ballast copolymer chains but leaves the top PMMA layer undamaged. As an example, the exposure pattern of the sample measured in the experiment on the quasiparticle energy relaxation, and the pattern for the proximity effect experiment will be detailed in section 1.1.3.

2.1.2.2   Development

Bilayers are usually developed for 35 s in a solution of MIBK diluted at 25% vol. in propanol-2, and rinsed in propanol-2. The suspended mask is then ready for the metal deposition step.

Trilayers can be developed either similarly, or for 10 s in a solution of cellosolve (glycol ethyl monoethyl ether), diluted at 30% vol. in methanol, and rinsed in propanol-2. This development only dissolves the fragments in the top layer since the solvent cannot reach the MAA layer, which is protected by the germanium. The undercut in the MAA will be realized through a wet etching step subsequent to the transfer to the germanium of the pattern in the PMMA.

2.1.2.3   Etching of the germanium layer (trilayer process)

The openings in the PMMA are transferred to the germanium layer by an anisotropic reactive ion etching of the sample in a low-pressure SF6 plasma. (SF6 throughput 5 standard cube centimeter per second (sccm), $P = 2 \times 10^{-3}$ mbar, accelerating voltage $V = 100$ V, 40 to 80 s-long etch. It is extremely useful to monitor this step with laser interferometry, in order to avoid broadening the openings in the mask). The copolymer layer is then etched in an anisotropic oxygen plasma (O_2 throughput 10 sccm, $P = 2 \times 10^{-3}$ mbar, $V = 300$ V, duration 8 min). If regular undercuts are needed, this anisotropic etch can be followed by an isotropic etch in a high-pressure oxygen plasma (O_2 throughput 10 sccm, $P = 0.1$ mbar, $V = 100$ V during 10 min). If large undercuts are needed, it is best to perform a wet etch by dissolving the exposed MAA fragments in MIBK-propanol-2, at room temperature for 20 to 80 s. However, fine copolymer fragments may then remain in the fine mask openings. These are removed easily by a 5 mn-long anisotropic dry etch with the same parameters as previously.

2.1.2.4 Metal deposition and oxidation

Once the mask is completed, the deposition of metals and fabrication of tunnel barriers proceed in an electron gun evaporator. The sample is positioned on a tiltable sample holder. Metals are deposited in a pressure of 10^{-6} mbar, at a typical rate of 1 nm/s. The principle of the evaporation is sketched in Fig. 2.4 for the example of a deposition at two angles through a single slit. Contacts or junctions between different materials are obtained by deposition
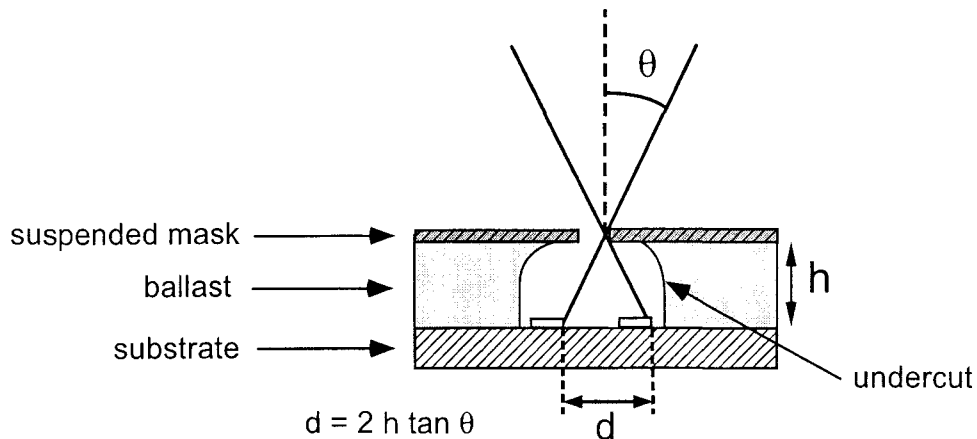
Fig. 2.4. Principle of the metal deposition at two angles through a suspended mask.

through several slits, as shown in Fig. 2.3 and 2.5. The first shadow of one slit overlaps with part of the second shadow of the other slit. Tunnel barriers are formed by introducing a few mbar of an $oxygen_{10\%}$-$argon_{90\%}$ mixture between depositions of the materials forming the overlap, thereby oxidizing the first metal. After deposition, the sample is placed in a bath of acetone at 50 °C until the resist and the mask are lifted off. The contacts and junctions are then tested at room temperature, by measuring the circuit resistances in parallel with a variable resistor $(0 \rightarrow 6 \ M\Omega)$, and connected to a multimeter through 1 $M\Omega$ resistors. In order to avoid destroying the junctions or melting the long narrow wires, a lead shorting all the connection pads was patterned along with the sample, and opened just before measurement.

2.1.3 Examples: two particular samples fabricated with the trilayer process

2.1.3.1 Sample measured in the quasiparticle energy relaxation experiment

As explained in chapter 4, in the experiment on the energy relaxation of quasiparticles, the
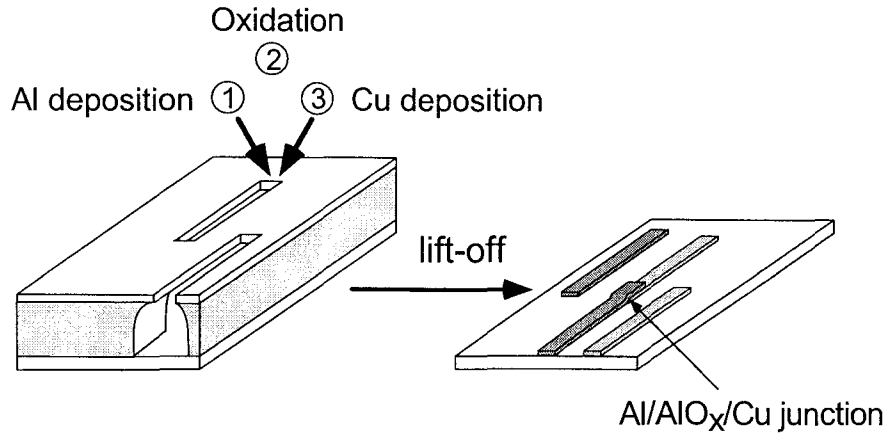
Fig. 2.5. Fabrication of a superconducting/normal tunnel junction in a two-angle deposition process. In all our experiments, the superconductor is aluminum, the normal metal is copper, and the insulating layer is aluminum oxide.

energy distribution function at a given position of a copper wire was deduced from the conductance of a tunnel junction formed between the wire and a superconducting probe. The copper wire itself was connected to two much thicker copper pads which played the role of reservoirs. These different elements were produced by the evaporation of successively 30 nm of Al at a $30°$ angle (top shadow in the SEM picture of Fig. 2.6), oxidized right afterwards, 30 nm of Cu at a $0°$ angle, and 450 nm of Cu at a $-30°$ angle with respect to the normal to the sample plane. These materials were deposited through a germanium mask obtained with an exposure pattern described hereafter. The top panel of Fig. 2.6 shows the pattern of exposure to the electron beam, with the doses encoded in shades of grey. The two horizontal lines will produce the 1.5 and 5 μm-long copper wires; they are connected to a common large pad to the left (corresponding to the grounded reservoir in the experiment) and to two distinct large pads to the right, which will produce the reservoirs (biased at a finite potential in the experiment). The patterns shaped as crooked fingers below the wires will produce the openings through which the superconducting probes will be deposited. The light shaded areas correspond to a region exposed with a dose of 25% the nominal dose. The key feature of this design is that the regions around the fingers are exposed with this low dose, whereas the regions around the wires are not. The consequence of this can be seen from the SEM picture of a typical germanium mask obtained from a chip exposed with this pattern, and presented below: there is a large undercut below the germanium mask around these fingers (light-colored region around

DETAIL OF e-BEAM
EXPOSURE PATTERN

3d evap
(Cu)

2nd evap
(Cu)

1st evap
(Al)

5 µm

additional low-dose exposure

DETAIL OF
GERMANIUM MASK

limit of overetched
region

SAMPLE AFTER METAL
DEPOSITION THROUGH
MASK, AND LIFT-OFF
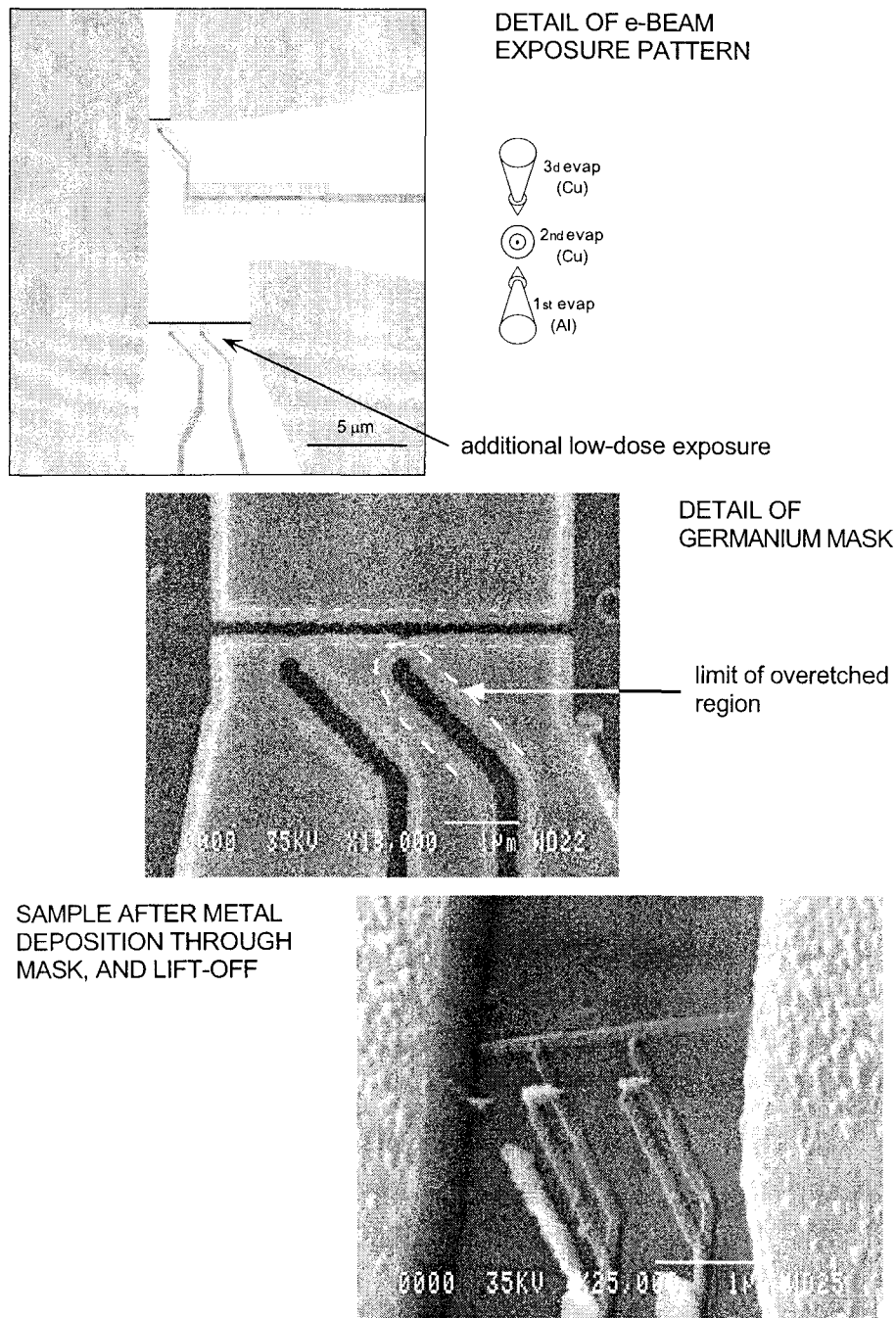
Fig. 2.6. Fabrication of a sample for the quasiparticle energy relaxation experiment. Top: exposure pattern of the center of the chip, with dose encoded in levels of gray. The arrows indicate schematically the order and angle of deposition of the different metals. Middle: micrograph of the Ge mask on the copolymer, after development and etch of the exposed trilayer. Dark regions correspond to the silicon substrate seen through the openings of the mask. Light regions around the openings delimit the undercut region. The regions around the vertical fingers have had an additional low dose exposure, and consequently have a greater undercut. Lower micrograph: actual sample, seen at an angle, obtained by deposition of Al at 30°, oxidation, and Cu depositions at 0 and -30° relatively to the normal to the sample, through a mask such as the one figured above, although probably with broader overetched regions.

the dark openings, due to the absence of MAA under the germanium), whereas the undercut around the opening of the wire is much smaller. As a result, only the vertical copper deposition will project the image of the wire opening onto the substrate. The upward aluminum deposition will send the projection of the wire opening into the ballast resist, thereby avoiding an unwanted aluminum projection which would have been in parallel with the copper wire. The same could in principle be expected of the shadow produced by the downward copper deposition. But as can be seen from the SEM micrograph of the finished sample, traces of a shadow below the wire do appear due to the extra-dose boxes around the fingers. On the contrary, the projection of the finger openings during the upward aluminum deposition is wanted in order to produce the aluminum tunnel probes, which explains why some areas received an extra dose. The copper projection obtained with the vertical deposition is of no nuisance. The image obtained with the last downward deposition could be a problem, however, because of the thickness of this last Cu deposition. Thick images of fine details can prevent a proper lift-off of the resist. To avoid such problems, the deposition angles were chosen large, so that the fine openings clog up well before the entire 450 nm of Cu have been deposited through them. Clogging is insignificant for the large pads, through which the reservoirs are deposited on each side of the wires in the last downward evaporation.

2.1.3.2   Sample for the proximity effect measurement

This sample comprised four different elements (see Fig. 2.7). The two first elements were two similar circuits (labeled **a** and **b**, where **a** is pictured at the bottom) made of a superconducting aluminum wire (wire at an angle in the picture) in good contact with a normal copper metal wire (horizontal). The density of states in the copper wire at a given position was probed by measuring the conductance of the tunnel junction formed by this copper wire and another copper wire (vertical in the picture) overlapping the wire at that position. Two such tunnel probes were fabricated in the circuit shown in the SEM photograph (corresponding to exposure pattern **a**), and a probe placed at an intermediate position was fabricated on the second circuit (exposure pattern **b**). These two circuits require a good NS contact and an NIN tunnel barrier. A third element of the sample was a reference NIS tunnel junction, designed to measure the density of states of the superconductor. The fourth element (**d**) was a long SNIN sandwich, the critical temperature of which provided a lower limit for the transparency of the NS contact.

All these elements were produced by tilting the sample counterclockwise by 45° in its plane, and depositing the normal and superconducting metals at three angles respectively to the sample plane. The first deposition was a 20 nm evaporation of aluminum normally to the sample plane, immediately followed by the deposition of 25 nm of copper at a -20° angle. In this experiment, a tunnel junction with normal electrodes in zero magnetic field was required, since the proximity effect is destroyed by a weak magnetic field. Therefore the usual Al-Al_2O_3-Al junctions could not be used. Instead we fabricated Cu-Al_2O_3-Cu junctions, by depositing thin Al layers and then oxidizing them completely. We first deposited a 1.4 nm-thick layer of Al at a -20° angle, in a He pressure of 10^{-4} mbar in order to insure an isotropic deposition of the Al. Without this precaution, the sides of the Cu electrodes may remain uncovered, resulting in shorts. The Al was then oxidized in a 80 mbar mixture of oxygen (10%) and argon (90%) for 10 min. This sequence was repeated at an angle of 20°. We then deposited 30 nm of copper at a 20° angle. Figure 2.7 explains how the different features could be obtained with this sequence. The top box figures the e-beam exposure pattern of the center of the chip, done at magnification 1000, with the doses encoded in shades of grey. The patterns denoted by **a** and **b** are the proximity circuits, of which **a** is magnified below. The light gray region corresponds to the region which is exposed with 25% of the nominal dose, and thus gives the extension of the region under the germanium mask where the MAA will be removed. As can be seen in the SEM photograph below, the consequence is that the three projections of the vertical openings are reproduced on the substrate, and so are the three projections of the horizontal wire. On the contrary, only the central shadow of the tilted opening extends continuously from the contact with the horizontal wire to the lead. The side shadows are projected onto the substrate only near the contact region, but are projected onto the resist further out, and thus are stripped off in the lift-off process.

The pattern denoted by **c,** and magnified below, is the pattern which produces the NIS tunnel junction pictured in the bottom right SEM micrograph. As in the proximity circuit, the superconducting wire is the tilted central shadow. But in this device, it is not covered by the copper wire immediately deposited after the aluminum (lower horizontal shadow). Instead, because of the relative disposition of the two openings in the mask, the superconducting wire is oxidized in all three oxidation steps and then covered by the top projection of the horizontal
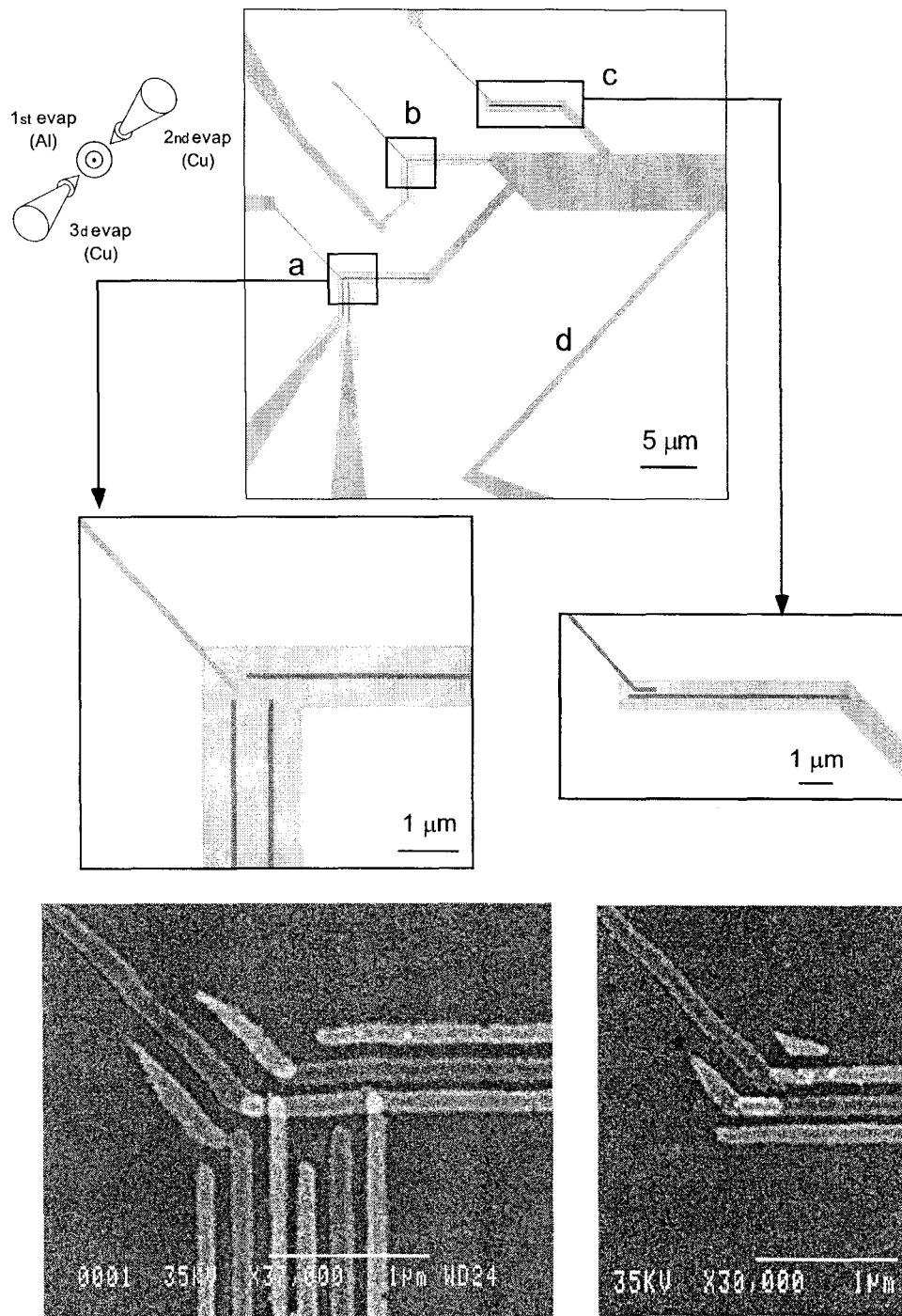
Fig. 2.7. Steps in the fabrication of the sample measured in the experiment on the proximity effect. Top: exposure pattern of the central part of chip. Circuits a and b: proximity circuits; c: pattern leading to the reference SIN junction; d: strip leading to the NS sandwich. The arrows represent the order and angle of deposition of the various metals. Bottom: Left: SEM micrograph of finished circuit a. Right: SEM micrograph of finished circuit c.

opening. Here also, because of the absence of low dose box around the tilted opening, the lower shadow, which would otherwise form a good SN contact in parallel with the SIN junction, is stripped away.

Finally, the materials deposited through the opening in the mask produced by the exposure of the strip labeled **d** will overlap in a central region, forming a SNIN sandwich, the resistance of which will be measured as a function of temperature.

2.2   Sample measurement at low temperature

The chip is glued with silver paint to a thin copper plate fixed onto an integrated circuit connector, which plays the role of the sample holder. The pads of the circuit are connected to the pins of the connector with 25 μm-wide gold wires, using ultrasonic bonding. The sample holder is then plugged into a socket installed in a copper box thermally anchored to the mixing chamber of the dilution refrigerator. The chip is thermally anchored through a copper braid tightly screwed onto the copper plate of the sample holder. The sample box and the last stage of electrical filtering lie in another shielded copper box anchored to the mixing chamber of the dilution refrigerator. The sample box contains a small superconducting coil, which was used to apply a small magnetic field to the NS-QUIDs.

Electrical connections to the sample are made through filtered coaxial lines (see Fig. 2.8). Lossy inductive filters as well as microfabricated distributed RC filters [2] are used. They are carefully anchored to the dilution refrigerator, thereby insuring the thermalization of the electrical lines. The current-voltage characteristics of the sample are obtained by measuring the voltage drop across the sample in series with the last stage filter, amplified at the output of a twisted pair by a low-noise, battery powered pre-amplifier (Ithaco model 1201), as a function of current. The current I in the sample is produced by applying an input bias voltage V_b to a bias line consisting of a voltage divider in series with a resistance. According to the desired load line, this resistance can be switched to either 3 MΩ or $\sim$ 30 kΩ with a mechanical switch in a shielded box in the helium bath at 4 K. The current is thus not directly measured, but is calculated from the input voltage, the measured voltage on the sample and the resistance values of the filters and resistors in lines, which are determined at each cool-down. To measure differential $dI/dV(V)$ conductance curves, a small AC component is added to the DC bias voltage, and a lock-in detection is performed with a SR830. The bias and output voltages were recorded on a digital oscilloscope (NicoletPro34).

An important feature of the measurement apparatus is the possibility to measure in one cool-down several circuits with a single bias line and a single twisted pair. To this end, the output of the last filter common to the bias and measuring lines is connected to a 12-position commercial commutator in which the friction was minimized, of which every other position is wired to the sample. The positions are marked by six resistors of known value connected
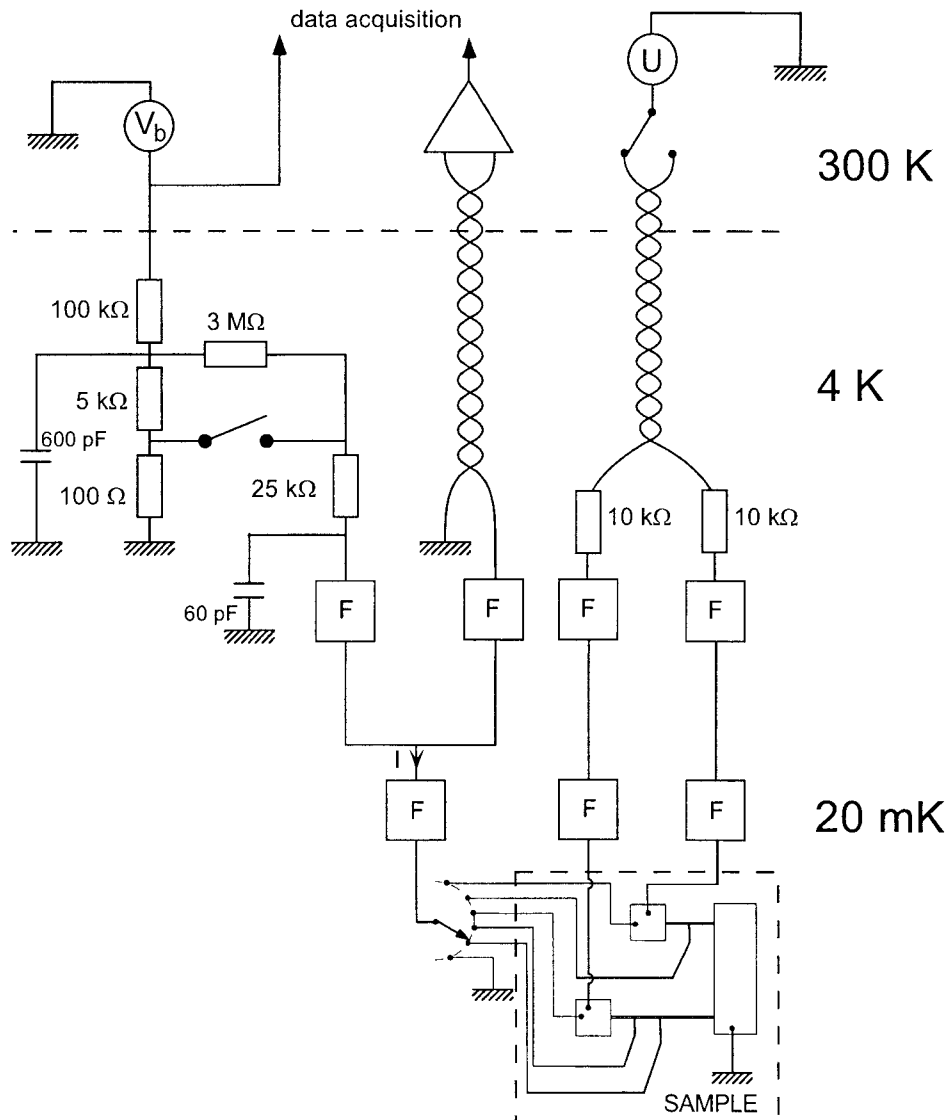
Fig. 2.8. Schematics of the electrical wiring of the experiment inside the dilution refrigerator, in the case of the quasiparticle energy relaxation experiment. The current through the sample is supplied by a bias voltage V_b applied to a resistance of 3 MΩ or 25 kΩ. The voltage across the sample in series with a filter F is brought to a preamplifier at room temperature through a twisted pair. An additional twisted pair is used to bias the mesoscopic wire to a voltage U.

in between. Positions are switched by a motor (ESCAP, M915L61) anchored to the still of the dilution refrigerator. The commutator itself is thermally anchored to the mixing chamber. Transmission between motor and commutator is done with a plastic fiber. Commutation produces a 20-50 mK rise in temperature.

A second twisted pair was added between room temperature and the 1 K pot (see Fig. 2.8), in order to enable measurements of small resistances. Following the technique of D. C. Glattli *et al.* [3] adapted by P. Joyez, this twisted pair consists in two intertwined microcoaxial cables. Each coaxial cable is made of a manganin wire of diameter 0.1 mm (resistance $\sim$ 60 Ω/m) coated by a polyimide insulating layer, glued into a stainless steel tube of internal diameter 0.4 mm and external diameter 1 mm. This cable has a distributed capacitance of about 20 pF/m. A 10 kΩ resistance was added at the bottom end of the cable, producing a cut-off frequency of 200 kHz. Both lines of the pair were also used as independent bias lines, for instance in the case in the experiment on the quasiparticle energy relaxation (see Fig. 2.8).

REFERENCES

[1] V. Bouchiat, Ph.D. thesis, Université Paris 6 (1997).

[2] D. Vion, P. F. Orfila, P. Joyez, D. Esteve, and M. H. Devoret, *J. Appl. Phys.* **77**, 2519 (1994).

[3] D. C. Glattli, P. Jacques, A. Kumar, P. Pari and L. Saminadayar, *J. Appl. Phys.* **81**, 7350 (1997).

Chapter 3
Observation of energy redistribution between quasiparticles in mesoscopic wires

3.1 Can the interaction between quasiparticles be probed?

Electrons in metals constitute the most common example of a Fermi fluid. Despite the underlying complexity of this many-body interacting system, the independent electron model can quantitatively account for most properties of bulk metals, provided that proper effective parameters are chosen for the electrons [1]. The explanation of this amazing simplification is due to Landau who showed that any fluid of interacting fermions maps onto a fluid of independent fermions, the Landau quasiparticles. A quasiparticle excitation involves a many-body rearrangement of the electron ground state wave-function. The residual interaction between quasiparticles is small because the interactions between the real particles are almost completely encapsulated inside each quasiparticle. An "electron-like" quasiparticle can be viewed as an extra electron surrounded by a screening cloud. The Coulomb interaction between electrons is thus replaced by a screened Coulomb interaction between quasiparticles.

The theory of Fermi liquids [2], which extends Landau's pioneering work, succeeds in predicting the quasiparticle spectrum, the response to external fields, and the residual interaction between quasiparticles, which is well described by two-body quasiparticle-quasiparticle scatter-

ing. It gives a finite width to the quasiparticle levels, and provides an internal thermalization mechanism for the quasiparticles. In a metal with perfect crystalline arrangement, the width of a level of energy E above the Fermi energy is predicted to follow a E^2 law, so that quasiparticles at the Fermi level are perfectly defined. In the case of metals in which quasiparticles undergo elastic scattering by impurities or by the sample surface, the theory of diffusive conductors developed in the 80s by Altshuler and coworkers [3] predicts a series of different behaviors, which depend on the energy considered compared to the Thouless energies characteristic of the sample dimensions. In all cases, it predicts that, unless the elastic scattering is extremely important, quasiparticles are still well defined excitations near the Fermi energy. Evidence for the existence of a residual interaction is provided by the observation of quasiparticle thermalization in samples cooled below 1K. Indeed, whereas at temperatures above 1K quasiparticles and phonons are well coupled so that the quasiparticles are directly thermalized by the phonons to the phonon temperature, the two systems are decoupled below 1K. The experiment described in this chapter provides direct evidence for energy redistribution between quasiparticles, and gives access to the corresponding scattering rate.

In order to observe energy redistribution between quasiparticles, one must bring the conductor which contains them out of thermal equilibrium. We have implemented such a situation by placing a thin wire between two thick electrodes biased at different potentials. These electrodes act as quasiparticle reservoirs [4]: they absorb all incoming quasiparticles, and emit quasiparticles with an energy distribution given by their own Fermi distribution. Quasiparticles interact while they diffuse across the wire. Since the energy redistribution process is expected to affect the energy distribution function of quasiparticles at all points in the wire, one can in principle extract the energy redistribution rate between quasiparticles by measuring this distribution in a few points along the wire. In our experiments, the energy distribution at a given position wire is deduced from the conductance of a tunnel junction between the wire and a superconducting electrode underneath. Information on the energy-dependence of the energy redistribution rate is only accessible if measurable redistribution occurs, but is still too weak to establish thermal equilibrium. We have fabricated samples with different diffusion times, in order to cover the whole range of possible regimes, from the non-interacting case to the fully thermalized one. These limiting regimes are discussed in the next section.

3.2   Energy distribution function of quasiparticles in a mesoscopic diffusive wire

We choose as the reference energy the electrochemical potential of the reservoir situated at $X < 0$. When the reservoir at $X > L$ is biased at potential U, its electrochemical potential is $-eU$.
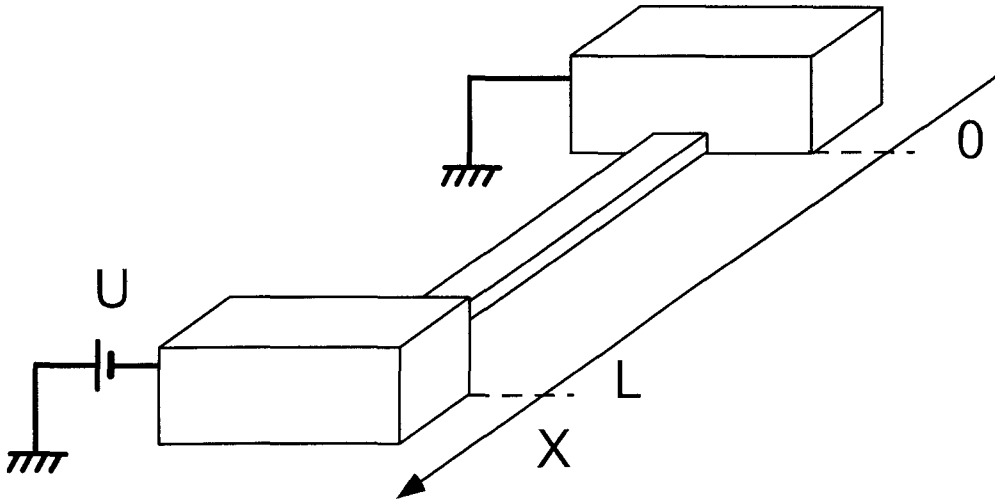
Fig. 3.1. Principle of the experiment: a wire of length L is connected to two thick and large electrodes. A bias voltage U is applied between the electrodes.

The distribution functions in the reservoirs are therefore Fermi-Dirac functions at the temperature T of the reservoirs, shifted in energy by eU. The shape of the distribution function $f(x, E)$ in the wire at position $x = X/L$ is determined by the diffusion and the inelastic scattering processes. We consider here the different quasiparticle scattering mechanisms occurring in metals: scattering by phonons and scattering by quasiparticles. Several authors have evaluated the distribution function of quasiparticles for a wire in the different limiting regimes [5–7] , and we hereafter present their results.

3.2.1   No quasiparticle scattering, no phonon scattering

In the absence of inelastic scattering, the total energy of each quasiparticle is conserved along the wire. The distribution function $f(x, E)$, which reflects the probability to find an electron of energy E at position x, therefore obeys the stationary quasiclassical Boltzmann
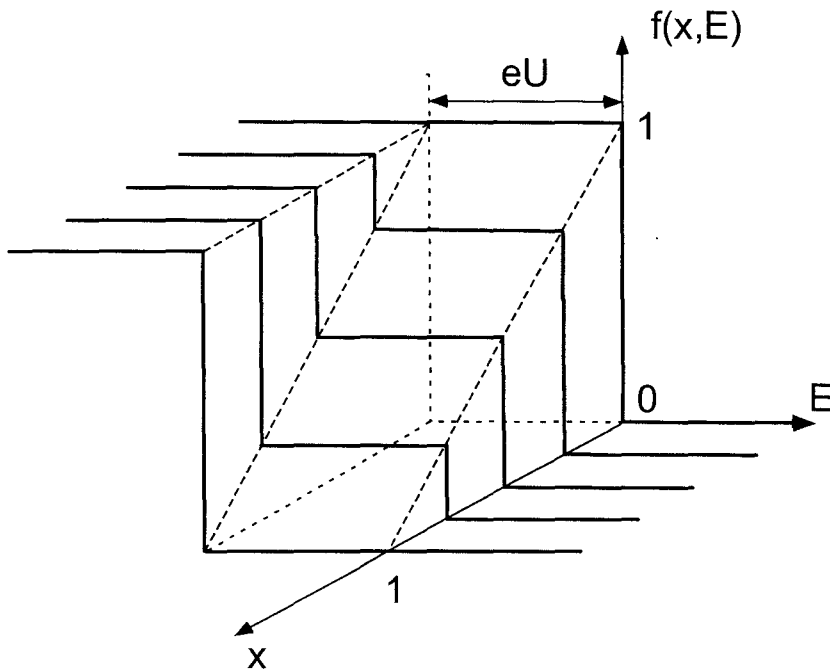
Fig. 3.2. Distribution function $f(x, E)$ as a function of the energy E (horizontal axis) and position $x = X/L$ (oblique axis), in the limit of non-interacting quasiparticles. Here we have taken $k_B T \ll eU$.

equation [5]

$$\frac{\partial^2 f(x, E)}{\partial x^2} = 0. \tag{3.1}$$

The distribution function thus linearly interpolates between the boundary distribution functions and reads:

$$f(x, E) = (1 - x) f_T(E) + x f_T(E + eU), \tag{3.2}$$

where $f_T(\varepsilon) = \left(1 + \exp\frac{\varepsilon}{k_B T}\right)^{-1}$ is the Fermi-Dirac function at the reservoir temperature T. If $k_B T \ll eU$, the distribution function has a step at $f(x, E) = x$ for $-eU < E < 0$, as shown in Fig. 3.2. In this regime, neither the electrochemical potential nor the electronic temperature is defined. However, the electric potential is still given by Ohm's law and varies linearly.

3.2.2   Strong interaction between quasiparticles

In the case of strong interaction between quasiparticles, and in the absence of interaction between quasiparticles and phonons, thermal equilibrium is achieved locally. The distribution function is a Fermi-Dirac function: $f(x, E) = f_{T_e(x)}(E - \mu(x))$ where $\mu(x) = -eUx$ is the local electrochemical potential, and $T_e(x)$ the local electron temperature. The temperature
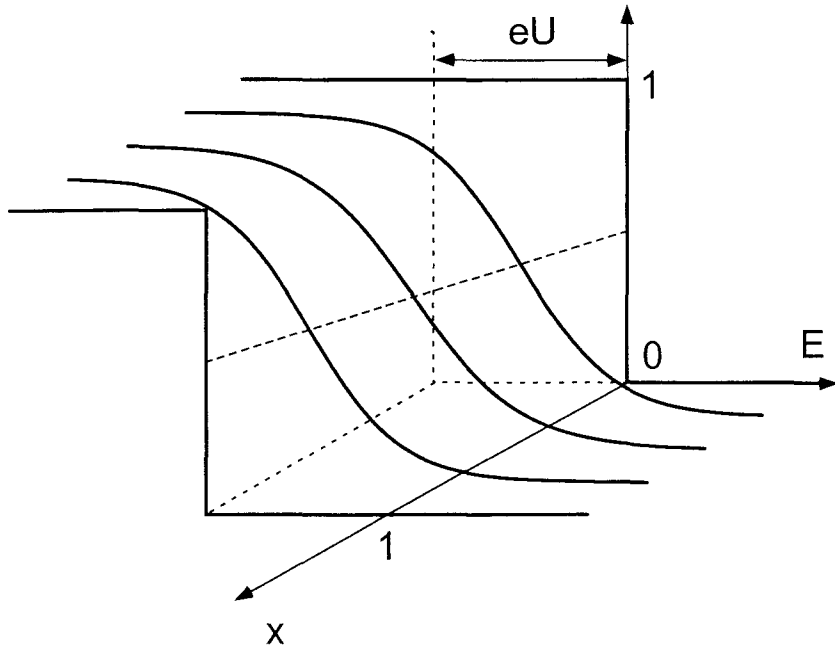
Fig. 3.3. Distribution function in the limit of strong interaction between quasiparticles, and negligible quasiparticle-phonon interaction.

$T_e\left(x\right)$ obeys the heat equation [7,9,10] :

$$\frac{\partial}{\partial x}\left(\kappa\frac{\partial T_e}{\partial x}\right) + \sigma U^2 = 0, \tag{3.3}$$

where σ is the electrical conductivity and κ is the electronic heat conductivity. Using the Wiedemann-Franz law $\kappa = \mathcal{L}\sigma T_e$, where $\mathcal{L} = \frac{\pi^2}{3}\left(\frac{k_B}{e}\right)^2$ is the Lorenz number, and given the boundary conditions $T_e\left(0\right) = T_e\left(L\right) = T$, we find

$$T_e\left(x\right) = \sqrt{T^2 + x\left(1 - x\right)U^2/\mathcal{L}}. \tag{3.4}$$

The spatial variation of the resulting distribution function is shown in Fig. 3.3 for $T = 0$. A recent measurement by Steinbach et al. [10] of the shot noise in this "hot electron regime" agrees with these predictions.

3.2.3   Limit of strong interaction between quasiparticles and phonons

In the presence of strong quasiparticle-phonon interaction, quasiparticles and phonons thermalize: $f\left(x,E\right) = f_T\left(E - \mu\left(x\right)\right)$ with $\mu\left(x\right) = -eUx$. The spatial variations of the distribution function in this case is shown in Fig. 3.4.
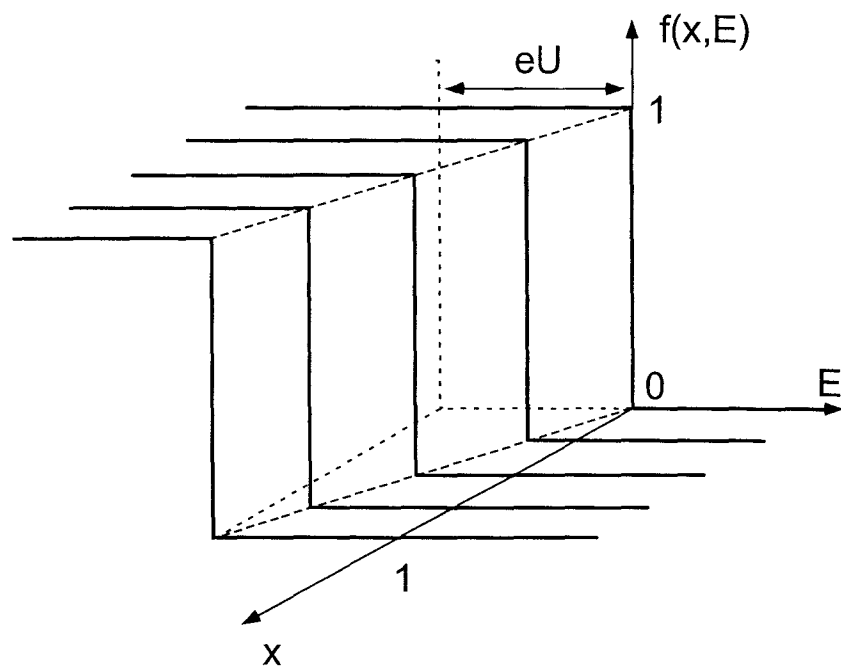
Fig. 3.4. Distribution function in the limit of strong interaction between quasiparticles and phonons.

3.2.4 Relevant mechanisms in copper wires at low energy and temperature

In the case of the copper wires with lengths of the order of a micrometer, the effect of electron-phonon scattering on the distribution function is negligible at the energies of our experiments. Indeed, in the sub-meV energy range, the thermalization by phonons is significant only in wires of length greater than a few centimeters [8] . The interaction between quasiparticles is thus the sole mechanism able to redistribute the energy among quasiparticles. Other possible inelastic processes such as spin-flip scattering by magnetic impurities, discussed in the proximity effect experiments, can destroy the quantum coherence of quasiparticles but cannot alter the energy distribution function, since they conserve the quasiparticle energy.

3.3   Measurement of the energy distribution function in metallic wires (article)

We hereafter reprint the article "Energy distribution function of quasiparticles in mesoscopic wires", by H. Pothier, S. Guéron, Norman O. Birge, D. Esteve, and M. H. Devoret, published in Physical Review Letters **79**, 3490 (1997).

A detailed description of the measurement of the distribution function in the middle of wire 1 was also given in "Energy distribution of electrons in an out-of-equilibrium metallic wire", Z. Phys. B **104**, 178-182 (1997).

Measurement of the energy distribution function of quasiparticles in mesoscopic wires

H. Pothier, S. Guéron, Norman O. Birge*, D. Esteve, and M. H. Devoret

Service de Physique de l'Etat Condensé, Commissariat à

l'Energie Atomique, Saclay, F-91191 Gif-sur-Yvette, France

(to be published October 1997)

Abstract

We have measured with a tunnel probe the energy distribution function of Landau quasiparticles in metallic diffusive wires connected to two reservoir electrodes, between which a bias voltage was applied. The distribution function in the middle of a 1.5 μm-long wire resembles the half sum of the Fermi distributions of the reservoirs. The distribution functions in 5 μm-long wires are more rounded, due to interactions between quasiparticles during the longer diffusion time across the wire. From the scaling of the data with bias voltage, we find that the scattering rate between two quasiparticles varies as ε^{-2}, where ε is the energy transferred.

PACS numbers: 73.23.-b, 71.10.Ay, 72.10.-d

The present understanding of metals is based on Landau's theory of Fermi liquids. In this model, the elementary excitations of the fluid of interacting electrons are nearly independent fermionic quasiparticles [1]. In disordered metals, residual interactions between quasiparticles lead in mesoscopic samples to measurable corrections to the density of states, and limit the phase coherence of quasiparticles [2]. These effects have been widely investigated experimentally and theoretically in the last twenty years [3]. However, the most elementary manifestation of interactions, namely the transfer of energy between quasiparticles, has only been observed at energies of order 1 eV by time-resolved spectroscopy of a metallic film following a laser pulse [4], and in the meV range through the establishment of an electron temperature in the so-called hot-electron regime [5]. Indications as to the speed at which this thermalization proceeds were obtained in recent shot noise experiments [6].

In this Letter, we report a direct measurement of the energy transfer rates between quasiparticles in diffusive metallic wires. We have measured the energy distribution function of quasiparticles in wires in a stationary out-of-equilibrium situation, at low enough temperature so that quasiparticle-quasiparticle interaction is the dominant inelastic process. The deviations of the energy distribution function from the Fermi distribution give access to the energy transfer rates. We force the wire out of equilibrium by placing it between two reservoir electrodes [7] biased at different potentials, 0 and U, as shown in Fig. 1. The local distribution function is probed with a superconducting electrode connected to the wire by a tunnel junction. The experiment exploits the property of the distribution function to have different shapes depending on the amount of inelastic collisions a quasiparticle experiences during its diffusion time through the wire.

The steady-state distribution function $f(x, E)$ in a metallic wire of length L, which depends on the position $X = xL$ measured from the right electrode, and on the energy E, results from the combined action of the elastic diffusion and of interactions. It obeys the Boltzmann equation [8,9]:

$$\frac{1}{\tau_D} \frac{\partial^2 f(x, E)}{\partial x^2} + \mathcal{I}_{\text{coll}}(x, E, \{f\}) = 0. \tag{1}$$

48

Here $\tau_D = L^2/D$ is the diffusion time through the wire, and $\mathcal{I}_{\text{coll}}(x, E, \{f\})$ is the collision integral due to the inelastic scattering processes. In the absence of electron-phonon scattering, $\mathcal{I}_{\text{coll}}(x, E, \{f\})$ is due to interactions between quasiparticles only. The boundary conditions are imposed by the reservoir electrodes: $f(0, E) = \left(1 + \exp\frac{E}{k_B T}\right)^{-1}$ and $f(1, E) = \left(1 + \exp\frac{E + eU}{k_B T}\right)^{-1}$. If no scattering between quasiparticles occurs during the diffusion time, the distribution function is the solution $f_0(x, E)$ of equation (1) with no collision integral [8]:

$$f_0(x, E) = (1 - x)f(0, E) + xf(1, E). \tag{2}$$

The function $f_0(x, E)$ has a well-defined intermediate step for $|eU| \gg k_B T$, as shown as solid lines in Fig. 1. If, on the contrary, many inelastic collisions occur during the diffusion time, quasiparticles reach local thermal equilibrium. In this hot-electron regime, the distribution function is a Fermi function with electrochemical potential $\mu(x) = -eUx$ and effective temperature $T_{\text{eff}}(x) = \sqrt{T^2 + x(1 - x)U^2/\mathcal{L}}$, where $\mathcal{L} = \frac{\pi^2}{3}\left(\frac{k_B}{e}\right)^2$ is the Lorenz number [6,9] (see dotted lines in Fig. 1). In intermediate situations, the shape of the distribution function depends on the collision integral $\mathcal{I}_{\text{coll}}(x, E, \{f\})$, thereby giving information on how quasiparticles interact [10].

The distribution function $f(E) \equiv f(x_J, E)$ at the position x_J of the tunnel junction is related to the differential conductance of the junction through

$$\frac{dI}{dV}(V) = \frac{1}{R_T}\int dE\, \frac{\partial n_S}{\partial E}(E - eV)\{f(E) + \Theta(E - eV) - 1\}, \tag{3}$$

where R_T is the tunnel resistance of the junction, $n_S(E) = \text{Re}\left(E/\sqrt{E^2 - \Delta^2}\right)$ is the normalized BCS density of states with Δ the energy gap of the superconducting electrode, and $\Theta(E)$ is the Heavyside function. Equation (3) is written in the limit $k_B T \ll \Delta$. Effects of the electromagnetic environment [11] and the modification of the density of states due to interactions [12] have been neglected. The distribution function $f(E)$ is obtained from the deconvolution of the measured $\frac{dI}{dV}(V)$ using Eq. (3) [13].

All samples were fabricated by depositions at several angles through a germanium mask patterned with e-beam lithography [14]. The wires, made of copper, are 110 nm wide and

49

45 nm thick. Wire 1 and wire 2 were deposited simultaneously, and have lengths 1.5 μm and 5 μm, respectively. Wire 3, fabricated separately, is also 5 μm-long. The electrodes at the ends of the wires are 500 nm-thick copper pads with an area of about 1 mm^2, thereby implementing adequate reservoirs. The film forming the wires forms the bottom layer of the pads, which were thickened in a subsequent evaporation [10]. The superconducting probes, made of aluminum, were positioned in the middle of each wire. An additional superconducting probe was positioned 1.1 μm away from the right end of wire 3. The areas of the tunnel junctions are 300×110 nm^2 in wires 1 and 2, and less than 50×50 nm^2 in wire 3. The samples were mounted in a copper box thermally anchored to the mixing chamber of a dilution refrigerator. Electrical connections were made through filtered coaxial lines [15], and measurements were carried out at a temperature of 25 mK. From the low-temperature resistances of wire 1 and 2, 14.5 Ω and 53 Ω, we estimate the diffusion constant in the wires $D \sim 65$ cm^2/s (± 10 cm^2/s, given the uncertainties on the geometry) and the diffusion times $\tau_D \sim 0.35$ ns and $\tau_D \sim 4$ ns. Wire 3 is more resistive, $R = 76$ Ω, yielding $D \sim 45$ cm^2/s and $\tau_D \sim 6$ ns.

The distribution functions in the center of wire 1 for $U = 0, 0.1$ and 0.2 mV are shown in the top left panel of Fig. 2. They are obtained from the deconvolution of $dI/dV(V)$ curves such as the one shown in the inset, which is taken at $U = 0.2$ mV. The parameters for the deconvolution of the $dI/dV(V)$ curves were obtained from a fit of Eq. (3) to the measured $dI/dV(V)$ at $U = 0$, with $f(E)$ a Fermi function. From the fit we find a value of the gap of our aluminum $\Delta = 0.20$ meV, close to the bulk value, the tunnel resistance $R_T = 10$ kΩ, and the temperature of the Fermi function $T = 30$ mK. This latter value is in reasonable agreement with the measured temperature $T = 25$ mK. For $U \neq 0$, the functions $f(E)$ resemble the staircase shape expected from Eq. (2). For comparison, we have plotted as a dotted line in Fig. 2 the predicted non-interacting quasiparticle distribution for $U = 0.2$ mV. Deviations from the prediction of Eq. (2) are much more apparent in the data from wire 2 ($L = 5$ μm), shown in the top right panel of Fig. 2 for the same values of U. As could be expected from the diffusion time through this wire which is more than ten times greater

than through wire 1, the distribution functions are more rounded. An almost complete thermalization of the quasiparticles occurs in wire 3, as shown by the distribution functions plotted in the bottom left panel of Fig. 2. The curves of this latter panel can be fitted with a Fermi function at a temperature 5% higher than the effective temperature corresponding to the voltages U applied, given by $T_{\text{eff}} = \sqrt{T^2 + \frac{U^2}{4\mathcal{E}}}$. These distributions show that phonon emission, which would tend to cool the electrons below T_{eff}, can indeed be neglected. The fact that the observed temperatures are 5% higher than the calculated T_{eff} is consistent with an incomplete thermalization, as better seen from the distribution functions measured with the junction positioned 1.1 μm away from the grounded reservoir, shown in the bottom right panel of Fig. 2. The kink in these curves at zero energy reflects the sharp discontinuity at zero energy of the Fermi distribution of the nearby reservoir, which has not been washed out by interactions at this distance.

A striking scaling property of the data is shown in Fig. 3 where the distribution functions, measured for voltages increasing from $U = 0.05$ mV to $U = 0.3$ mV by steps of 0.05 mV, are plotted as a function of the reduced parameter E/eU. Except for the smallest voltage $U = 0.05$ mV, all the curves measured at a given position coincide. This property leads to a phenomenological expression for the collision integral in Eq. (1), as we now show.

The collision term $\mathcal{I}_{\text{coll}}(x, E, \{f\})$ in the Boltzmann equation is the difference of two terms: an in-collision term, the rate at which particles are scattered in the state of energy E, and an out-collision term:

$$\mathcal{I}_{\text{coll}}(x, E, \{f\}) = \mathcal{I}_{\text{coll}}^{\text{in}}(x, E, \{f\}) - \mathcal{I}_{\text{coll}}^{\text{out}}(x, E, \{f\}) \tag{4}$$

with

$$\mathcal{I}_{\text{coll}}^{\text{in,out}}(x, E, \{f\}) = \int d\varepsilon dE' dx' K(x, x', \varepsilon) f_{E+\varepsilon, E}^x \left(1 - f_{E, E-\varepsilon}^x\right) f_{E'}^{x'} \left(1 - f_{E'+\varepsilon}^{x'}\right) \tag{5}$$

where the shorthand f_E^x stands for $f(x, E)$. Following the Landau approach [1], we have assumed that the dominant process is a two-quasiparticle interaction. The kernel function $K(x, x', \varepsilon)$ is proportional to the squared matrix element of the interaction during which

an energy ε is transferred between two particles at positions x and x'. We assume that $K(x, x', \varepsilon)$ only depends on ε since $E \simeq E_F$, $E' \simeq E_F$ and $\varepsilon \ll E_F$. The energy dependence of $K(x, x', \varepsilon)$ is inferred from the scaling property of the data, assuming that the scaling observed at the middle of all three wires and at the side position of wire 3 persists everywhere along each wire. Then, given that the steady state distributions as well as the boundary conditions all depend on E/eU only (if $k_B T \ll eU$), the collision integral must have the same property. Equation (5) then implies that $U^2 K(x, x', \varepsilon)$ is a function of ε/eU only, yielding $K(x, x', \varepsilon) = \frac{g(x, x')}{\varepsilon^2}$, where $g(x, x')$ is a function of space variables. When fitting the solution of Eq. (1), computed for $eU \gg k_B T$, to the experimental curves, we found that the shape of the simulated distribution functions is practically insensitive to the spatial extent of $g(x, x')$: taking a delta function or a constant produces the same shapes. In the following, we assume that the interaction is local, and $g(x, x') \equiv \tau_0^{-1}$ has the dimension of a rate. The shape of the distribution function is then determined by the ratio τ_0/τ_D only. The fits yield $\tau_0/\tau_D = 2.5 \pm 0.2$ for wire 1, $\tau_0/\tau_D = 0.3 \pm 0.05$ for wire 2, and $\tau_0/\tau_D = 0.08 \pm 0.02$ for the lateral position on wire 3. The calculated distribution functions, plotted with open symbols on Fig. 3, account well for the measurements. We have taken for the middle position of wire 3 the same value τ_0/τ_D as for the side position, and find excellent agreement with the data. Given the additional uncertainties on the diffusion times, these results are compatible with an identical value $\tau_0 \sim 1$ ns for wire 1 and wire 2, whereas we get $\tau_0 \sim 0.5$ ns for wire 3. This is consistent with the assumption that the interaction is local, and that its strength does not depend on the length of the wire. The fact that the scaled $U = 0.05$ mV curves do not coincide with the other scaled curves is explained by the rounding effect of the reservoir temperature, which is relatively more important at lower U [16].

In order to test the robustness of our determination of $K(x, x', \varepsilon)$, we have tried to fit our data with a different powerlaw for $K(x, x', \varepsilon)$. We have found that exponents of ε differing from -2 by more than 0.1 are incompatible with the scaling displayed by the data. In addition, we have found that the distribution function is practically insensitive to the interaction law below $eU/4$. The data presented here therefore impose $K(x, x', \varepsilon) \propto 1/\varepsilon^{2 \pm 0.1}$

in the energy range $[E_0, 0.30$ meV$]$ with $E_0 \leq 0.01$ meV.

This energy dependence differs from the prediction $K(x, x', \varepsilon) \propto \varepsilon^{-3/2}$ of the direct calculation of the screened Coulomb interaction between quasiparticles in a homogeneous diffusive medium in the 1D regime [3]. However, the $1/\varepsilon^2$ dependence can be obtained from another calculation in which the quasiparticle interactions are treated by considering the coupling between a quasiparticle and the fluctuating electromagnetic field produced by all the others. This point of view was already successfully used to calculate the dephasing time of a given quasiparticle when the others are in thermal equilibrium [3,17]. In a generalization of this reasoning, we treat the energy transfer between quasiparticles with an arbitrary distribution function, and consider the fluctuations of the electromagnetic field at the scale of the elastic mean free path [18].

Finally, let us mention that our result $K(x, x', \varepsilon) = \frac{\tau_0^{-1}}{\varepsilon^2}$ in the experimental energy window $[E_0, 0.30$ meV$]$ implies an upper bound for the quasiparticle lifetime. For E within this energy range, we obtain $\tau(E) < \tau_0 / \ln(E/E_0)$ where $\tau_0 \sim 1$ ns. At $E = 0.1$ meV, this upper bound is two orders of magnitude *shorter* than the quasiparticle lifetime predicted in diffusive 1D metals [3] with the same diffusion constants as in our samples. Further experiments are needed to clarify this issue.

REFERENCES

* Michigan State University, East Lansing, MI 48824, USA.

[1] D. Pines and P. Nozière, *The Theory of Quantum Liquids,* W.A. Benjamin (1966).

[2] *Mesoscopic Quantum Physics,* Ed. E. Akkermans, G. Montambaux, J.-L. Pichard and J. Zinn-Justin, North Holland (1991).

[3] For a review, see B. L. Altshuler and A. G. Aronov, in *Electron-Electron Interactions in Disordered Systems,* Ed. A. L. Efros and M. Pollak, Elsevier Science Publishers B.V. (1985).

[4] W.S. Fann, R. Storz, H.W.K. Tom and J. Bokor, Phys. Rev. B **46**, 13592 (1992).

[5] C. G. Smith and M. N. Wybourne, Solid State Commun. **57**, 411 (1986); F. C. Wellstood, C. Urbina, and John Clarke, Phys. Rev. B **49**, 5942 (1994).

[6] A. H. Steinbach, J. M. Martinis, and M. H. Devoret, Phys. Rev. Lett. **76**, 3806 (1996); R. J. Schoelkopf, P.J. Burke, A. A. Kozhevnikov, D. E. Prober, and M. J. Rooks, Phys. Rev. Lett. **78**, 3370 (1997).

[7] R. Landauer, IBM J. Res. Develop. **1**, 223 (1957); **32**, 306 (1988).

[8] K. E. Nagaev, Phys. Lett. A **169**, 103 (1992); Phys. Rev. B **52**, 4740 (1995).

[9] V. I. Kozub and A. M. Rudin, Phys. Rev. B **52**, 7853 (1995).

[10] A detailed discussion of the different regimes, as well as details of the sample fabrication and preliminary experimental results, can be found in H. Pothier, S. Guéron, Norman O. Birge, D. Esteve, and M. H. Devoret, Z. Phys. B **104**, 178 (1997).

[11] G.-L. Ingold and Yu. V. Nazarov, in *Single Charge Tunneling,* edited by H. Grabert and M. H. Devoret (Plenum Press, New York, 1992), p. 21.

[12] The relative corrections on the density of states predicted in ref. [3] are at most of the

order of one percent in our copper wires. Experimentally, our neglecting this effect is justified by the good fit of our data at $U = 0$ with Eq. (3) in which $f(E)$ is a Fermi function.

[13] In the experiment, R_T is more than 200 times the resistance of the wire, and we measure $\frac{dI}{dV}(V)$ with V of the order of U, so that the perturbation induced by the probe current can be neglected.

[14] By a selective etching of the polymer underneath the mask, we could control which features of the pattern were reproduced on the substrate for each evaporation. This was achieved by a low-dose electronic exposure of the regions where the polymer below the stencil needed to be dissolved.

[15] D. Vion, P. F. Orfila, P. Joyez, D. Esteve, and M. H. Devoret, J. Appl. Phys. **77**, 2519 (1995).

[16] The experimental curves are well fitted (data not shown) by taking $T_{\mathrm{res}} = 50$ mK for wire 1 and $T_{\mathrm{res}} = 35$ mK for wires 2 and 3. The reservoir temperature T_{res} is higher than the phonon temperature due to the injected power from the wires (see ref. [5]).

[17] B. L. Altshuler, A. G. Aronov, and D. E. Khmelnitskii, J. Phys. **C15**, 7367 (1982).

[18] M. H. Devoret, D. Esteve, S. Guéron, and H. Pothier, in preparation.

FIG. 1. Experimental layout: a metallic wire of length L is connected at its ends to reservoir electrodes, biased at potentials 0 and U. In the absence of interaction, the distribution function at a distance $X = xL$ from the grounded electrode has an intermediate step $f(E) = 1 - x$ for energies between $-eU$ and 0 (solid curves) (we assume $U > 0$). When interactions are strong enough to thermalize electrons, the distribution function is a Fermi function, with a space-dependent temperature and electrochemical potential (dotted curves). In the experiment, the distribution function is obtained from the differential conductance $dI/dV(V)$ of the tunnel junction formed by the wire and a superconducting electrode placed underneath.

FIG. 2. Inset of the top left panel: measured $dI/dV(V)$ of the tunnel junction to wire 1 for $U = 0.2$ mV. In the four panels, distribution functions, obtained from the deconvolution of such $dI/dV(V)$ curves, for $U = 0$, 0.1 mV and 0.2 mV in the middle of a 1.5 μm-long wire with a diffusion constant $D \sim 65$ cm^2/s (wire 1, top left); in the middle of a 5 μm-long wire with the same diffusion constant (wire 2, top right); in the middle (bottom left) and at 1.1 μm from the grounded reservoir electrode (bottom right) of a 5 μm-long wire (wire 3) with $D \sim 45$ cm^2/s. Also plotted as a dotted line in the top left panel is the prediction for the non-interacting distribution function (Eq. (2)) for $U = 0.2$ mV. All measurements were performed at 25 mK. The cross-sectional area of the three wires is nominally the same: 45×110 nm^2. The tunnel resistances of the junctions were $R_T = 10$ kΩ for wires 1 and 2, $R_T = 200$ kΩ for the middle junction on wire 3, and $R_T = 75$ kΩ for the side junction on wire 3.

FIG. 3. Continuous lines in all four panels: distribution functions, for U ranging from 0.05 to 0.3 mV by steps of 0.05 mV, plotted as a function of the reduced energy E/eU, for the same positions as in Fig. 2. Open symbols are best fits of the data to the solution of the Boltzmann equation with an interaction kernel $K(x, x', \varepsilon) = \frac{\tau_0^{-1}}{\varepsilon^2}$: in top panel, open circles correspond to the calculated distribution function in the middle of the wires 1 and 2 ($x = 0.5$), with $\tau_0/\tau_D = 2.5$ and $\tau_0/\tau_D = 0.3$, respectively (both compatible with $\tau_0 \sim 1$ ns). In bottom panels, open diamonds are computed at $x = 0.5$ and $x = 0.25$ with $\tau_0/\tau_D = 0.08$ ($\tau_0 \sim 0.5$ ns).
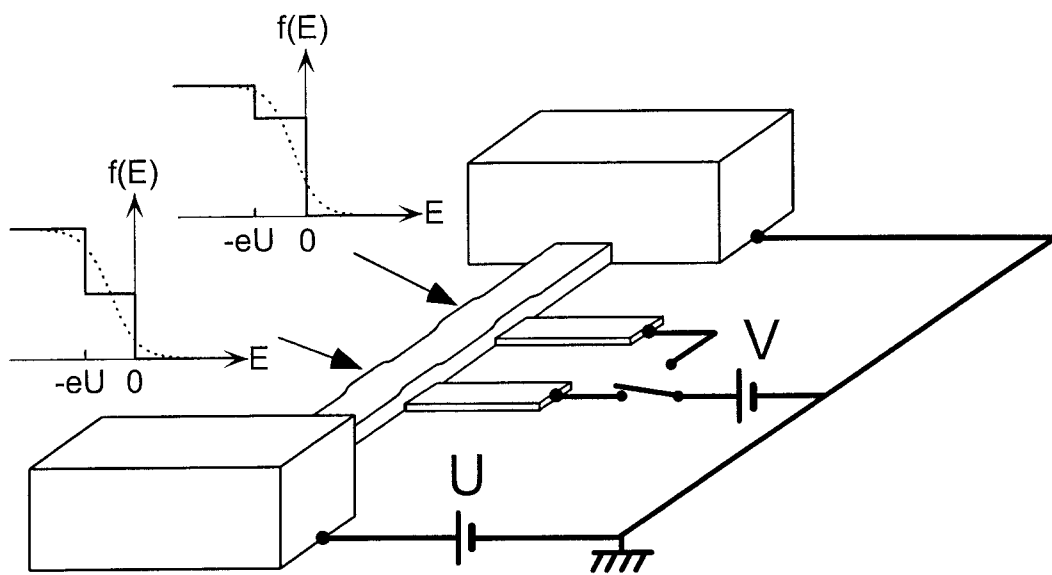
Fig. 1
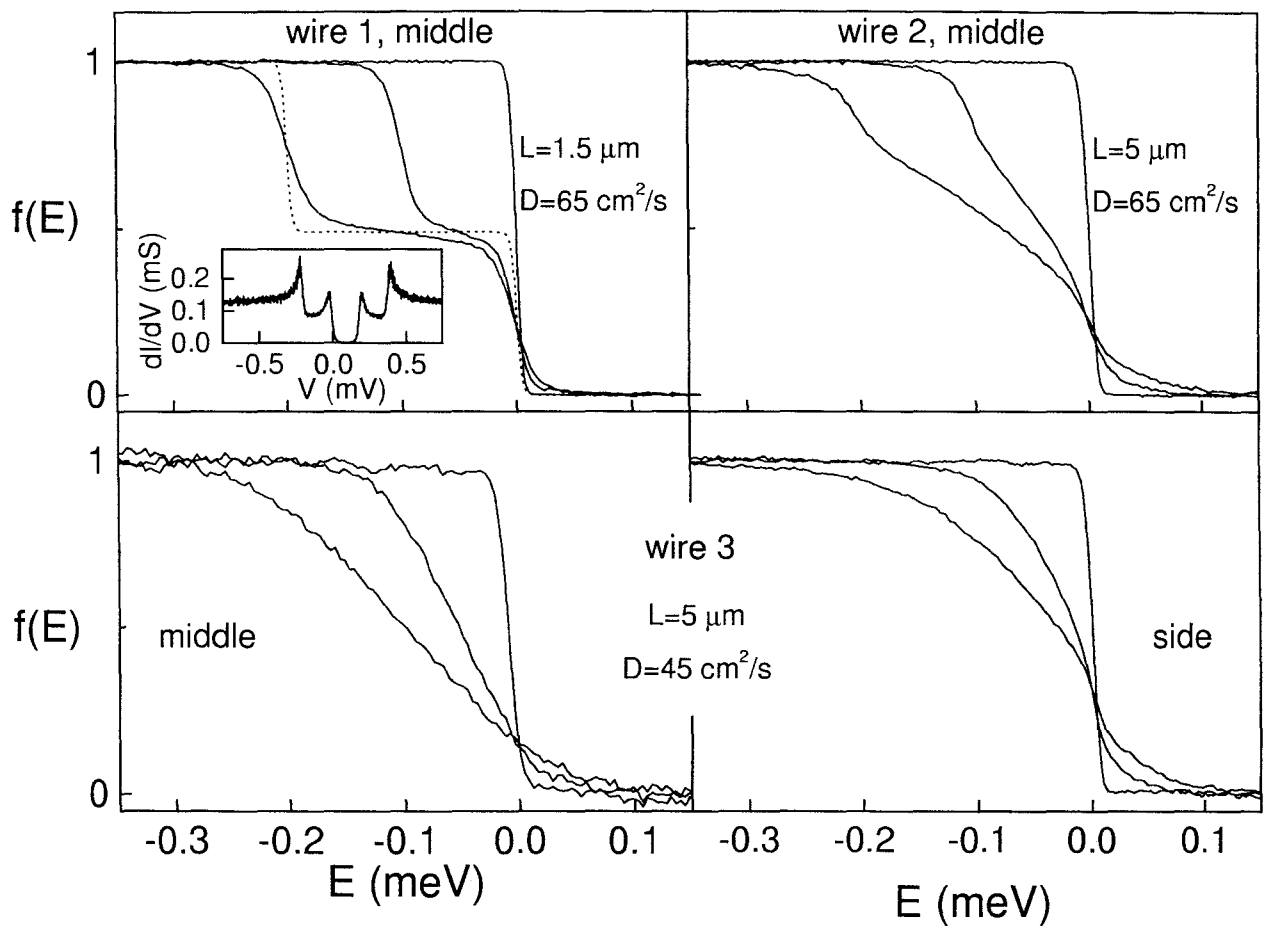
Fig. 2
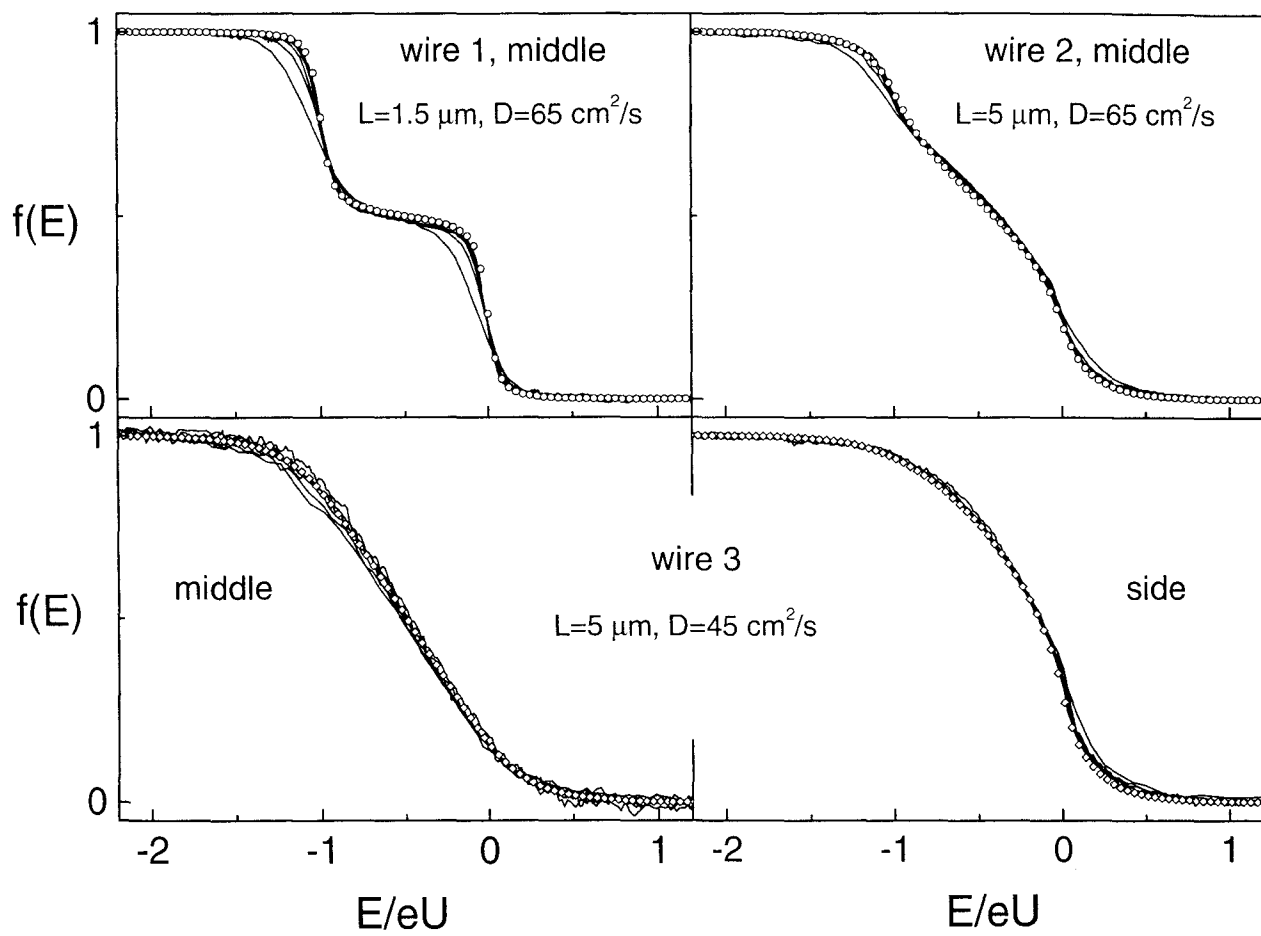
Fig. 3

The main characteristics of the samples measured are summarized in the following table.

	wire 1	wire 2	wire 3	
wire length L	1.5 μm	5 μm	5 μm	
wire width w	110 nm	110 nm	125 nm	
wire thickness d	45 nm	45 nm	45 nm	
junction position: −nominal	middle	middle	middle	side
− from Ohm's law (x_J)	0.52	0.44	0.46	0.25
tunnel junction resistance R_T	8 kΩ	7 kΩ	240 kΩ	70 kΩ
wire resistance R	14.5 Ω	53 Ω	76 Ω	
diffusion constant D	65 cm^2/s ± 10 cm^2/s		45 cm^2/s	
diffusion time $\tau_D = L^2/D$	0.35 ns	4 ns	6 ns	
typical interaction time τ_0 (fit)	1 ns		0.5 ns	
Thouless energy $\hbar D/L^2$	1.8 μeV	0.16 μeV	0.11 μeV	
Thouless energy $\hbar D/w^2$	0.33 meV	0.33 meV	0.18 meV	
Thouless energy $\hbar D/d^2$	2 meV	2 meV	2 meV	
scaling verified over	0.05 − 0.3 meV	0.05 − 0.3 meV	0.02 − 0.5 meV	

3.4 Experimental procedures and controls

3.4.1 Test of the tunnel probe

3.4.1.1 Is the density of states in the wire modified by the proximity effect from the superconducting probe?

The modification of the density of states by the proximity effect at the Fermi energy is of the order of $(R_{\text{wire}}G_T)^2/2$ (see chapter 5), which is in all cases smaller than 10^{-4}. This effect can therefore be completely neglected.

3.4.1.2 Is the distribution function in the wire modified by the measuring current?

The tunnel current injected in the wire in order to probe the distribution function acts as an additional source of quasiparticles, distributed according to the distribution of the super-conducting tunnel probe. One can wonder whether this injection of quasiparticles sensibly modifies the distribution function, in particular at the gap energy where the BCS density of states diverges. We calculate here this effect in the case of no interaction between quasiparticles. We take as an example a point junction positioned in the middle of the wire ($x_J = 0.5$, see Fig. 3.5).

The increase in the occupation factor due to the tunnel current is deduced from the conservation of the total number of quasiparticles, energy by energy (we neglect here inelastic tunneling):

$$\frac{1}{R}\frac{\partial f}{\partial x}\left(x_{J+}, E\right) = \frac{1}{R}\frac{\partial f}{\partial x}\left(x_{J-}, E\right) + \frac{1}{R_T}\, n_S\left(E + eV\right)\left\{f\left(x_J, E\right) + \Theta\left(E + eV\right) - 1\right\}$$

Given the linear variations of f on either side of the junction, and taking $x_J = 0.5$, this yields at each energy

$$f\left(0.5, E\right) = \frac{\bar{f}\left(E\right) + rn_S\left(E + eV\right)\left[1 - \Theta\left(E + eV\right)\right]}{1 + rn_S\left(E + eV\right)},$$

where $r = R/4R_T$ and $\bar{f}\left(E\right) = \left[f\left(1, E\right) + f\left(0, E\right)\right]/2$. The expression for the tunnel current is then

$$I_{NS}\left(0.5, V\right) = \frac{G_T}{e}\int_{-\infty}^{+\infty} dE\, \frac{n_S\left(E + eV\right)}{1 + rn_S\left(E + eV\right)}\left\{\bar{f}\left(E\right) + \Theta\left(E + eV\right) - 1\right\}. \tag{3.5}$$

This expression is the same as obtained when the probe current is neglected (see Eq. (3) in
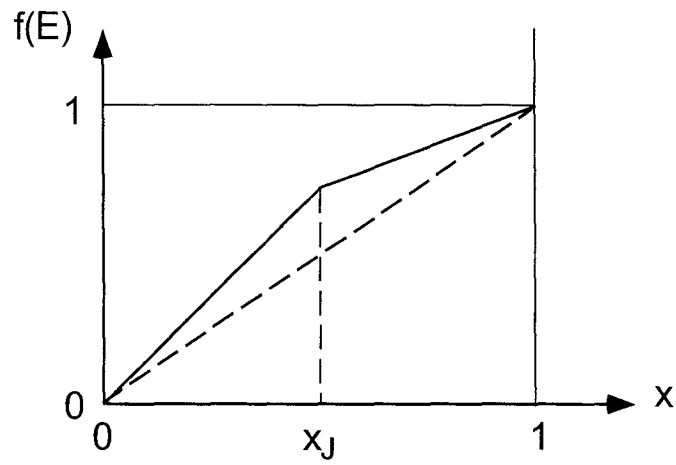
Fig. 3.5. Spatial variation of the distribution function at an energy E comprised between $-eU$ and 0, in the case of non interacting quasiparticles, and considering the additional occupation factors due to the electron injection through the tunnel junction. Outside the tunnel junction region, f interpolates linearly between the value at the reservoirs (situated in $x = 0$ and $x = 1$) and the value at the tunnel junction (situated at x_J). At the position of the tunnel junction, the occupation of the states is increased with respect to the linear interpolation.

the article), but with the density of states of the superconductor n_S replaced by the factor $n_S/\left(1 + rn_S\right)$. In our samples the ratio $r = R/2R_T \lesssim 5 \times 10^{-3}$ is small enough for the corrections to be negligible. We have numerically checked that the deconvolutions of the data with $r = 5 \times 10^{-3}$ and with $r = 0$ yield the same distribution function.

3.4.1.3 Comparison of dI/dV curve at $U = 0$ to the BCS quasiparticle density of states

A direct check that neither the proximity effect nor the tunnel current influence the distribution function is provided by the excellent agreement of the measured conductance with the conductance expected from Eq. (3) of the article with a BCS density of states, with $U = 0$ across the wire (see Fig. 3.6). The value of the gap Δ, the tunnel conductance G_T, and temperature were adjusted in order to obtain the best fit (the fit temperature $T = 22$ mK is in agreement with the temperature of the thermometer). The values of Δ and G_T were subsequently used for the determination of the distribution function.
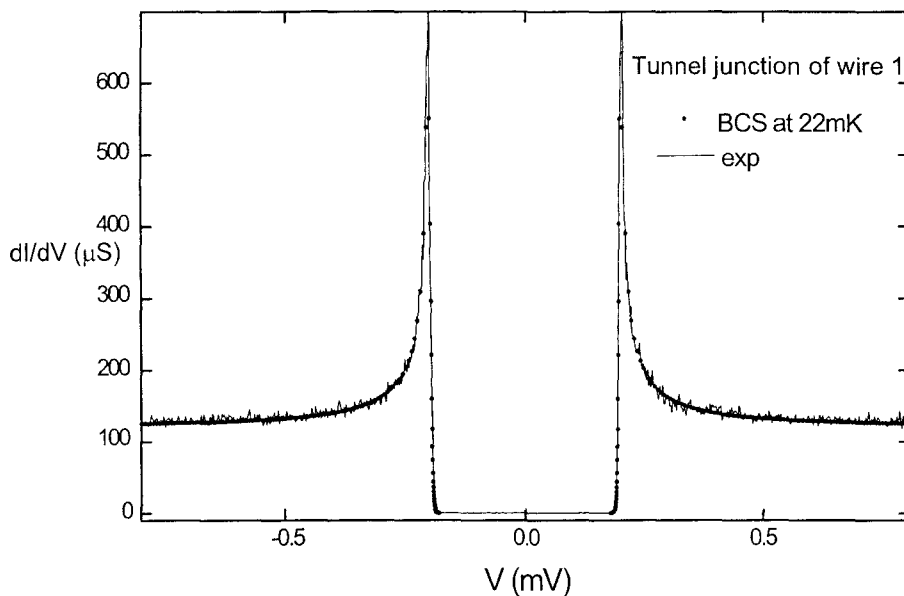
Fig. 3.6. Measured conductance of the NS tunnel junction of wire 1 (continuous lines) with no voltage across the wire ($U = 0$), and best fit using a BCS density of states. The fit parameters are $\Delta = 0.1994$ mV, $T = 22$ mK, and normal state tunnel conductance of the junction $G_T = 121.3$ μS.

3.4.2 From the tunnel probe differential conductance to the energy distribution function
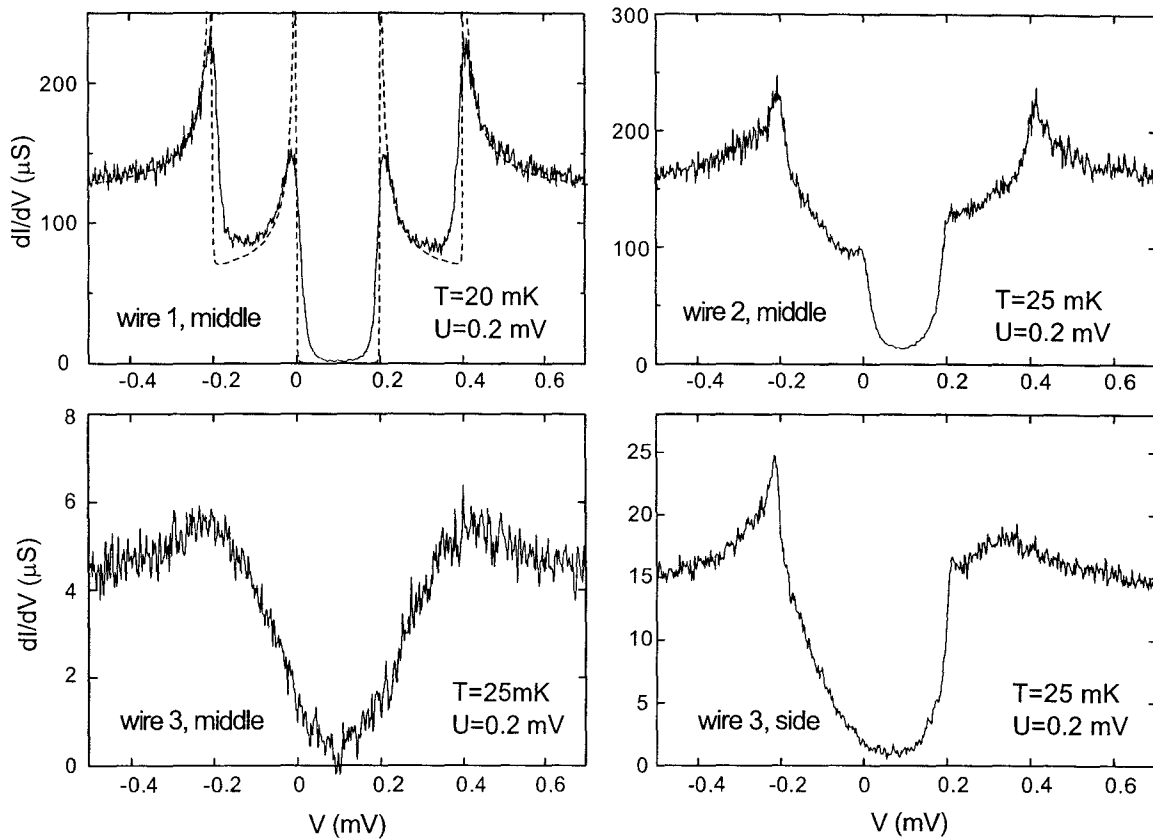
Fig. 3.7. Differential conductance as a function of voltage of the four tunnel probes, for a voltage $U = 0.2$ mV applied across the wires. Dashed lines in top left panel: conductance predicted for the non interacting case at zero temperature.

3.4.2.1   Differential conductance of the four tunnel junctions

As mentioned in the article, the energy distribution functions were deduced from the measurement of the differential conductance of the probe tunnel junctions as a function of the voltage applied across the junction. We present in Fig. 3.7 the different conductance curves of the four different tunnel probes, for a voltage $U = 0.2$ mV across the wire. The features of the underlying distribution functions are already visible.

The conductance curve of the junction probing the middle of wire 1, the shortest one (upper left panel), resembles the half sum of two shifted BCS density of states, plotted as dashed lines. In the non interacting case and at zero temperature, the distribution function expected in the middle of the wire is the step function, so that by linear superposition the conductance is expected to be the half sum of two BCS density of states shifted by the

energy eU. Therefore, the differential conductance already indicates that wire 1 is close to the non interacting regime. At the opposite, the rounded features of the curves of wires 2 and 3 suggest that the distribution functions are more rounded, as expected from greater quasiparticle-quasiparticle scattering. Finally, the asymmetry of the conductance curve of the side junction of wire 3 reflects the position of the junction.

3.4.2.2 Deconvolution procedure

The distribution function is deduced from the measured differential conductance using Eq. (3) of the article. The procedure, which uses a steepest descent method [11] , is illustrated in Fig. 3.8. To accelerate the convergence, we start with a well chosen initial distribution function (half sum of Fermi functions at the reservoir temperature for the short wire, thermal Fermi distribution for the distribution in the middle of the long wire with lowest diffusion constant). We have checked that the initial shape of f has no influence. Using Eq. (3) of the article we compute the conductance corresponding to this distribution, and compare it to the measured conductance. As long as the difference between both curves is greater than the desired precision, the occupation probability at each energy is incremented by a fraction of the partial derivative of the square deviation χ^2 respectively to the occupation factor f^k at that energy:

$$\chi^2 = \sum_k \left(\left.\frac{\partial I}{\partial V}\right|^k_{\text{calc}} - \left.\frac{\partial I}{\partial V}\right|^k_{\text{meas}} \right)^2$$

$$
\begin{aligned}
f^k_{\text{it}+1} &= f^k_{\text{it}} + \lambda \frac{\partial \chi^2}{\partial f_k} \\
&= f^k_{\text{it}} + \lambda' n'_{\text{BCS}} \cdot \left(\left.\frac{\partial I}{\partial V}\right|^k_{\text{calc}} - \left.\frac{\partial I}{\partial V}\right|^k_{\text{meas}} \right)
\end{aligned}
$$

and the procedure is iterated. This method produces the distribution functions of Fig. 2 of the article.

3.4.2.3 Are the distribution functions compatible with Ohm's law?

A first check of the coherence of the distributions obtained is that Ohm's law is recovered from these distributions. From charge neutrality, one obtains the expression of the electric potential in terms of distribution functions:
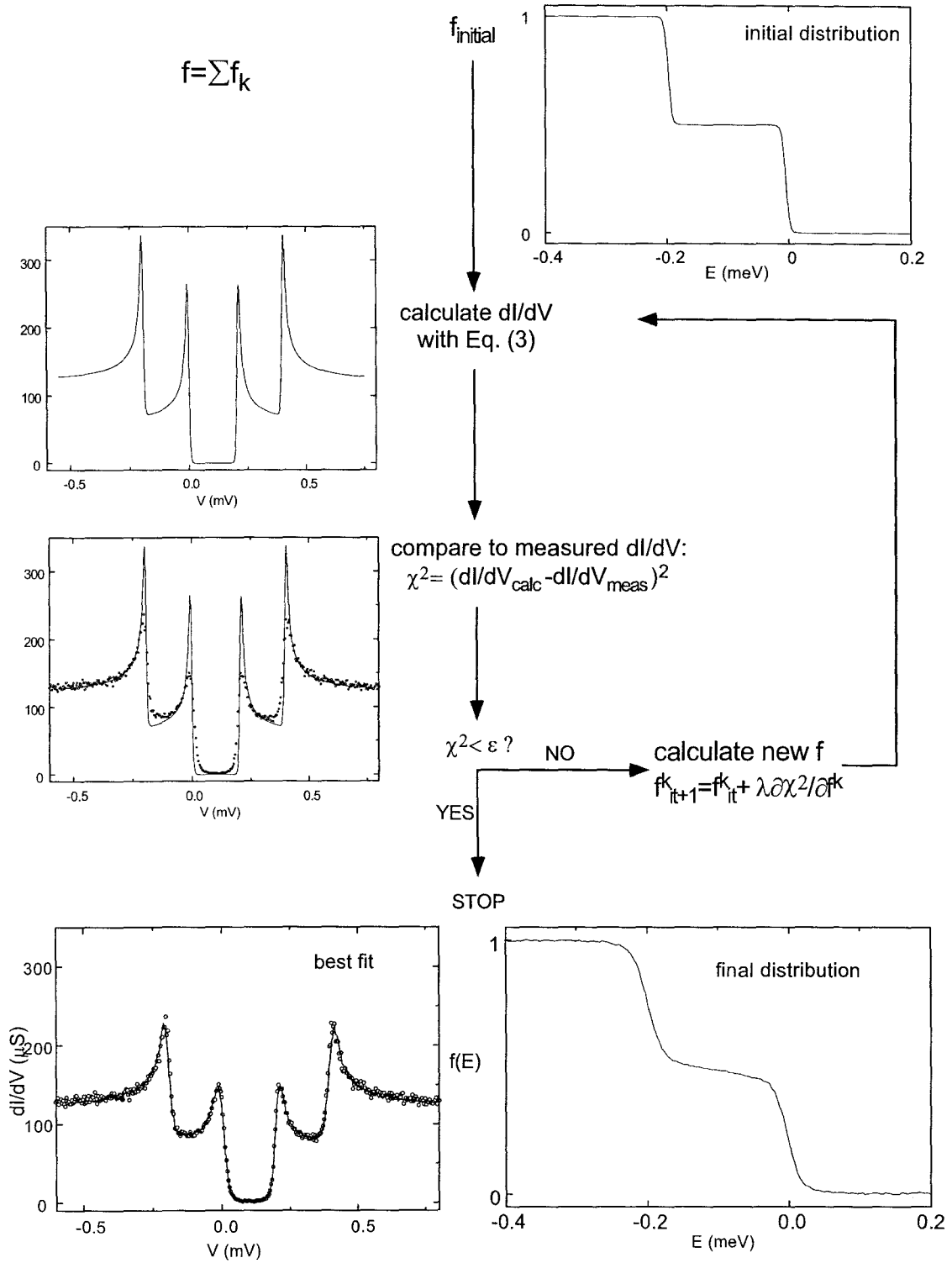
Fig. 3.8. Outline of the procedure used to deduce the distribution function from the measured conductance curve. In this example, we show how the distribution function in the middle of the short wire, when the two end reservoirs are biased by a potential difference $U = 0.2$ mV, is recovered. We choose as the initial distribution function the half sum of two Fermi functions at $T = 30$ mK, shifted by $eU = 0.2$ mV.

$$\Phi\left(x,U\right) = Ux = \frac{1}{e}\int_{-\infty}^{+\infty} dE\left[f\left(x,E,0\right) - f\left(x,E,eU\right)\right].\tag{3.6}$$

One can thus check that the variations of this integral are linear with the applied voltage U. Figure 3.9 shows the value of the right hand side of Eq. (3.6) as a function of the voltage U between reservoirs, for the four sets of distributions. The dependence is indeed linear, except for an unexplained discrepancy at high voltages in the side junction of wire 3. We attribute the small offsets in voltage (a few microvolts) to a thermoelectric voltage drop between the source at room temperature which provides the bias voltage U and the sample.

In addition, the precise position x_J of the measuring tunnel probes can be determined from the slope of the curves. We deduce from Fig. 3.9 that the tunnel probes are positioned respectively at $x_J = 0.52$ (wire 1), $x_J = 0.44$ (wire 2), $x_J = 0.46$ (central junction of wire 3), and $x_J = 0.25$ (lateral junction of wire 3). In comparison, the positions determined from SEM micrographs were: $x = 0.49$ (wire 1), $x = 0.53$ (wire 2), $x = 0.52$ (central junction of wire 3) and $x = 0.2$ (lateral junction of wire 3). In the comparison with theory, we have used the positions determined from the electrical measurements, which integrate irregularities in the cross section of the wire.

3.4.3 Influence of the reservoir temperature on the scaling property

The scaling of the distribution functions with voltage U is not expected to be perfect, given that the reservoirs, which impose the boundary conditions, are kept at a constant temperature as U is varied. In this section, we first consider the influence of the reservoir temperature on the scaling law in the hot electron regime, where the form of the distribution function is known theoretically. We then directly show how the scaling property of the data is improved when the reservoir temperature is kept proportional to U.

3.4.3.1 Scaling in the "hot electron" regime

The distribution function in the hot electron regime is a Fermi function at a voltage-dependent effective temperature and chemical potential

$$f_{T_e}\left(x,E\right) = \left(1 + \exp\frac{E - eUx}{k_B T_e\left(x\right)}\right)^{-1},\tag{3.7}$$
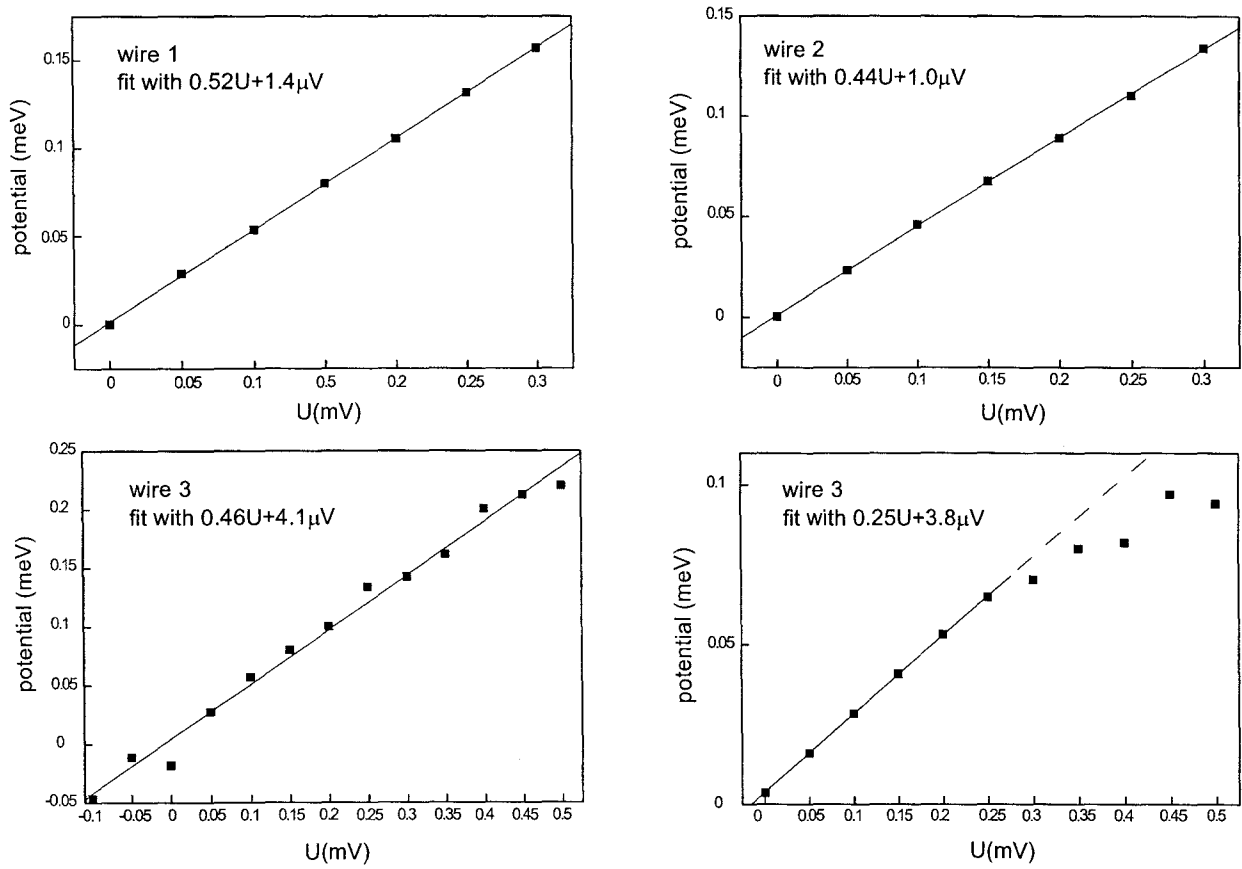
Fig. 3.9. Electric potential at the position of the four junctions, deduced from the area beneath the distribution function, as a function of the bias voltage U.

where

$$T_e(x) = \sqrt{T^2 + x(1-x)U^2/\mathcal{L}}. \tag{3.8}$$

The effective temperature T_e, and consequently the whole distribution function f_{T_e}, will scale with the voltage U only if the reservoir temperature $T = 0$ or $T \propto eU/k_B$. The dependence with voltage U of the temperature deduced from the distribution functions in the middle of wire 3 are plotted in Fig. 3.10. The dependence is clearly not linear at low voltages U, where the finite reservoir temperature T is not negligible with respect to eU/k_B.

The temperatures extracted by fitting the distributions to Fermi functions are compared to the temperatures expected from Eq. (3.8) in the same graph of Fig. 3.10, for U varying between 0 and 0.5 mV. Taking the reservoir temperature $T = 45$ mK, extracted from the best fit of the data at $U = 0$, we find an agreement within 5% for voltages $U > 0.15$ mV, and within 20% for smaller voltages. As seen from the bottom graph on the example of a distribution corresponding to $U = 0.2$ mV, the distributions are not *perfectly* fitted by a Fermi function, indicating that the incomplete thermalization is at the origin of this discrepancy. The simulated distribution function, also shown on this graph, reproduces the measured distribution better.

3.4.3.2 Distribution functions with a constant eU/k_BT ratio

In order to check the role of the fixed temperature of the reservoirs for an arbitrary distribution function, we have measured a series of conductance curves for the side tunnel junction of wire 3, with a constant ratio eU/k_BT. The corresponding distributions are plotted as a function of E/eU in Fig. 3.11. The scaling property is obeyed much more precisely than when the temperature was kept constant (bottom panel).
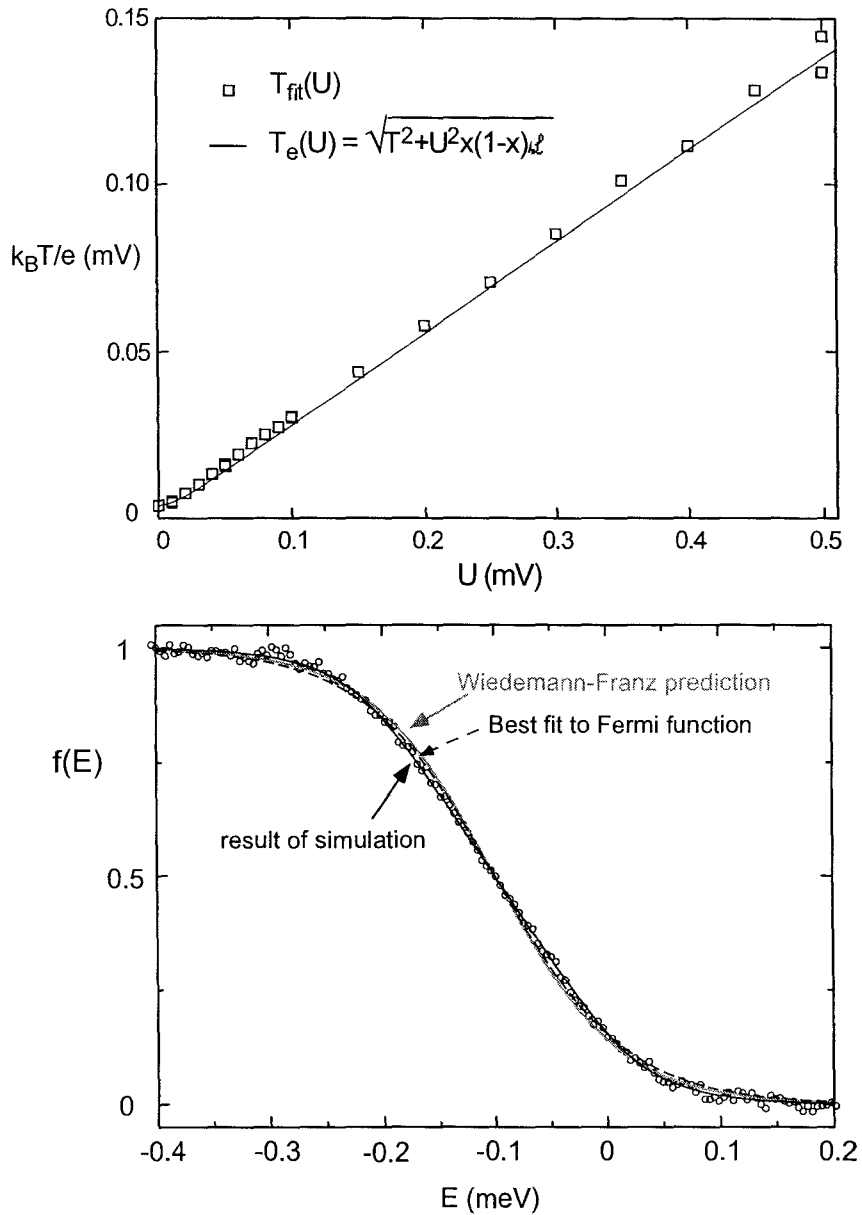
Fig. 3.10. Nearly thermalized regime. Top graph: comparison between the temperatures deduced from the fit of the distributions at the middle of wire 3 by Fermi functions, and the temperatures given by the heat equation, taking $x_J = 0.49$ and a reservoir temperature of $T = 45$ mK. Bottom graph: example of the distribution for $U = 0.2$ mV (open symbols). The heat equation predicts an effective temperature of 635 mK for this voltage difference (grey curve), and the best fit of a Fermi function to the data (thin black curve) yields a temperature of 665 mK. The simulated curve fits the actual distribution better.
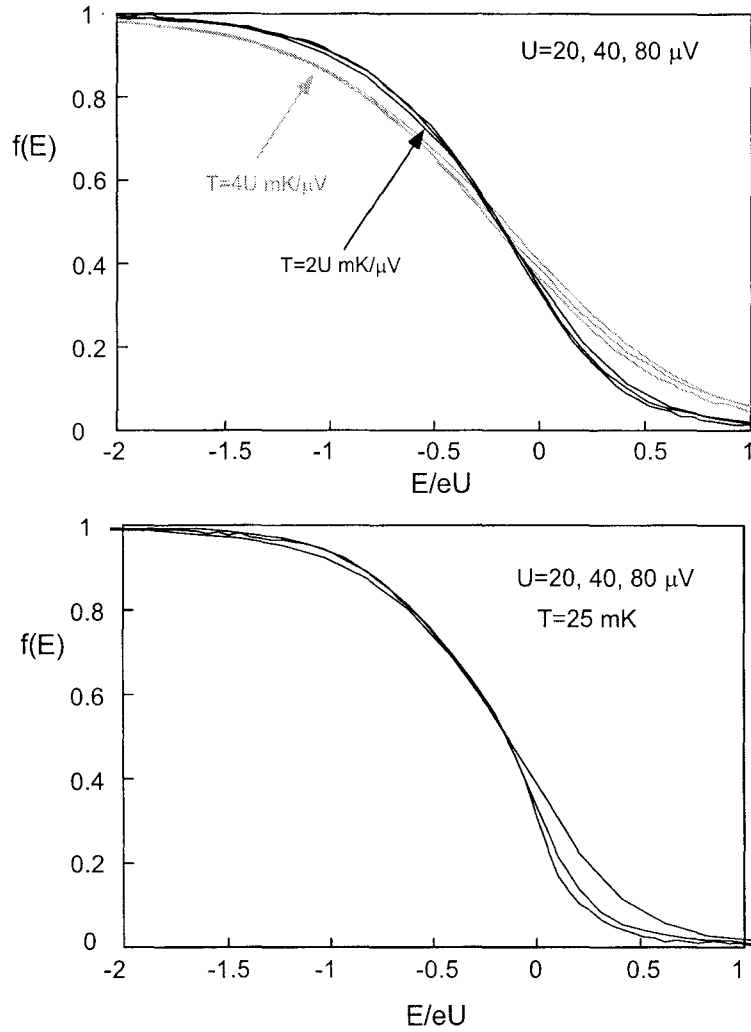
Fig. 3.11. Distribution functions at the side junction of wire 3 as a function of E/eU, for U=20, 40, and 80 μV, with a constant ratio $k_B T/eU$ (top), or a constant temperature$T$=25 mK (bottom). The scaling property is verified much more precisely with a constant ratio $k_B T/eU$.

3.5 Interpretation of the data within the quantum Boltzmann equation

Following Nagaev [5] and Kozub and Rudin [6] , we use the quantum Boltzmann equation to determine the energy distribution function in the wire. Note that, although this formalism is strongly reminiscent of the classical Boltzmann equation, it describes situations in which electron quantum states are coherent throughout the entire system. This leads to equation (1) in the article, in which the collision integral provides information on the interaction between quasiparticles.

3.5.1 Interaction kernel inferred from the scaling property of the data

The collision term (Eq. (4) of the article) of the Boltzmann equation is non zero only for out-of-equilibrium distribution functions. Therefore information on the quasiparticle-quasiparticle interaction is provided only by the distribution functions in the intermediate regime (wire 1, wire 2 and side junction of wire 3). For these junctions, we show how the scaling property of the distribution functions imposes a specific energy dependence of the interaction kernel.

We assume that the scaling with U observed on the distribution functions at the middle of all three wires and at the side position of wire 3 is true at all positions of the wires. For the Boltzmann equation to be obeyed, the collision term must also scale with voltage U, $i.e.$ $\mathcal{I}_{\text{coll}}$ must be a function of E/eU only. This collision term can also be written as

$$\mathcal{I}_{\text{coll}}^{\text{in,out}}\left(x,E,\{f\}\right) = \int \mathrm{d}\left(\frac{\varepsilon}{eU}\right)\mathrm{d}\left(\frac{E'}{eU}\right)\mathrm{d}x'\,(eU)^2\,K\left(x,x',\varepsilon\right)f_{E+\varepsilon,E}^x\left(1-f_{E,E-\varepsilon}^x\right)f_{E'}^{x'}\left(1-f_{E'+\varepsilon}^{x'}\right)$$

Since $f_E^x = f\left(x,E\right)$ is a function of E/eU, this requires that $(eU)^2\,K\left(x,x',\varepsilon\right)$ be a function of ε/eU, $i.e.$

$$K\left(x,x',\varepsilon\right) = \frac{g(x,x')}{\varepsilon^2},$$

where $g(x,x')$ has the dimension of a rate.

3.5.2 Numerical implementation of the quantum Boltzmann equation

We simulate energy distribution functions which are solutions of the quantum Boltzmann

equation with the interaction kernel

$$K\left(x, x', \varepsilon\right) = \begin{cases} \frac{g(x,x')}{\varepsilon^2} & \text{for } \varepsilon > \varepsilon_0 \\[2mm] \frac{g(x,x')}{\varepsilon_0^2} & \text{for } \varepsilon < \varepsilon_0 \end{cases}, \tag{3.9}$$

where ε_0 is a cut-off energy. The boundary distributions are Fermi functions at 30 mK, shifted in energy by eU. The wire is partitioned into eleven segments of equal length in which f is homogeneous. We have checked that a finer partitioning doesn't change the results.

3.5.2.1   Spatial dependence of the interaction kernel

The physical interaction kernel $\mathcal{K}$ is a function of the absolute coordinates $X = Lx$ and $X' = Lx'$:

$$\mathcal{K}\left(X, X', \varepsilon\right) = \frac{K\left(x, x', \varepsilon\right)}{L}.$$

The scaling law does not *a priori* impose any specific spatial dependence of the interaction kernel $\mathcal{K}\left(X, X', \varepsilon\right)$. We have considered the two limiting cases of local and global interaction. In the local limit $\mathcal{K}\left(X, X', \varepsilon\right) = \tau_0^{-1}\delta\left(X - X'\right)/\varepsilon^2$, *i.e.* $g\left(x, x'\right) = \tau_0^{-1}\delta\left(x - x'\right)$, only interactions between quasiparticles situated at the same position are allowed. In the global limit, $\mathcal{K}\left(X, X', \varepsilon\right) = k/\varepsilon^2$, *i.e.* $g\left(x, x'\right) = kL$, quasiparticles can interact with any other quasiparticle in the wire.

We find that a distribution function calculated within the local model, for a given rate τ_0^{-1}, can also be obtained within the global model, if one takes for k the value τ_0^{-1}/L. However, the models can be discriminated by their prediction for wires differing by their length only.

3.5.2.2   Computation of the distribution function within the hypothesis of local interaction

Figure 3.12 shows the distribution functions computed within the local approximation, at the eleven positions along the two wires of lengths L and $3L$, using the same interaction time τ_0. The corresponding ratios τ_D/τ_0 are in this case $\tau_D/\tau_0 = 0.4$ and $\tau_D/\tau_0 = 3.5$. These ratios are also those which best describe the interaction in wires 1 and 2, as shown by the distribution functions for $U = 0.2$ meV, also plotted on the graphs. One should note however that in the case of wires 1 and 2, the ratio $\tau_{D2}/\tau_{D1} = \left(L_2/L_1\right)^2 = \left(5/1.5\right)^2 \simeq 11$, within 20% of the value 9 which best fits the data.
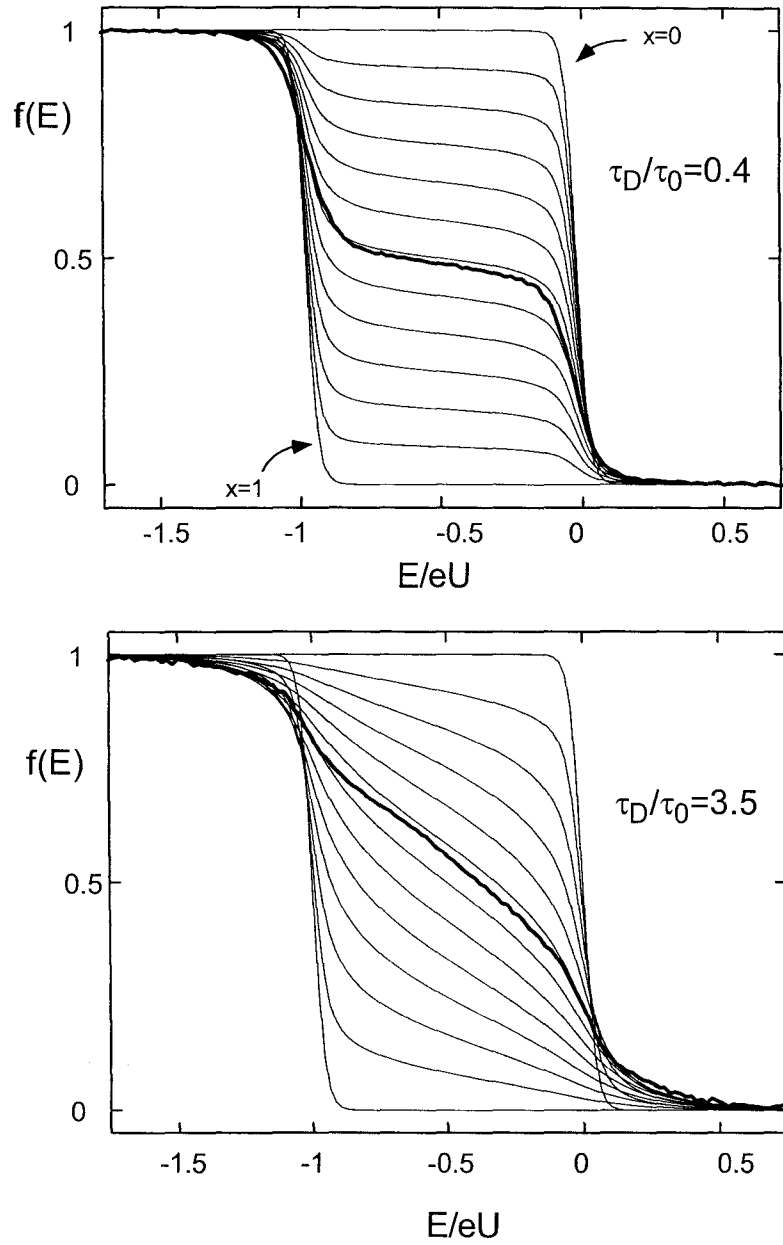
Fig. 3.12. Simulated distribution functions in 11 positions along two wires of length L and 3L, taking a reservoir temperature $T = eU/(48k_B)$ and the same interaction time τ_0. The ratios τ_D/τ_0 are those which best fit the data, as seen from the comparison with the distribution functions taken with U=0.2 mV (thick curves).

3.5.2.3   Sensitivity to the cut-off energy

The interaction time is limited by the diffusion time τ_D across the wire. The energy exchanged in a collision can therefore not be defined better than the Thouless energy $E_C = \hbar/\tau_D$. In practice, we find the cut-off energy has no influence on the simulated distribution function, as long as it is inferior to $eU/4$, which is much greater than the Thouless energy (see table at end of section **3.3**).

3.5.3   What does the experiment imply for the interaction kernel?

3.5.3.1   Is the interaction local or global?

Simulations with the local model could reproduce the measured distribution functions in the middle of wire 1 and 2, fabricated simultaneously, using the same interaction rate τ_0^{-1} (see article). Therefore the interpretation within the global model would require an interaction constant which scales with the inverse wire length. This is in favor of the hypothesis of a local interaction, or at least an interaction whose range is much smaller than the length $L = 1.5 \ \mu\mathrm{m}$ of wire 1.

3.5.3.2   Different power laws for the interaction kernel?

With what precision can the exponent of the interaction kernel be inferred? Figure 3.13 compares the simulated distribution functions plotted as a function of E/eU, for $U = 0.05 \ \mathrm{mV}$ and $U = 0.2 \ \mathrm{mV}$, using interaction kernels proportional to $\varepsilon^{-1.8}$, $\varepsilon^{-1.9}$, $\varepsilon^{-2.1}$ and $\varepsilon^{-2.2}$ (lateral curves), to the measured distribution functions (central curves). The comparison of the scaled curves near $f(E) = 0.5$, where the rounding of the distributions due to interaction is such that the distribution functions are insensitive to the ratio eU/k_BT, for the different exponents α of ε, indicates that a superposition as perfect as in the experimental data can only be reproduced for $\alpha = -2 \pm 0.1$.
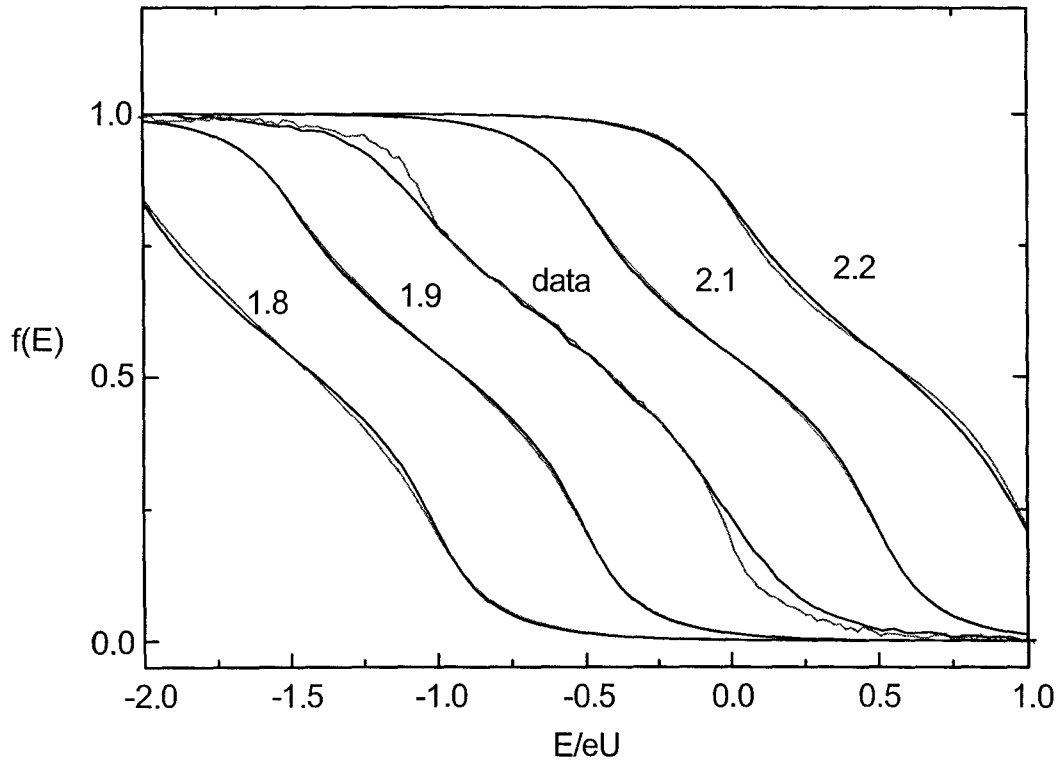
Fig. 3.13. Comparison between simulated distribution functions using interaction kernels with different power laws. Central curves: distributions measured with $U = 0.05$ mV.and $U = 0.3$ mV. Lateral curves: simulated distribution functions for $U = 0.05$ mV (grey curves) and $U = 0.2$ mV (black curves), using an interaction kernel proportional to $\varepsilon^{-1.8}$, $\varepsilon^{-1.9}$, $\varepsilon^{-2.1}$, and $\varepsilon^{-2.2}$, and a constant value of eU/k_BT. Pairs of curves have been offset horizontally for clarity.

3.6   Conclusion

In the 45 nm-thick copper films we have fabricated, it takes roughly $\tau_0 \simeq 1$ ns for quasi-particles to redistribute their energy. The spatial range of the interaction is small compared to the length of the shortest wire (1.5 μm) , and the rate of a process in which two quasi-particles exchange an energy ε is proportional to ε^{-2} over the energy range $0.01 - 0.3$ meV. From the interaction kernel we can deduce a quasiparticle lifetime $\tau_{ee}(E)$, given by the time after which a quasiparticle of energy E will have decayed to another quasiparticle state of the metal (see Fig. 3.14). At zero temperature, this time is given by
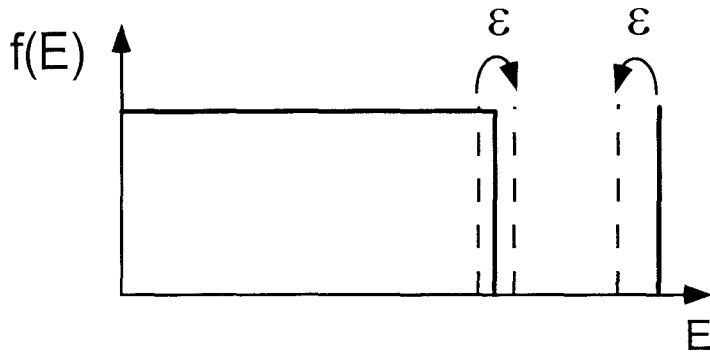
Fig. 3.14. Illustration of the calculation of the quasiparticle lifetime at zero temperature.

$$\tau_{ee}(E) = \left(\int_0^E d\varepsilon \, K(\varepsilon)\varepsilon \right)^{-1}.$$

Taking the kernel deduced from our experiments in the range $0.01 - 0.3$ meV, and a constant interaction kernel τ_0^{-1}/E_0^2 for energies inferior to $E_0 = 0.01$ meV, we find

$$1/\tau_{ee}(E) > \tau_0^{-1} \int_0^{E_0} \varepsilon \frac{d\varepsilon}{E_0^2} + \int_{E_0}^E \frac{d\varepsilon}{\varepsilon},$$

i.e.

$$\tau_{ee}(E) < \frac{\tau_0}{\frac{1}{2} + \ln \frac{E}{E_0}}.$$

The lifetime is thus shorter than 2 ns at 0.01 meV, or 0.4 ns at 0.1 meV. These upper bounds are however still longer than the coherence times inferred from weak localization experiments in metallic thin films. The corresponding upper bound for the quality factor

$Q(E) = E / (\hbar/\tau_{ee}(E))$ is then

$$Q(E) < \frac{E_0 \tau_0}{\hbar} \frac{E/E_0}{\frac{1}{2} + \ln\frac{E}{E_0}}.$$

We have plotted this function for the energy range probed by the experiment in Fig. 3.15.
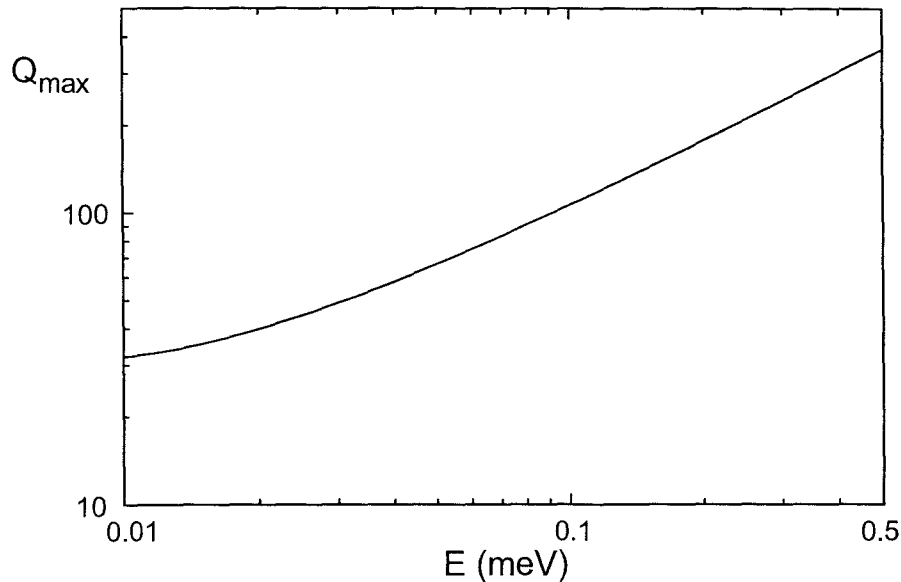
Fig. 3.15. Quality factor associated to the quasiparticle lifetime deduced from the experiment.

Quasiparticles are well defined excitations, but the overall behavior indicates that the quality factor degrades as the Fermi level is approached. Measurements at smaller energies and at lower temperatures might reveal whether Landau's scheme applies at the Fermi level.

Note that if Q tends towards a finite value at the Fermi energy, then $\tau_{ee}(E) \propto 1/E$, so that the length over which coherence persists is $\sqrt{\hbar D/E}$. A sample of length L could then exhibit coherence over its entire size if it is probed with energies smaller than the Thouless energy $\hbar D/L^2$.

REFERENCES

[1] N.W. Ashcroft and N.D. Mermin, *Solid State Physics*, CBS Publishing (1975).

[2] D. Pines and P. Nozière, *The Theory of Quantum Liquids. 1: Normal Fermi Liquids*, W.A. Benjamin (1966).

[3] B. L. Altshuler and A. G. Aronov, in *Electron-Electron interactions in Disordered Systems*, Ed. by A. L. Efros and M. Pollak, Elsevier, (1985).

[4] R. Landauer, IBM J. Res. Develop. **1**, 223 (1957); **32**, 306 (1988).

[5] K.E. Nagaev, Phys. Lett. A **169**, 103 (1992); Phys. Rev. B **52**, 4740 (1995).

[6] V.I. Kozub and A. M. Rudin, Phys. Rev. B **52**, 7853 (1995).

[7] M.J.M. de Jong and C.W.J. Beenakker, Physica A **230**, 219 (1996).

[8] See for example, F. C. Wellstood, C. Urbina, and John Clarke, Phys. Rev. B **49**, 5942 (1994).

[9] D.E. Prober, M.N. Wybourne, and M. Kansakar, Phys. Rev. Lett. **75**, 3964 (1995).

[10] A.H. Steinbach, J.M. Martinis, and M.H. Devoret, Phys. Rev. Lett. **76**, 3806 (1996).

[11] Numerical recipes, Cambridge University Press (Cambridge), Chapter 10.

Chapter 4
Theory of electron-electron interaction in diffusive metals

In this chapter, we first compare the interaction kernel deduced from the theory of diffusive metals to the interaction kernel deduced from the experiment presented in the previous chapter. Neither the energy dependence nor the magnitude of the predicted interaction can explain the experimental results. We then present a phenomenological model which leads to the correct energy dependence.

4.1 Predictions of the theory of diffusive metals

Following Schmid [1] , Altshuler *et al.* [2] have calculated electron-electron interactions in diffusive conductors. They consider quasiparticles with a diffusive motion which interact by the Coulomb interaction screened by an effective medium constituted by all the electrons of the metal (see Fig. 4.1). These quasiparticles interact more than in the clean metal because the overlap of their wavefunctions is greater and screening is less effective.

4.1.1 Derivation of the kernel of the quasiparticle-quasiparticle interaction in the simple case of a potential $V(r - r')$

The theory of Altshuler *et al.* is based on the Green function formalism and on diagrammatic expansions. In order to understand the meaning of its prediction for $K(\varepsilon)$, we first consider the simple case of particles which interact through a potential $V(r - r')$ which depends only on the relative positions of two quasiparticles. The matrix element for the interaction

Fig. 4.1. In the theory of Altshuler *et al.*, two quasiparticles with a diffusive motion interact *via* the Coulomb interaction, screened by the other electrons, whose diffusive motion in the metal is also considered.

with an energy transfer ε is (see Fig. 4.2):

$$M\left(\varepsilon\right) = \sum_{\substack{E_{j,j'}-E_{i,i'}=-\varepsilon \\ E_{l,l'}-E_{k,k'}=\varepsilon}} \int dr\,dr'\Psi_i\left(r\right)\Psi_j^*\left(r\right)V\left(r-r'\right)\Psi_k\left(r'\right)\Psi_l^*\left(r'\right),$$

where the $\Psi\left(r\right)$ are the wave functions of the particles considered. This matrix element is a random quantity, of which the average of the modulus squared, computed following usual disorder averaging procedures, precisely gives the kernel function:
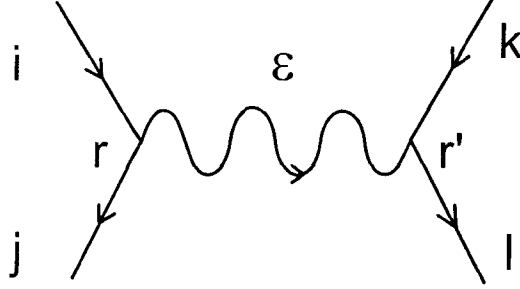
Fig. 4.2. Diagram representing the exchange of an energy ε between two quasiparticles situated in r and r'.

$$
\begin{aligned}
K\left(\varepsilon\right) &= \frac{2\pi}{\hbar}\left(n_0\mathcal{V}\right)^3\left\langle\left|M\right|^2\left(\varepsilon\right)\right\rangle \\
&= \frac{2\pi}{\hbar}\left(n_0\mathcal{V}\right)^3 < \sum_{\substack{E_{j,j'}-E_{i,i'}=-\varepsilon \\ E_{l,l'}-E_{k,k'}=\varepsilon}} \int dr\,dr'\Psi_i\left(r\right)\Psi_j^*\left(r\right)V\left(r-r'\right)\Psi_k\left(r'\right)\Psi_l^*\left(r'\right) \\
&\quad \times \int dr''dr'''\Psi_{i'}\left(r''\right)\Psi_{j'}^*\left(r''\right)V\left(r''-r'''\right)\Psi_{k'}\left(r'''\right)\Psi_{l'}^*\left(r'''\right) > .
\end{aligned}
$$

Here, n_0 is the density of states and $\mathcal{V}$ is the sample volume. After averaging over disorder, only the diagrams for which $j' = i$, $j = i'$, $l = k'$, $l' = k$ contribute (see Fig. 4.3). Therefore

$$
\begin{aligned}
K\left(\varepsilon\right) &= \frac{2\pi}{\hbar}\left(n_0\mathcal{V}\right)^3 < \sum_{\substack{E_j-E_i=-\varepsilon \\ E_l-E_k=\varepsilon}} \int dr\,dr'dr''dr'''\Psi_i\left(r\right)\Psi_i^*\left(r''\right)\Psi j\left(r''\right)\Psi_j^*\left(r\right) \\
&\quad \times V\left(r-r'\right)V\left(r''-r'''\right)\Psi_k\left(r'\right)\Psi_k^*\left(r'''\right)\Psi_l\left(r'''\right)\Psi_l^*\left(r'\right) > . \quad\quad (4.1)
\end{aligned}
$$

It has been shown [2–4] that in a diffusive conductor the product

$\sum_{E_k'-E_k=\hbar\omega}\Psi_k\left(r\right)\Psi_k^*\left(r'\right)\Psi_{k'}\left(r'\right)\Psi_{k'}^*\left(r\right)$ averaged over disorder is just the Fourier transform
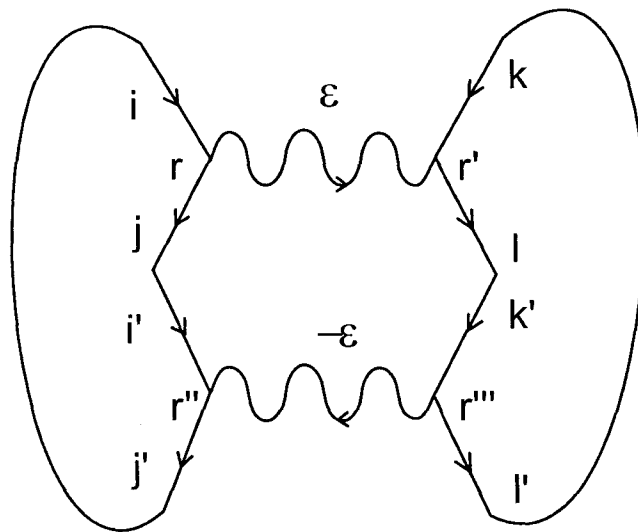
Fig. 4.3. Diagrams which contribute to the disorder-averaged modulous squared of the interaction matrix element.

of the symmetrized classical probability $P(r, r', |t|)$ to diffuse from r to r' in a time t :

$$< \sum_{\substack{k,k' \\ E'_k - E_k = \hbar\omega}} \Psi_k(r) \Psi_k^*(r') \Psi_{k'}(r') \Psi_{k'}^*(r) >= \frac{1}{\hbar n_0 \mathcal{V}} \tilde{P}(r, r', \varepsilon) \qquad (4.2)$$

$$= \frac{1}{\hbar n_0 \mathcal{V}} \int dt e^{i\varepsilon t/\hbar} P(r, r', |t|).$$

Therefore,

$$K(\varepsilon) = \frac{2\pi}{\hbar} \frac{n_0 \mathcal{V}}{\hbar^2} \int dr dr' dr'' dr''' \tilde{P}(r, r'', -\varepsilon) \tilde{P}(r', r''', \varepsilon) V(r - r') V(r'' - r'''). \qquad (4.3)$$

Taking the spatial Fourier transform of $P(r, r', |t|)$ yields

$$\begin{aligned}
\tilde{P}(r, r', \varepsilon) &= \int_{-\infty}^{\infty} dt e^{i\varepsilon t/\hbar} P(r, r', |t|) \\
&= \int_0^{\infty} dt \left(e^{i\varepsilon t/\hbar} + e^{-i\varepsilon t/\hbar} \right) \frac{1}{2\pi \mathcal{V}} \int_0^{\infty} dk e^{-Dk^2 t} e^{ik(r-r')} \\
&= \frac{1}{2\pi \mathcal{V}} \int_0^{\infty} dk e^{ik(r-r')} \mathrm{Re} \left[\frac{1}{i\varepsilon/\hbar - Dk^2} \right] \\
&= \frac{1}{2\pi \mathcal{V}} \int_0^{\infty} dk e^{ik(r-r')} \frac{Dk^2}{(\varepsilon/\hbar)^2 + D^2 k^4}.
\end{aligned}$$

With the change of variables

$$\begin{aligned}
\rho &= r - r'; \quad \rho' = r'' - r''' \\
R &= (r + r')/2; \quad R' = (r'' + r''')/2 \\
q &= (k + k')/2; \quad q' = (k - k')/2
\end{aligned}$$

the kernel becomes

$$\begin{aligned}
K(\varepsilon) &= \frac{1}{2\pi\hbar} \frac{n_0}{\hbar^2} \int dq d\rho d\rho' V(\rho) V(\rho') e^{iq(\rho-\rho')} \left(\frac{Dq^2}{(\varepsilon/\hbar)^2 + D^2 q^4} \right)^2 \\
&= \frac{1}{2\pi\hbar} \frac{n_0}{\hbar^2} \int dq \left| \int d\rho V(\rho) e^{iq\rho} \right|^2 \left(\frac{Dq^2}{(\varepsilon/\hbar)^2 + D^2 q^4} \right)^2 \\
&= \frac{1}{2\pi\hbar} \frac{n_0}{\hbar^2} \int dq \left| \tilde{V}(q) \right|^2 \left(\frac{Dq^2}{(\varepsilon/\hbar)^2 + D^2 q^4} \right)^2. \qquad (4.4)
\end{aligned}$$

The kernel therefore contains the Fourier transform of the interaction potential, multiplied by a term directly related to the motion of the electrons. The expression derived by Altshuler et al. is the same, but with the energy dependent Fourier transform $V(q, \varepsilon)$ of the screened Coulomb interaction instead of $\tilde{V}(q)$.

4.1.2   Interaction potential in infinite diffusive metals

The screened Coulomb interaction is expressed in q space in terms of the dielectric constant $\Sigma(q, \varepsilon)$ of the metal as

$$V(q, \varepsilon) = \frac{V_0(q)}{\Sigma(q, \varepsilon)},$$

where $V_0(q)$ is the bare Coulomb potential. This is reexpressed by Altshuler *et al.* in terms of the polarizability $\Pi(q, \varepsilon)$ of the electronic fluid:

$$V(q, \varepsilon) = \frac{V_0(q)}{1 + \Pi(q, \varepsilon) V_0(q)}. \tag{4.5}$$

The polarizability, calculated taking into account the diffusive motion of the quasiparticles, and considering that the quasiparticles are at equilibrium, is [6] :

$$\Pi(q, \varepsilon) = n_0 \frac{Dq^2}{Dq^2 - i\varepsilon/\hbar} \tag{4.6}$$

where n_0 is the density of states of the metal. In a metal, n_0 is so large that Eq. (4.5) simplifies to

$$V(q, \varepsilon) = \frac{1}{\Pi(q, \varepsilon)}. \tag{4.7}$$

4.1.3   Prediction for the kernel function

The expression of $K(\varepsilon)$ is obtained form Eq. (4.4) with the use of Eq. (4.7):

$$K(\varepsilon) = \frac{1}{2\pi\hbar} \frac{1}{n_0\hbar^2} \int \frac{q^2 dq}{(\varepsilon/\hbar)^2 + D^2 q^4} \propto \varepsilon^{-1/2}. \tag{4.8}$$

This is the central prediction of the theory of Altshuler *et al.* Note that this result is at strong variance with the prediction for clean metals $K(\varepsilon) = \int \frac{1}{q^2 + q_0^2} \frac{1}{qv_F} q^2 dq$, which is independent of ε.

4.1.4   Extension to finite systems

In finite size systems, only those dimensions for which the Thouless energy $\hbar D/L^2$ associated with the length L along the dimension considered is smaller than the energy ε considered

contribute to $K(\varepsilon)$. Therefore the extension to systems of effective dimension d is:

$$K(\varepsilon) = \frac{1}{2\pi\hbar} \frac{1}{n_d \hbar^2} \int \frac{q^{d-1} dq}{(\varepsilon/\hbar)^2 + D^2 q^4} \propto \varepsilon^{-2+d/2} \tag{4.9}$$

where n_d is the density of states n_0 multiplied by the dimensions of the system in the directions which do not contribute.

For a wire of square section S which, for energies smaller than $\hbar D/S$, is an effectively one-dimensional system, the predicted kernel is therefore $K(\varepsilon) \propto \varepsilon^{-3/2}$, which gives a quasiparticle lifetime τ_{ee} of [2] :

$$\tau_{ee}(E) = \sqrt{2}\hbar n_0 S L_E = \sqrt{2}\hbar n_0 S \sqrt{\frac{\hbar D}{E}}.$$

4.1.5 One-dimensional wire connected to reservoirs

In the case of a one-dimensional wire of length L connected to reservoirs, the diffusive motion along the wire decomposes onto discrete modes, so that a sum replaces the integration on q in Eq. (4.9). In this case, the interaction kernel reads:

$$K(\varepsilon) \propto \frac{\pi}{L} \sum_{qL/\pi=1}^{\infty} |V(q,\varepsilon)|^2 \left\{ \operatorname{Re}\left(\frac{1}{Dq^2 - i\varepsilon}\right) \right\}^2. \tag{4.10}$$

The mode $q = 0$ is excluded because the quasiparticles are absorbed in the reservoirs. Blanter then obtains [8] :

$$K(\varepsilon) = K_0 \, g\left(\sqrt{2\varepsilon/E_C}\right) \tag{4.11}$$

where $K_0 = 8/\left(\pi\hbar n_0 S L E_C^2\right)$, $E_C = \hbar/\tau_D$, and

$$g(u) = -\frac{4}{u^4} + \frac{2}{u^3} \frac{\sinh u + \sin u}{\cosh u - \cos u}. \tag{4.12}$$

Asymptotically, for large values of ε, $K(\varepsilon) = \frac{K_0}{\sqrt{2}} \left(\frac{E_C}{\varepsilon}\right)^{3/2}$, in agreement with the one dimensional result of Eq. (4.9).

4.1.6 Can this theory explain the experimental results?

In the case of the wires we have measured, the effective dimensionality lies between 1 and 2 over the energy range probed (see table containing Thouless energies associated to each dimension in the previous chapter). One thus predicts a behavior for $K(\varepsilon)$ intermediate between $\varepsilon^{-3/2}$ and ε^{-1}. This prediction is incompatible with the experimental result ε^{-2}. In

the case of wire 1, we nevertheless tried to fit one of the experimental distribution functions numerically with Eq. (4.11). Instead of the theoretical value $K_0 = 7 \text{ ps}^{-1}\text{meV}^{-2}$, we needed to take $K_0 = 100 \text{ ps}^{-1}\text{meV}^{-2}$ in order to fit the curve at $U = 0.3$ meV. This parameter however does not reproduce the curves taken with different voltages U (see Ref. [9]).

4.1.7   Could a modified theory explain the experimental results?

The central ingredient of the theory is that the quasiparticle dynamics is fully described by a diffusive motion, entirely characterized by a diffusion constant D. This description is valid in a homogeneous thin film at energies smaller than $\hbar/\tau_{el}$. In the case of the copper wires we have fabricated, we have no precise control of the homogeneity. And indeed, atomic force microscopy shows a grain size of the order of 50 nm. If the grain boundaries significantly contribute to the wire resistance, the diffusion model should be replaced by a model of coupled grains inside which quasiparticles diffuse rapidly. In principle, the theory of Altshuler et al. can be extended to treat such a modified diffusion motion. The calculation proceeds in two steps:

i) calculation of the Fourier transform $\tilde{P}(r, r', \omega)$ which describes the spreading of a quasi-particle.

ii) calculation of the polarizability taking into account the modified dynamics.

It is presently not known wether a modified theory following Altshuler et al. can explain the experimental results.

We now discuss an alternate explanation.

4.2 Phenomenological model leading to the experimentally observed interaction kernel

The energy dependence of the interaction kernel found in the experiments $K(\varepsilon) \propto \varepsilon^{-2}$ can be obtained in a model in which the wire, supposed homogeneous, is described as an array of small resistors. Each resistor contains quasiparticles characterized by a certain distribution function. The fluctuating current produced by transitions in one resistor induces transitions between the quasiparticle states of another resistor. This mechanism is responsible for the interaction in this model.

Note that a film in which the resistance would be dominated by grain boundaries would be described better by an array of tunnel junctions. It turns out that such a model also yields the result $K(\varepsilon) \propto \varepsilon^{-2}$.
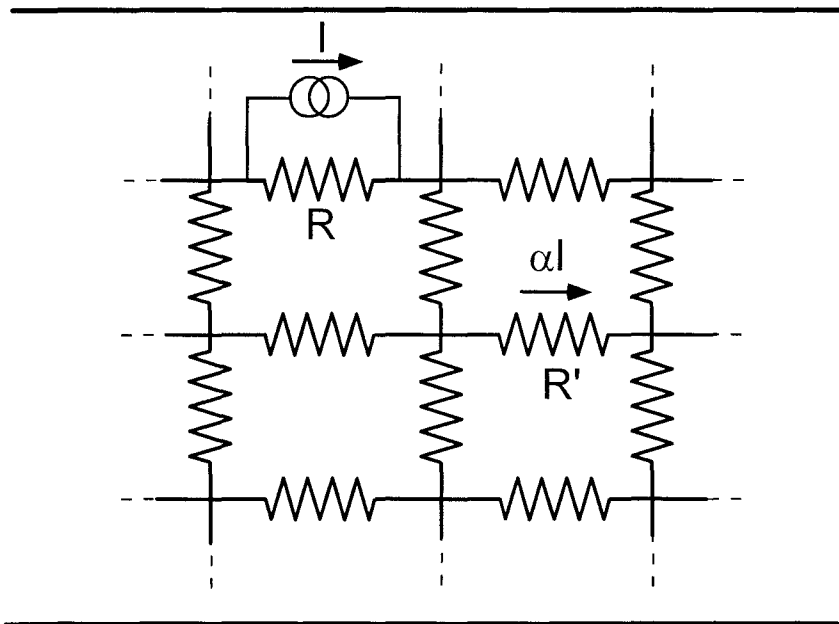
Fig. 4.4. A diffusive wire is modelled by an array of small resistors. The fluctuating current I, caused by possible transitions in resistor R, and represented as a current source in parallel with resistor R, induces transitions between quasiparticle states in resistor R'.

4.2.1 Fluctuations of the current in a resistor

The fluctuations of the current in a resistor R of dimensions smaller than the coherence length are due to the possible transitions of the quasiparticles composing the resistor from states of energy E to states of energy $E - \hbar\omega$. The current noise at frequency ω associated

with these transitions is [10] :

$$S_I(\omega) = \int_{-\infty}^{+\infty} dt\, e^{i\omega t} \langle I(0)\, I(t) \rangle = \frac{2}{R} \int_{-\infty}^{+\infty} f(E)\,(1 - f(E - \hbar\omega))\, dE. \qquad (4.13)$$

The fluctuations with $\omega > 0$ lead to emission of energy, those with $\omega < 0$ to absorption. The symmetrized current noise $\mathcal{S}_I(\omega)$ is

$$
\begin{aligned}
\mathcal{S}_I(\omega) &= \int_{-\infty}^{+\infty} dt\, e^{i\omega t} \frac{1}{2} \langle I(0)\, I(t) + I(t)\, I(0) \rangle \\
&= \frac{S_I(\omega) + S_I(-\omega)}{2} \\
&= \frac{1}{R} \int_{-\infty}^{+\infty} [f(E)\,(1 - f(E - \hbar\omega)) + f(E)\,(1 - f(E + \hbar\omega))]\, dE. \qquad (4.14)
\end{aligned}
$$

If the quasiparticle distribution functions are Fermi functions, the usual current noise [11] is found:

$$\mathcal{S}_I(\omega) = \frac{\hbar\omega}{R} \coth \frac{\beta\hbar\omega}{2}.$$

4.2.2   Rate of transitions between quasiparticle states in a resistor connected to an AC voltage source

Following Chakravarty and Schmid, we calculate the rate of absorption of an energy $\hbar\omega$ in a resistor characterized by its distribution function, biased by an alternating voltage $V_\omega e^{-i\omega t}$.

The quasiparticles are subject to the perturbation

$$H = -\frac{e}{m} \vec{p}.\vec{A},$$

where

$$\vec{\mathcal{E}}_\omega e^{-i\omega t} = -\frac{\partial \vec{A}}{\partial t}$$

is the electric field in the conductor.

In perturbation theory, the transition rate between a state k of energy E_k and a state l of energy $E_l = E_k + \hbar\omega$ occurs at a rate:

$$\Gamma_{k \to l}(\omega) = \frac{2\pi}{\hbar} \left| \left\langle k \left| \frac{e}{m} p_x \frac{\mathcal{E}_\omega}{\omega} \right| l \right\rangle \right|^2 \delta(E_l - E_k - \hbar\omega).$$

The decay rate of state k is then

$$
\begin{aligned}
\Gamma_k^{\text{out}}(\omega) &= \frac{2\pi}{\hbar} n_0 \mathcal{V} \left(\frac{e\mathcal{E}_\omega}{m\omega}\right)^2 \int \langle k\,|p_x|\,l\rangle\,\langle l\,|p_x|\,k\rangle\,\delta\left(E_l - E_k - \hbar\omega\right)\left[1 - f\left(E_l\right)\right] dE_l \\
&= \frac{1}{\hbar^2} n_0 \mathcal{V} \left(\frac{e\mathcal{E}_\omega}{m\omega}\right)^2 \int dE_l dt\, e^{i\omega t}\,\langle k\,|p_x|\,l\rangle\,e^{-i(E_l - E_k)t/\hbar}\,\langle l\,|p_x|\,k\rangle\left[1 - f\left(E_k + \hbar\omega\right)\right] \\
&= \frac{1}{\hbar^2}\left(\frac{e\mathcal{E}_\omega}{m\omega}\right)^2 \left[1 - f\left(E_k + \hbar\omega\right)\right] \int dt\, e^{i\omega t}\,\langle k\,\left|e^{-iHt}p_x e^{iHt}p_x\right|\,k\rangle \\
&= \frac{1}{\hbar^2}\left(\frac{e\mathcal{E}_\omega}{m\omega}\right)^2 \left[1 - f\left(E_k + \hbar\omega\right)\right] \int dt\, e^{i\omega t}\,\langle p_x\left(t\right)p_x\left(0\right)\rangle,
\end{aligned}
$$

where $\mathcal{V}$ is the volume of the resistor and n_0 is the density of states. Since in a diffusive conductor, at $\omega \ll 1/\tau_{el}$,

$$
\frac{1}{m^2}\int_{-\infty}^{+\infty} dt\,\langle p_x\left(t\right)p_x\left(0\right)\rangle\,e^{i\omega t} = 2v_F^2\frac{\tau_{el}}{3} = 2D, \tag{4.15}
$$

we find for the decay rate of a state of energy E by emission $(\omega > 0)$ or absorption $(\omega < 0)$ of the energy $\hbar\omega$:

$$
\begin{aligned}
\left.\frac{\partial f}{\partial t}\right|_{\text{out}}(E,\omega) &= f\left(E\right)\Gamma^{\text{out}}\left(E\right) \\
&= \frac{2}{n_0\mathcal{V}}\frac{V_\omega^2}{R}\frac{1}{(\hbar\omega)^2}f\left(E\right)\left[1 - f\left(E + \hbar\omega\right)\right]. \tag{4.16}
\end{aligned}
$$

This expression can be generalized to the decay rate caused by any fluctuating voltage source, by replacing V_ω^2 by the noise spectrum of the source $S_V\left(\omega\right)d\omega$ in the frequency range $[\omega, \omega + d\omega]$. Therefore

$$
\left.\frac{\partial f}{\partial t\partial\omega}\right|_{\text{out}}(E,\omega) = \frac{2}{n_0\mathcal{V}}\frac{S_V\left(\omega\right)}{R}\frac{1}{(\hbar\omega)^2}f\left(E\right)\left[1 - f\left(E + \hbar\omega\right)\right]. \tag{4.17}
$$

Similarly, the rate at which states of energy E are populated is

$$
\left.\frac{\partial f}{\partial t\partial\omega}\right|_{\text{in}}(E,\omega) = \frac{2}{n_0\mathcal{V}}\frac{S_V\left(\omega\right)}{R}\frac{1}{(\hbar\omega)^2}f\left(E - \hbar\omega\right)\left[1 - f\left(E\right)\right]. \tag{4.18}
$$

The power absorbed $(\omega > 0)$ or emitted $(\omega < 0)$ at frequency ω is then:

$$
\begin{aligned}
P\left(\omega\right) &= \hbar\omega \int_{-\infty}^{\infty} \left.\frac{\partial f}{\partial t\partial\omega}\right|_{\text{out}}(E,\omega)\,n_0\mathcal{V}dE \\
&= \frac{2}{\hbar\omega}\int_{-\infty}^{\infty}\frac{S_V\left(\omega\right)}{R}f\left(E\right)\left[1 - f\left(E + \hbar\omega\right)\right]dE \\
&= \frac{1}{\hbar\omega}S_V\left(\omega\right)S_I\left(-\omega\right).
\end{aligned}
$$

The total power is

$$
\begin{aligned}
P &= \int_{-\infty}^{\infty} P(\omega)\, d\omega \\
&= \int_{-\infty}^{\infty} \frac{2}{\hbar\omega} \frac{S_V(\omega)}{R} f(E)\left[1 - f(E + \hbar\omega)\right] dE\, d\omega \\
&= \frac{1}{R} \int_{-\infty}^{\infty} dE \frac{d\omega}{\hbar\omega} \left[S_V(\omega) f(E)\left[1 - f(E + \hbar\omega)\right] - S_V(-\omega) f(E + \hbar\omega)\left[1 - f(E)\right]\right].
\end{aligned}
$$

In the case of a classical voltage source for which $S_V(\omega) = S_V(-\omega)$, one recovers Ohm's law:

$$
\begin{aligned}
P &= \frac{1}{R} \int_{-\infty}^{\infty} dE\, d\omega\, S_V(\omega) \frac{\left[f(E) - f(E + \hbar\omega)\right]}{\hbar\omega} \\
&= \frac{1}{R} \int_{-\infty}^{\infty} d\omega\, S_V(\omega) \\
&= \frac{\left\langle V(t)^2 \right\rangle}{R}.
\end{aligned}
$$

The dissipation is then still characterized by R, so that relation (4.14) can be understood as a generalized dissipation-fluctuation theorem for out-of-equilibrium distribution functions.

4.2.3   Rate of the transitions induced in a resistor by the current fluctuations in another

The fluctuating current I associated to resistor R at position x is divided into the other branches of the network. A fraction αI of this current flows through a second resistance $R' = R$ situated in x', inducing transitions between quasiparticle states. The fluctuating voltage source across R' due to current fluctuations in R has a spectrum $S_V(\omega) = \alpha^2 R'^2 S_I(\omega)$. The decay rate of a state of energy E' of R' induced by the fluctuations $S_I(\omega)$ is therefore:

$$
\begin{aligned}
\left.\frac{\partial f}{\partial t \partial \omega}\right|_{\text{out}, x \to x'} (E', \omega) &= \frac{2\alpha_{x,x'}^2 R'}{n_0 \mathcal{V}} \frac{S_I(\omega)}{(\hbar\omega)^2} f_{x'}(E')\left[1 - f_{x'}(E' + \hbar\omega)\right] \\
&= \frac{4\alpha_{x,x'}^2}{n_0 \mathcal{V}} \frac{1}{(\hbar\omega)^2} \int f_{x'}(E')\left[1 - f_{x'}(E' + \hbar\omega)\right] f_x(E)\left(1 - f_x(E - \hbar\omega)\right) dE.
\end{aligned}
$$

$$
(4.19)
$$

Expression (4.19) integrated over ω has the same form as the out-collision term of the quantum Boltzmann equation corresponding to quasiparticle-quasiparticle interaction.

4.2.4   Kernel of the effective quasiparticle-quasiparticle interaction

For this model to predict the actual magnitude of the quasiparticle-quasiparticle interaction,

the partitioning of the wire must be fine enough so that no fluctuations are averaged out. The resistors should however be larger than the elastic mean free path. Consequently, to describe a diffusive wire with this model, the resistors should have a size slightly larger than l_e.

The identification yields $K(x, x', \varepsilon) = \frac{4\alpha^2_{x,x'}}{\hbar n_0 \mathcal{V}}/\varepsilon^2$, which is the energy dependence found in the experiment. This model predicts a rapid decrease with distance of the interaction, since at distances large compared with the size of the resistor, $\alpha^2_{x,x'} \propto 1/(x - x')^6$. The typical interaction time can thus be written as

$$\tau_0^{-1} = \frac{4 \sum \alpha^2_{x,x'}}{\hbar n_0 \mathcal{V}}$$
$$= \frac{4(d-1)/d^2}{\hbar n_0 \mathcal{V}},$$

where d is the dimensionality of the array.

The interaction time $\tau_0 = 1$ ns found in the experiment corresponds to resistors of size $\mathcal{V}^{1/3} \simeq 50$ nm, $i.e.$ a few elastic mean free paths. This is compatible with the picture of an array of resistors. Moreover, this size is smaller than the coherence length in metallic thin films at low temperatures. In addition, in volumes of this size, the distribution function is well defined on an energy scale of the order of the typical level spacing $1/n_0\mathcal{V} \approx 1$ μeV. This is smaller than the energy resolution of the experiment.

However, our model is inconsistent in that each resistor is treated as a coherent object, but the correlations between different resistors are neglected. Nevertheless, this seemingly contradictory procedure yields the same result as an exact quantum calculation, in the case of the zero frequency noise in diffusive conductors, whether coherent or not. Indeed, Nagaev [13] has shown that:

$$\mathcal{S}_V = \frac{4}{RL} \int_0^L dx \int dE f_x(E)(1 - f_x(E)).$$

This expression corresponds exactly to the incoherent addition of the voltage noise found through Eq. (4.13) across elementary resistors in series composing the wire. It is thus plausible that a similar effect occurs for the calculation of $K(\varepsilon)$.

4.3   Towards a fully quantum microscopic theory

The phenomenological model outlines the importance of elastic collisions, which enable the transitions between quasiparticle states. The resulting fluctuations induce the emission and absorption of energy, which is localized in the elementary resistors considered. A microscopic extension of this model is provided by the picture of the Landauer dipoles [14] . These fluctuating dipoles, situated on the impurities, result from the elastic collisions of quasiparticles against the impurities. They produce a fluctuating electromagnetic field, to which neighboring quasiparticles can couple. This description, which preserves the spatial coherence in the sample, has not yet been completed.

REFERENCES

[1] A. Schmid, Z. Phys. **271**, 251 (1974).

[2] B. L. Altshuler and A. G. Aronov, in *Electron-Electron Interactions in Disordered Systems*, Ed. A. L. Efros and M. Pollak, Elsevier Science Publishers B.V. (1985), p. 29.

[3] W. L. McMillan, Phys. Rev. B **24**, 2739 (1981).

[4] G. Montambaux, in *Quantum Fluctuations*, S. Reynaud, E. Giacobino and J. Zinn-Justin, eds. (Elsevier, Amsterdam, 1997), p. 387.

[5] B. L. Altshuler, A. G. Aronov, and D. E. Khmelnitskii, J. Phys. **C15**, 7367 (1982).

[6] Note that the polarizability of an out-of-equilibrium fermionic system, such as the one created in our experiment, might have a different form (M. Combescot, C. Caroli, private communication).

[7] B. L. Altshuler and A. G. Aronov, in *Electron-Electron Interactions in Disordered Systems*, Ed. A. L. Efros and M. Pollak, Elsevier Science Publishers B.V. (1985), formula (4.4).

[8] Ya. Blanter, private communication.

[9] H. Pothier, S. Guéron, Norman O. Birge, D. Esteve, and M. H. Devoret, Z. Phys. B **104**, 178 (1997).

[10] M. Büttiker, Phys. Rev. B **45**, 3807 (1992); S.-R. Eric Yang, Solid State Comm. **81**, 375 (1992).

[11] R. Kubo, M. Toda, N. Hashitsume, *Statistical Physics II* (Springer Verlag, Berlin, 1991), p. 170.

[12] S. Chakravarty and A. Schmid, Phys. Rep. **140**, 193 (1986).

[13] K. E. Nagaev, Phys. Lett. A **169**, 103 (1992).

[14] R. Landauer, IBM J. Res. Develop. **1**, 223 (1957); **32**, 306 (1988).

Chapter 5
Theoretical description of the proximity effect

The "proximity effect" is a rather general term describing the modifications induced in a non-superconducting metal (which we will call normal, N) when it is in contact with a superconducting (S) metal. Although the term also covers the modifications induced in the superconductor, we will concentrate on describing the nature of the order induced in the normal metal. As has been predicted theoretically and has been observed in our experiments and in others, the nature of this order is subtle and different from that of a bulk superconductor. This leads to curious manifestations of the proximity effect: a normal diffusive wire connecting two superconductors can sustain a supercurrent [1,2] , but the resistance of a normal metal in good contact with only one superconductor does not go to zero as the temperature is lowered. In fact, at zero temperature the resistance of this metal recovers its normal state value.

The proximity effect was first analyzed within the framework of the Ginzburg-Landau theory [3] . In this phenomenological approach, the superconducting order is described by a single complex order parameter $\Psi(r)$ whose modulus is related to the amount of pair correlations and whose phase is the superconducting phase. The spatial variations of this order parameter are determined by minimizing the Ginzburg-Landau free energy functional. This approach however does not take into account the strong energy dependence of the propagation of the pair correlations, which can be understood as follows.

Let us start by considering the ground state of a bulk BCS superconductor. This ground state is a coherent superposition of the states of the electrode in the normal state, in which
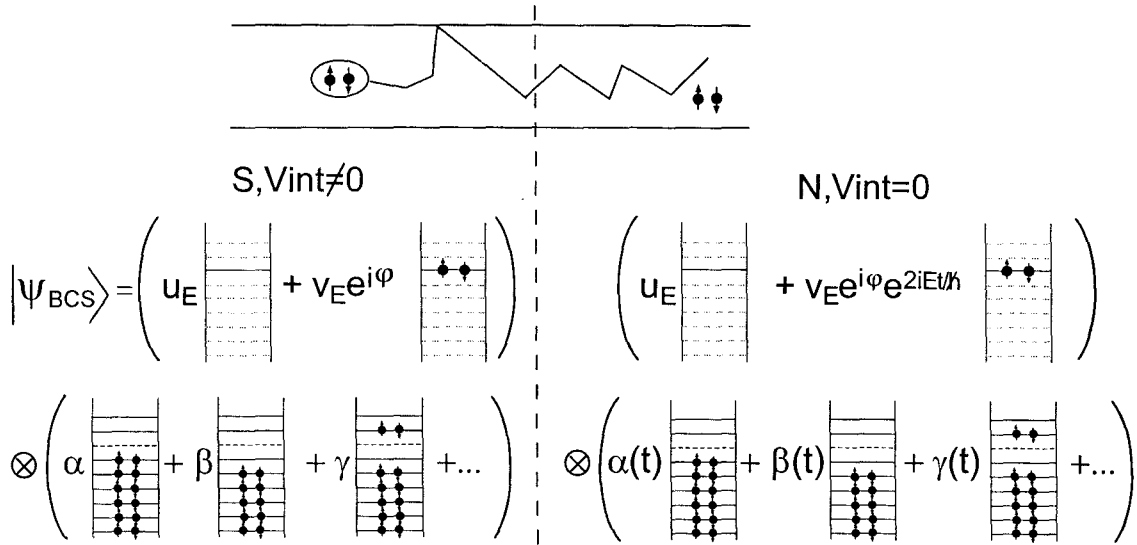
Fig. 5.1. top: Cooper pair entering a normal metal. bottom: BCS ground state and its transformation upon entering the normal metal. On the left hand side is pictured the BCS wave function, as a coherent superposition of empty and doubly occupied states with a constant phase difference imposed by the pairing interaction V_{int}. A Cooper pair corresponding to the state of energy E doubly occupied with probability amplitude $v_E e^{i\varphi}$ and empty with probability amplitude u_E transforms in the normal metal into the sum of two contributions with phases differing by $\varphi+2Et/\hbar$.

each single quasiparticle energy level is either doubly occupied or empty. The wave function describing this ground state is given in second quantization by [4] :

$$|\Psi_{BCS}\rangle = \prod_{\{E\}} \left(u_E + v_E e^{i\varphi}c^\dagger_{\uparrow E}c^\dagger_{\downarrow E}\right)|0\rangle .$$

Here u_E and v_E are real amplitudes: v_E^2 is the probability that the state at energy E is doubly occupied and $u_E^2 = 1 - v_E^2$ is the probability that this state is empty. The effective interaction in the superconductor imposes that φ, called the superconducting phase, be energy-independent. What happens to this coherent superposition when the superconducting interaction vanishes? In other words, what happens to a Cooper pair entering a normal metal? This has been pictured in Fig. 5.1. A state which was a coherent superposition of a states of the electrode in which the energy level at E was empty and doubly occupied now becomes a superposition of two eigenstates with an energy difference of $2E$. The relative amplitude of these two states dephases in time as the pair propagates in the normal metal by a factor $\exp\left(-i2Et/\hbar\right)$, where t is the time elapsed after the pair has left the superconductor. A dephasing of order 1 is obtained for $t \sim \hbar/E$, i.e. after diffusion on a length $\sqrt{\hbar D/E}$, where D is the diffusion constant. Thus,

$\sqrt{\hbar D/E}$ is the typical energy-dependent length at which pair correlations decay in the normal metal. For small energies, the propagation of superconducting order extends far away, but is limited, however, by other dephasing processes like spin flip scattering by magnetic impurities in the sample, or by inelastic collisions with other electrons.

Two theories take into account the energy dependence of the pair correlations propagation. The first is the microscopic treatment provided by the Bogoliubov-de Gennes [5] equations, which are the Schrödinger equations for the electron and hole-like excitations. In NS samples these equations are coupled, and the solutions describe coherent superpositions of the electron and hole-like excitations of the normal state. This approach is particularly well adapted to ballistic samples, in which the normal state wavefunctions are plane waves. It provides an elegant means to compute the conductance of NS circuits, as shown in the appendix.

The second theory, also called "theory of non-equilibrium superconductivity" [8–10] , is based on Green functions. It provides equations for the disorder-averaged pair correlations. It has succeeded in explaining quantitatively all the experiments on the proximity effect realized so far in thin metallic films. In this chapter I present the general formalism of this theory, along with those results which are essential to the understanding of the experiments performed during the course of this thesis.

5.1 Definitions of the Green functions used in the description of the proximity effect

5.1.1 The impurity averaged Green function

The theory of non-equilibrium superconductivity describes a system of electrons in terms of correlations for the electron field operator $\Psi(r, t)$. The completeness of the theory stems from the fact that it treats the normal-like correlations and the superconducting-like correlations all at once. This is done by grouping these correlations in 2×2 matrices in the electron-hole Nambu space, of which a basis is

$$\Psi = \begin{pmatrix} \Psi_\uparrow(r, t) \\ \Psi_\downarrow^\dagger(r, t) \end{pmatrix},$$

where $\Psi_\uparrow(r, t)$ and $\Psi_\uparrow^\dagger(r, t)$ are the annihilation and creation operators of a fermionic quasiparticle with spin $\uparrow$ at position r in the Heisenberg representation. These correlations are grouped in two matrices $\hat{M}$ and $\hat{M}'$, where $\hat{M}$ is a matrix of the anti-commutator of these operators, and $\hat{M}'$ is the same matrix but with commutators replacing the anticommutators:

$$\hat{M}(r, t - t') = \begin{pmatrix} \left\langle \left\{ \Psi_\uparrow(r, t), \Psi_\uparrow^\dagger(r, t') \right\} \right\rangle & \left\langle \left\{ \Psi_\uparrow(r, t), \Psi_\downarrow(r, t') \right\} \right\rangle \\ -\left\langle \left\{ \Psi_\downarrow^\dagger(r, t), \Psi_\uparrow^\dagger(r, t') \right\} \right\rangle & -\left\langle \left\{ \Psi_\downarrow^\dagger(r, t), \Psi_\downarrow(r, t') \right\} \right\rangle \end{pmatrix}. \tag{5.1}$$

Here $\langle \rangle$ is the statistical and disorder-averaging operation, and $\{O, O'\} = OO' + O'O$. The diagonal elements of $\hat{M}$ and $\hat{M}'$ are the one-particle Green functions for spin-up electrons and spin down holes respectively, corresponding to "normal" correlations, while the off-diagonal elements are related to the amplitude for substracting or adding a pair of particles to the system without creating excitations, i.e. are superconducting-type correlations.

The basic objects of the theory are the retarded, advanced, and Keldysh Green functions $\hat{R}$, $\hat{A}$, and $\hat{K}$, given by [8] :

$$\hat{R}(r, \varepsilon) = \frac{1}{n_0} \mathcal{F} \left[-i\theta(\tau) \hat{M}(r, \tau) \right], \tag{5.2}$$

$$\hat{A}(r, \varepsilon) = \frac{1}{n_0} \mathcal{F} \left[i\theta(-\tau) \hat{M}(r, \tau) \right], \tag{5.3}$$

$$\hat{K}(r, \varepsilon) = \frac{1}{n_0} \mathcal{F} \left[-i\hat{M}'(r, \tau) \right], \tag{5.4}$$

where $\mathcal{F}$ denotes the Fourier transform in time and n is the density of states at the Fermi energy. The θ function selects $\tau > 0$ for $\hat{R}$ and $\tau < 0$ for $\hat{A}$. The Green function $\hat{K}$, called

the Keldysh function, differs from the Green functions $\hat{R}$ and $\hat{A}$ in that it contains no time ordering, and is the commutator instead of the anti-commutator of operators. It is related to $\hat{R}$ and $\hat{A}$ by the relation $\hat{K} = \hat{R}\hat{f} - \hat{f}\hat{A}$, where $\hat{f}$ is the quasiparticle filling matrix. For a system in equilibrium, $\hat{f} = (1 - 2f_T)\,\hat{1}$, where f_T is the usual Fermi function. In out-of-equilibrium situations, the filling matrix is more complex. Because of the time ordering function, $\hat{R}$ and $\hat{A}$, called equilibrium Green functions, contain the information on the one-particle spectrum of the system. The Keldysh function $\hat{K}$ contains in addition the filling of these one particle states. It differs from the functions $\hat{R}$ and $\hat{A}$ in out-of-equilibrium situations, for instance when a current is flowing through the structure. The goal of the theory is to determine the Green functions $\hat{R}$, $\hat{A}$, $\hat{K}$ and calculate afterwards the physical quantities of interest.

5.1.2 The global Green function

The three Green functions introduced previously can be handled together. They can be grouped in a 4×4 matrix noted $\check{G}$, which obeys the "normalization" condition $\check{G}^2 = \check{1}$:

$$\check{G}(r,\varepsilon) = \left(\begin{array}{cc} \hat{R} & \hat{K} \\ 0 & \hat{A} \end{array} \right)$$

The equation for the global Green function $\check{G}(r,\varepsilon)$, which contains the equations for the three Green functions, is obtained diagrammatically from a Hamiltonian which contains elastic scattering with impurities, spin-flip scattering on magnetic impurities, and the electron-phonon coupling:

$$\hbar D \check{\nabla} . \left(\check{G}\check{\nabla}\,\check{G} \right) + i\left[\check{H}_0, \check{G} \right] - \frac{\hbar}{\tau_{sf}} \left[\check{\tau}_z \check{G} \check{\tau}_z, \check{G} \right] = 0. \tag{5.5}$$

Here $\check{H}_0 = \left(\begin{array}{cc} \hat{H}_0 & 0 \\ 0 & \hat{H}_0 \end{array} \right)$ and $\check{\tau}_i = \left(\begin{array}{cc} \hat{\tau}_i & 0 \\ 0 & \hat{\tau}_i \end{array} \right)$, with

$$\hat{H}_0 = \left(\begin{array}{cc} E & i\Delta^* \\ i\Delta & -E \end{array} \right), \quad \hat{\tau}_x = \left(\begin{array}{cc} 0 & 1 \\ 1 & 0 \end{array} \right), \quad \hat{\tau}_y = \left(\begin{array}{cc} 0 & -i \\ i & 0 \end{array} \right), \quad \text{and } \hat{\tau}_z = \left(\begin{array}{cc} 1 & 0 \\ 0 & -1 \end{array} \right),$$

where E is the energy, Δ is the effective pair potential that must be determined self-consistently, τ_{sf} is the spin-flip scattering time, and the $\hat{\tau}_i$ are the usual Pauli matrices. In a magnetic field, the derivative operator $\check{\nabla}$ must be replaced by its covariant form $\left(\check{\nabla} + 2i\frac{e}{\hbar}\vec{A}\hat{\tau}_z \right)$. The inelastic scattering between quasiparticles can be incorporated by adding an imaginary part to the energy E.

The self-consistent equation for Δ is [10] :

$$\Delta = n_0 V_{eff} \int_0^{\hbar \omega_D} \mathcal{F} \left[\left\langle \left\{ \Psi_\uparrow(r,t), \Psi_\downarrow(r,t') \right\} \right\rangle \right] dE \tag{5.6}$$

$$= n_0 V_{eff} \int_0^{\hbar \omega_D} \frac{1}{4i} \operatorname{Tr} \left[(\hat{\tau}_x - i\hat{\tau}_y) \hat{K} \right] dE, \tag{5.7}$$

where n_0, V_{eff} and ω_D are the normal metal density of states, the strength of the pair interactions and the Debye frequency, respectively. In a normal metal, the pairing interaction V_{eff} is either repulsive or zero. For simplicity, we will consider exclusively that there is no pairing interaction ($V_{\text{eff}} = 0$) in a normal metal. So, although superconducting-type correlations $\left\langle \left\{ \Psi_\uparrow(r,t), \Psi_\downarrow(r,t') \right\} \right\rangle$ may exist in a normal metal, the pair potential Δ is zero.

The central equation (5.5) is supplemented with the boundary conditions for the various Green functions in the different electrodes of the sample. We will analyze in detail the equations obeyed by the functions $\hat{R}$, $\hat{A}$, $\hat{K}$, called the Usadel equations [11] , which are obtained by projecting Eq. (5.5).

Compared to the Bogoliubov-de Gennes equations, this formalism does not require solving the Schrödinger equation for the microscopic wavefunctions, but directly leads to a set of diffusion-like equations for averaged quantities which, as will be seen, are directly related to physical properties.

5.2 Equilibrium proximity effect

At thermal equilibrium, all the equilibrium properties of a system are contained in the advanced or retarded Green function.

5.2.1 Parametrization of Green functions by angles on the complex unit sphere

The angular parametrization of $\hat{R}$ and $\hat{A}$ [18] not only simplifies the equations of the proximity effect, but also provides a useful geometrical description of the equilibrium Green functions:

$$\hat{R} = \cos\theta\hat{\tau}_z + \sin\theta(\cos\varphi\hat{\tau}_x + \sin\varphi\hat{\tau}_y) = \begin{pmatrix} \cos\theta & e^{-i\varphi}\sin\theta \\ e^{i\varphi}\sin\theta & -\cos\theta \end{pmatrix} \tag{5.8}$$

$$\hat{A} = -\cos\bar{\theta}\hat{\tau}_z + \sin\bar{\theta}(\cos\varphi\hat{\tau}_x + \sin\varphi\hat{\tau}_y) = \begin{pmatrix} -\cos\bar{\theta} & e^{-i\varphi}\sin\bar{\theta} \\ e^{i\varphi}\sin\bar{\theta} & \cos\bar{\theta} \end{pmatrix},$$

where $\theta = \theta(r, E)$ is a complex angle which quantifies the pairing and $\varphi = \varphi(r, E)$ is the real superconducting phase. In general the superconducting phase $\varphi(r, E)$ depends on energy, in contrast with the case of a bulk superconductor. The decomposition of a 2×2 matrix
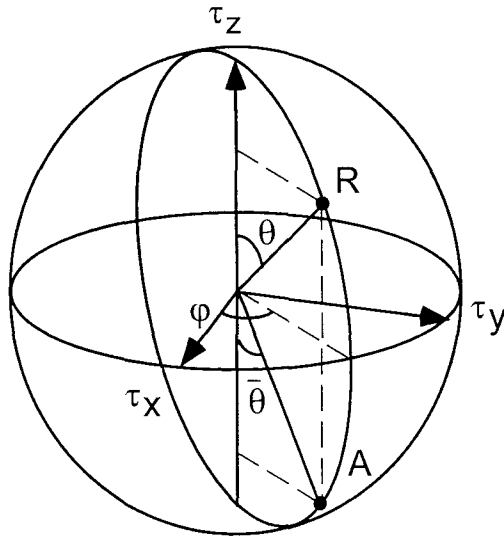
Fig. 5.2. Representative points R and A on the complex unit sphere of the retarded and advanced Green functions.

on the basis of the Pauli matrices translates into the three coordinates of a representative vector in a 3-dimensional space. The extremity of this vector lies on the complex unit sphere,

defined as the set of points with polar coordinates θ and φ, for complex θ and real φ. The two representative points R and A are pictured in Fig. 5.2. Because of the electron hole symmetry, the functions $\hat{R}$ and $\hat{A}$ are redundant, and in the following we concentrate on the representative point of the retarded Green function $\hat{R}$.

5.2.1.1   Special points on the sphere

Normal reservoir

The correlation function of normal quasiparticles is a delta function of space and time. Therefore the retarded Green function is the unit matrix $\hat{1}$, and the pairing angle θ is zero at all energies. The north pole of the sphere therefore represents an electrode anchored in the normal state, which we will call in the following normal reservoir.

Superconducting reservoir

The representative point of a S reservoir, $i.e.$ an electrode anchored in the superconducting state, is located at an angle $\theta = \theta_{\mathrm{BCS}}(E) = \arctan i\frac{\Delta}{E}$, and at an energy-independent longitude φ equal to the superconducting phase of the reservoir. At zero energy, the representative point of a superconducting reservoir lies on the equator.

5.2.1.2   Representative point of the retarded Green function of any point of an NS structure

The proximity effect in normal-superconducting structure is described by assigning to each position r along the circuit, at each energy E, a point P representative of the function $\hat{R}$ on the complex unit sphere.   In general, the representative points P of any NS structure form an energy-dependent trajectory which is continuous except at tunnel junction interfaces. This trajectory determines how the properties of the metal interpolate between those of the S and N metals.

5.2.1.3   Real unit sphere at zero energy

At zero energy, all parameters are real: all trajectories lie on the real unit sphere. A typical trajectory joining a normal and a superconducting reservoir at zero energy is represented Fig. 5.3.

In the following paragraphs we give the expressions of the physical quantities as a function of the pairing angle θ, and explain how to determine the trajectory followed by the pairing
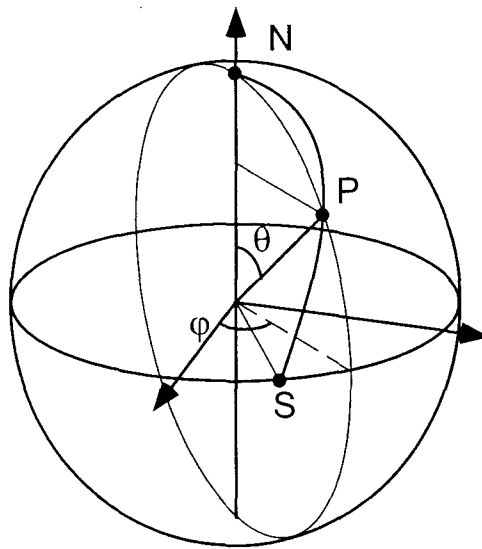
Fig. 5.3. Graphical representation of the proximity effect in a normal structure between a normal reservoir (N) and a superconducting reservoir (S). The curved line figures a typical set of points P representing the retarded Green function at zero energy along the structure.

angle.

5.2.2   Physical properties in terms of the pairing angle θ

5.2.2.1   Single particle density of states

The single particle density of states $n(r, E)$ at position r and at energy E is related to the pairing angle $\theta(r, E)$ by

$$n(r, E) = n_0 \operatorname{Re}\left[\cos \theta(r, E)\right] \tag{5.9}$$

where n_0 is the normal density of states at the Fermi level (the normal density of states is taken as independent of the energy on the scale of the superconducting gap).

A constraint on this density of states is that it should obey the sum rule, which states that the total number of single particle states in any metal, whatever its pairing state, is constant and equal to number of states in the normal metal:

$$\int (n(E) - n_0)\, dE = 0.$$

5.2.2.2   Supercurrent density and density of pairs

In NS structures containing several superconducting reservoirs biased at different phases, or in structures with one superconductor and a normal metal loop threaded by a magnetic field, equilibrium supercurrents flow in the sample. As in a BCS superconductor, the supercurrent density j_S is related to the covariant phase gradient [10] :

$$j_S = \frac{\sigma}{e} \int_{-\infty}^{+\infty} dE \tanh\left(\frac{E}{2k_B T}\right) \operatorname{Im}\left[\sin^2 \theta\right]\left(\nabla \varphi + \frac{2e}{\hbar} A\right) \tag{5.10}$$

where σ is the normal state conductivity and A is the vector potential. At high temperature, the dominant contribution to the integral arises from small energies and one can neglect the energy dependence of the phase. We can identify the above expression with the Ginzburg-Landau result $j_S = -\frac{\hbar e}{m}|\Psi|^2\left(\nabla \varphi + \frac{2e}{\hbar} A\right)$, to express the modulus squared of the Ginzburg-Landau order parameter in terms of the pairing angle θ :

$$|\Psi|^2 = \frac{m}{e^2\hbar}\sigma \int_0^{+\infty} dE \tanh\left(\frac{E}{2k_BT}\right) \text{Im}\left[\sin^2\theta\right] \tag{5.11}$$

In the Ginzburg-Landau theory, $|\Psi|^2$ represents the density of superconducting electrons. It thus appears to be the weighted average of $\text{Im}\left[\sin^2\theta\right]$, which can be interpreted as an effective energy dependent density of pairs.

In contrast, with this parametrization, the self-consistency equation for $\Delta(r)$ is:

$$\Delta(r) = n_0 V_{eff} \int_0^{\hbar\omega_D} dE \tanh\left(\frac{E}{2k_BT}\right) \text{Im}\left[\sin\theta\left(r,E\right)\right] \exp i\varphi\left(r,E\right). \tag{5.12}$$

The factor $\text{Im}[\sin\theta]$ which appears here instead of the effective pair density $\text{Im}\left[\sin^2\theta\right]$ can thus be considered an energy-dependent pair amplitude.

5.2.3 The equilibrium Usadel equations

For simplicity, we consider in the following quasi-one dimensional NS systems such as the one represented in Fig. 5.4. In this one-dimensional regime, the equation for $\hat{R}$ deduced from
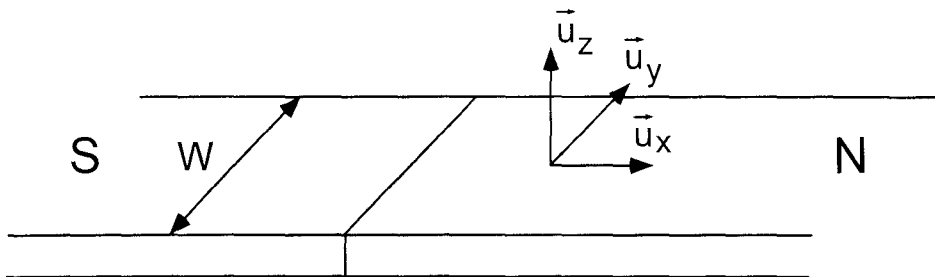
Fig. 5.4.

Eq. (5.5) reads:

$$\hbar D \frac{\partial}{\partial x}\left(\hat{R}\frac{\partial}{\partial x}\hat{R}\right) + i\left[\hat{H}_0, \hat{R}\right] - \frac{\hbar}{\tau_{sf}}\left[\hat{\tau}_z\hat{R}\hat{\tau}_z, \hat{R}\right] = 0. \tag{5.13}$$

Since the commutator of two 2×2 matrices is proportional to the vectorial product of the vectors associated with these matrices, Eq. (5.13) can be understood in terms of forces acting on the point R, which can be decomposed in horizontal and longitudinal forces. For instance, the part of the Hamiltonian containing the pair potential Δ acts as a force directed downward, tending to bring the point R closer to the equator. The Usadel equations are the projection

of Eq. (5.13) along the local tangent plane:

$$\frac{\hbar D}{2}\frac{\partial^2 \theta}{\partial x^2} + \left[iE - \left(\frac{\hbar}{\tau_{sf}} + \frac{\hbar D}{2} \left(\frac{\partial \varphi}{\partial x} + \frac{2e}{\hbar}A_x \right)^2 \right) \cos\theta \right] \sin\theta + \Delta(x)\cos\theta = 0, \qquad (5.14)$$

$$\frac{\partial}{\partial x}\left[\left(\frac{\partial \varphi}{\partial x} + \frac{2e}{\hbar}A_x \right) \sin^2\theta \right] = 0, \qquad (5.15)$$

where A_x is the vector potential component along the wire.

5.2.3.1   Equilibrium Usadel equation in a perpendicular magnetic field

In a constant magnetic field applied perpendicularly to the plane of the sample, as is sketched in Fig.5.5, the magnetic field enters as an additional spin-flip rate.   Indeed, if the thickness
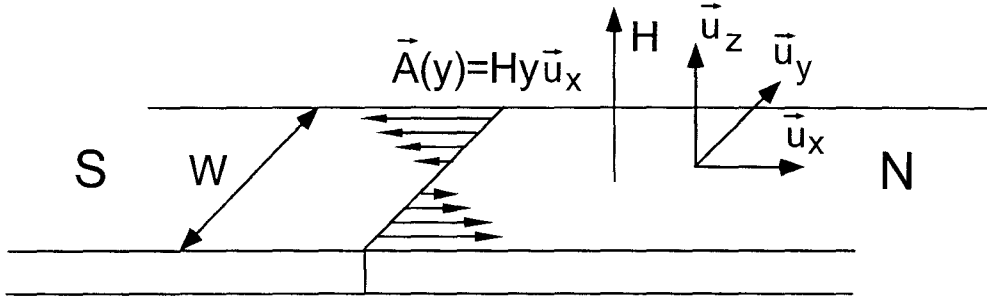
Fig. 5.5. Sketch of a superconducting wire in contact with a normal wire, in a perpendicular magnetic field.

of the superconducting film is inferior to its London penetration depth, screening of the field can be neglected and the vector potential can be taken to be

$$\vec{A} = A_x\left(y\right)\vec{u}_x = Hy\vec{u}_x.$$

The effect of the magnetic field is included in the one-dimensional Usadel equation by inserting in Eq. (5.14) the square of the vector potential averaged over the width of the wire $\langle A^2 \rangle_y = \frac{H^2 w^2}{12}$. The perpendicular magnetic field then simply enters through an additional depairing term of rate γ_H given by

$$\gamma_H = \frac{1}{\tau_H} = \frac{e^2}{6\hbar^2}w^2 DH^2, \qquad (5.16)$$

and the Usadel equation for the normal wire reads

$$\frac{\hbar D}{2}\frac{\partial^2 \theta}{\partial x^2} + \left[iE - \left(\frac{\hbar}{\tau_{sf}} + \frac{\hbar}{\tau_H} \right) \cos\theta \right] \sin\theta = 0. \qquad (5.17)$$

5.2.3.2 Integrated Usadel equation

In the case where the pair potential $\Delta(x)$ can be considered constant, Eq. (5.14) can be integrated once, yielding

$$\frac{\hbar D}{4}\left(\frac{\partial\theta}{\partial x}\right)^2 - iE\cos\theta + \left(\frac{\hbar}{4\tau_{sf}} + \frac{\hbar D}{8}\left(\frac{\partial\varphi}{\partial x} + \frac{2e}{\hbar}A_x\right)^2\right)\cos 2\theta + \Delta\sin\theta = F(E), \quad (5.18)$$

where the function $F(E)$ is imposed by the boundary conditions.

5.2.4 Example of a solution to the Usadel equation: disordered BCS Superconductor

5.2.4.1 BCS pairing angle

In bulk superconductors, or in superconducting wires of transverse dimensions inferior to the penetration depth of the field, the order parameter $\Delta = \Delta_{BCS}$ is constant, and Eq. (5.14) simply reduces to

$$\tan\theta_{BCS}(E) = i\frac{\Delta}{E}, \quad (5.19)$$

i.e.
$$\theta_{BCS}(E) = \begin{cases} \frac{\pi}{2} + i\arg\tanh\frac{E}{\Delta} & \text{if } |E| < \Delta \\ i\arg\tanh\frac{\Delta}{E} & \text{if } |E| > \Delta \end{cases} \quad (5.20a)$$

We have represented the variation with energy of the pairing angle θ in Fig. 5.6. The BCS pairing angle is real only at zero energy: $\theta_{BCS}(0) = \frac{\pi}{2}$. As the energy increases, the real part of $\theta_{BCS}(E)$ remains equal to $\frac{\pi}{2}$ and the imaginary part increases. At the gap energy, the pairing angle becomes purely imaginary and decreases down to zero for increasing energy. The quantities which will lead to the physical characteristics of the superconductor are the cosine and sine of this BCS pairing angle:

$$\cos\theta_{BCS}(E) = \frac{|E|}{\sqrt{E^2 - \Delta^2}} \quad (5.21)$$

$$\sin\theta_{BCS}(E) = \frac{\Delta}{\sqrt{\Delta^2 - E^2}}. \quad (5.22)$$

5.2.4.2 BCS density of states

From the definition (5.9), the BCS density of states is readily found as
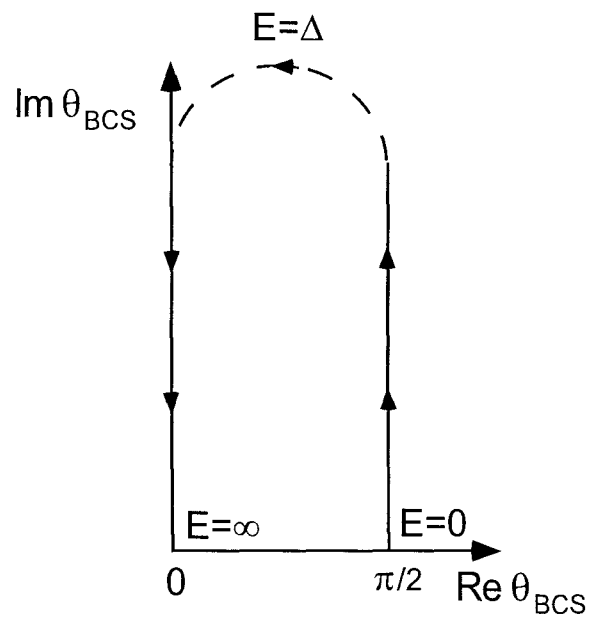
Fig. 5.6. Energy dependence of the pairing angle in a homogeneous superconductor, in the complex plane.
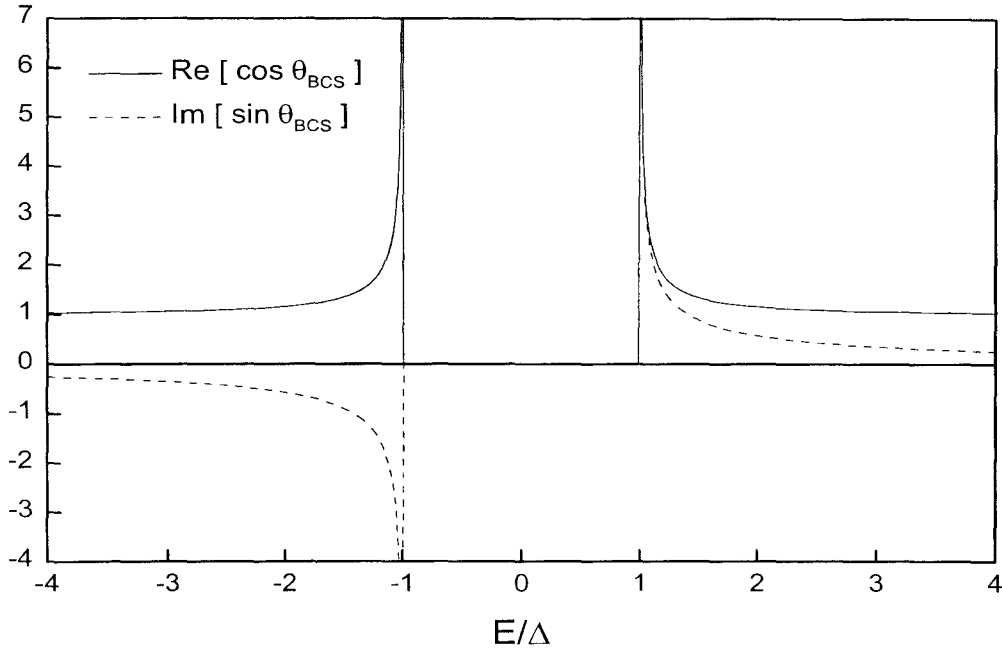
Fig. 5.7. Real part of the cosine (density of states) and imaginary part of the sine (pair amplitude) of the pairing angle in a homogeneous BCS superconductor.

$$n_{\mathrm{BCS}}(E) = n_0 \operatorname{Re}[\cos\theta_{\mathrm{BCS}}(E)] = \begin{cases} 0 & \text{if } |E| < \Delta \\ n_0 \dfrac{|E|}{\sqrt{E^2 - \Delta^2}} & \text{if } |E| > \Delta. \end{cases}$$

One recognizes the BCS result, which appears not to be affected by disorder. Note that the pair potential Δ coincides here with a real gap in the density of states. This density of states is plotted in Fig. 5.7.

5.2.4.3 Pair amplitude, density of pairs and Ginzburg-Landau order parameter

The pair amplitude [6] is

$$\operatorname{Im}[\sin\theta_{\mathrm{BCS}}] = \begin{cases} 0 & \text{if } |E| < \Delta \\ \dfrac{\Delta}{\sqrt{E^2 - \Delta^2}} \dfrac{E}{|E|} & \text{if } |E| < \Delta \end{cases}$$

The effective density of pairs is non zero only at the gap energy, and is given by (see Fig. 5.7):

$$\mathrm{Im}[\sin^2 \theta_{\mathrm{BCS}}(E)] = \frac{\pi\Delta}{2}[\delta(E - \Delta) - \delta(E + \Delta)], \tag{5.23}$$

leading to a supercurrent density (see Eq. 5.10)

$$j_S = \sigma\frac{\pi\Delta}{e}\tanh\left(\frac{\Delta}{2k_B T}\right)\left(\nabla\varphi - \frac{2e}{\hbar}A\right). \tag{5.24}$$

The presence of the conductivity σ in expression (5.24) shows that the supercurrent amplitude is a function of the disorder in the wire.

5.3 Boundary conditions for the Green functions

5.3.1 Reservoirs

The reservoirs impose fixed boundary conditions: $\theta = 0$ at a normal reservoir, and $\theta = \theta_{\mathrm{BCS}}$ at a superconducting reservoir, the phase φ being given by the phase of the superconductor. Note that if there is only one superconducting electrode in the system, the phase at all energies is equal to the superconducting phase of the single S reservoir.

5.3.2 Spectral current conservation at an interface

The continuity equation on the global Green function at an interface reads [22]

$$\sigma_l \left(\check{G}_l \vec{\nabla} \check{G}_l \right) = \sigma_r \left(\check{G}_r \vec{\nabla} \check{G}_r \right) = \frac{g_{\mathrm{int}}}{2} \left[\check{G}_l, \check{G}_r \right], \tag{5.25}$$

where the subscripts l and r designate the left and right electrode respectively, and g_{int} is the conductance of the interface per unit area when both right and left electrodes are in the normal state: $g_{\mathrm{int}} = G_{\mathrm{int}}/\mathcal{A}$, with $\mathcal{A}$ the area of the interface. This continuity equation can be understood as the conservation equation of a "spectral" current $\sigma \check{G} \vec{\nabla} \check{G}$. It translates into continuity equations for the advanced and retarded Green functions (diagonal terms of Eq. (5.25)), and provides the expression for the current through an interface (off-diagonal term of Eq. (5.25)), as will be developed further on.

The continuity equation for the retarded Green function $\hat{R}$ in terms of the pairing angle θ and phase φ at the contact reads:

$$\sigma_{l,r} \left[e^{-i\varphi_{l,r}} \left(\frac{\partial \theta_{l,r}}{\partial x} - \frac{i}{2} \sin 2\theta_{l,r} \frac{\partial \varphi_{l,r}}{\partial x} \right) \right]_{x=0} = g_{\mathrm{int}} \left[\cos \theta_r \sin \theta_l e^{-i\varphi_l} - \cos \theta_l \sin \theta_r e^{-i\varphi_r} \right]_{x=0}. \tag{5.26}$$

In the case of a contact between a normal electrode N and a superconducting one S, if the phase φ_N in the normal metal is the same as the phase in the superconductor across the interface, the continuity equation for the pairing angle $\theta_N (x, E)$ becomes:

$$\sigma_N \left. \frac{\partial \theta_N}{\partial x} \right|_{x=0} = \sigma_S \left. \frac{\partial \theta_S}{\partial x} \right|_{x=0} = g_{\mathrm{int}} \sin \left(\theta_S (0, E) - \theta_N (0, E) \right). \tag{5.27}$$

This equation expresses the conservation of the spectral current $\sigma \frac{\partial \theta}{\partial x}$ at the interface position $x = 0$. The discontinuity in pairing angle is greatest when the angle gradient is strongest, and increases for increasing interface resistances. Equation (5.27) holds for a good contact, in

which case $\theta_S\left(0, E\right) = \theta_N\left(0, E\right)$, as well as for a tunnel junction.

5.4 Application to simple cases

5.4.1 NS bilayers

5.4.1.1 Critical temperature and interface resistance of an NS bilayer

In experiments where the strongest proximity effect is desired, one tries to make as good a contact as possible between the normal and superconducting electrodes. The value of the resistance of the interface, which is then usually much smaller than the overall resistance of the structure, is not directly measurable. It is however a crucial piece of information because in this strong proximity regime, the degree of induced pairing depends highly on the transparency of the interface. This information can be derived from the value of the critical temperature of an NS bilayer with the same interface. We compute in the following the dependence of the critical temperature on the interface resistance, in a similar fashion as done in ref. [14] : near T_C, the superconducting correlations are very small, $|\theta| \ll 1$, but the gap equation (5.12) has a solution for $\Delta \neq 0$. The critical temperature is obtained by simplifying both sides of Eq. (5.12) by Δ, and imposing $\theta \to 0$. We have used these results to determine the quality of an NS contact in the experiment presented in chapter 6.

Parabolic approximation

In bilayers of films thin enough, the derivatives $\frac{\partial^n \theta}{\partial x^n}$ of order higher than two can be neglected. We suppose that enough non-specular scattering occurs against the interfaces of the films for the electronic motion to be diffusive. Since $|\theta| \ll 1$, Eq. (5.14) can be linearized:

$$\frac{\hbar D}{2} \frac{\partial^2 \theta}{\partial x^2} + iE\theta + \Delta(x) = 0. \tag{5.28}$$

Here we have neglected spin-flip scattering. The pairing angle in the superconductor at the interface θ_S is then straightforwardly determined:

$$\theta_S = \frac{i\Delta}{E} \left[1 - \frac{\mathcal{N}_N}{\mathcal{N}_N + \mathcal{N}_S} \frac{1}{1 - iE/\tau} \right]. \tag{5.29}$$

The quantity $\mathcal{N}_X = \mathcal{A}d_X n_X$ is the number of states per unit energy around the Fermi energy in the layer X of thickness d_X. The coefficient $\tau^{-1} = 4\pi \frac{\mathcal{N}_N \mathcal{N}_S}{\mathcal{N}_N + \mathcal{N}_S} \frac{R_{int}}{R_K}$ is the product of the geometrical average of these integrated densities of states by the interface resistance in units of the quantum of resistance $R_K = \frac{h}{e^2} \simeq 25.8$ kΩ. Injecting the imaginary part of this pairing
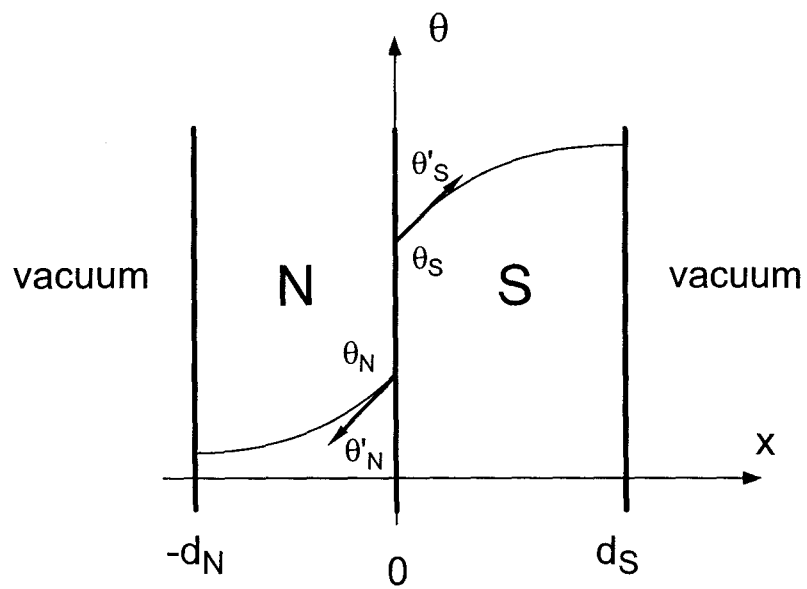
Fig. 5.8. Spatial variations of the pairing angle in a Normal/Superconducting bilayer.

angle into the gap equation Eq. (5.12) yields

$$\frac{1}{n_S V_{eff}} = \int_0^{\hbar\omega_D} \frac{dE}{E} \left[1 - \frac{\mathcal{N}_N}{\mathcal{N}_N + \mathcal{N}_S} \frac{1}{1 + E^2/\tau^2} \right] \tanh \frac{E}{2k_B T_C}. \tag{5.30}$$

The first term in the brackets leads to the integral appearing in the BCS gap equation, which determines the critical temperature T_{C_0} of the bulk superconductor:

$$\frac{1}{n_S V_{eff}} = \int_0^{\hbar\omega_D} \frac{dE}{E} \tanh \frac{E}{2k_B T_{C_0}} \simeq \ln \frac{1.13\hbar\omega_D}{k_B T_{C_0}}, \tag{5.31}$$

so that Eq. (5.30) can be rewritten as an integral equation for T_C :

$$\ln \frac{T_C}{T_{C_0}} = - \int_0^{\hbar\omega_D} \frac{dE}{E} \frac{\mathcal{N}_N}{\mathcal{N}_N + \mathcal{N}_S} \frac{1}{1 + E^2/\tau^2} \tanh \frac{E}{2k_B T_C}. \tag{5.32}$$

This result can be compared to the calculation of McMillan [13] who considered N and S layers separated by a tunnel barrier. In McMillan's approach, the possibility for an electron to tunnel into the other slab translates into an additional contribution to the energies $i\Gamma$ proportional to the rate at which the electron escapes from one slab to enter into the other:

$$\Gamma = \frac{\hbar}{\tau_X} \propto \frac{v_X}{d_X} \mathcal{T},$$

where $\mathcal{T}$ is the probability to cross the barrier and v_X is the Fermi velocity in slab X. If the Fermi velocities in the N and S metals are comparable, we find that Eq. (5.32) coincides numerically with McMillan's result for interface resistances such that $\left(R_{int}/\frac{\hbar}{2e^2} \right) > 1/ \left(100\mathcal{N} k_B T_C \right)$. However, in the case where the Fermi surface parameters of the N and S layers differ, McMillan's simplified approach is incorrect.

We have plotted in Fig. 5.9 the value of the ratio T_C/T_{C_0} computed with Eq. (5.32) for the case where $\mathcal{N}_N = \mathcal{N}_S$ (corresponding to similar S and N materials of identical thicknesses d), as a function of the parameter $k_B \Theta_D \mathcal{N} R_{int}/R_K = k_B \Theta_D d n \lambda_F^2 / (8\mathcal{T})$. The interface transmission $\mathcal{T}$ is related to the interface conductance through $G_{int} = 2\mathcal{T} N_{ch} G_K$, where $N_{ch} = \mathcal{A}/ (\lambda_F/2)^2$ is the number of effective channels in the barrier. In the particular case of our experiment on the proximity effect (see article reprinted in the next chapter), the critical temperature of an NS sandwich of 25 nm of Cu deposited over 20 nm of Al was inferior to 20 mK. This corresponds to a T_C/T_{C_0} ratio inferior to 0.02, yielding an interface transmission $\mathcal{T}$ greater than 0.01, or an interface conductance larger than 8 S for a surface of 100 nm×100 nm.

In the following, we present analytical solutions of Eq. (5.32) in limiting cases.
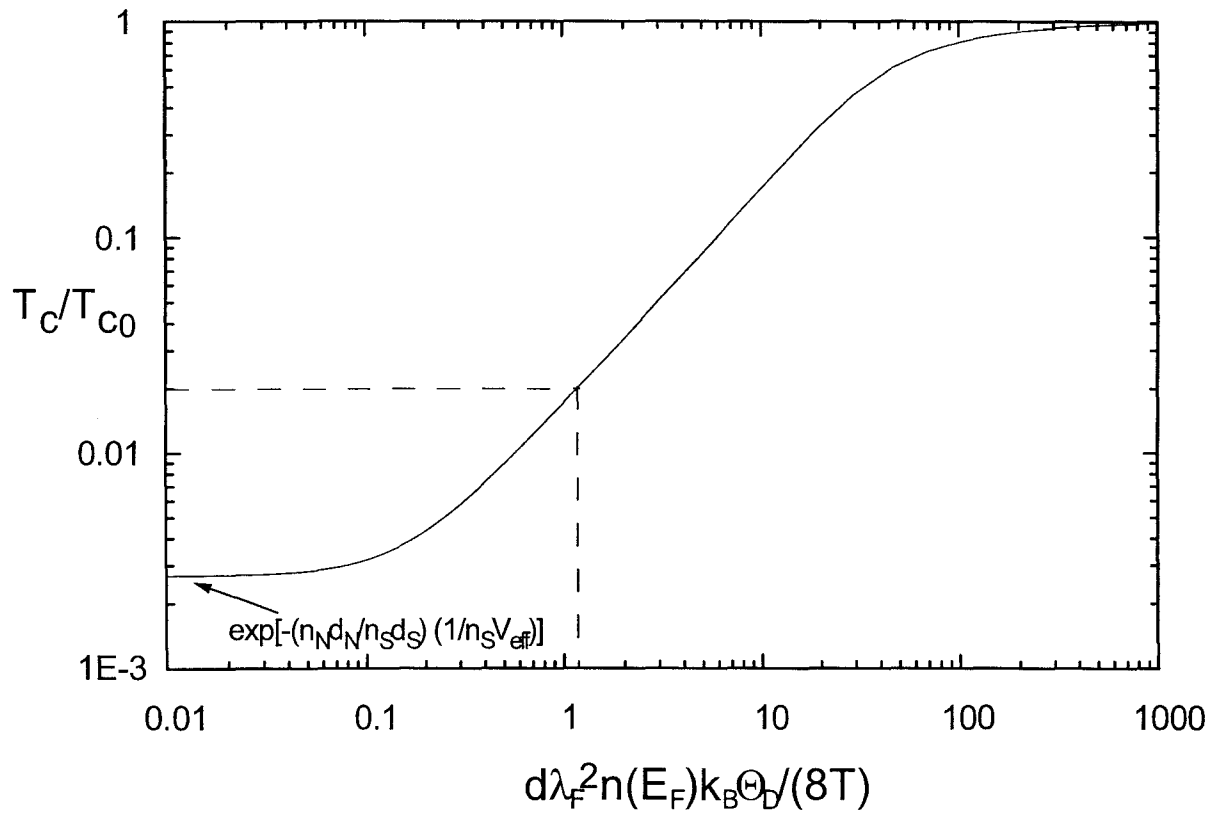
Fig. 5.9. Ratio of the critical temperature of an NS sandwich over the critical temperature of the bulk superconductor, plotted versus a function of the transmission T of the NS contact. We have used the Debye temperature of Al $\Theta_D = 394$ K.

Critical temperature of a NS bilayer with a transparent interface

For large values of τ, Eq. (5.30) can be approximated by

$$\frac{T_C}{T_{C_0}} = \left[\exp(-\frac{1}{n_S V_{eff}})\sqrt{1 + (\hbar\omega_D)^2/\tau^2}\right]^{\frac{\mathcal{N}_N}{\mathcal{N}_S}} \quad \text{if } \tau \gg k_B T_C , \qquad (5.33)$$

yielding for a perfect interface, i.e. for $\tau \sim \infty$

$$k_B T_C = 1.13 \hbar\omega_D \exp -\frac{1}{n_S V_{eff} \mathcal{N}_S/\left(\mathcal{N}_N + \mathcal{N}_S\right)},$$

as found by de Gennes [5]. In the limit of a perfect interface, the critical temperature of the bilayer is related in the usual way to the Debye frequency and the effective interaction, but this interaction is renormalized by a factor $\mathcal{N}_S/\mathcal{N}$. The main prediction is that the critical temperature is exponentially suppressed as the normal metal thickness increases.

Critical temperature of a NS bilayer with an opaque interface

In the case of high tunnel resistances, the critical temperature is given by

$$\frac{T_C}{T_{C_0}} = \left[\exp(-\frac{\pi}{8 G_K \mathcal{N}_S R_{\text{int}} k_B T_C})\right] \quad \text{if } \tau \ll k_B T_C, \qquad (5.34)$$

thus the critical temperature is in this case only weakly modified, by a factor which is independent of the normal metal layer.

5.4.1.2 Gap induced in the normal layer

Other features of NS bilayers can be calculated within the theory presented in the previous paragraphs. For instance, an energy gap is induced in the normal layer even though no interaction is assumed in the metal. Note the parameter $\Delta(x)$ in the Usadel equation is still zero, since $\Delta(x) \propto V_{\text{eff}} = 0$. This gap can be seen as arising from the fact that, since all states are delocalized over the N and the S layer, they all feel the pairing interaction. In the case of a perfectly transparent barrier $(\tau \to \infty)$ and if the linear approximation is still valid, $\theta_S = \theta_N$, the density of states in the normal metal at the interface has the the same gap $\Delta \mathcal{N}_S/(\mathcal{N}_S + \mathcal{N}_N)$ as the superconductor, and of smaller value further away from the interface. Belzig and Bruder[20] have calculated self-consistently the gap induced in a finite normal layer in perfect contact with a bulk superconductor. For thicknesses d_N greater than $\sqrt{\hbar D_N/\Delta}$, they find that the gap at the free surface of the normal layer roughly follows $\hbar D_N/d_N^2$. Such energy gaps in normal layers have been measured through the differential

conductance of SININ sandwiches [29] . These induced gaps are characteristic of *finite sized* systems, in which no normal reservoirs are present, in contrast with the system considered in the next paragraph.

5.4.2   Semi-infinite normal wire connected to a superconducting one

We now discuss the simple one-dimensional case of two semi-infinite normal and super-conducting wires in contact at $x = 0$, through an interface of conductance G_{int}. We will concentrate on the proximity effect in the normal wire, and hereafter assume that the superconducting pair potential Δ is constant in the superconductor. This approximation is justified by the self-consistent resolution of the Usadel equation in both N and S, performed by Belzig and Bruder [20] , which shows that the BCS gap is recovered in the superconductor at distances of the order of $\sqrt{\hbar D_S/\Delta}$, even in the case of a perfect contact.

5.4.2.1   Universal regime: pairing angle in the normal metal, at large distance

In a normal wire much longer than the spin-flip scattering length, beyond a certain position the pairing angle is zero at all energies. The integrated Usadel equation in the absence of phase gradients reduces to

$$\frac{\hbar D}{4}\left(\frac{\partial \theta}{\partial x}\right)^2 + 2\sin^2\frac{\theta}{2}\left[iE - \frac{\hbar}{\tau_{sf}}\cos^2\frac{\theta}{2}\right] = 0. \tag{5.35}$$

We present the solutions [21] of this equation in different situations, starting with the non realistic case of no spin-flip scattering, which nevertheless pictures the spatial variations of pair correlations.

Universal solution in the case of no spin-flip scattering

If spin-scattering is neglected Eq. (5.35) yields

$$\theta(x, E) = 4 \arg \tan\left[\tan\frac{\theta_0(E)}{4}\exp\left((i-1)\sqrt{\frac{x}{L_E}}\right)\right] \tag{5.36}$$

where $L_E = \sqrt{\hbar D/E}$. In general, the value θ_0 of the normal pairing angle at the NS interface depends on the energy and on the value of the pairing angle on the superconducting side through Eq. (5.27). Let us consider here a perfect interface and make the hypothesis that the pairing angle at the interface is given by the BCS value (5.6). For energies E small compared to Δ, we can neglect the energy dependence of the pairing angle and take $\theta_0(E) = \pi/2$. The
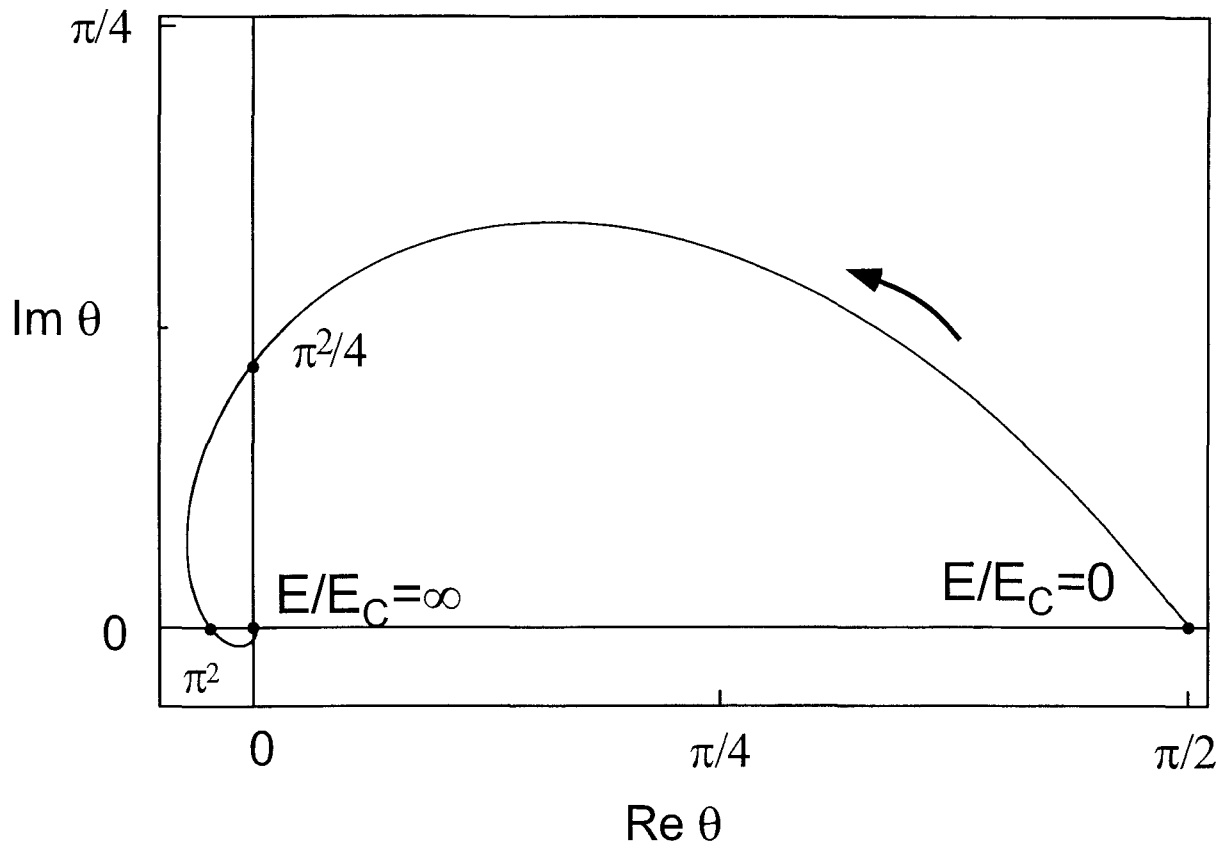
Fig. 5.10. Energy dependence of the pairing angle θ_N in a semi-infinite normal wire in perfect contact with a superconducting wire in the universal regime, i.e. at energies small enough that the angle is a function of E/E_C only, in the complex plane.

pairing angle in the normal wire then takes a simple universal form which is a function of the energy divided by the Thouless energy $E_C = \hbar D/x^2$:

$$\theta\,(x,E) = 4\arg\tan\left[\left(\sqrt{2}-1\right)\exp\left((i-1)\sqrt{\frac{E}{E_C}}\right)\right].\qquad(5.37)$$

We have plotted in Fig. 5.10 the energy dependence of this angle as the reduced energy E/E_C increases from 0 to infinity. These snail-shaped variations can be compared to the BCS variations shown in Fig. 5.6. As in the BCS case, the real part of the normal angle is $\pi/2$ at zero energy. But whereas the real part of the BCS angle keeps this value for energies inferior to the gap energy, and then takes the value zero for energies above the gap, the real part of the universal normal angle departs from $\pi/2$ and decreases in an oscillatory manner, i.e. with changes in sign, toward the value zero. The imaginary part of the angle does not go to infinity as in the BCS case at the gap energy, but is inferior to $\pi/4$ and also oscillates
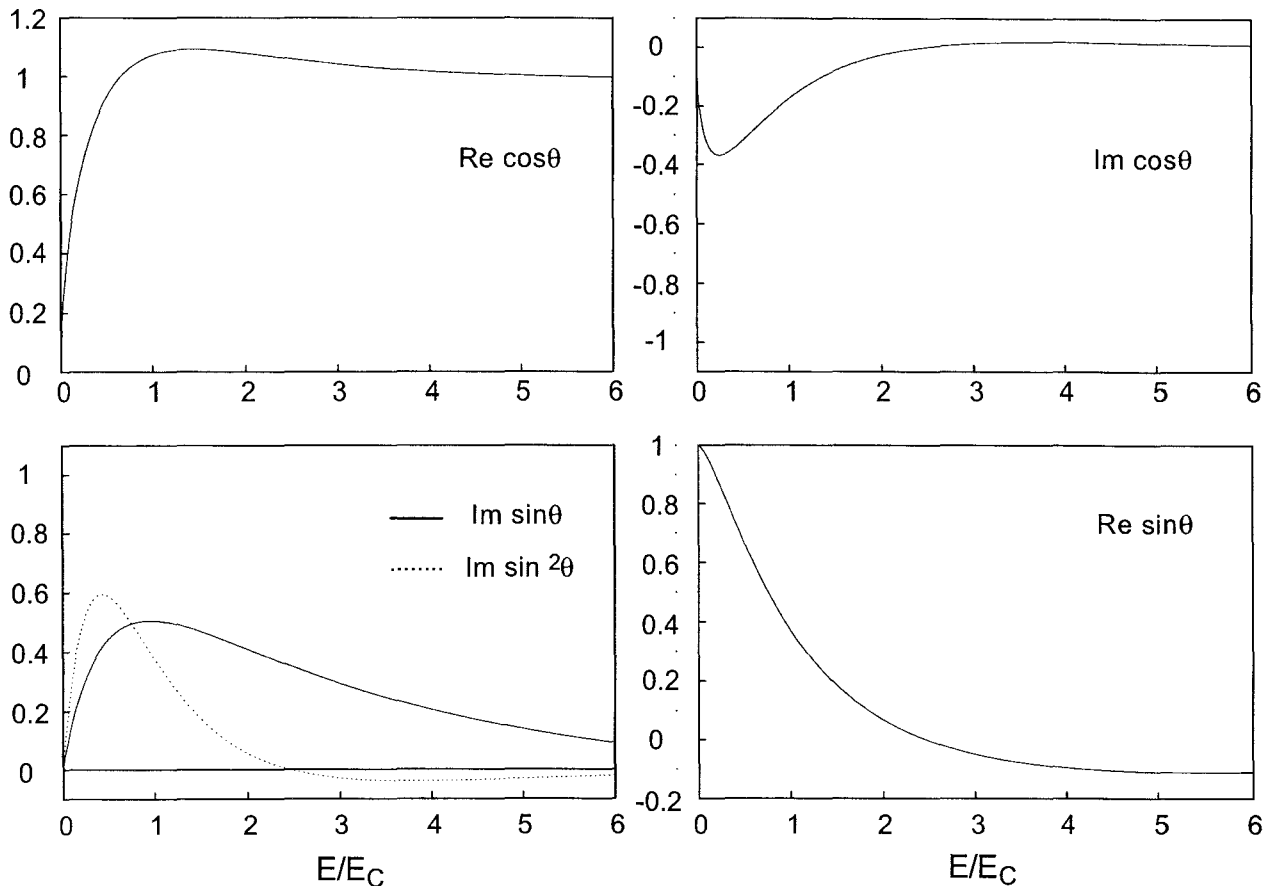
Fig. 5.11. Left column: Real part of the cosine, imaginary part of the sine, and imaginary part of the square of the sine of the pairing angle in the normal metal in the universal regime. These quantities are proportional to the single particle density of states, the pair amplitude and the pair density in the normal metal, respectively. Right column: Imaginary part of the cosine and real part of the sine of the universal pairing angle.

down to zero. This universal pairing angle corresponds to a universal density of states curve plotted in the upper left panel of Fig. 5.11. The curve shows no states at zero energy, but no finite energy gap. The density of states is maximal near the energy E_C, and returns to the normal metal value for energies of the order of five E_C, corresponding to distances from the interface $x \approx 5L_E = 5\sqrt{\hbar D/E}$. The pair amplitude $\mathrm{Im}\sin\theta$ and the pair density $\mathrm{Im}\sin^2\theta$ are plotted underneath. The pair amplitude also has a maximum value 0.5 at $E = E_C$ and slowly decreases to zero at higher energies. The pair density $\mathrm{Im}\sin^2\theta$ is more sharply peaked around $E_C/2$, rapidly decays to zero and for energies above $2E_C$ oscillates around the value zero, interestingly taking negative values at higher energies, which implies that some energies give a small paramagnetic contribution to the supercurrent in a normal metal loop in proximity to

a superconductor.

A striking feature of this universal regime is that the superconducting gap does not come into play. This stems from the fact that we have considered energies much smaller than the gap energy, which is equivalent to stating that we have described the proximity effect at distances larger than $L_\Delta = \sqrt{\hbar D/\Delta}$ from the interface. A second feature is that at zero energy, the pairing angle in the normal wire is equal to $\pi/2$ at every finite coordinate, indicating that correlations at zero energy penetrate infinitely far. This is an artefact of our neglecting inelastic scattering, as we now show.

Linearized equation with spin-flip scattering

An analytical solution of Eq. (5.35) including the spin-flip scattering is available only in the limit of small pairing angle, where Eq. (5.35) can be linearized, yielding

$$\frac{\hbar D}{2} \left(\frac{\partial \theta}{\partial x}\right)^2 + \theta^2 \left[iE - \frac{\hbar}{\tau_{sf}}\right] = 0 \text{ for } \theta \ll 1. \tag{5.38}$$

The pairing angle is then given by

$$\theta(x, E) = \theta_{NS} \exp\left[(i-1)\sqrt{\frac{E + i\frac{\hbar}{\tau_{sf}}}{E_C}}\right] \tag{5.39}$$

where θ_{NS} is the value of the angle on the normal side of the interface. This expression is no longer a universal function of E/E_C. At zero temperature, one can deduce from (5.39) the value of the Ginzburg-Landau parameter given in Eq. (5.11). We find

$$|\Psi|^2 \propto \frac{1}{x^2} \left(2\sqrt{2}\frac{x}{L_{sf}} + 1\right) \exp\left(-2\sqrt{2}\frac{x}{L_{sf}}\right) \text{ at } T = 0, \tag{5.40}$$

where $L_{sf} = \sqrt{D\tau_{sf}}$. This formula only applies when it gives a result much smaller than one, i.e. if $x > L_{sf}$. From $x = L_{sf}$ to $x = 3.5 \, L_{sf}$, $|\Psi|^2$ falls by three orders of magnitude, and its spatial variations can be well approximated by $|\Psi|^2 \propto 5.1 \, \exp(-3.37 \, x/L_{sf})$. This exponential decay is similar to the Ginzburg-Landau result, if L_T is replaced by $0.3L_{sf}$ [19].

From equation (5.39) we also deduce the dependence on distance of the density of states at zero energy:

$$n(0)/n_0 \simeq 1 - \frac{\pi^2}{8} \exp\left(-2\sqrt{2}\frac{x}{L_{sf}}\right). \tag{5.41}$$

Both these results show that the normal character of the metal is recovered at distances of a few L_{sf}.

5.4.2.2   General solution

We now solve the non linearized Usadel equation, still considering a constant pair potential in the superconductor.

Pairing angles at the NS boundary

By combining the integrated Usadel (5.18) in N and S, in which the proximity angle is supposed to recover its normal (respectively superconducting) value at x→ ∞ (respectively -∞), with the continuity Eq. (5.27), we get:

$$
\begin{cases}
-i\varepsilon(1 + \cos\theta_S - \cos\theta_N) + \sin\theta_S + \frac{1}{2\tau^*}\sin^2\theta_N - \sqrt{1 - \varepsilon^2} = 0 \\[2mm]
\sin(\theta_S - \theta_N) - 2L_t^*(1 - i)\sqrt{\varepsilon + \frac{i}{\tau^*}\cos^2\frac{\theta_N}{2}}\sin\frac{\theta_N}{2} = 0 \\[2mm]
L_t\frac{\partial\theta}{\partial x} - \sin(\theta_S - \theta_N) = 0.
\end{cases}
\qquad (5.42)
$$

where $\varepsilon = \frac{E}{\Delta}$, $\tau^* = \frac{\tau_{sf}}{\hbar/\Delta}$, $L_t = \frac{\sigma A}{G_{int}}$, and $L_t^* = \frac{L_t}{L\Delta}$. We have neglected the mismatch between the Fermi velocities in the normal and superconducting metal. Here θ_N, θ_S, $\frac{\partial\theta_N}{\partial x}$ and $\frac{\partial\theta_S}{\partial x}$ denote the values at the boundary. The solution of this set of equations is plotted in Fig 5.12. We have plotted in the complex plane the pairing angle on the normal side of the boundary and on the superconducting side, for energies varying between 0 and 2Δ, interface resistance parameters L_t^* ranging from 0 to 100, and taking a spin-flip parameter $\tau^* = 20$. The behavior of the imaginary and real part of the angle is an interpolation between the limiting cases of a perfectly transparent interface and that of an opaque one.

Perfect contact

In this case, $L_t^* = 0$, $\theta_S = \theta_N = \theta$ and $\frac{\partial\theta}{\partial x} = 0$. The pairing angle at the boundary is then given by

$$
\sin\theta = \tau^*\left[-1 + \sqrt{1 + \frac{1}{\tau^*}\left(\sqrt{1 - \varepsilon^2} + i\varepsilon\right)}\right]
\qquad (5.43)
$$

If spin-flip scattering is neglected ($\tau^* = \infty$), $\sin\theta = \sqrt{1 - \varepsilon^2} + i\varepsilon$ and the pairing angle at energy Δ is $\theta = i\ln\left(1 + \sqrt{5}\right)$.

Opaque barrier

In this case, the interface parameter L_t^* is large: $L_t^* \gg 1$. One can consequently develop the superconducting angle around its BCS value, and assume a small proximity-induced pairing
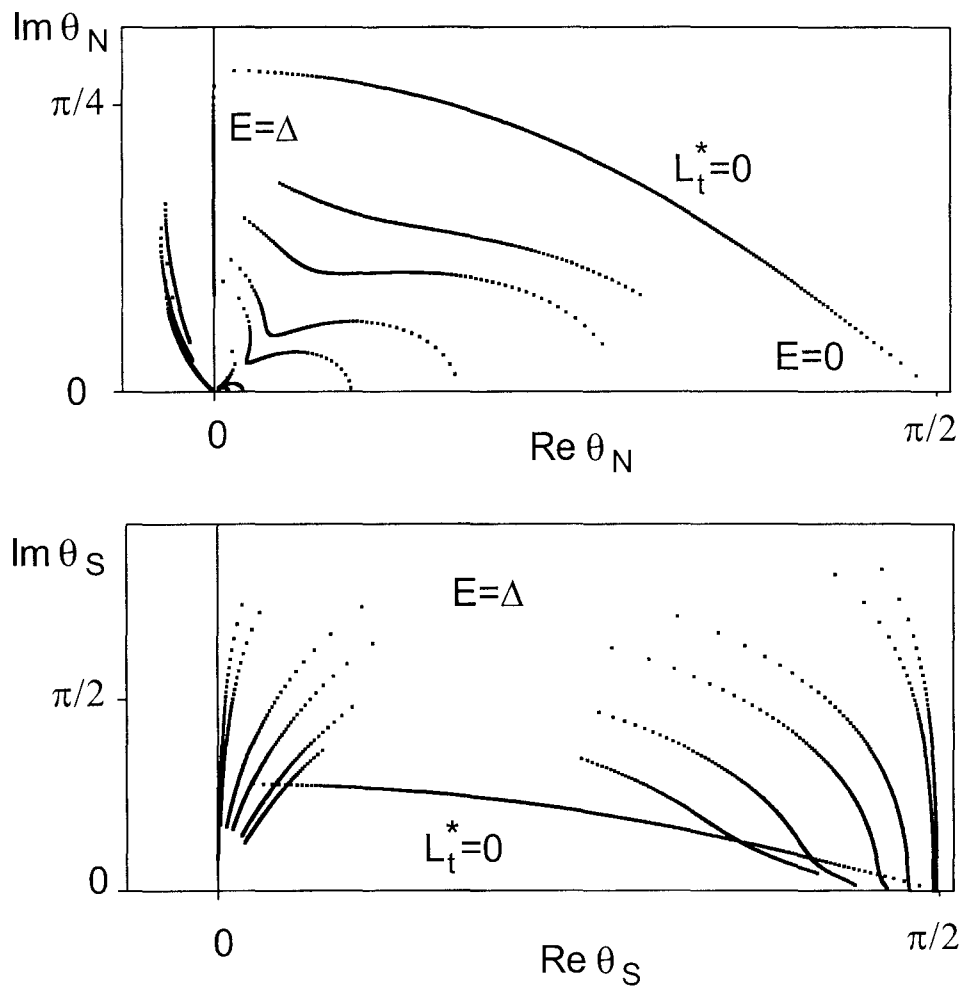
Fig. 5.12. Energy dependence of the pairing angle on the normal (top panel) and superconducting (bottom panel) side of an NS interface, for energies E varying from 0 to 2Δ. The energy separation between two adjacent points is 0.02Δ. Each curve corresponds to a given value of the interface resistance. The curves were computed for a reduced interface resistance L_t^* of 0, 1, 2, 10, 50, and 100.

angle in the normal metal. At zero energy the expression for the normal pairing angle at the boundary is then

$$\theta_N \left(\varepsilon = 0 \right) = \frac{\sqrt{\tau^*}}{\sqrt{2} L_t^*} = \frac{R \left(L_{\mathrm{sf}} \right) G_T}{\sqrt{2}}, \tag{5.44}$$

and the pairing angle on the superconducting side of the boundary is

$$\theta_S \left(\varepsilon = 0 \right) = \frac{\pi}{2} - \frac{1}{\sqrt{2} L_t} = \frac{\pi}{2} - \frac{R \left(L_\Delta \right) G_T}{\sqrt{2}}, \tag{5.45a}$$

where we note $R\left(L\right)$ the resistance of a length L of normal wire. From these two expressions one deduces that the superconductor is indeed weakly modified if $R\left(L_\Delta\right) G_T \ll 1$, whereas the condition for the weak proximity effect in the normal metal is $R\left(L_{\mathrm{sf}}\right) G_T \ll 1$.

Therefore the density of states at zero energy on the normal side of an opaque boundary is slightly depleted by $1 - \mathrm{Re}\cos\theta_N \left(\varepsilon = 0 \right) = \left[R\left(L_{\mathrm{sf}}\right) G_T \right]^2 / 4$.

Spatial variations of the pairing angle along the wire

Once the pairing angle at the NS boundary is determined, the differential equation Eq. (5.35) is numerically integrated to yield the spatial dependence of the pairing angle at every energy. To picture the spatial dependence of the proximity effect, we have plotted in Fig. 5.13 the density of states computed at different positions along an NS structure made of a semi-infinite normal wire in perfect contact with a semi-infinite superconducting wire, neglecting spin-flip scattering and assuming a constant pair potential Δ in the superconductor. The progressive filling of the states below the gap energy and the change in curvature of the spectrum as the interface is passed are typical. In the next chapter, we will compare quantitatively the densities of states computed with the theory presented above and the densities of states measured in different positions of a normal wire in contact with a superconducting one.
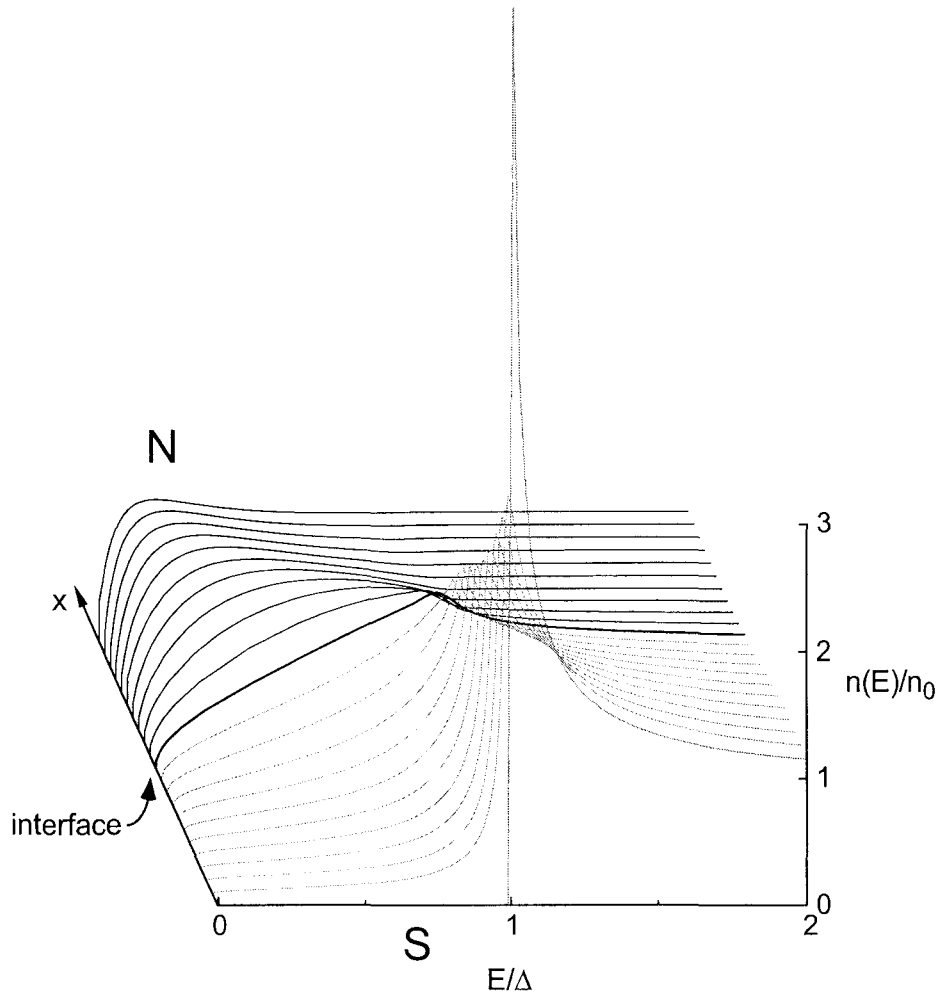
Fig. 5.13. Calculated density of states for positive energies up to 2 Δ along a semi-infinite one-dimensional NS system with no spin-flip scattering. The various curves correspond to positions separated by 0.2 L_Δ. The black and grey curves are the densities of states in the normal and superconducting wires respectively. The thick curve is the density of states at the interface. The BCS density of states is also plotted for reference.

5.5   A variational principle for the Usadel equations

We mentioned that the Usadel equations for $\hat{R}$ and $\hat{A}$ appear as the static equilibrium condition of the total forces acting on the representative point of the Green function. We will see that these forces derive from a potential which is extremal at equilibrium. Although this approach is mathematically equivalent to solving the differential Usadel equations, it provides a convenient mechanical analogy: at zero energy, the pairing and depairing forces acting on a representative point of the NS system are analogous to springs pulling towards the equator or the north pole of the unit sphere. This approach, inspired by the work of Nazarov [16] , can be extended to finite energy and finite magnetic field [17,18] . It is particularly well adapted to finite-sized systems between reservoirs which impose boundary conditions for the pairing angles.

5.5.1   The effective potential U

It is straightforward to check that the Usadel equations (5.14-5.15) are the equations for an extremum of a global dimensionless potential U with respect to θ and φ :

$$\begin{cases} \delta U|_\theta = 0 \\ \delta U|_\varphi = 0 \end{cases},$$

where $U = \int_{vol.} \mathcal{U} \, dv$ with the energy density functional $\mathcal{U}$ given by:

$$\mathcal{U} = n_0 \left[\frac{\hbar D}{4} \left(\frac{ds}{dx} \right)^2 - iE \cos\theta - \frac{\hbar}{\tau_{\rm sf}} \frac{\sin^2\theta}{2} + \Delta(x)\sin\theta \right]. \tag{5.46}$$

The gauge invariant metric, defined by:

$$ds^2 = d\theta^2 + (d\varphi - d\varphi_A)^2 \sin^2\theta \tag{5.47}$$

with $d\varphi_A = -\frac{2e}{\hbar} A_x \, dx$, is just a generalization of the metrics of the sphere. The integral is taken over the volume of the sample. The phase field $\varphi_A(x)$ results from the applied magnetic field but also from the field produced by supercurrents in the structure. In the following, we will assume that the superconducting currents are too small to significantly screen the applied magnetic field and that $\varphi_A(x)$ is an externally applied phase field in a given gauge. The first term $\frac{\hbar D}{4} \left(\frac{ds}{dx} \right)^2$ in $\mathcal{U}$ can be understood as an elastic energy term for the trajectory, while the other ones are potential energy terms. The set of Usadel equations at all energies can thus
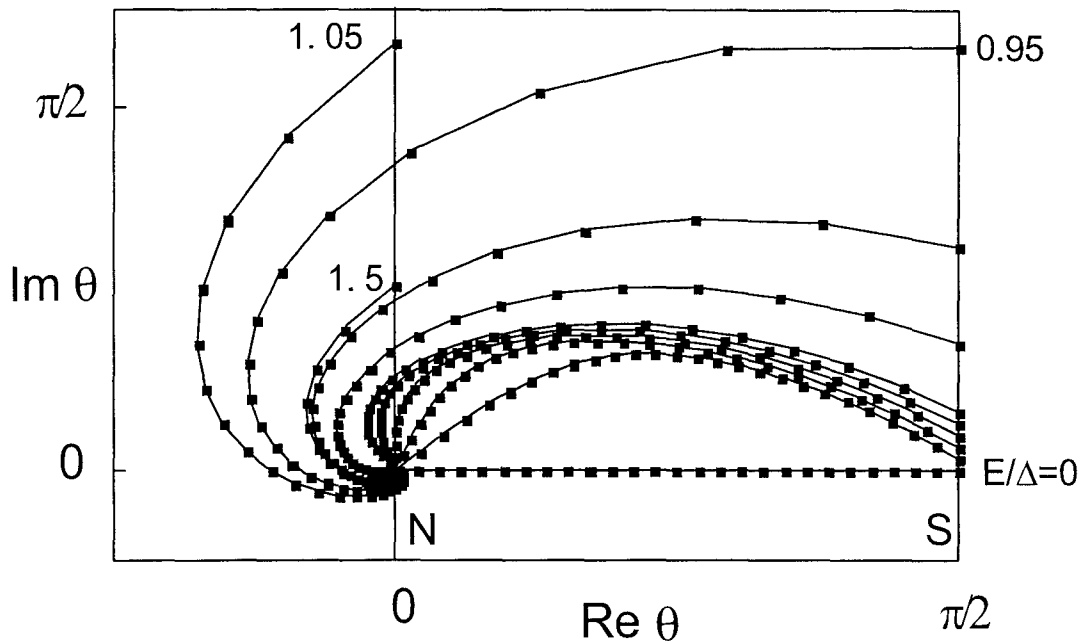
Fig. 5.14. Spatial dependence of the pairing angle along a normal wire of length $L = 5L_\Delta$ between a normal and a superconducting reservoir, at different energies $E/\Delta = 0, 0.05, 0.1, 0.15, 0.2, 0.25, 0.5, 0.75, 0.95, 1.05$, and 1.5. Successive points of a given curve correspond to positions along the wire $0.2\ L_\Delta$ apart.

be considered as a generalization of the Ginzburg-Landau equation for Ψ, and the density $\mathcal{U}$ then generalizes the Ginzburg-Landau energy functional.

5.5.2   Pairing angle in a normal wire of finite length between a superconducting and a normal reservoir

To illustrate the variational method, we have computed the variations of the pairing angle along a wire of length $L = 5L_\Delta$ connected to a superconducting reservoir at $x = 0$ and to a normal one at $x = L$, in the absence of spin-flip scattering. The procedure is a straightforward steepest-descent method, starting with the pairing angle at zero energy, *i.e.* the linear interpolation between the reservoir values 0 and $\pi/2$. The variations of the pairing angle are shown in Fig. 5.14, and differences with the infinite wire (compare for instance with the universal curve of Fig. 5.10) can be seen in the curves at low energy, less curled and closer to the real axis. At zero energy, the pairing angle anywhere in the wire is real and is the linear interpolation between the normal value $\theta = 0$ and the BCS value $\theta = \pi/2$. This fact, along with the boundary conditions at an interface, allowed Nazarov to construct an intuitive description of the proximity effect at zero energy, which will be presented next.

5.5.3   Wires and tunnel junctions as springs on the unit sphere

We will consider systems at zero energy, devoid of inelastic scattering, and containing normal and superconducting reservoirs. The restrictiveness of these requirements is counter-balanced by the complexity of the NS systems which can be modeled. Given these conditions, the contribution of each element (diffusive wire or tunnel junction) to the global potential U is a simple function of the position of its representative end points on the unit sphere. The problem is thus reduced to the determination of the positions on the unit sphere of the representative points of the nodes of the structure.

In the case of a N wire of length L and with representative end points P and Q, the minimal potential trajectory is the geodesic of the unit sphere with the metric (5.47). The trajectory thus follows the circular arc joining P to Q with the shortest possible length $\mathcal{L}$. Since the geodesic has the property that $\frac{ds}{dx}$ is constant along it and given by $\frac{ds}{dx} = \mathcal{L}/L$, one deduces the contribution u of a diffusive wire to the global potential:

$$u = \left(\frac{R_K}{4\pi R} \right) \frac{\mathcal{L}^2}{2} \tag{5.48}$$

where $R_K = h/e^2$ and R is the wire resistance. In the absence of a magnetic field, $\mathcal{L}$ is simply the length of the arc PQ. In this case one gets $ds = d\theta$ so that the pairing angle θ along a normal wire of length L stretched between a normal reservoir and a superconducting one varies linearly with position: $\theta(x) = \frac{\pi}{2} \frac{x}{L}$, as was mentioned in the previous section. A magnetic field acts as an extra rotation field which affects the length of a trajectory in the same way that winds modify the effective distances airplanes must travel around the earth. The length $\mathcal{L}$ is in this case the length of the arc PQ′ where Q′ is at the same latitude as Q but at a longitude increased by $(\varphi_A(Q) - \varphi_A(P))$. If instead of a wire we consider a tunnel junction of normal state tunnel resistance R_T, the contribution u' to the global potential takes the form:

$$u' = \left(\frac{R_K}{4\pi R_T} \right) \frac{\gamma^2}{2} \tag{5.49}$$

where $\gamma^2 = 2(1 - \cos \mathcal{L})$ is the square of the length of the cord stretched between the representative points of both sides of the junction.

The form of the potentials (5.48) and (5.49) suggests that diffusive wires and tunnel junctions can be considered as springs, given that:

i) A diffusive wire of resistance R is represented by a spring of stiffness R^{-1} which lies on

the surface of the unit sphere, stretched between its end points.

ii) A tunnel junction of normal state resistance R_T is represented by a spring of stiffness R_T^{-1} which is stretched along the cord joining its end points.

iii) The springs are connected in the same way as the elements they correspond to. The arcs of springs forming a loop are modified as explained above.

The global potential for the whole structure is then simply the sum of the contributions of the different elements. Finding the minimum of the global potential, and thus the pairing angle at all points of the circuit, is equivalent to finding the equilibrium positions of the set of springs corresponding to the structure.

These rules are equivalent to the conservation law of the spectral current at the nodes found by Nazarov [16] . The determination of the angles θ and φ at zero energy yields all equilibrium properties at zero energy. We will see in the next chapter that it suffices to determine the conductance of any part of a system at zero voltage and zero temperature.

5.5.4 Example: the NS-QUID

As an illustration of the aforementioned rules, we will compute the pairing angle at point A in the structure pictured in Fig. 5.15. This structure, called NS-QUID (Normal Superconducting Quantum Interference Device), is a fork-shaped superconductor connected through an insulating layer to a normal diffusive wire. The circuit corresponding to the structure is, if one neglects the small resistance of the normal branch of the loop, a diffusive resistor in series with two NS tunnel junctions in parallel, as sketched in the figure. In an external magnetic field perpendicular to the plane of the structure, the loop encloses a flux Φ. If one neglects the small dephasing induced in the normal metal, the flux dephases the two ends of the superconducting fork by a quantity $\Delta\varphi = \Phi/\Phi_0$, where $\Phi_0 = h/2e \simeq 2 \ 10^{-15}$ T.m^2 is the flux quantum.

The pairing angle in point A is straightforwardly obtained by minimizing the total potential:

$$u \propto r^{-1}\frac{\mathcal{L}_{NA}^2}{2} + \frac{G_T}{2}\left(2 - \cos\mathcal{L}_{AS_1} - \cos\mathcal{L}_{AS_2}\right) = r^{-1}\frac{\theta^2}{2} + G_T\left(1 - \sin\theta\cos\frac{\varphi}{2}\right). \qquad (5.50)$$

In the perturbative limit where the tunnel conductance G_T is much smaller than r^{-1}, the pairing angle induced in the normal metal θ is small and given by

$$\theta = rG_T\cos\frac{\varphi}{2} = rG_T\cos\frac{\Phi}{\Phi_0} \qquad\qquad \text{for } \theta \ll 1. \qquad (5.51)$$
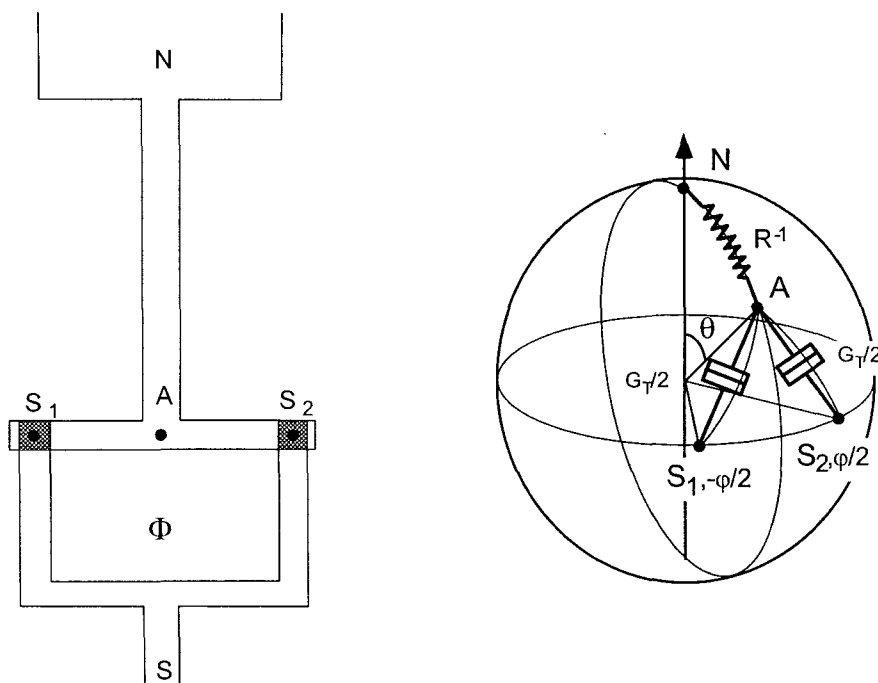
Fig. 5.15. Sketch of the NS-QUID and circuit representation on the unit sphere

Thus the point A oscillates between the latitude rG_T (weak proximity effect) when the flux in the NS loop is an integer multiple of the flux quantum, and the pole (no proximity effect) when the flux in the loop is a half integer multiple of Φ_0. We will see further on that the conductance of this whole structure is modulated in the same way by the magnetic field, thereby justifying the name NS-QUID.

5.6   Non-equilibrium proximity effect

In this section, we consider NS structures with normal reservoirs biased at voltages differing from the common potential of superconducting reservoirs. We suppose that the Usadel equations for $\hat{R}$ and $\hat{A}$ have been solved, *i.e.* $\theta\,(E, x)$ and $\varphi\,(E, x)$ are known. One then needs to determine the out of equilibrium Green function $\hat{K} = \hat{R}\hat{f} - \hat{f}\hat{A}$, which contains the filling of the quasiparticle states, in order to calculate the current through the structure.

5.6.1   Equation for the Keldysh Green function $\hat{K}$ and expression for the current

We restrict ourselves here also to one-dimensional systems. In particular, the expressions for the current apply to systems with a single superconductor. The Keldysh Green function $\hat{K}$, which describes the departure from the equilibrium situation, obeys the following equation derived from Eq. (5.5):

$$D\frac{\partial}{\partial x}\left(\hat{R}\frac{\partial}{\partial x}\hat{K} + \hat{K}\frac{\partial}{\partial x}\hat{A}\right) + i\left[\hat{H}_0, \hat{K}\right] - \frac{1}{\tau_{sf}}\left[\hat{\tau}_z\hat{K}\hat{\tau}_z, \hat{K}\right] = 0. \tag{5.52}$$

Once this equation is solved, the current at any place in the structure is derived from the first term in the sum [10] , leading to an expression for the current in a wire of cross section area S and conductance σ given by

$$I = -\frac{\sigma S}{8e}\int_{-\infty}^{+\infty} dE\,Tr\left\{\hat{\tau}_z\left(\hat{R}\frac{\partial\hat{K}}{\partial x} + \hat{K}\frac{\partial\hat{A}}{\partial x}\right)\right\}, \tag{5.53}$$

and for the current across a tunnel junction of normal state conductance G_T between left l and right r electrodes:

$$I_{lr} = \frac{G_T}{8e}\frac{1}{2}\int_{-\infty}^{+\infty} dE\,Tr\left\{\hat{\tau}_z(\hat{R}_r\hat{K}_l + \hat{K}_r\hat{A}_l - \hat{R}_l\hat{K}_r - \hat{K}_l\hat{A}_r\right\}. \tag{5.54}$$

5.6.2   Equation for the filling function f

The filling matrix $\hat{f}$, which relates $\hat{K}$ to $\hat{R}$ and $\hat{A}$, is usually decomposed into the sum of an odd function of energy f_0 and an even function of energy f_1 [8,9] :

$$\hat{f} = f_0\hat{1} + f_1\hat{\tau}_z \tag{5.55}$$
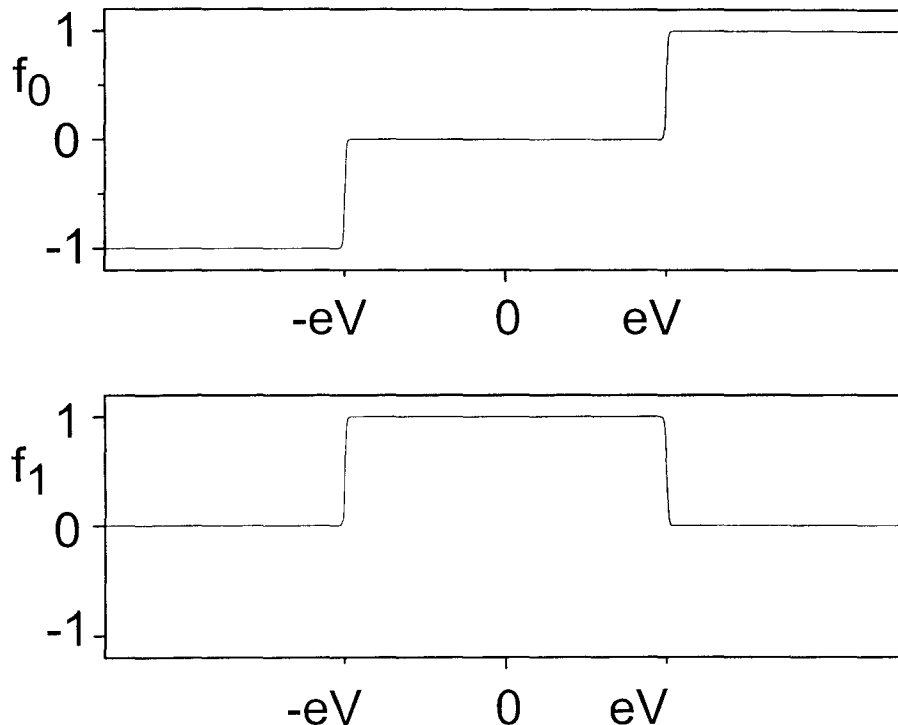
Fig. 5.16. Odd and even part of the energy distribution function used in the theory of non-equilibrium superconductivity, in the case where the system is a reservoir at a potential V.

In a reservoir at potential V these two functions are given by:

$$f_0 = \frac{1}{2} \left(\tanh \frac{(E + V)}{2k_B T} + \tanh \frac{(E - V)}{2k_B T} \right) \tag{5.56}$$

$$f_1 = \frac{1}{2} \left(\tanh \frac{(E + V)}{2k_B T} - \tanh \frac{(E - V)}{2k_B T} \right). \tag{5.57}$$

These two functions are plotted in Fig. 5.16.

Neglecting spin-flip scattering, Eq. (5.52) leads to equations combining the pairing angle θ and the filling functions f_0 and f_1:

$$\frac{\partial}{\partial x} \left(\cos^2 \theta_1 \frac{\partial f_0}{\partial x} - \text{Im} \left(\sin^2 \theta \right) f_1 \frac{\partial \varphi}{\partial x} \right) = 0 \tag{5.58}$$

$$\frac{\partial}{\partial x} \left(\cosh^2 \theta_2 \frac{\partial f_1}{\partial x} - \text{Im} \left(\sin^2 \theta \right) f_0 \frac{\partial \varphi}{\partial x} \right) = 0, \tag{5.59}$$

where θ_1 and θ_2 denote the real and imaginary parts of the pairing angle θ. In the derivation of Eq. (5.59), we have used the fact that the product Δf_1 is zero: f_1 is zero in superconductors in the regime where they don't sustain a voltage drop. In a normal wire between two normal

reservoirs, the pairing angle is zero, and Eq. (5.58) and Eq. (5.59) simply reduce to the diffusion equation for $\hat{f}$, implying that the distribution function varies linearly with position at every energy (see chapter 3). But these equations show that in the presence of proximity effect the distribution function is not just the linear interpolation between boundary conditions.

We now turn to the calculation of the current in an out-of-equilibrium situation.

5.6.3   Current expressed in terms of pairing angle and filling functions

Once both the pairing angle and distribution functions are determined, the current can be computed as a sum of three contributions, the quasi-particle current I_{qp}, the Andreev current I_A, and Josephson current I_J :

$$I_{rl} = I_{qp} + I_A + I_J. \tag{5.60}$$

Through a tunnel junction these three contributions are

$$I_{qp} \;=\; \frac{G_T}{2e} \int_{-\infty}^{+\infty} dE \, (f_{1l} - f_{1r}) \operatorname{Re} \cos \theta_r \operatorname{Re} \cos \theta_l \tag{5.61}$$

$$\;=\; \frac{G_T}{2en_0^2} \int_{-\infty}^{+\infty} dE \, (f_{1l} - f_{1r}) \, n_r n_l \tag{5.62}$$

$$I_A \;=\; \frac{G_T}{2e} \int_{-\infty}^{+\infty} dE \, (f_{1l} - f_{1r}) \cos(\varphi_l - \varphi_r) \operatorname{Re} \sin \theta_r \operatorname{Re} \sin \theta_l \tag{5.63}$$

$$\;=\; \frac{G_T}{2e} \int_{-\infty}^{+\infty} dE \, (f_{1l} - f_{1r}) \cos(\varphi_l - \varphi_r) \operatorname{Im} \sin \theta_r \operatorname{Im} \sin \theta_l, \tag{5.64}$$

the second equality being deduced from the Kramers-Krönig relation for $\sin \theta$.

$$I_J = \frac{G_T}{2e} \int_{-\infty}^{+\infty} dE \sin(\varphi_r - \varphi_l) \left[f_{0l} \operatorname{Re} \sin \theta_r \operatorname{Im} \sin \theta_l + f_{0r} \operatorname{Re} \sin \theta_l \operatorname{Im} \sin \theta_r \right]. \tag{5.65}$$

The current in a normal wire is

$$I = \frac{\sigma S}{2e} \int_{-\infty}^{+\infty} dE \left\{ - \cosh^2 \theta_2 \frac{\partial f_1}{\partial x} + \operatorname{Im} \left(\sin^2 \theta \right) f_0 \frac{\partial \varphi}{\partial x} \right\}. \tag{5.66}$$

In a normal wire with constant phase,

$$I = -\frac{\sigma S}{2e} \int_{-\infty}^{+\infty} dE \, \cosh^2 \theta_2 \, \frac{\partial f_1}{\partial x}. \tag{5.67}$$

This expression is similar to the result obtained in the absence of the proximity effect but with a renormalized diffusion constant $D \cosh^2 \theta_2$ which is energy dependent [21] . The current is obtained by integrating the contributions I_E from quasiparticles at different energies, $I_E = -\frac{\sigma S}{2e} \cosh^2 \theta_2 \frac{\partial f_1}{\partial x}$, conserved at each energy. The conservation of this partial current I_E is due to our neglecting all inelastic processes, which would mix correlations at different energies. The current I_E is not proportional to the gradient of the quasiparticle *density* at the energy considered, as one could expect for a dilute gas of diffusive quasiparticles, but to the gradient of the *filling* factor. The quasiparticles which represent excitations of the condensate cannot be considered as local objects and the current cannot therefore be identified to a quasiparticle flux.

A simple application of formula (5.67) is the case of a normal wire connected between a superconductor and a normal reservoir. At zero temperature, the pairing angle is real, so that the normal resistance of the wire is recovered. At finite temperature however Eq. (5.67) shows that the resistance is modified with respect to its normal value, as has been demonstrated experimentally by Charlat *et al.* (see chapter 9).

From these equations for the current we proceed to deduce the expression for the zero voltage, zero temperature conductance of diffusive wires and tunnel junctions, and of any circuit containing these elements.

5.6.4 Zero voltage conductance of NS structures at zero temperature

Nazarov has derived the relation between the conductance of a NS circuit at zero temperature and the angles θ and φ at zero energy along the various branches of the circuit [16] . His derivation is based on the low energy limit of the non-equilibrium Usadel equations given above. At zero temperature, and for small applied voltages, Eq. (5.59) is a simple diffusion equation with the normal state diffusion constant since $\theta_2 = 0$ at zero energy. Furthermore, the current (5.67) can be simply expressed as the gradient of a fictitious potential $\varsigma = \int_{-\infty}^{+\infty} dE \ f_1(E)$, through $I = -(\sigma S/2e) \nabla \varsigma$. This potential ς is just the electric potential eV at a reservoir biased at a voltage V, but is different from the electric potential $\phi = \int_{-\infty}^{+\infty} dE \ n(E) f_1(E)$ in structures in proximity with a superconductor. Nevertheless it is possible to use the usual rules of circuit theory with this fictitious potential replacing the

electric potential. The existence of this potential implies that the current in a wire AB with normal state conductance g is simply $I = g(\varsigma_A - \varsigma_B)$. On the other hand, the normal current through a tunnel junction with normal state conductance G_T, calculated using expression (5.54) or (5.60), is $I = G_T \cos \mathcal{L} \; (\varsigma_A - \varsigma_B)$ where $\mathcal{L}$ is the angle between representative points A and B of both sides of the junction on the unit sphere. The discontinuity of the representative point on crossing the tunnel barrier results in the reduction of the conductance by a geometrical factor determined by the equilibrium positions of the representative points at zero energy. The renormalized tunnel conductance is given by

$$\tilde{G}_T = G_T \cos \mathcal{L}. \tag{5.68}$$

In particular, the effective tunnel conductance of a tunnel junction between perfect N and S reservoirs is zero.

In conclusion, to determine the zero voltage conductance of any circuit between N and S reservoirs, one must:

  i) first find the equilibrium pairing angles, *i.e.* those which minimize the total circuit energy

  ii) once the pairing angles are determined, the zero voltage, zero temperature conductance is given by the usual parallel and series rules of circuit theory, with shunts installed between all the superconducting electrodes, renormalized tunnel conductances, and non-renormalized wire conductances.

5.6.5   Examples

5.6.5.1   Conductance of an NS junction in series with a diffusive resistor

Consider the circuit pictured in Fig. 5.17, and its equivalent circuit, a resistance connected to a normal reservoir at one end, in series with a tunnel junction which is itself connected to a superconducting reservoir. The value of the resistance is the resistance of the normal wire, whereas the conductance of the tunnel junction at zero energy is renormalized by $\cos \mathcal{L}_{AS}$, where the angle $\mathcal{L}_{AS}$ is obtained by minimizing the total energy

$$u \propto R^{-1} \frac{\mathcal{L}_{NA}^2}{2} + G_T \left(1 - \cos \mathcal{L}_{AS}\right) = G \frac{\theta^2}{2} + G_T \left(1 - \sin \theta\right).$$

We consider here the case where the tunnel conductance is much smaller than the wire
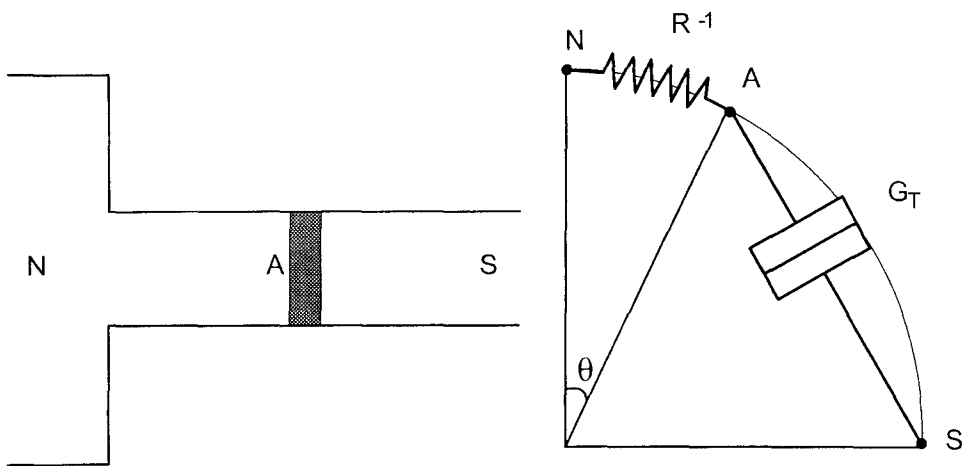
Fig. 5.17. Normal diffusive conductor in series with an NS tunnel junction, between a normal reservoir N and a superconducting reservoir S.

conductance $G = R^{-1}$. In this case, the proximity effect is just a weak perturbation: the spring pulling A to the normal reservoir is much stiffer (G) than the one pulling them to the superconducting reservoir (of stiffness G_T), so that the pairing angle θ of point A is small. Minimizing u with respect to θ then yields the value of the pairing angle $\theta \approx RG_T$. Finally, the total conductance of the NS system is

$$\tilde{G}_{NS} = G_T \cos \mathcal{L}_{AS} = G_T \sin \theta \approx RG_T^2.$$

In the paragraph on the perturbative proximity effect, we will return to this result, which states that the more resistive the diffusive wire, the greatest the NS conductance, or in other words that more resistance in series implies more conductance.

5.6.5.2   Conductance of an NS-QUID

In the NS-QUID described in the previous paragraph, we computed the pairing angle in the normal metal, and showed that it oscillates periodically with the magnetic flux enclosed in the loop of the structure. We can now calculate the conductance. Referring to Fig. 5.15, the total conductance of the NS circuit is that of the diffusive wire in series with two tunnel junctions in parallel, whose conductance must be renormalized:

$$R_{NS} = r + \frac{1}{2\tilde{G}_T/2} = r + \frac{1}{G_T \cos \mathcal{L}_{AS_1}} = r + \frac{1}{G_T \sin \theta \cos \frac{\varphi}{2}}.$$

We have seen that in the case of opaque tunnel junctions $\theta = rG_T \cos \frac{\varphi}{2}$, so that

$$R_{NS} = r + \frac{1}{rG_T^2 \cos^2 \frac{\varphi}{2}}$$

and thus, since $rG_T \ll 1$,

$$G_{NS} = \frac{1}{2} rG_T^2 (1 + \cos \varphi) \tag{5.69}$$

Therefore the conductance of the entire NS structure is also modulated periodically.

5.7 Tables of expressions contained in this chapter

Green functions and the formal equations they obey	
correlation matrices	$\hat{M}(r,t,t') = \begin{pmatrix} \left\langle \left\{ \Psi_\uparrow(r,t), \Psi_\uparrow^\dagger(r,t') \right\} \right\rangle & \left\langle \left\{ \Psi_\uparrow(r,t), \Psi_\downarrow(r,t') \right\} \right\rangle \\ -\left\langle \left\{ \Psi_\downarrow^\dagger(r,t), \Psi_\uparrow^\dagger(r,t') \right\} \right\rangle & -\left\langle \left\{ \Psi_\downarrow^\dagger(r,t), \Psi_\downarrow(r,t') \right\} \right\rangle \end{pmatrix}$ $\hat{M}'(r,t,t') = \begin{pmatrix} \left\langle \left[\Psi_\uparrow(r,t), \Psi_\uparrow^\dagger(r,t') \right] \right\rangle & \left\langle \left[\Psi_\uparrow(r,t), \Psi_\downarrow(r,t') \right] \right\rangle \\ -\left\langle \left[\Psi_\downarrow^\dagger(r,t), \Psi_\uparrow^\dagger(r,t') \right] \right\rangle & -\left\langle \left[\Psi_\downarrow^\dagger(r,t), \Psi_\downarrow(r,t') \right] \right\rangle \end{pmatrix}$
retarded GF	$\hat{R}(r,\varepsilon) = \frac{1}{n_0}\mathcal{F}\left[-i\theta(t-t')\hat{M}(r,t,t') \right]$
advanced GF	$\hat{A}(r,\varepsilon) = \frac{1}{n_0}\mathcal{F}\left[i\theta(t'-t)\hat{M}(r,t,t') \right]$
Keldysh GF	$\hat{K}(r,\varepsilon) = \frac{1}{n_0}\mathcal{F}\left[-i\hat{M}'(r,t,t') \right]$
global matrix $\check{G}$	$\check{G}(r,\varepsilon) = \begin{pmatrix} \hat{R} & \hat{K} \\ 0 & \hat{A} \end{pmatrix}$
equation for $\check{G}$	$\hbar D \vec{\nabla}.\left(\check{G}\vec{\nabla}\,\check{G} \right) + i\left[\check{H}_0, \check{G} \right] - \frac{\hbar}{\tau_{sf}}\left[\check{\tau}_z \check{G} \check{\tau}_z, \check{G} \right] = 0,$ with $\check{H}_0 = \begin{pmatrix} \hat{H}_0 & 0 \\ 0 & \hat{H}_0 \end{pmatrix}$ and $\hat{H}_0 = \begin{pmatrix} E & i\Delta^* \\ i\Delta & -E \end{pmatrix}$
pair potential	$\Delta = n_0 V_{eff}\int_0^{\hbar\omega_D} \frac{1}{4i}\,\mathrm{Tr}\left[(\hat{\tau}_x - i\hat{\tau}_y)\,\hat{K} \right] dE$
spectral current conservation at the interface between l and r	$\sigma_l \left(\check{G}_l \vec{\nabla} \check{G}_l \right) = \sigma_r \left(\check{G}_r \vec{\nabla} \check{G}_r \right) = \frac{G_{\mathrm{int}}}{2\mathcal{A}}\left[\check{G}_l, \check{G}_r \right],$ with σ the conductivity, G_{int} the interface resistance, and $\mathcal{A}$ the junction area.

Green functions in terms of the pairing angle $\theta = \theta_1 + i\theta_2$ and superconducting phase φ	
parametrization of retarded GF	$\hat{R} = \begin{pmatrix} \cos\theta & e^{-i\varphi}\sin\theta \\ e^{i\varphi}\sin\theta & -\cos\theta \end{pmatrix}$
parametrization of advanced GF	$\hat{A} = \begin{pmatrix} -\cos\bar{\theta} & e^{-i\varphi}\sin\bar{\theta} \\ e^{i\varphi}\sin\bar{\theta} & -\cos\bar{\theta} \end{pmatrix}$
normal reservoir	$\theta_N = 0$
BCS superconductor	$\theta_{BCS}(E) = \arctan i\frac{\Delta}{E}$, i.e. $\begin{cases} \cos\theta_{BCS}(E) = \frac{|E|}{\sqrt{E^2 - \Delta^2}} \\ \sin\theta_{BCS}(E) = \frac{\Delta}{\sqrt{\Delta^2 - E^2}} \end{cases}$
density of states	$n(r, E) = n_0 \,\mathrm{Re}\left[\cos\theta(r, E)\right]$
equation for the pair potential	$\Delta(r) = n_0 V_{\mathrm{eff}} \int_0^{\hbar\omega_D} dE \tanh\left(\frac{E}{2k_B T}\right) \mathrm{Im}\left[\sin\theta(r, E)\right] \, e^{i\varphi(r,E)}$
Usadel equation	$\frac{\hbar D}{2}\frac{\partial^2\theta}{\partial x^2} + \left[iE - \left(\frac{\hbar}{\tau_{sf}} + \frac{\hbar}{\tau_H}\right)\cos\theta\right]\sin\theta + \Delta\cos\theta = 0$
spectral current conservation	$j_s = \sigma_r \frac{\partial\theta_r}{\partial x} = \sigma_l \frac{\partial\theta_l}{\partial x} = \frac{G_{\mathrm{int}}}{A}\sin(\theta_l - \theta_r)$
quasiparticle current at the interface between l and r	$I_{qp} = \frac{G_T}{2e}\int_{-\infty}^{+\infty} dE\,(f_{1l} - f_{1r})\,\mathrm{Re}\cos\theta_r\,\mathrm{Re}\cos\theta_l$
Andreev current at the interface between l and r	$I_A = \frac{G_T}{2e}\int_{-\infty}^{+\infty} dE\,(f_{1l} - f_{1r})\cos(\varphi_l - \varphi_r)\,\mathrm{Re}\sin\theta_r\,\mathrm{Re}\sin\theta_l$
Josephson current at the interface between l and r	$I_J = \frac{G_T}{2e}\int_{-\infty}^{+\infty} dE\,\sin(\Delta\varphi)\left[f_{0l}\,\mathrm{Re}\sin\theta_r\,\mathrm{Im}\sin\theta_l + f_{0r}\,\mathrm{Re}\sin\theta_l\,\mathrm{Im}\sin\theta_r\right]$
quasiparticle current in a wire	$I = -\frac{\sigma S}{2e}\int_{-\infty}^{+\infty} dE\,\cosh^2\theta_2\,\frac{\partial f_1}{\partial x}$
equations for f_0 and f_1	$\frac{\partial}{\partial x}\left(\cos^2\theta_1\frac{\partial f_0}{\partial x} - \mathrm{Im}(\sin^2\theta)f_1\frac{\partial\varphi}{\partial x}\right) = 0$ $\frac{\partial}{\partial x}\left(\cosh^2\theta_2\frac{\partial f_1}{\partial x} - \mathrm{Im}(\sin^2\theta)f_0\frac{\partial\varphi}{\partial x}\right) = 0$
thermal distributions f_{0T} and f_{1T}	$f_{0T} = \frac{1}{2}\left(\tanh\frac{(E+V)}{2k_B T} + \tanh\frac{(E-V)}{2k_B T}\right)$ $f_{1T} = \frac{1}{2}\left(\tanh\frac{(E+V)}{2k_B T} - \tanh\frac{(E-V)}{2k_B T}\right)$

REFERENCES

Note: This chapter is based on the articles by D. Esteve, H. Pothier, S. Guéron, N. O. Birge, and M. H. Devoret, in *Correlated fermions and transport in mesoscopic systems*, edited by T. Martin, G. Montambaux et J. Trân Thanh Vân (Editions Frontières, Paris, 1996), and D. Esteve, H. Pothier, S. Guéron, N. O. Birge, and M. H. Devoret, in *Introduction to mesoscopic electron transport*, edited by L. Sohn, G. Schön, and L. Kouwenhoven (Kluwer Academic, Amsterdam, 1997.

[1] H. Courtois, Ph. Gandit, and B. Pannetier, Phys. Rev. B **52**, 1162 (1995); Phys. Rev. Lett. **76**, 130 (1996).

[2] P. Charlat, H. Courtois, Ph. Gandit, D. Mailly, A. F. Volkov and B. Pannetier, Czech. J. Phys. **46**, Supplement S6, 3107 (1996).

[3] M. Tinkham, *Introduction to Superconductivity* (Mc Graw Hill, 1985), chapter 4.

[4] M. Tinkham, *Introduction to Superconductivity* (Mc Graw Hill, 1985).

[5] P. G. de Gennes, Rev.Mod. Phys **36**, 225 (1964).

[6] A. Barone and G. Paterno, *Physics and Applications of the Josephson Effect* (Wiley,1982).

[7] G. Deutscher and P. G. de Gennes, in *Superconductivity*, edited by R. D. Parks (Marcel Dekker, New York, 1969), p. 1005.

[8] A. I. Larkin and Yu. N. Ovchinnikov, in *Nonequilibrium Superconductivity*, edited by D. N. Langenberg and A. I. Larkin (North Holland, Amsterdam, 1986), p. 531; A. I. Larkin and Yu. N. Ovchinnikov, Sov. Phys.-JETP **41**, 960 (1975).

[9] A. Schmid, in *Nonequilibrium Superconductivity, Phonons, and Kapitza Boundaries*, edited by K. E. Gray (Plenum Press, New York, 1981), p. 423.

[10] J. Rammer and H. Smith, Rev. Mod. Phys. **58**, 323 (1986).

[11] K. D. Usadel, Phys. Rev. Lett. **25**, 507 (1970).

[12] A. F. Volkov, A. V. Zaitsev, and T. M. Klapwijk, Physica (Amsterdam) **210C**, 21 (1993); A. F. Volkov, Phys. Rev. Lett. **74**, 4730 (1995).

[13] W. L. McMillan, Phys. Rev. **175,** 537 (1968).

[14] These results can be found in A. A. Golubov, in *Superconducting Superlattices and Multilayers*, edited by I. Bozovic, SPIE proceedings Vol. 215 (SPIE, Bellingham, WA, 1994), p.353.

[15] G. Eilenberger, Z. Phys. **214**, 195 (1968).

[16] Yu. V. Nazarov, Phys. Rev. Lett. **73**, 1420 (1994).

[17] D. Esteve, H. Pothier, S. Guéron, N. O. Birge, and M. H. Devoret in *Correlated fermions and transport in mesoscopic systems*, edited by T. Martin, G. Montambaux et J. Trân Thanh Vân (Editions Frontières, Paris, 1996).

[18] T. H. Stoof and Yu. Nazarov Phys. Rev. B **54**, R772 (1996).

[19] P. G. de Gennes, *Superconductivity of Metals and Alloys* (W. A. Benjamin, New York, 1966), (7-64) p. 232.

[20] W. Belzig and C. Bruder, Phys. Rev. B **54**, 9443 (1996).

[21] F. Zhou, B. Spivak, and A. Zyuzin, Phys. Rev. B 52, 4467 (1995).

[22] S. Yip, Phys. Rev. B **52**, 15504 (1995).

[23] W. J. Hekking and Yu. V. Nazarov, Phys. Rev. Lett. **71**, 1625 (1993) and Phys. Rev. B **49** 6847 (1994).

[24] A. Kastalsky, A. W. Kleinsasser, L. H. Greene, R. Bhat, F. P. Milliken, and J. P. Harbison, Phys. Rev. Lett. **67**, 3026 (1991).

[25] A. F. Volkov, Physica B **203**, 267 (1994) and refs. therein to earlier work.

[26] C. W. J. Beenakker, Phys. Rev. B **46**, 12841 (1992) and in *Mesoscopic Quantum Physics*, edited by A. Akkermans et al., (Elsevier, Amsterdam, 1995), course 5.

[27] S. Guéron, H. Pothier, N. O. Birge, D. Esteve, and M. H. Devoret, Phys. Rev. Lett. **77**, 3025 (1996).

[28] H. Pothier, S. Guéron, D. Esteve, and M. H. Devoret, Phys. Rev. Lett. **73**, 2488 (1994) and Physica B **203**, 226 (1994).

[29] J. R. Toplicar and D. K. Finnemore, Phys. Rev. B **16**, 2072 (1977)

Chapter 6
Measurement of the density of states in the presence of proximity effect

6.1 Introduction

The experiments of the 1960s on the proximity effect mostly consisted in measuring the properties of unpatterned layers of thin films, such as the critical temperature and field of NS bilayers [1]. The density of states in a normal layer over a superconducting layer was also measured by Claeson *et al.* [2]. A few years ago, new experiments on intricate NS systems emerged thanks to the possibility of patterning complex structures with electron-beam lithography. Petrashov *et al.* measured a modulation stronger than expected of the resistance of a normal wire connected in two points to a superconductor, of which the superconducting phase difference could be controlled [4]. Courtois *et al.* measured the temperature dependence of the maximum supercurrent flowing in a long normal wire over which fine strips of superconductor were deposited [5]. Although these experiments are by now quantitatively explained by the theory of the proximity effect, they appeared at first as puzzling mesoscopic effects. This constituted the motivation to probe the nature of the order induced by a superconductor in normal metal wires such as the ones measured in those experiments. We report in this chapter an experiment which achieves energy and space resolved spectroscopy of the quasiparticle excitations in a metal subject to the proximity effect.

6.2   Measurement of the density of states in a normal wire in good contact with a superconductor (article)

We reproduce the article published in Phys. Rev. Lett. **77**, 3025 (1996).

Superconducting Proximity Effect Probed on a Mesoscopic Length Scale

S. Guéron, H. Pothier, Norman O. Birge,* D. Esteve, and M. H. Devoret

Service de Physique de l'Etat Condensé, Commissariat à l'Energie Atomique, Saclay, F-91191 Gif-sur-Yvette Cedex, France

We have measured by tunneling spectroscopy the electronic density of states in a nonsuperconducting wire in good contact with a superconductor, at distances of 200, 300, and 800 nm from the interface. Closest to the interface, the density of states near the Fermi energy is reduced to 55% of its normal value. At the farthest measurement point, this dip has nearly completely disappeared. We compare our data to predictions based on the Usadel equations. [S0031-9007(96)01337-3]

How does superconducting order propagate spatially? This question motivates the renewed interest in contacts between a nonsuperconducting metal and a superconductor (NS interface) [1]. In the 1960s, the propagation of superconductivity through an NS interface, a phenomenon called the proximity effect, was analyzed within the framework of the Ginzburg-Landau (GL) theory based on a superconducting order parameter $\Psi(x)$ which is a function of space only [2]. While the GL theory predicts well macroscopic equilibrium properties near the transition temperature, it makes no prediction at $T = 0$. Moreover, it does not address the energy dependence of pair correlations and therefore offers no understanding of transport properties. In the case of an NS interface with an applied voltage, such an understanding is provided by an extension of the BCS theory [3] but only in the special case of ballistic electrons. The recent observation of a large modulation in the conductance of a normal diffusive wire in contact with two superconductors with different phases appealed for a more thorough understanding [4]. It is now believed that all the experiments on NS structures can be understood from a unified point of view [5–7] based on the theory of "nonequilibrium superconductivity" [8]. In this general theory, correlations between electrons of opposite spin induced in the normal metal at equilibrium are described by a complex function of both space and energy $\theta(x, E)$. The nonequilibrium superconductivity theory establishes a bridge between the GL theory and the BCS theory. The function $\theta(x, E)$ contains the spatial and energy dependence of the density of states: $n(x, E) = N(0)\mathrm{Re}[\cos\theta(x, E)]$, where $N(0)$ is the density of states at the Fermi energy for the metal in the normal state. It also gives the GL order parameter via an integral over energy [9]. In this Letter, we report a basic test of the theory: We have measured the density of states $n(x, E)$ as a function of energy in a long normal wire in contact with a superconductor at one end, at different distances from the NS interface, and well below the transition temperature [10].

Tunneling has been used extensively to measure the density of states (DOS) [11]: At zero temperature, the differential conductance $dI/dV(V)$ of a tunnel junction

between a normal metal electrode and a metal with a DOS $n(E)$ is, disregarding single-electron charging effects [12], proportional to $n(eV)$. In particular, tunneling spectroscopy has already been applied to the proximity effect, but only in normal metal/superconductor bilayers [13]. In such a confined geometry, the spatial dependence of pair correlations can be neglected and the results were explained without the full arsenal of nonequilibrium superconductivity [14]. In our experiment, on the contrary, the lengths of superconductor and normal metal on either side of the interface are large enough that unperturbed superconducting and normal states are recovered far from the interface, thus forcing a gradient of pair correlations. Figure 1 shows a photograph of our sample, which consists of two similar circuits. On the bottom one, two copper
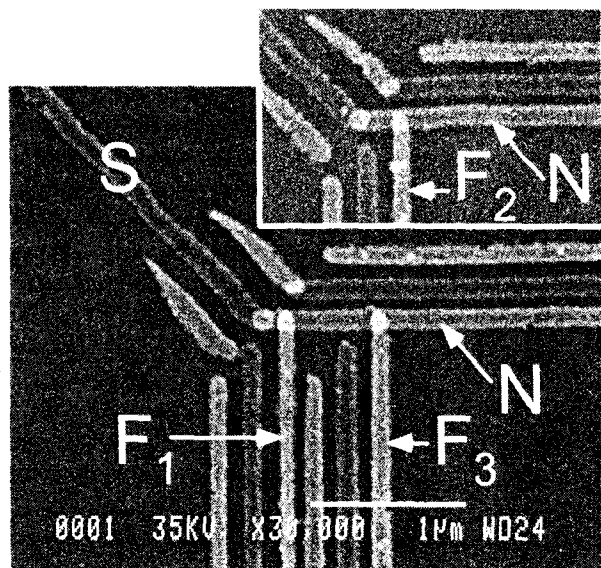

FIG. 1. SEM photograph of the sample: a normal (copper) wire N, horizontal, is in good contact with a superconducting (aluminum) wire S, diagonal on the left, at their overlap. Two normal (copper) fingers, vertical, labeled F_1 and F_3, are connected to the wire through very opaque tunnel barriers. The density of states in the normal wire is given by the differential conductance of the tunnel junction as a function of voltage. On a similar device, a third finger, labeled F_2, is placed at an intermediate distance.

electrodes (called "fingers" in the following, and labeled F_1 and F_3), are in contact through very opaque tunnel barriers (resistances in the $M\Omega$ range) with a normal wire N, whose left end makes an overlapping contact with a superconductor S. On the top circuit, a single finger, labeled F_2, is placed at an intermediate distance from the NS contact, between F_1 and F_3. The three fingers, positioned 200, 300, and 800 nm from the left end of the normal wire, constitute the tunneling spectroscopy probes. Since the quality of the NS contact is known to be a critical parameter in the proximity effect [2], all the layers were deposited through a suspended mask in a single vacuum process [15]. The mask, made of germanium, was fabricated by e-beam lithography with reactive ion etching. We first evaporated 20 nm of aluminum perpendicularly to the mask in order to obtain the S superconducting electrode. We then immediately evaporated 25 nm of copper at an angle to obtain the N normal wire. The angle was chosen so as to produce an overlap with the aluminum electrode on the left, presumably making a good contact. The insulating barrier was grown from two 1.4 nm thick layers of aluminum oxidized in a 80 mbar O_2 (10%) Ar (90%) mixture for 10 min. Lastly, we evaporated 30 nm of copper at an angle to produce the fingers $F_{1,2,3}$. In order to separate the three shadows of the mask, the MAA resist layer carrying the germanium mask was overetched. This was obtained with a low-dose preexposure of the sample around the normal wires and the fingers. The parasitic replicas on both sides of the superconducting electrode produced by the angle evaporations were lifted off in the nonoveretched regions. Two reference structures were simultaneously fabricated on the chip: a long narrow Cu/Al sandwich during the first two evaporation steps (i.e., without oxidation) and an NS tunnel junction formed by the first and third layers (with a thick oxide barrier). The critical temperature of the sandwich is directly related to the transparency of the NS contact [16]; the tunnel junction was used to measure the unperturbed DOS in the S film.

The sample was mounted in a copper box thermally anchored to the mixing chamber of a dilution refrigerator. Measurements were performed through properly filtered coaxial lines [17]. Using lock-in detection, we measured the differential conductance dI/dV of each of the three probe junctions as a function of the voltage V applied between the finger and the right end of the normal wire. The differential conductance displayed a V-shaped groove at low voltages, which became less pronounced at larger distances from the interface. This behavior is shown in Fig. 2, where we plot the $dI/dV(V)$ characteristic of the F_1, F_2, and F_3 junctions, taken at 20 mK. We have normalized each trace by the conductance $G_i = R_i^{-1} = dI/dV$ measured at $V = 0.3$ meV.

The differential conductance of the reference NS tunnel junction (inset of Fig. 2) is well fitted by a BCS density
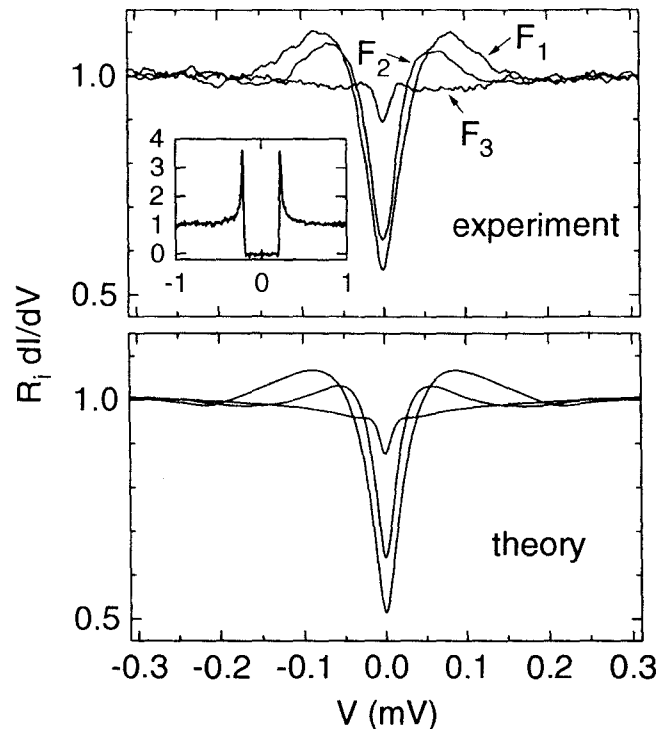

FIG. 2. Top panel: differential conductance of the tunnel junctions at F_1, F_2, and F_3 as a function of the applied voltage V, taken at 20 mK. The ac voltage modulation was kept below 2 μV. The data were normalized by the differential conductance of each junction at $V = 0.3$ mV : $G_1 = 0.19$ μS, $G_2 = 0.38$ μS, $G_3 = 0.27$ μS. Inset, differential conductance of the reference NS tunnel junction. Bottom panel: predicted differential conductance at the three distances to the NS contact obtained from the convolution of the density of states calculated from the Usadel equation [Eq. (1)] with the function $P(E)$ which describes the Coulomb blockade at the junctions. We used $\Delta = 0.212$ meV for the gap of aluminum, $D = 70 \times 10^{-4}$ m²/s for the diffusion constant of copper, and $\gamma_{sf} = 1.5 \times 10^{10}$ s⁻¹ for the spin-flip scattering rate.

of states for the superconducting electrode [18] and yields the energy gap $\Delta = 0.212$ meV.

We repeated the differential conductance measurement of the three fingers with an external magnetic field perpendicular to the chip. In Fig. 3 we present the F_1 data taken at $T = 30$ mK for $H = 0$, 0.06, and 0.1 T. As the field is increased, the groove structure progressively disappears, as shown in the inset of Fig. 3. Above 0.1 T, only a weak, broad-winged, field-independent structure remains (curve c). This structure, which extends to 3 mV, is the same for the three fingers. We attribute it, as explained below, to single-electron charging effects. When the temperature was increased (data not shown), the V-shaped low-voltage groove structure was progressively washed out, whereas the weak broad-winged structure was unaffected.

We now present the theoretical predictions tested by the experiment. In the theory of nonequilibrium superconductivity, the complex angle $\theta(x, E)$ describing pair
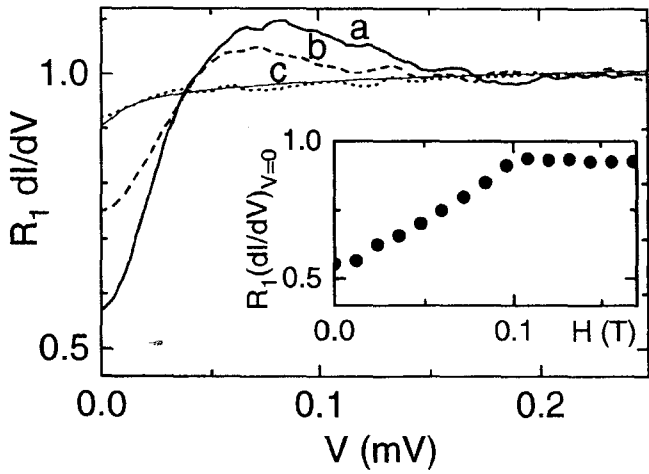
FIG. 3.   Differential conductance as a function of the voltage V measured at 30 mK and in a magnetic field $H = 0$ (curve a), 0.06 T (curve b), and 0.1 T (curve c). The thin solid line is a fit of curve c using Eq. (4), in which the DOS $n(x, E)$ was taken constant. It accounts for the influence of single-electron charging effects on the conductance of a tunnel junction between normal electrodes. Inset: zero-voltage conductance of F_1 as a function of the field.

correlations, supplemented with the superconducting phase φ, parametrizes the retarded 2×2 matrix Green function $G^R = (\tau_x \cos \varphi + \tau_y \sin \varphi) \sin \theta + \tau_z \cos \theta$, where $\tau_{x,y,z}$ are the Pauli matrices. At zero energy, θ is real and the superconducting order can be represented as a point on the unit sphere with polar coordinates θ and φ [6]. In this representation, the normal state is at the north pole ($\theta = 0$), and the BCS superconducting state is on the equator ($\theta = \pi/2$) at longitude φ. At finite energy, $\theta = 0$ in the normal state, whereas $\tan \theta_{BCS} = i\Delta/E$. At zero magnetic field, and in an experiment such as ours where the normal metal is in contact with a single superconductor, φ is constant and $\theta(x, E)$ obeys the Usadel equation [8]:

$$\frac{\hbar D}{2} \frac{\partial^2 \theta}{\partial x^2} + (iE - \hbar\gamma_{sf} \cos \theta) \sin \theta + \Delta(x) \cos \theta = 0.$$

(1)

In this equation γ_{sf} is the spin-flip scattering rate and the inelastic scattering rate is assumed to be zero. We will make the approximation that $\gamma_{sf} = 0$ in the superconductor. In a normal metal with no electron-electron interaction, $\Delta = 0$, whereas in a superconductor the pair potential $\Delta(x)$ obeys the self-consistency equation involving the DOS $N_S(0)$ of the superconductor in its normal state, the pairing interaction strength $\mathcal{V}$, and the Debye energy $\hbar\omega_D$:

$$\Delta(x) = N_S(0)\mathcal{V} \int_0^{\hbar\omega_D} \tanh\left(\frac{E}{2k_B T}\right) \text{Im}[\sin \theta] \, dE.$$

(2)

Equation (1) is supplemented with boundary conditions: far from the interface, $\theta_N = 0$ in the normal metal, and

$\theta_S = \theta_{BCS}$ in the superconductor. At the interface,

$$\sigma_{N,S}\left(\frac{\partial \theta_{N,S}}{\partial x}\right)_{x=0} = \frac{G_{int}}{A} \sin[\theta_S(0, E) - \theta_N(0, E)],$$

(3)

where $\sigma_X = N_X(0)e^2 D_X$ is the conductivity and $N_X(0)$ is the DOS at the Fermi energy in electrode X and A is the area of the contact [19]. Although the conductance of the interface G_{int} is not measured, the absence of superconductivity in the sandwich down to 18 mK provides a lower limit: $G_{int} > 2$ S [16]. With such a high conductance, a good approximation is $\theta_S(0, E) = \theta_N(0, E)$. The resolution of the Usadel equation is greatly simplified if Δ is assumed to be independent of x in the superconductor: Eq. (1) then admits a first integral. The DOS is obtained by a second integration performed numerically. We used the value of Δ given by the measurement of the reference NS tunnel junction and the diffusion constant $D_N = 70 \times 10^{-4}$ m^2/s in copper deduced from the conductivity of the wire between F_1 and F_3. The rate γ_{sf} was taken as an adjustable parameter. The 1D theory [Eqs. (1) and (3)] does not account for the overlap region of the N and S wires. Nevertheless, the theory produces good agreement with the data if we take the effective NS interface ($x = 0$) to be 20 nm away from the extremity of the normal wire, in the overlap region. We calculate the DOS at the position of the center of each finger. (Calculating the spatially averaged DOS over the width of the finger hardly changes the result.)

For quantitative comparison of the Usadel theory with the experimental data, we must take into account the influence of single-electron charging effects on the conductance. At zero temperature, the differential conductance of the probe tunnel junction at a finger is related to the DOS through

$$\frac{dI}{dV} = \frac{1}{R_t} \int_0^{eV} n(x, E) P(eV - E) \, dE,$$

(4)

where R_t is the tunnel resistance of the junction and $P(E)$ is the probability for the electromagnetic environment of the tunnel junction to absorb an energy E [12]. Finite but low temperatures can be accounted for by convolving expression (4) with the derivative of the Fermi function. For a tunnel junction of capacitance C in series with a resistance R such that $\alpha = 2R/(h/e^2) \ll 1$, $P(E) = \alpha/E_0(E/E_0)^{\alpha-1}$ for E smaller than $E_0 = e^2/\pi\alpha C$. The high field data for F_1, F_2, and F_3 are well fitted by Eq. (4) with $n(x, E)$ constant (see fit of curve c in Fig. 3) and yield $\alpha = 0.022$. The fit corresponds to $R = 300\ \Omega$ and $C = 1$ fF, in good agreement with the estimated values.

The comparison between the zero field data taken at 20 mK for the three fingers F_1, F_2, and F_3, and the prediction of Eq. (4) calculated with the DOS $n(x, E)$ previously discussed, is shown in the bottom panel of Fig. 2. The calculation is performed with the value $\gamma_{sf} = 1.5 \times 10^{10}$ s^{-1}, which provides the best overall agreement

and is consistent with values found in previous experiments on copper films [20]. As seen in the figure, the theoretical curves reproduce the general features of the experimental data, especially the evolution of the characteristic energy scale with distance from the NS interface [21]. The present theory does not produce maxima as pronounced as those observed, but the exact resolution of the Usadel equation (1) including the gap self-consistency equation (2) improves the agreement [22].

In conclusion, we find that the space and energy dependence of the DOS in a diffusive normal wire in contact with a superconductor is well accounted for by the Usadel equation of the theory of nonequilibrium superconductivity. This DOS is somewhat similar to that of a gapless superconductor. Moreover, it is well known that a supercurrent can flow through a short normal metal wire connected to two superconducting electrodes [23–25]. However, one should not conclude that the proximity effect induces superconductivity in the usual sense: A normal metal wire connected to a single superconductor remains resistive [4,24]. Recent transport calculations [7,26] also based on the Usadel equation account for this seemingly paradoxical behavior.

We acknowledge Yu. Nazarov for introducing us to the theoretical formalism and W. Belzig and C. Bruder for fruitful discussions and communication of their results prior to publication. N. O. B. would like to thank the CEA for its hospitality during the course of this work.

*On leave from Michigan State University, East Lansing, MI 48824.

[1] See, for instance, Proc. of the NATO Adv. Res. Workshop on Mesoscopic Superconductivity [Physica (Amsterdam) 203B, 201 (1993)].

[2] G. Deutscher and P. G. de Gennes, in Superconductivity, edited by R. D. Parks (Marcel Dekker, New York, 1969), p. 1005.

[3] G. E. Blonder, M. Tinkham, and T. M. Klapwijk, Phys. Rev. B 25, 4515 (1982).

[4] V. T. Petrashov, V. N. Antonov, P. Delsing, and T. Cleason, Phys. Rev. Lett. 74, 5268 (1995); P. G. N. de Vegvar, T. A. Fulton, W. H. Mallison, and R. E. Miller, Phys. Rev. Lett. 73, 1416 (1994).

[5] A. F. Volkov, A. V. Zaitsev, and T. M. Klapwijk, Physica (Amsterdam) 210C, 21 (1993).

[6] Yu. V. Nazarov, Phys. Rev. Lett. 73, 1420 (1994).

[7] Yu. V. Nazarov and T. H. Stoof, Phys. Rev. Lett. 76, 823 (1996); T. H. Stoof and Yu. V. Nazarov, Phys. Rev. B 53, 14 496 (1996).

[8] A. Schmid, in Nonequilibrium Superconductivity, Phonons, and Kapitza Boundaries, edited by K. E. Gray (Plenum Press, New York, 1981), p. 423; J. Rammer and

H. Smith, Rev. Mod. Phys. 58, 323 (1986); A. I. Larkin and Yu. N. Ovchinikov, in Nonequilibrium Superconductivity, edited by D. N. Langenberg and A. I. Larkin (North-Holland, Amsterdam, 1986), p. 493; K. D. Usadel, Phys. Rev. Lett. 25, 507 (1970).

[9] Identification of the expressions for the supercurrent in the GL theory and the nonequilibrium superconductivity theory yields $(\hbar e^*/m^*)[\Psi(x)]^2 = (e/2)N(0)D \int_{-\infty}^{+\infty} dE[1 - 2f(E)]\mathrm{Im}\{\sin^2 \theta(x, E)\}$, where D is the diffusion constant and $f(E)$ the Fermi function.

[10] A complementary experiment was performed by S. H. Tessmer, D. J. Van Harlingen, and J. W. Lyding, Phys. Rev. Lett. 70, 3135 (1993), on the DOS in thin ballistic N islands on an S substrate.

[11] J. M. Rowell, in Tunneling Phenomena in Solids, edited by E. Burstein and S. Lundqvist (Plenum, New York, 1969), p. 385; T. Claeson, ibid., p. 443.

[12] M. H. Devoret, D. Esteve, H. Grabert, G.-L. Ingold, H. Pothier, and C. Urbina, Phys. Rev. Lett. 64, 1824 (1990); G.-L. Ingold and Yu. V. Nazarov, in Single Charge Tunneling, edited by H. Grabert and M. H. Devoret (Plenum Press, New York, 1992), p. 21.

[13] C. J. Adkins and B. W. Kington, Phys. Rev. 177, 777 (1969); J. R. Toplicar and D. K. Finnemore, Phys. Rev. B 16, 2072 (1977); A. Kastalsky, L. H. Greene, J. B. Barner, and R. Bhat, Phys. Rev. Lett. 64, 958 (1990).

[14] W. L. McMillan, Phys. Rev. 175, 537 (1968).

[15] G. J. Dolan and J. H. Dunsmuir, Physica (Amsterdam) 152A, 7 (1988).

[16] A. A. Golubov, in Superconducting Superlattices and Multilayers, edited by I. Bozovic, SPIE Proceedings Vol. 215 (SPIE, Bellingham, WA, 1994), p. 353.

[17] D. Vion, P. F. Orfila, P. Joyez, D. Esteve, and M. H. Devoret, J. Appl. Phys. 77, 2519 (1995).

[18] M. Tinkham, Introduction to Superconductivity (McGraw Hill, New York, 1985), p. 41.

[19] S. Yip, Phys. Rev. B 52, 15 504 (1995).

[20] B. Pannetier, J. Chaussy, and R. Rammal, Phys. Scr. T13, 245 (1986).

[21] At distances x from the NS interface of the order of $\sqrt{\hbar D/\Delta} \approx 140$ nm, the dominant energy scale of the spectrum is the gap Δ; at larger distances, the characteristic energy is $\hbar D/x^2$ and the spectrum is rounded by the spin-flip scattering rate γ_{sf}.

[22] W. Belzig, C. Bruder, and G. Schön, Phys. Rev. B (to be published).

[23] A. L. De Lozanne and M. R. Beasley, in Nonequilibrium Superconductivity, edited by D. N. Langenberg and A. I. Larkin (North-Holland, Amsterdam, 1986), p. 111.

[24] H. Courtois, Ph. Gandit, and B. Pannetier, Phys. Rev. B 52, 1162 (1995); H. Courtois, Ph. Gandit, D. Mailly, and B. Pannetier, Phys. Rev. Lett. 76, 130 (1996).

[25] A. F. Volkov, Phys. Rev. Lett. 74, 4730 (1995).

[26] F. Zhou, B. Spivak, and A. Zyuzin, Phys. Rev. B 52, 4467 (1995).

6.3 Density of states in a perpendicular magnetic field

The measured DOS when a magnetic field was applied perpendicularly to the sample has been fitted by the self-consistent calculation of Belzig and Bruder [3]. We present hereafter the DOS calculated within the same hypothesis as in our article, namely, a constant super-conducting gap in the superconductor. This simplified approach with respect to the work of Belzig and Bruder nevertheless reproduces quite well the experimental curves.

We have seen in chapter 5 that the Usadel equation for the normal wire in a constant perpendicular magnetic field is

$$\frac{\hbar D}{2}\frac{\partial^2\theta}{\partial x^2} + \left[iE - \left(\frac{\hbar}{\tau_{\mathrm{sf}}} + \frac{\hbar}{\tau_H}\right)\cos\theta\right]\sin\theta = 0 \tag{6.1}$$

where the depairing rate due to the magnetic field is given by

$$\gamma_H = \frac{1}{\tau_H} = \frac{e^2}{6\hbar^2}w^2DH^2. \tag{6.2}$$

The voltage dependences of the differential conductance of the junctions F_1 and F_2 are plotted in the top panels of Fig. 6.1 and 6.2, for different values of the magnetic field applied perpendicularly to the sample plane. The dip in conductance at zero voltage is weakened by the magnetic field, but persists up to fields of the order of 1 T.

We have computed the density of states predicted by the Usadel equation (6.1), using the same parameters as those used to fit the low temperature, zero magnetic field curves (see paper). We find that the experimental curves are reproduced correctly only if the depairing rate due to the magnetic field $\gamma_{H\mathrm{eff}}$ is four times smaller than the rate γ_H related to the applied field H through Eq. (6.2). The discrepancy between the rate γ_H computed with the values of the applied field and width of the sample, and the rate $\gamma_{H\mathrm{eff}}$ which would best describe the data (corresponding to a product Hw half as large), has already been reported [7,8], but is not yet understood. The computed curves with $\gamma_{H\mathrm{eff}} = \gamma_H/4$ are plotted in the bottom panel of Fig. 6.1 and 6.2. The overall shape of the curve is reproduced rather well, but, as in the case of the curves measured in zero magnetic field, the theory does not predict as marked bumps in the DOS.
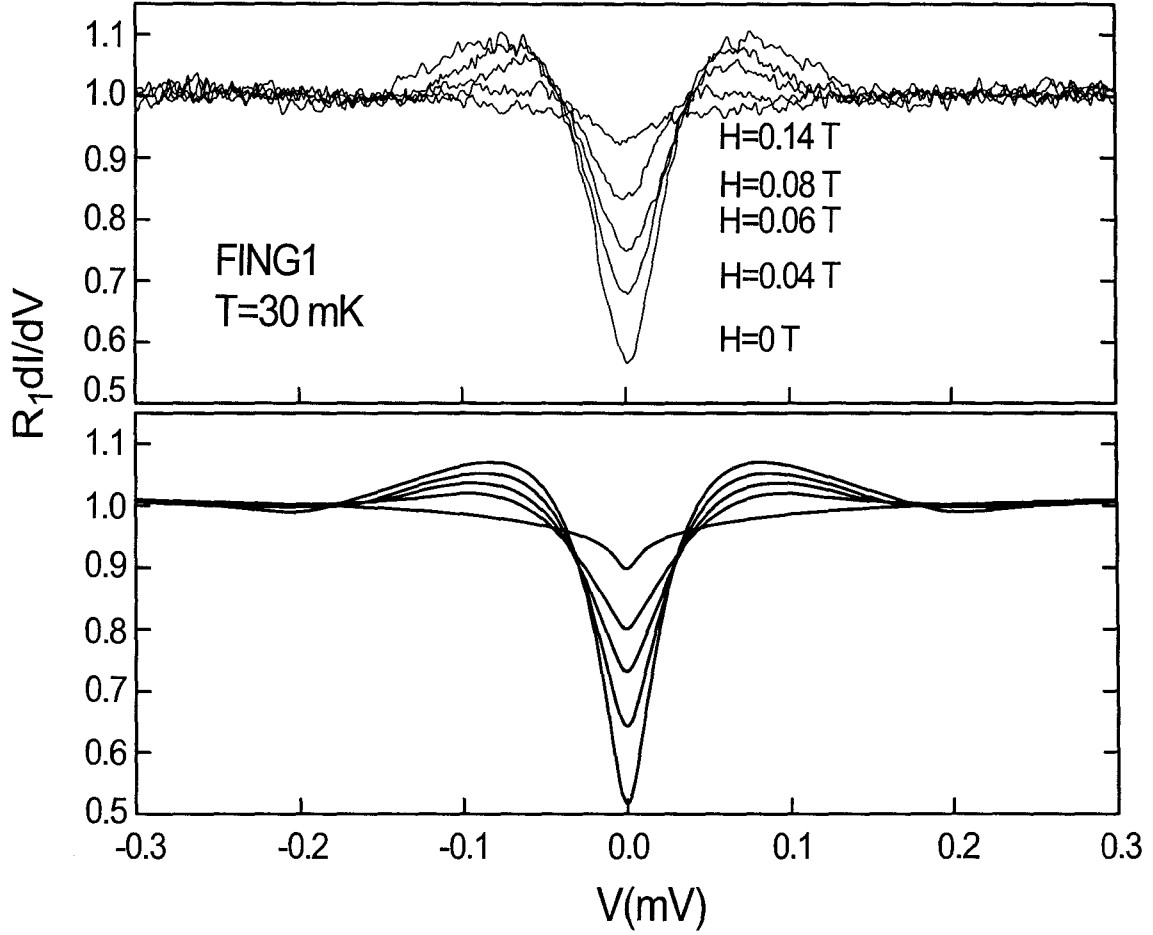
Fig. 6.1. Proximity effect at junction 1 in a magnetic field perpendicular to the plane of the sample. Top panel: differential conductance of junction 1, normalized to the conductance $R_1^{-1} = 0.19$ μS at V=0.3 mV, in a magnetic field of 0, 0.04, 0.06, 0.08 and 0.14 T. Bottom panel: predicted differential conductance using $\tau_{sf} = 65$ ps, D=70 cm^2/s, and $\tau_{Heff} = 4\tau_H$.
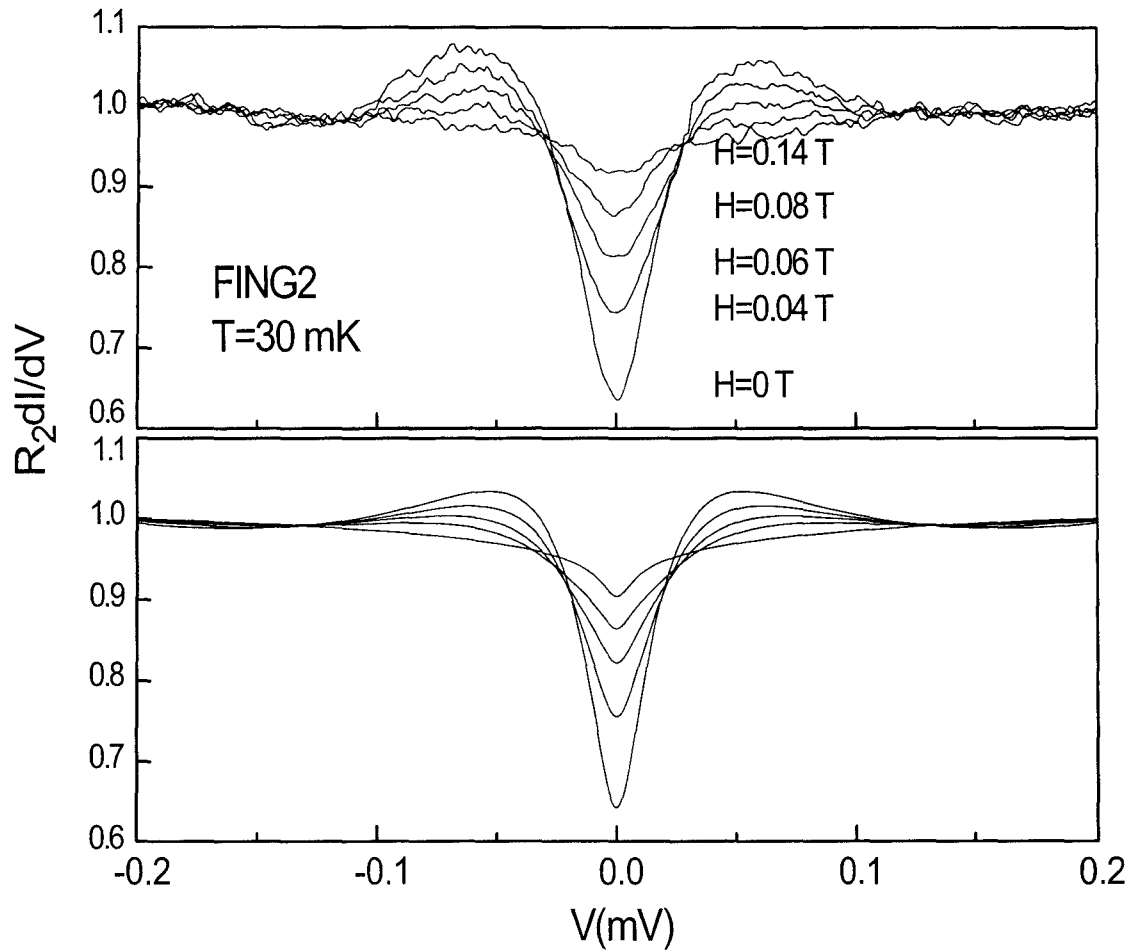
Fig. 6.2. Proximity effect at junction 2 in a magnetic field perpendicular to the plane of the sample. Top panel: differential conductance of junction 2, normalized to the conductance $R_2^{-1} = 0.38$ μS at V=0.3 mV, in a magnetic field of 0, 0.04, 0.06, 0.08 and 0.14 T. Bottom panel: predicted differential conductances using $\tau_{sf} = 65$ ps, D=70 cm^2/s, and $\tau_{Heff} = 4\tau_H$.

6.4   Contribution of charging effects to the measured DOS

6.4.1   What is measured by the differential conductance?

The general expression for the current through a tunnel junction contains not only the distribution functions and density of states of both electrodes, but in addition the probability $P(\varepsilon)$ that a part ε of the available energy is released to the electric circuit surrounding the junction, when a tunneling event occurs [6]. The tunnel current can be expressed as the difference between two tunneling rates

$$I(V) = e\left(\Gamma_{LR}(V) - \Gamma_{RL}(V)\right) \tag{6.3}$$

with the forward tunneling rate given by (see Fig. 6.3):

$$\Gamma_{LR}(V) = \frac{1}{n_0^2 e^2 R_T} \int_{-\infty}^{+\infty} dE \int_{-\infty}^{+\infty} d\varepsilon\, n_L(E)\, n_R(E - \varepsilon + eV)\, f_L(E)\left[1 - f_R(E - \varepsilon + eV)\right] P(\varepsilon, T).$$

The current can then be expressed as
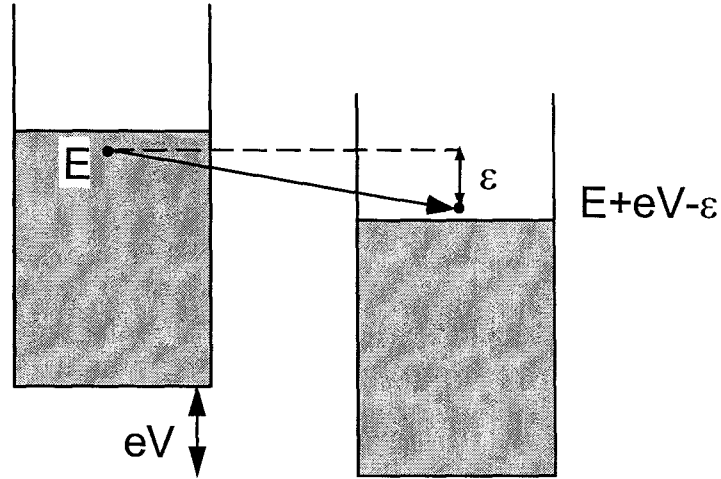
Fig. 6.3. Current at a tunnel junction: an electron tunnels from a state of energy E in the left electrode to a state of energy $E + eV - \varepsilon$ in the right electrode, exciting modes with a total energy ε in the environment.

$$I(V) = \frac{1}{n_0^2 e R_T} \int_{-\infty}^{+\infty} dE \int_{-\infty}^{+\infty} d\varepsilon\, n_L(E - \varepsilon)\, n_R(eV - E)\left[\, f_L(\varepsilon - E) - f_R(eV - E)\right] P(\varepsilon, T).$$

$$\tag{6.4}$$

In the experiment on the proximity effect, we assume that the populations of both electrodes (the normal finger and the copper wire with the modified DOS) are distributed according to a

Fermi function at the sample temperature. This is a reasonable assumption since only a small tunnel current flows in the structure. In addition, we consider that the finger electrode has a constant normal density of states n_0, since it is separated from the proximity superconductor by a weak transparency tunnel junction. Therefore, only the energy-dependence of the modified DOS n_L remains in the integral. The differential conductance is then

$$\frac{dI}{dV}(V) = \frac{1}{n_0 R_T} \int_{-\infty}^{+\infty} dE \int_{-\infty}^{+\infty} d\varepsilon \, n_L (E - \varepsilon) P (\varepsilon, T) \frac{\partial f_R}{\partial E} (eV - E). \qquad (6.5)$$

This formula shows that in general the differential conductance of the tunnel junction is not directly proportional to the density of states of the electrode being probed. Instead, formula (6.5) shows that the differential conductance is proportional to an effective density of states $\mathcal{N}$ which is the convolution of the density of states by the function $P(\varepsilon, T)$:

$$\mathcal{N}_L (E, T) = \int_{-\infty}^{+\infty} n_L (E - \varepsilon) P (\varepsilon, T) \, d\varepsilon. \qquad (6.6)$$

The differential conductance then reads:

$$\frac{dI}{dV}(V) = \frac{1}{n_0 R_T} \int_{-\infty}^{+\infty} \mathcal{N}_L (E, T) \, \frac{\partial f_R}{\partial E} (eV - E) \, dE. \qquad (6.7)$$

From formula (6.7) it is seen that the differential conductance depends on temperature through two terms

i) the usual occupation factor term $\frac{\partial f}{\partial E}$

ii) the rather complex temperature dependence of $P(\varepsilon, T)$.

In the following, we will always neglect the temperature dependance of $P(\varepsilon, T)$ with respect to the temperature dependance of $\frac{\partial f}{\partial E}$. However, we do keep track of the effect of $P(\varepsilon)$, as was done in the comparison between experiment and theory in the article, and in Fig. 6.1 and 6.2.

6.4.2   Form of $P(\varepsilon, T = 0)$ for an RC environment

At zero temperature the derivative of the Fermi function is a delta function, so that the conductance is just the convolution of the DOS by the probability $P(\varepsilon, T = 0)$:

$$\frac{dI}{dV}(V, T = 0) = \frac{1}{n_0 R_T} \mathcal{N}_L (eV, T = 0) = \frac{1}{n_0 R_T} \int_0^{eV} n_L (eV - \varepsilon) P (\varepsilon, T = 0) \, d\varepsilon \qquad (6.8)$$

Here we have used the fact that at zero temperature the environment cannot provide energy: $P(\varepsilon < 0, T = 0) = 0$. From expression (6.8) we check that if the excitation of environmental modes can be neglected (i.e. when the environment has a vanishingly small impedance), $P(\varepsilon)$

is a delta function and the conductance at voltage V is indeed given by the reduced DOS $n\left(eV\right)/n_0$ of the normal electrode divided by the tunnel resistance of the junction.

We model our sample by the equivalent circuit pictured in Fig. 6.4. The tunnel junction is
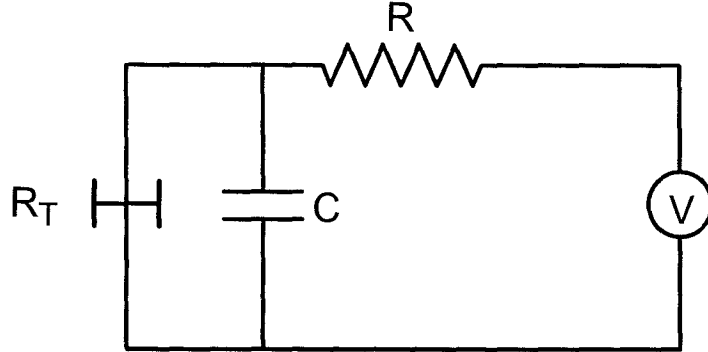
Fig. 6.4. Electrical circuit representing the sample and its electric environment: the junction between the wire and the finger probe can be decomposed into a tunnel element of resistance R_T in parallel with a capacitance, whereas the wire and leads are represented as a resistance R.

decomposed into a pure tunnel element of resistance R_T, in parallel with a capacitance C. The resistance of the leads is figured by a resistance R, which in our case is orders of magnitude inferior to the resistance quantum R_K. At zero temperature, the probability $P\left(\varepsilon\right)$ of exciting such an RC environment is then given at low energy ε by [6]

$$P\left(\varepsilon\right) = \frac{\alpha}{\varepsilon_0}\left[\frac{\varepsilon}{\varepsilon_0}\right]^{\alpha-1} \quad \text{for } 0 < \varepsilon \ll \varepsilon_0, \tag{6.9}$$

where $\alpha = 2R/R_K$, and $\varepsilon_0 = \frac{e^2}{\pi\alpha C}$. This function is plotted in Fig. 6.5 for $\alpha = 0.02$ and $\alpha = 0.2$. The contribution of this environment can be determined by measuring the differential conductance of the junction when the proximity effect has been cancelled by applying a magnetic field superior to the critical field of the superconductor, for then the density of states in the normal metal is constant, and the conductance is given by

$$\frac{dI}{dV}\left(V\right) = \frac{1}{R_T}\left|\frac{eV}{\varepsilon_0}\right|^{\alpha} \quad \text{for } eV \ll \varepsilon_0. \tag{6.10}$$

6.4.3   Control experiment on the contribution of charging effects

The high field differential conductance of all three junctions F_1, F_2 and F_3 could be fitted with this model, yielding a junction capacitance of 1 fF and an environment resistance of $R = 300 \ \Omega$ (see fit of high-field conductance of junction F_2 in Fig. 6.6). Both these values
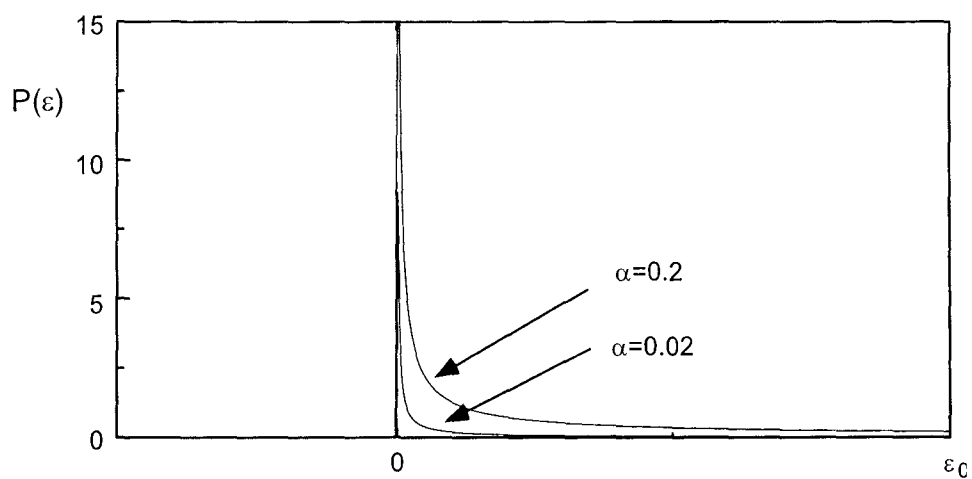
Fig. 6.5. Function $P(\varepsilon)$ at T=0 for a resistive environment, plotted for $\alpha = R/R_K = 0.02$ and 0.2.
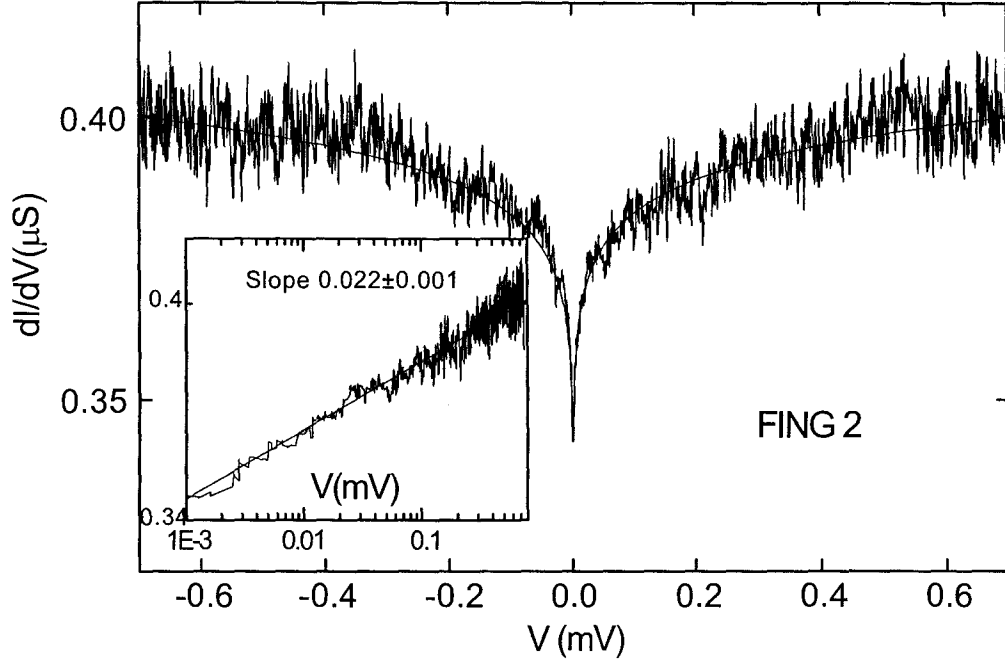
Fig. 6.6. High field conductance of junction F_2, at T=30 mK and in an applied field of 0.14 T, plotted on a linear scale and a logarithmic scale (inset). The smooth line is the powerlaw fit to the data (see text), which yields an environment resistance of 300 Ω.

are consistent with the area of the junction and geometry of the sample, and correspond to an energy $\varepsilon_0 \approx 2$ meV, indeed much larger than the voltages at which all conductance curves were measured.

To conduct a more thorough check of formula (6.9), we have performed a control experiment. We have measured the differential conductance of three devices, each consisting of a tunnel junction between two wires of aluminum-silicium (Al 70%, Si 30%) of thickness and width comparable to the wires of the previous experiment (width 150 nm and thickness 20 nm). Only the length of the wires was varied, in order to test formula (6.9) for different values of the resistance of the environment.   The three circuits were fabricated in a single process, in order to ensure the same tunnel barriers and same diffusion constants for all wires. The environment resistance of the three devices should therefore scale with the total length of the wires. The differential conductance of the three circuits, measured in an applied magnetic field of 0.3 T, are shown in Fig. 6.7. The power law (6.9) predicted by the zero temperature theory fits the data well for voltages in the 0.1 − 5 mV range, where the condition $k_B T_e \ll eV \ll \varepsilon_0$ is fulfilled, where T_e is the effective electronic temperature. The departure from the power law
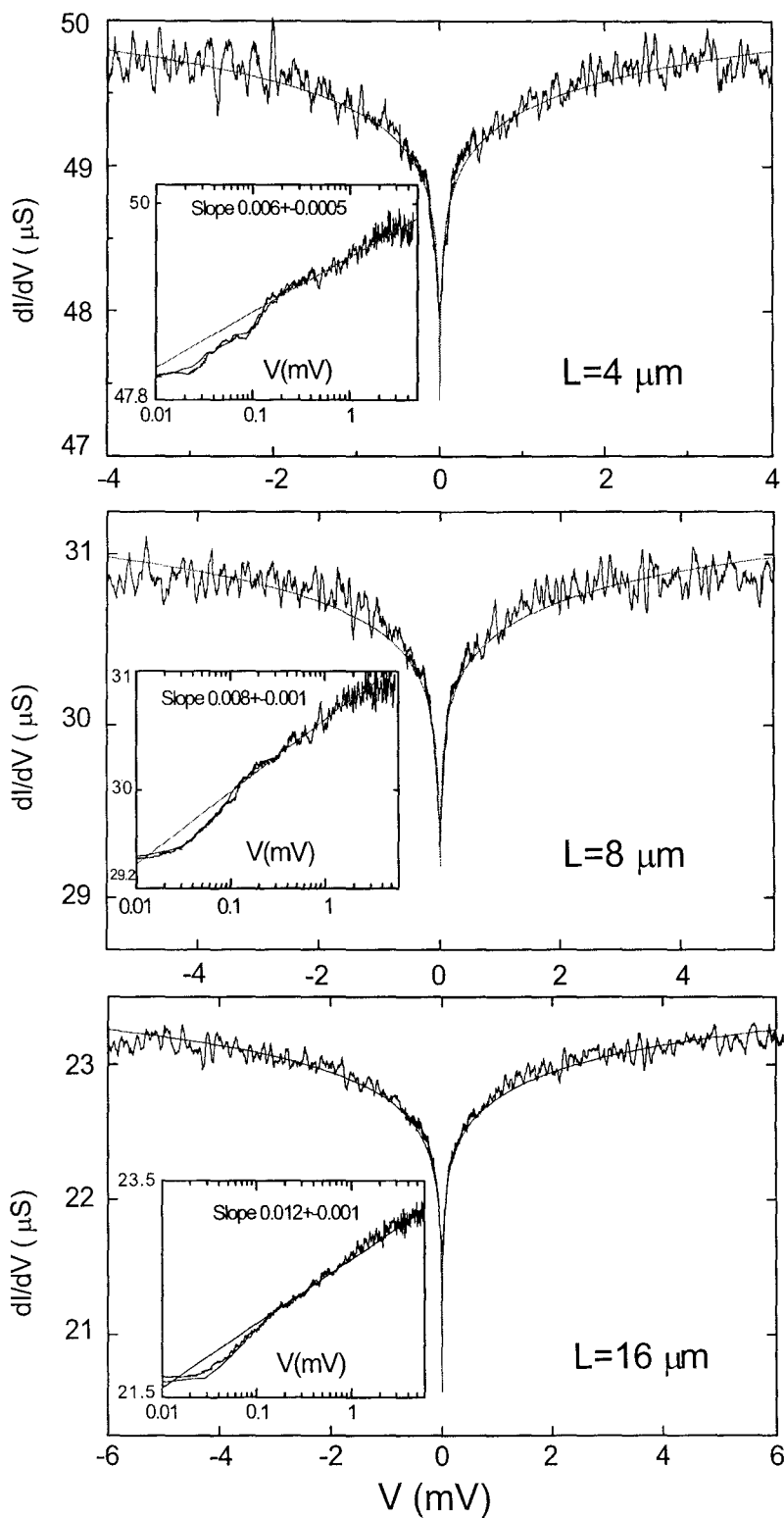
Fig. 6.7. High-field differential conductance of three devices made of a tunnel junction between AlSi wires of width 150 nm, thickness 25 nm, and lengths of respectively 4, 8 and 16 μm. The smooth curves are power law fits to the data. The insets are log-log plots of the differential conductances and fits. The measurements were performed at T=30 mK, in an applied field of 0.3 T.

at low voltage is due to the heating of the electrons above the phonon temperature because of the power supplied to the sample, and of the poor electron-phonon coupling. Such an effect was not observed in the first experiment (see Fig. 6.6) because of the ten-fold larger tunnel resistance of the junction.

Indeed, the electronic temperature is related to the power P deposited in the wire of resistance R and volume $\mathcal{V}$ by the voltage source through [9]

$$T_e = \left(\frac{P}{\Sigma \mathcal{V}} + T_{\mathrm{ph}} \right)^{1/5},$$

where the coefficient $\Sigma \sim 2 \ \mathrm{nW}.\mu\mathrm{m}^{-3}.\mathrm{K}^{-5}$. If the phonon temperature is taken to be zero, the voltage dependence of the electron temperature is therefore given by

$$T_e = \left(\frac{1}{\Sigma \mathcal{V}} R \left(\frac{V}{R_T} \right)^2 \right)^{1/5},$$

thereby explaining the important difference between two samples with very different tunnel resistances.

From the exponent of the power law, we deduce environment resistances of 80, 105 and 160 (± 6) Ω for the wires of length 4, 8 and 16 μm respectively. These values are plotted as a function of the number of squares in each circuit, deduced from the electron micrograph, in Fig. 6.8. The environment resistance indeed increases linearly with the length of the wire, but does not extrapolate to zero resistance for zero length: the extrapolation to zero is 58 Ω. We attribute this offset resistance to the real part of the impedance of the rest of the circuit in the range of wavelengths associated to the frequencies of the applied voltages, that is the centimetric range. A rough estimate of the capacitance between the evaporated circuit and the copper sample-holder, and of the geometric and kinetic inductance of the circuit yields a characteristic impedance of the order of 100 Ω.
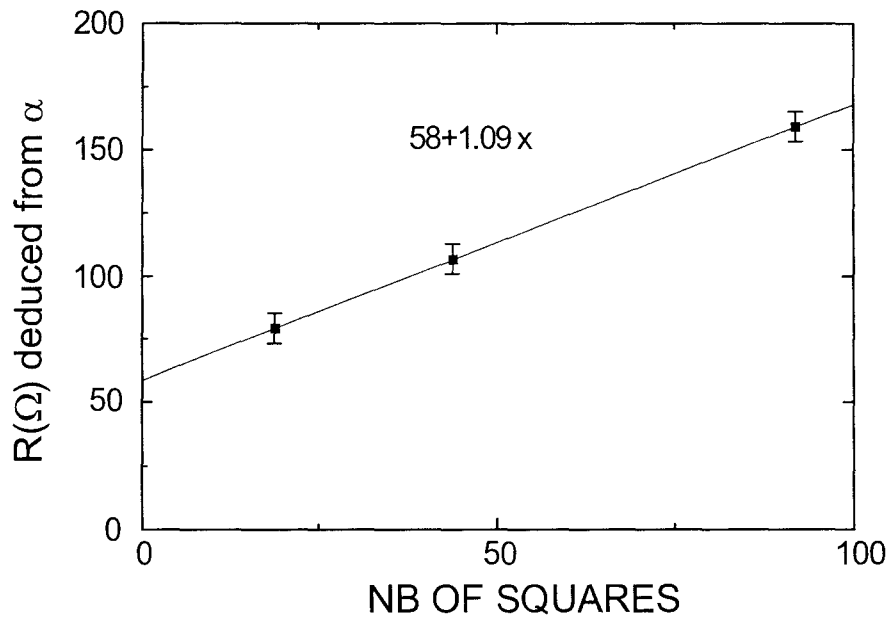
Fig. 6.8. Resistance of the electromagnetic environment of the three junctions deduced from the power law fit discussed in text, as a function of the number of resistance squares of the measured circuits.

6.5   Effect of a finite temperature on the measurements

At finite temperature expression (6.7) shows that because of the temperature dependence of $P(\varepsilon)$, the conductance at temperature T is not just the zero-temperature DOS convolved with the derivative of a Fermi function at temperature T. However, the magnitude of $P(\varepsilon)$ is sufficiently weak that the variations with temperature of the measured conductance are in fact well fitted by convolving the low temperature curve with a derivative of a fermi function at the temperature of the experiment. Figure 6.9 shows the differential conductance of junction 1, normalized by the junction conductance at $V = 0.3$ mV, measured at temperatures ranging from 20 to 565 mK. The typical features of the differential conductance are
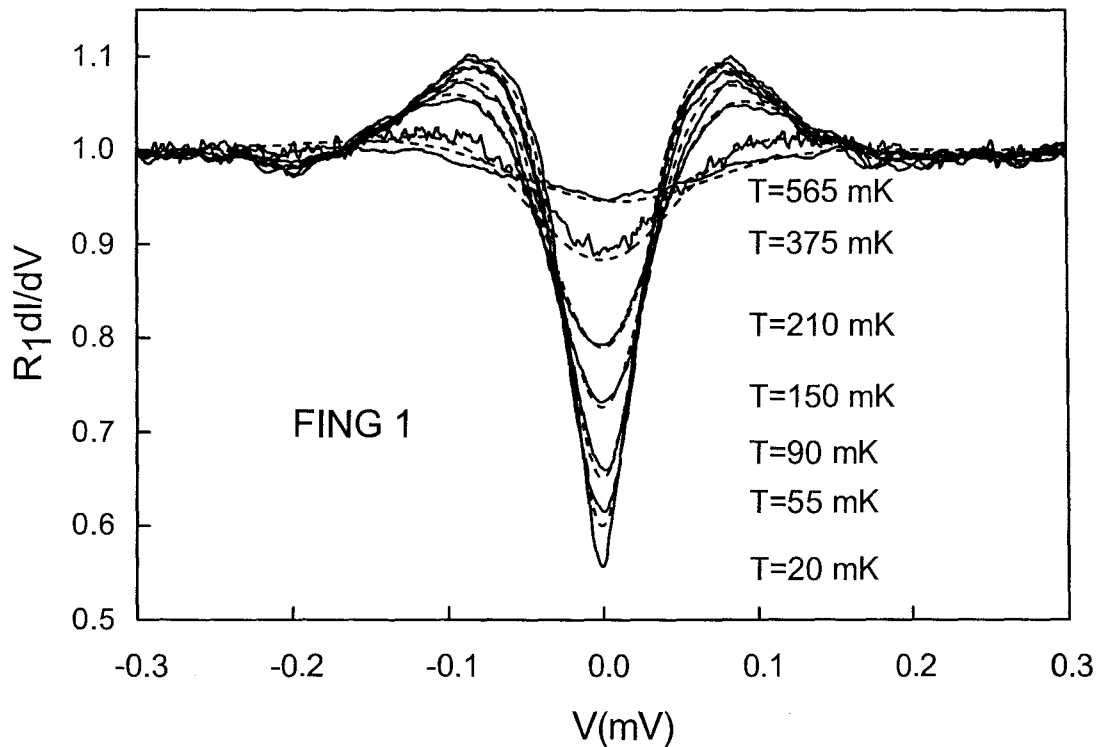
Fig. 6.9. Differential conductance of junction 1 measured at different temperatures, and, plotted as hatched lines, convolution of the 20 mK curve with the derivative of the Fermi function at the measurement temperature.

progressively washed out as the sample temperature is increased, in contrast with the behavior of the junction conductance in an increasing magnetic field. The dashed curves are obtained by convolving the curve measured at 20 mK by the derivative of the Fermi function at the measurement temperatures. These convolved curves practically coincide with the mea-

sured curves, even though we have neglected the temperature dependance of the environment excitation probability $P(\varepsilon)$.

In conclusion, as predicted by the theory of the proximity effect, we do not detect any temperature dependence of the proximity-induced density of states at temperatures T such that $k_B T \ll \Delta$. The temperature dependence of the differential conductance is entirely explained by the occupation factors.

6.6   Influence of the deposition order of the normal and superconducting metals

We have found, like others before [10] , that the proximity effect between two metals depends on which one is deposited first. We present in Fig. 6.10 the density of states measured in a sample with a geometry similar to the one presented in the paper, but in which the copper was deposited before the aluminum. The tunnel junction is positionned 50 nm away from the NS interface. The qualitative difference in the shape of the measured density of states, which cannot be reproduced with the theory used to fit the other experiment, might be due to interdiffusion of the Al and Cu atoms. The proximity effect could be in this case induced by a superconducting alloy rather than by a BCS superconductor. When aluminum is deposited first, we suppose that it develops a very thin oxide layer which is thin enough to enable an excellent NS contact, but thick enough to prevent the interdiffusion of the two metals.
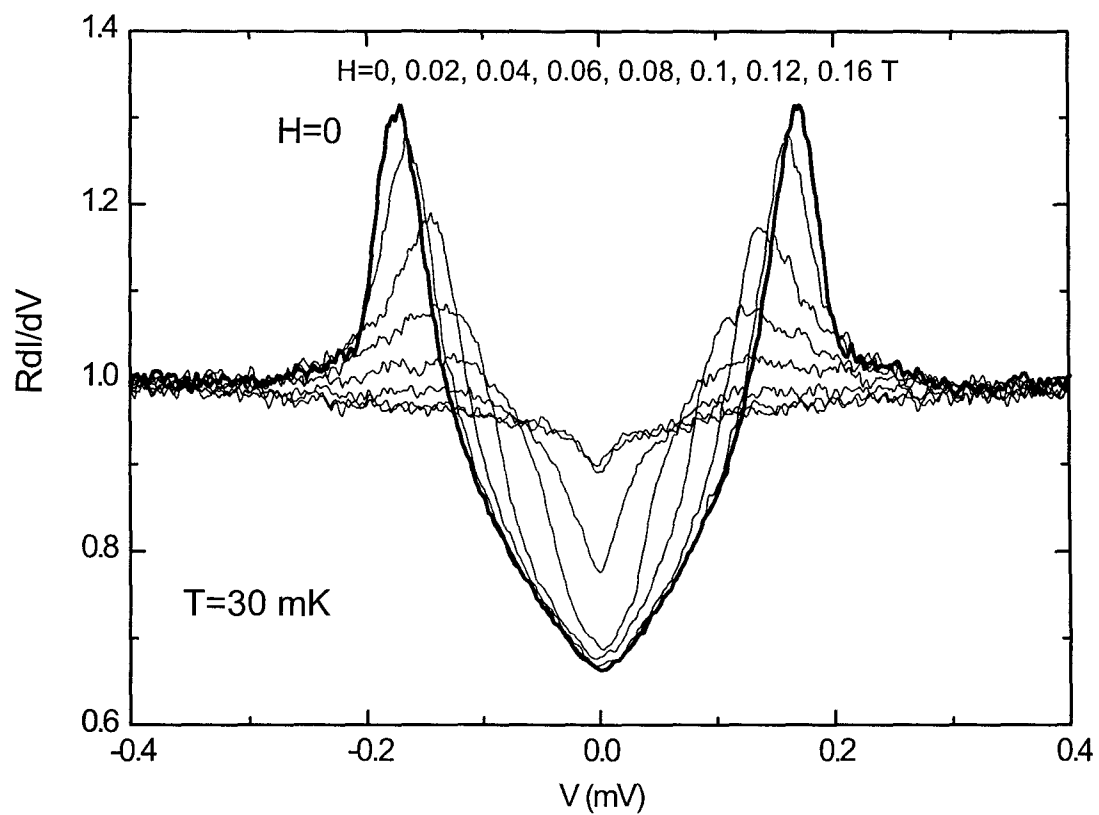
Fig. 6.10. Measured differential conductance of a tunnel probe placed above a normal copper wire, 50 nm away from the contact of the wire with a superconducting aluminum wire. The geometrical configuration is similar to the one described in the article. In this sample however, the copper wire was deposited before the aluminum wire.

REFERENCES

[1] J. J. Hauser and H. C. Theuerer, Phys. Letters **14**, 270 (1965). See also references in G. Deutscher and P.G. de Gennes, in *Superconductivity*, edited by R. D. Parks (Marcel Dekker, New York, 1969), p. 1005.

[2] T. Claeson and S. Gygax, Solid State Comm. 4:385 (1966); see also references in T. Claeson, in *Tunneling Phenomena in Solids*, edited by E. Burnstein and S. Lundqvist (Plenum, New York,1969), p. 443.

[3] W. Belzig and C. Bruder, Phys. Rev. **B54**, 9443 (1996).

[4] V. T. Petrashov, V.N. Antonov, P. Delsing and T. Claeson, Phys. Rev. Lett. **74**, 5268 (1995); V. T. Petrashov, R. Sh. Shaikhaidarov, I. A. Sosnin, Czech. J. Phys. **46**, 3303 (1996).

[5] H. Courtois, Ph. Gandit, and B. Pannetier, Phys. Rev. B **51**, 9360 (1995); Phys. Rev. B **52**, 1162 (1995).

[6] G.-L. Ingold and Yu. Nazarov, in *Single Charge Tunneling*, edited by H. Grabert and M. H. Devoret (Plenum Press, New York, 1992), p. 21; H. Pothier, Ph.D. Thesis, Université Paris 6 (1991).

[7] P. Charlat, H. Courtois, Ph. Gandit, D. Mailly, A.F. Volkov, and B. Pannetier, Phys. Rev. Lett. **77**, 4950 (1996).

[8] P. Lafarge, P. Joyez, D. Esteve, C. Urbina, and M. H. Devoret, Nature **365**, 422 (1993).

[9] F. C. Wellstood, C. Urbina, and John Clarke, Phys. Rev. B **49**, 5942 (1994).

[10] J. J. Hauser, H. C. Theuerer, and N. R. Werthamer, Phys. Rev. **136**, A637 (1964).

Chapter 7
Simplified theory of the proximity effect in the limit of small pair correlations

The general theory of the proximity effect can be simplified for the description of NS tunnel junction circuits. Indeed, when an opaque barrier separates the normal metal from the superconductor, the pairing induced in the normal metal is small, and the superconductor only slightly departs from a BCS behavior. The Usadel equations can then be linearized, leading to a series of simple expressions for the current and the conductance through an NS tunnel junction. In particular, the Andreev conductance directly measures the part of the pairing in the normal metal in phase with the superconductor.

In this chapter, we show that the weak proximity effect can be described in terms of quasi-classical trajectories originating at the NS tunnel junction and propagating in the normal metal. The pairing results from the interference of these trajectories, which each carry the phase of the superconductor they come from. The Andreev current at a tunnel barrier, which dominates at low voltage over the quasiparticle contribution, directly reveals these interferences.

The link between the subgap current through NS tunnel junctions and the proximity effect was completely overseen in the original interpretation of many experiments (including ours) [1]. The measured subgap currents were much larger than expected from a theory in which electrons incident at the barrier are treated as plane waves [2,3]. The puzzle was solved by

calculations *from scratch* using either the picture of Andreev reflection combined with normal reflection [4, 5], or in perturbation in the tunnel Hamiltonian [6], and keeping track of phase coherence. In the latter point of view, the tunneling rate for single-electrons is zero at sub-gap voltages because the density of single-particle states is zero in the superconductor, and the first contribution comes from two-electron tunneling. This two-electron process is allowed because the two tunneling electrons can be added to the superconductor at no energy cost as a pair. The large value of the two-electron current was explained by the constructive interference of several tunneling attempts of a pair of nearly time reversed states, which bounce back an forth between the junction and impurities in a diffusive material. In this transparent physical picture, the return probability of an electron to the barrier therefore plays a crucial role, like in the weak proximity effect formalism. In this chapter, we reconcile these two approaches.

Finally, we investigate in detail the case of NS-QUIDs.

7.1 Weak proximity effect

In this section we reformulate the theory of the proximity effect in the case of a small pairing angle in the normal metal $|\theta_N| \ll 1$, and a superconducting angle near its BCS value, $\theta_S \sim \theta_{\mathrm{BCS}}$. In addition, we concentrate on energies much smaller than the superconducting gap Δ. The Usadel equations are greatly simplified in this case, even in non strictly one-dimensional geometries relevant for the experimental situations.

7.1.1 Green functions in the perturbative limit

The pairing angle in the superconductor can be developed around the BCS value as

$$\theta_S(E) = \theta_{\mathrm{BCS}}(E) + \alpha(E), \text{ with } |\alpha| \ll 1 \tag{7.1a}$$

and the retarded Green function $\hat{R}_S$ is

$$\hat{R}_S(x,E) \simeq \hat{R}_{\mathrm{BCS}}(E) + \alpha(E) \begin{pmatrix} -\sin\theta_{\mathrm{BCS}}(E) & e^{-i\varphi_S}\cos\theta_{\mathrm{BCS}}(E) \\ e^{i\varphi_S}\cos\theta_{\mathrm{BCS}}(E) & \sin\theta_{\mathrm{BCS}}(E) \end{pmatrix}. \tag{7.2}$$

In the normal metal the pairing angle is small, so that the retarded Green function $\hat{R}_N$ (formula (5.8)) is parametrized by a single complex function $r(x,E)$, that we call the pairing parameter:

$$r(x,E) = \theta(x,E)e^{-i\varphi}, \quad |r| \ll 1 \tag{7.3}$$

$$\hat{R}_N(x,E) \simeq \begin{pmatrix} 1 & r(x,E) \\ \bar{r}(x,-E) & -1 \end{pmatrix}. \tag{7.4}$$

The advanced Green function $\hat{A}_N$ is in this limit

$$\hat{A}_N(x,E) \simeq \begin{pmatrix} 1 & -r(x,E) \\ -\bar{r}(x,-E) & -1 \end{pmatrix}.$$

7.1.2 Pairing parameters in the weak proximity effect in the one-dimensional case

The weak proximity effect regime in an infinite one-dimensional geometry was considered in chapter 5. The value of the pairing parameter on both sides of an interface of tunnel conductance G_T, at zero energy, was given (see Eq. (5.44) and Eq. (5.45a)). The pairing

parameters are, to first order in the tunnel conductance G_T:

$$r\left(E=0\right)=\frac{R\left(L_{\text{sf}}\right)G_T}{\sqrt{2}}e^{-i\varphi_S} \tag{7.5}$$

and

$$\theta_S\left(E=0\right)=\frac{\pi}{2}-\frac{R\left(L_{\Delta}\right)G_T}{\sqrt{2}}, \tag{7.6}$$

where $R\left(L_{\text{sf}}\right)$ is the resistance of a length L_{sf} of the normal wire, and is $R\left(L_{\Delta}\right)$ is the resistance of a length $L_{\Delta}=\sqrt{\hbar D_S/\Delta}$ of the superconducting wire in its normal state. These expressions clearly indicate the range of validity of the weak proximity effect approximation:

$R\left(L_{\text{sf}}\right)G_T\ll1$, and $R\left(L_{\Delta}\right)G_T\ll1$.

Equation (7.5) shows how the pairing induced in the normal metal results from the balance between the input through the tunnel barrier of pair correlations, and the loss of coherence in the normal metal.

Since the length L_{Δ} is usually shorter than the coherence length L_{sf}, the modifications induced in the superconductor are often neglected in comparison with those induced in the normal metal.

7.1.3   Expression for the current at an NS tunnel junction

7.1.3.1   General expressions

Given the simplified forms of the Green functions, the quasiparticle, Andreev and Josephson contributions to the current through an NS tunnel junction deduced from Eq. (5.61, 5.63, 5.65) are:

$$I_{qp}\left(V\right)=\frac{G_T}{e}\int_0^{+\infty}dEf_{1N}\left(E\right)\text{Re}\,\alpha\left(E\right), \tag{7.7}$$

$$\begin{aligned}I_A\left(V\right)&=\frac{G_T}{e}\int_0^{+\infty}\frac{dE}{2}f_{1N}\left(E\right)\text{Re}\left[r\left(E\right)e^{i\varphi_S}+\bar{r}\left(-E\right)e^{-i\varphi_S}\right]\\&=\frac{G_T}{e}\int_0^{+\infty}dE\cos\left(\varphi_S-\varphi\right)f_{1N}\left(E\right)\text{Re}\,\theta\left(E\right)\end{aligned} \tag{7.8}$$

and

$$\begin{aligned}I_J\left(V\right)&=\frac{G_T}{e}\int_0^{+\infty}dEf_{0N}\left(E\right)\text{Re}\left[r\left(E\right)e^{i\varphi_S}-\bar{r}\left(-E\right)e^{-i\varphi_S}\right]\\&=\frac{G_T}{e}\int_0^{+\infty}dE\sin\left(\varphi_S-\varphi\right)f_{0N}\left(E\right)\text{Im}\,\theta\left(E\right)\end{aligned} \tag{7.9}$$

Because of the high interface resistance, the currents through the structures are small, so that it is justified to take the thermal distributions as occupation factors. In the normal metal one has:

$$\left\{ \begin{array}{l} f_{0N} = \frac{1}{2} \left(\tanh \frac{(E+V)}{2k_BT} + \tanh \frac{(E-V)}{2k_BT} \right) \\ \\ f_{1N} = \frac{1}{2} \left(\tanh \frac{(E+V)}{2k_BT} - \tanh \frac{(E-V)}{2k_BT} \right) \end{array} \right.$$

(7.10)

and in the superconductor:

$$\left\{ \begin{array}{l} f_{0S} = \tanh \frac{E}{2k_BT} \\ \\ f_{1S} = 0. \end{array} \right.$$

(7.11)

7.1.3.2 Example of the zero voltage conductances at zero temperature in the one-dimensional infinite system

Given the expressions (7.5) and (7.6) of the pairing parameters, the Andreev conductance and quasiparticle conductance at zero voltage and zero temperature are, in second order in G_T:

$$\left(\frac{\partial I_A}{\partial V} \right)_{V=0} = \frac{1}{\sqrt{2}} R(L_{\text{sf}}) G_T^2$$

(7.12)

$$\left(\frac{\partial I_{qp}}{\partial V} \right)_{V=0} = \frac{1}{\sqrt{2}} R(L_\Delta) G_T^2$$

(7.13)

The expression of the Andreev conductance is of no surprise by now. The expression of the quasiparticle conductance is non-zero, in contrast with the case of a strictly unperturbed superconductor. The quasiparticle conductance is related to the departure of the supercon-ductor from the BCS state at the interface: the density of states $\mathrm{Re}\cos\theta_S$ is no longer zero at low energies.

We now turn to the analysis of the weak proximity effect in more experimentally relevant configurations.

7.1.4   Linearized Usadel equations in a normal wire with planar junctions to superconductors.

In the following, we solve the Usadel equation for the pairing parameter to first order in tunnel conductances.

To this order, the spectral current at the barrier, which provides the boundary conditions for the Usadel equation, can be taken as the spectral current between unperturbed electrodes. Furthermore, we limit the resolution to energies much smaller than the superconducting gap, so that the spectral current is independent of energy, and given by (see Eq. (5.26))

$$\sigma \vec{\nabla} r . \vec{n} = g_T e^{-i\varphi_S},$$
(7.14)

where $\vec{n}$ is a unit vector normal to the interface and g_T is the barrier tunnel conductance per unit area. Given these approximations, the superconductor provides a constant source of pairing, proportional to the tunnel conductance of the barrier and with the phase factor of the superconductor. The spectral current conservation is readily incorporated as a constant source term in the Usadel equation of the normal metal. We hereafter give the form of the solution for a realistic geometry in which the tunnel junctions between normal metal and superconductor are formed at the overlap of the two metals (see Fig. 7.1).

In the region of the NS junction, the variation of the spectral current in the normal metal is due to the spectral current flowing into the normal metal through the NS tunnel barrier, that is

$$wh\left[j_N\left(x + dx\right) - j_N\left(x\right)\right] = -wdx g_T e^{-i\varphi_S(x)},$$
(7.15)

with

$$g_T = \frac{G_T}{w_1 w}.$$
(7.16)

Here h is the thickness of the normal film. The linearized Usadel equation in a normal metal covered by a superconductor over a finite area is therefore

$$\frac{\hbar D}{2}\frac{\partial^2 r}{\partial x^2} + \left(iE - \frac{\hbar}{\tau_{\rm sf}}\right)r = -\frac{\hbar D}{2}\frac{g_T}{\sigma}\frac{e^{-i\varphi_S(x)}}{h}\Pi\left(x\right),$$
(7.17)

where $\Pi\left(x\right) = 1$ in the region of the junction and 0 elsewhere.
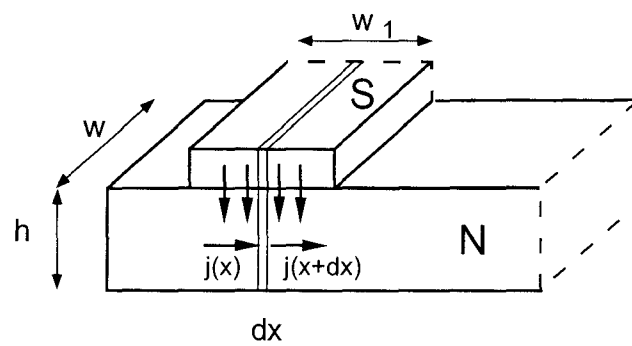
Fig. 7.1. Sketch of the typical layout of an NS junction: the junction is formed at the overlap of the normal and superconducting electrodes. In the weak proximity effect limit, the superconductor constitutes a constant source of spectral current over the area of the junction.

7.2   Solution of the linearized Usadel equation in terms of classical diffusion propagators

The most direct way to compute the Andreev current in a specific NS structure is to solve the linearized Usadel equation (7.17) for the layout of the structure, and then apply Eq. (7.8). This has been performed by Volkov [8] for a set of different layouts. Hereafter, we present an alternate approach to the resolution of the linearized Usadel equation. Instead of solving for the pairing parameter $r\,(x,E)$, we establish the link between $r\,(x,E)$ and the Fourier transform over time of the probability to diffuse from a tunnel barrier to position x in the normal metal. The pairing parameter $r\,(x,E)$, and consequently the current, are then expressed in terms of this classical diffusion probability. This time-domain approach, which is only a reformulation of the direct energy domain approach, provides physical insight into the weak proximity effect, and clearly demonstrates the role played by interference.

7.2.1   Solution of the linearized Usadel equation

The solution of Eq. (7.17) is straightforwardly obtained as

$$r\,(x,E) = \frac{g_T}{\sigma h} \int_{x_0 \in \text{barrier}} e^{-i\varphi_S(x_0)} g(x, x_0, E) dx_0,$$

where the Green function $g(x, x_0, E)$ obeys the equation

$$\frac{\hbar D}{2} \frac{\partial^2 g(x, x_0, E)}{\partial x^2} + \left(iE - \frac{\hbar}{\tau_{\text{sf}}} \right) g(x, x_0, E) = -\frac{\hbar D}{2} \delta\,(x - x_0) \qquad (7.18)$$

with the boundary conditions

$$\vec{\nabla} g.\vec{n} \;\;=\;\; 0 \text{ at the sample surface, and} \qquad (7.19)$$

$$g \;\;=\;\; 0 \text{ at a normal reservoir.}$$

7.2.2   Link to the classical diffusion probability

7.2.2.1   Equation for the diffusion probability

The probability $P\,(x_0, x, t)$ to find at position x and time t a diffusive particle, which was at position x_0 at time $t = 0$, obeys the equation

$$D\frac{\partial^2 P}{\partial x^2} - \frac{\partial P}{\partial t} = -\delta\,(x - x_0)\,\delta\,(t)\,. \qquad (7.20)$$

The Fourier transform $\tilde{P}(x_0, x, \omega)$ of this probability, defined as

$$\tilde{P}(x_0, x, \omega) = \int_{-\infty}^{\infty} e^{-i\omega t} P(x_0, x, t)\, dt \qquad (7.21)$$

where the probability $P(x_0, x, t)$ is non zero only for $t > 0$, obeys the equation

$$D\frac{\partial^2 \tilde{P}}{\partial x^2} - i\omega \tilde{P} = -\delta(x - x_0), \qquad (7.22)$$

with the same boundary conditions (7.19) as Eq. (7.18). The comparison between Eq. (7.22) and Eq. (7.18) shows that

$$r(x, E) = \frac{1}{n_0 e^2 h} \int_{x_0 \in \mathrm{barrier}} dx_0\, g_T(x_0)\, e^{-i\varphi_S(x_0)} \tilde{P}\left(x_0, x, -(\frac{2E}{\hbar} + \frac{i}{\tau_{\mathrm{sf}}/2})\right). \qquad (7.23)$$

This can be rewritten in the time domain as

$$
\begin{aligned}
r(x, E) &= \frac{1}{n_0 e^2 h} \int_0^{\infty} dt\, e^{2iEt/\hbar} e^{-2t/\tau_{\mathrm{sf}}} \int_{x_0 \in \mathrm{barrier}} dx_0\, g_T(x_0)\, e^{-i\varphi_S(x_0)} P(x_0, x, t) \\
&= \frac{1}{n_0 e^2 h} \int_0^{\infty} dt\, e^{2iEt/\hbar} e^{-2t/\tau_{\mathrm{sf}}} \sum_{\mathcal{B}_i} \int_{x' \in \mathcal{B}_i} dx'\, g_{Ti} e^{-i\varphi_{Si}} P(x', x, t),
\end{aligned} \qquad (7.24)
$$

thereby justifying our insertion of the spin-flip scattering time as an exponential cut-off time (see article reprinted in the next chapter).
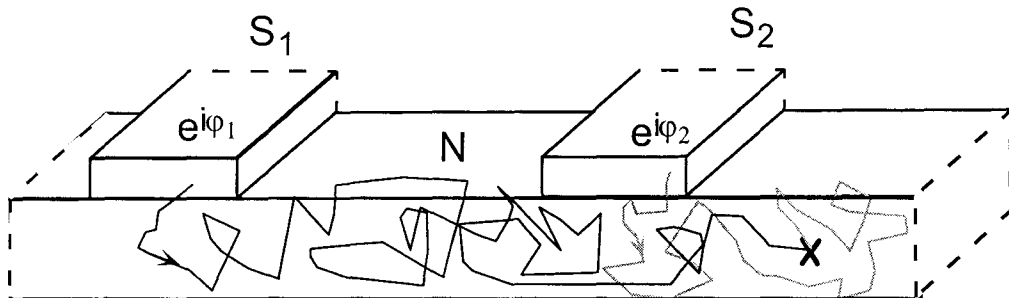
Fig. 7.2. Example of two quasi-classical trajectories originating at two different NS tunnel barriers, which contribute to the pairing parameter in the normal metal.

The significance of Eq. (7.24) is sketched in Fig. 7.2: the pairing parameter at a given point in the normal metal results from all the trajectories which have originated at an NS tunnel barrier $\mathcal{B}_i$ and which have reached that point. The contributions of trajectories emanating from the different tunnel barriers carry the phase of the superconductor across from that

barrier. The pairing parameter at each point in the normal metal results from the interference between these different sources.

In the next paragraph, it is seen that the Andreev current reveals the interferences which build the pairing parameter.

7.2.3   Current at an NIS tunnel junction

The Andreev current through a tunnel barrier $\mathcal{B}_j$, calculated with the pairing parameter determined to first order in tunnel conductances, is deduced from formulae (7.24) and (7.8). Expressed in terms of the diffusion probability, the Andreev current to second order in tunnel conductances is:

$$
\begin{aligned}
I_A\left(\mathcal{B}_j, V\right) \;=\;& \frac{g_{Tj}w}{n_0 e^3 h} \int_0^{+\infty} dE f_{0N}\left(E, V\right) \operatorname{Re} \int_0^\infty dt e^{2iEt/\hbar} e^{-2t/\tau_{sf}} \\
& \int_{x \in \mathcal{B}j} \sum_{\mathcal{B}_i} \int_{x' \in \mathcal{B}_i} dx' \, g_{Ti} P\left(x', x, t\right) \cos\left[\varphi_{Sj} - \varphi_{Si}\right] \\[2mm]
=\;& \frac{g_{Tj}w}{n_0 e^2 h} \operatorname{Re} \int_0^\infty dt e^{-2t/\tau_{sf}} \frac{\sin 2eVt/\hbar}{\frac{e}{\pi k_B T} \sinh \frac{2\pi k_B T t}{\hbar}} \\
& \int_{x \in \mathcal{B}j} \sum_{\mathcal{B}_i} \int_{x' \in \mathcal{B}_i} dx' \, g_{Ti} P\left(x', x, t\right) \cos\left[\varphi_{Sj} - \varphi_{Si}\right]. \quad (7.25)
\end{aligned}
$$

Whereas the pairing parameter at a given position of the normal metal was sensitive to the trajectories that originated in the junctions and ended at that point, the Andreev current is a function of only those trajectories which originate at a junction and end at a junction. This current through a given junction j is therefore decomposed in a first term due to the trajectories leaving that junction and returning to it, and as many additional terms as there are other junctions, due to the trajectories which go from these other junctions to junction j. These terms are proportional to the cosine of the phase difference between the superconducting phases at the two junctions, and to the tunnel conductances g_T of both junctions. They express the interference between different sources for the proximity effect.

7.3   Direct calculation of the Andreev current using second order perturbation

In this section we describe the Andreev reflection in terms of the tunneling of two electrons through an NS barrier. We show how disorder, by confining the electrons in the normal metal near the tunnel junction area, enhances constructive interference between the multiple tunnel attempts of a pair in multiple points of the barrier. The computation of the two electron tunneling rate with the second order perturbation theory leads, as in the derivations above, to a formulation of the Andreev current containing the classical diffusion probability.

7.3.1   Andreev reflection as a two quasiparticle tunnelling process

7.3.1.1   The process of Andreev reflection

The most intuitive way to picture the Andreev reflection process responsible for the conduction through an NS tunnel junction at voltages below the gap is to consider the tunneling of two electrons into the superconductor, which leave behind two hole-like quasiparticles, and add a pair to the superconducting condensate (see Fig. 7.3) [9] . In this process, the energy difference 2ε between the two quasiparticle states can vary between 0 and $2eV$, where V is the voltage across the junction.

This process can alternatively be seen as the reflection of a quasiparticle of energy $E_F - \varepsilon$ into a hole of energy $E_F + \varepsilon$, where E_F is the Fermi energy of the superconductor, taken as the reference energy. This is the common picture of Andreev reflection.

7.3.1.2   Role of disorder in Andreev reflection

The importance of disorder in Andreev reflection can be qualitatively understood if one considers the contribution to the current of nearly time-reversed quasiparticle states. Figure 7.4 is a quasi-classical representation of the trajectories of two such states i and j. Both trajectories encounter the barrier in the same points P_n, but with nearly opposite phases. The two-electron wavefunction at the barrier thus has a nearly constant phase, so that the contributions to the total tunnel amplitude A_{ij} add constructively, with an extra phase factor given by the superconducting phase φ_S. This suggests an amplitude of the form:

$$A_{ij} \propto \sum_{P_n} \Psi_i \Psi_j e^{i\varphi_S}$$
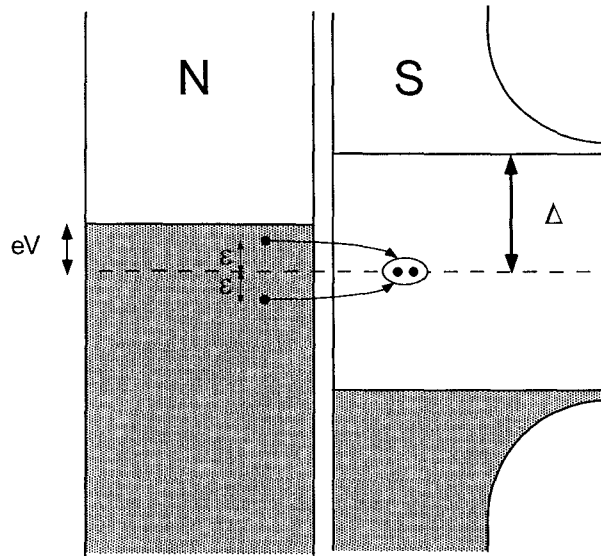
Fig. 7.3. Conduction process through an NS tunnel barrier at voltages V below the superconducting gap. Two electrons tunnel coherently from the normal side (N) into the superconductor (S), adding a pair to the condensate.
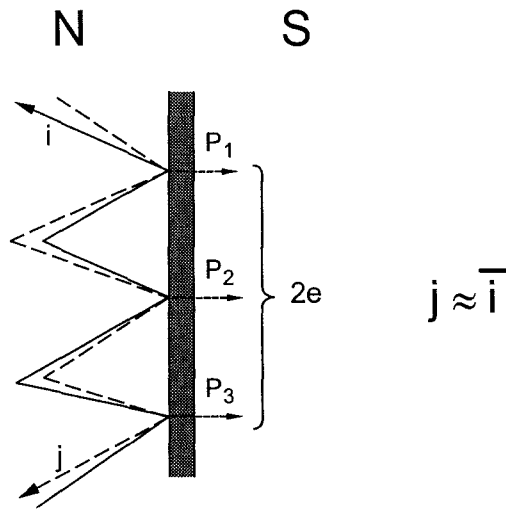

Fig. 7.4. Quasi-classical representation of the multiple tunnel attempts of two nearly time-conjugated electrons. The trajectories encounter the tunnel barrier at the same points P_n, with the same total phase. If the phase of the superconductor is uniform, the amplitudes at the different points contribute constructively to the total current.

In this picture, the scattering against impurities and the sample surface, by confining the quasiparticles near the barrier, enhances the constructive interference. Indeed, if all pairs of quasiparticles, instead of attempting to tunnel across the barrier once, are reflected onto it N times, the tunnel probability amplitude is N times larger, and the probability N^2 times larger. At the same time, there are N times less such states near the barrier than in the case without backscattering, since the metal density is not modified by weak disorder. In the end, the current (or conductance) is increased by a factor $N^2/N = N$. Such a constructive interference does not occur in the case of non time-reversed states.

Time-reversed states are also involved in the coherent backscattering responsible for the weak localization observed in mesoscopic samples. However, coherent backscattering only diminishes the conductance by a small fraction since the conductance is a single quasiparticle property. In contrast, the Andreev current is entirely due to time-reversed quasiparticle states.

7.3.1.3   Factors which limit constructive interference

The terms which limit the current in the previous formulation also appear in this qualitative description. In the case of quasiparticles with slightly different energies, constructive interference takes place over diffusion times smaller than $\hbar/2\varepsilon$, where 2ε is the energy difference. This energy difference is limited either by the voltage applied or by the temperature. In addition, constructive interference is destroyed by collisions with magnetic impurities, which destroy time-reversal symmetry. Therefore constructive interference can take place only if the diffusion time t between successive attempts is such that

$$t \ll \inf\left(\frac{\hbar}{eV}, \frac{\hbar}{k_B T}, \tau_{\mathrm{sf}}\right)$$

The effects of these limiting features are indeed observed in the experiments, as will be seen in the next chapter.

7.3.2   Calculation of the two quasiparticle tunneling rate

The qualitative picture given above is confirmed by the computation of the two quasiparticle tunneling rate, using second order perturbation theory in the tunneling Hamiltonian. In this section we give the outline of this computation, which has been performed by Hekking and Nazarov [6] .

7.3.2.1   Tunnel Hamiltonian

The rate at which two electron states with opposite spin are emptied from the normal electrode is given by the Fermi Golden rule

$$\Gamma = \frac{2\pi}{\hbar} \sum_f \sum_m \frac{\langle f \,|H_t|\, m\rangle \,\langle m \,|H_t|\, i\rangle}{E_m - E_f} \delta\left(E_f - E_i\right) \tag{7.26}$$

Here, i, f, and m designate the initial, final and intermediate state respectively. In the intermediate state, an electron is removed from the normal metal, and a quasiparticle is formed in the superconductor. The second electron couples to this quasiparticle to form a Cooper pair. The tunnel Hamiltonian H_t of formula (7.26) is [10]

$$H_t = \sum_{kp} t_{kp} c_p^\dagger c_k + h.c.,$$

where t_{kp} is the tunnel matrix element

$$t_{kp} = t \int_{r \in \text{barrier}} dr \Psi_k^*\left(r\right) \Psi_p^S\left(r\right). \tag{7.27}$$

In expression (7.27), the mode indices k and p refer to the wave functions in the normal and superconducting metals respectively, close to the tunnel barrier characterized by its transmission t. We have considered that the tunneling occurs only between points situated directly across the barrier from one another.

The rate as a function of voltage is then rewritten as

$$\Gamma\left(V\right) = \frac{2\pi}{\hbar} \sum_{k,k'} |A_{k\uparrow k'\downarrow}|^2 f\left(E_k\right) f\left(E_{k'}\right), \tag{7.28}$$

with the transfer amplitude given by

$$A_{k\uparrow k'\downarrow} = \sum_p t_{kp}^* t_{k'-p}^* u_p v_p e^{i\varphi_S} \left\{ \frac{1}{E_k - \epsilon_p} + \frac{1}{E_{k'} - \epsilon_p} \right\} \delta\left(E_k - E_{k'} + 2eV\right).$$

In these expressions, $E_{k,k'}$ are the energies of the normal quasiparticles, and ϵ_p is the energy of the superconducting quasiparticle created in the intermediate state. The amplitude of such a process is weighed by the BCS coherence factors u_p and v_p.

7.3.2.2 From the probability of transferring two quasiparticles to the classical diffusion probability for one particle

The main feature of the modulus squared of $A_{k\uparrow k'\downarrow}$ is that it contains the sum

$$\sum_{p,p'} t^*_{kp} t^*_{k'-p} t_{kp'} t_{k'-p'} \quad \propto \quad \sum_{p,p'} \int dr dr' dr'' dr''' [\Psi_k(r)\, \Psi_{k'}(r')\, \Psi^*_k(r'')\, \Psi^*_{k'}(r''')$$

$$\Psi^{S*}_p(r)\, \Psi^{S*}_{-p}(r')\, \Psi^S_{p'}(r'')\, \Psi^S_{-p'}(r''')]$$

In this product of eight quasiparticle wavefunctions, four are wavefunctions of quasiparticles in the superconductor, and four are wavefunctions of quasiparticles in the normal metal. Hekking and Nazarov have shown that the most important contribution to the tunnel rate comes from the constructive interferences occurring in the normal metal, represented by the diagram of Fig. 7.5. These interferences occur only for nearly conjugated trajectories, that is in the
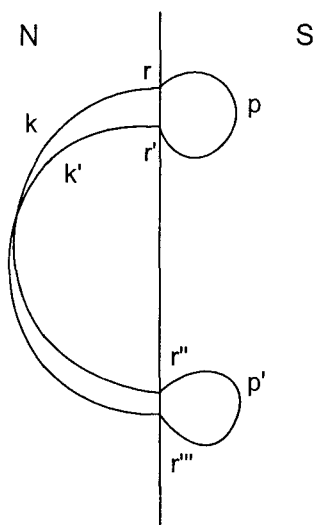
Fig. 7.5. Diagram representing the propagation of electrons of modes k and k'in the normal metal, and of superconducting excitations of modes p and p' in the superconductor. The electrons tunnel at positions $r \approx r'$ and $r'' \approx r'''$.

subsequent sum over modes k and k' only the terms with $r = r'$ and $r'' = r'''$ will give non negligible contributions. We therefore consider the average $\langle 4\Psi \rangle$ of the following integral over four wave functions:

$$\langle 4\Psi \rangle = \sum_{\substack{k,k' \\ E'_k - E_k = 2eV}} \int dr dr' \Psi_k(r)\, \Psi^*_k(r')\, \Psi_{k'}(r')\, \Psi^*_{k'}(r)$$

It has been shown [11, 12] that, in a diffusive conductor, this product is just the Fourier

transform of the classical diffusion probability $P(r, r', t)$:

$$\sum_{\substack{k,k' \\ E_{k'}-E_k=\hbar\omega}} \Psi_k(r)\,\Psi_k^*(r')\,\Psi_{k'}(r')\,\Psi_{k'}^*(r) \;=\; n_0\tilde{P}(r, r', \omega) \tag{7.29}$$

$$= \; n_0 \int dt\, e^{i\omega t} P(r, r', t)$$

7.3.2.3   Final expression for the subgap Andreev current

Given the previous identity, the final expression of Hekking and Nazarov for the current through a tunnel junction j can be recast in a form containing the one-dimensional probability of diffusing from one point of a tunnel barrier i to a point of a tunnel barrier j:

$$I(\mathcal{B}_j, V) \;=\; \frac{g_{Tj}w}{n_0 e^2 h} \int_0^{+\infty} dt\, e^{-2t/\tau_{\rm sf}} \frac{\sin 2eVt/\hbar}{\frac{e}{\pi k_B T}\sinh\frac{2\pi k_B Tt}{\hbar}} \tag{7.30}$$

$$\times \int_{x\in\mathcal{B}j} dx \sum_{\mathcal{B}_i} g_{Ti} \int_{x'\in\mathcal{B}_i} dx'\, e^{i\left[\varphi_{Si}-\varphi_{Sj}\right]} P(x', x, t),$$

where we have used $P(r, r', t) \equiv \frac{1}{wh} P(x', x, t)$. The symbols have the same signification as in Eq. (7.24).

Expression (7.30) confirms the qualitative description of the Andreev current being due to two nearly time-reversed quasiparticle states with energy difference inferior to the temperature or the voltage applied, whose multiple tunneling attempts contribute to the Andreev current as long as the pair remains phase-coherent. This expression is identical to the expression derived with the theory of the weak proximity effect (Eq. (7.25)).

7.4   The NS-QUID: modulation of the Andreev current

We calculate the amplitude of the current modulation in the NS-QUID.

7.4.1   Description of the NS-QUID

In order to confirm the picture of the Andreev mechanism described in the sections above, we have designed a device with the layout pictured in Fig. 7.6. In this device, the superconductor is shaped as an open loop, so that a magnetic field applied perpendicularly to the plane of the loop imposes a phase difference between the two extremities of the open loop. These extremities are oxidized and covered by a normal wire.   If the tunnel barriers between the
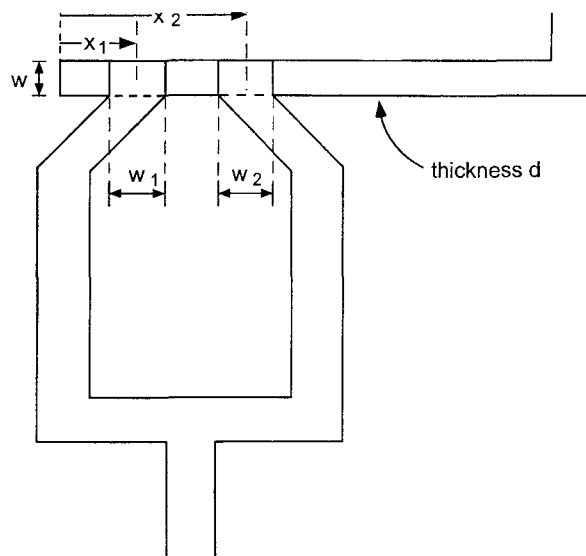
Fig. 7.6. Sketch of the NS-QUID

normal metal and the superconductor are thick enough, the supercurrent flowing in the loop is negligible, and the phase difference between the superconductors will be given by $2\pi\Phi/\Phi_0$, where $\Phi_0 = h/2e$ and Φ is the magnetic flux enclosed in the sample loop. The experiment consists in measuring the subgap current through this device (between the normal metal and the superconductor, as a function of the voltage applied, and of the magnetic field. The current is decomposed in two terms which contain the probability to return to a given tunnel barrier, and a third term which contains the probability to diffuse from one tunnel barrier to the other:

$$I\left(V\right) = I_{11}\left(t\right) + I_{22}\left(t\right) + 2I_{12}\left(t\right)\cos 2\pi\Phi/\Phi_0$$

This interference term is modulated by the magnetic field. We hereafter concentrate on this interference term.

7.4.2   Field-dependent contribution to the current

The total probability for going from junction 1 to junction 2 is straightforwardly calculated. In the case of junctions of equal width w and same tunnel conductance $G_T/2$, one has

$$P_{12}\left(t\right) = \int_{x\epsilon B_1} \int_{x'\epsilon B_2} dx dx' P\left(x, x', t\right) = \frac{8}{\pi d} \int_0^{+\infty} dk \frac{e^{-Dk^2 t}}{k^2} \sin^2 \frac{kw}{2} \cos kx_1 \cos kx_2 \quad (7.31)$$

The modulated current $I_{mod}\left(V\right) = 4I_{12}\left(V\right)$ deduced from formula (7.30) using the probability (7.31), at a given temperature, depends on the separation between the two junctions, and on the value of the spin-flip scattering time τ_{sf}. The formula is given in the paper which follows, in which "τ_{φ}" should be replaced by $\tau_{sf}/2$. We have plotted in Fig. 7.7 the modulated current as a function of voltage for different spacings between the two junctions, and for two different values of the spin-flip scattering time.

Figure 7.7 pictures the typical features of the modulated current-voltage curves. The current sharply increases at low voltage, with a zero-voltage slope given by $1/\sqrt{2}R\left(L_{sf}\right)G_T^2$. The modulated current decreases at high voltage, because of the dephasing introduced by the energy difference $2eV$. This decrease is stronger for distant junctions, and can even lead to a change of sign of the modulation. Finally, the modulation is greatest for closer junctions.

Volkov [8] has computed the expression of the modulated current in the NS-QUID geometry, directly from the resolution of the Usadel equation, without resorting to the time-dependent expression of the current as a function of the diffusion probability. Not surprisingly, both his expression and expression (7.30) with Eq. (7.31) yield the exact same voltage-dependence of the modulated current through NS-QUIDs with the same geometric characteristics, although the final expression of Volkov underestimates the modulated current by a factor of two.
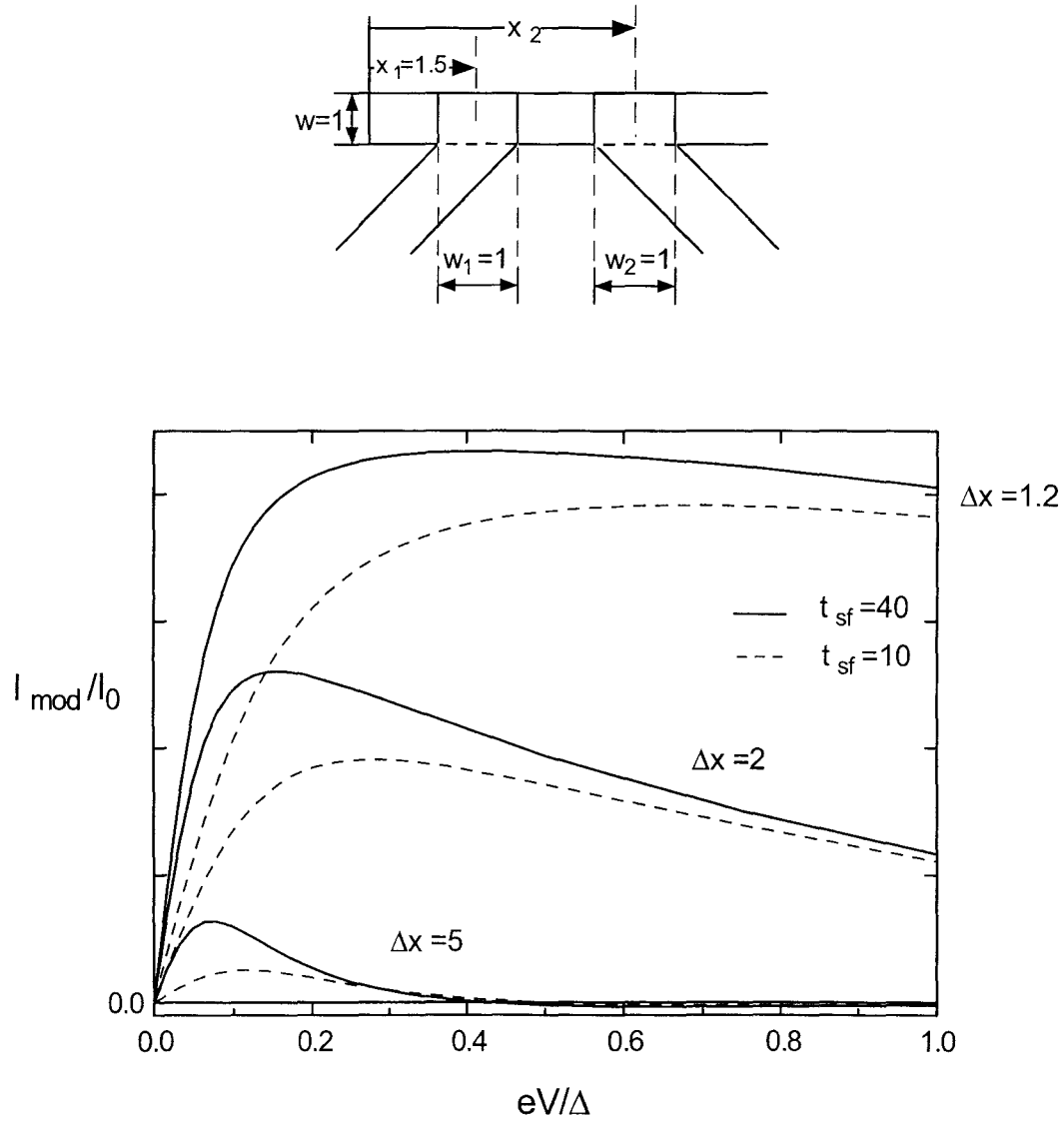
Fig. 7.7. Phase-dependent part I_{mod} of the Andreev current through a sample with two NS tunnel barriers, distant by $\Delta x/\sqrt{\hbar D/\Delta} = x_1 - x_2 = 1.2$, 2 and 5. The geometric characteristics of the layout are expressed in units of $\hbar D/\Delta$. The current has been computed for a spin-flip scattering time of respectively $\tau_{sf} = 40$ and 10 $\hbar/\Delta$.

7.5   Why spin-orbit scattering has no effect

The difference between spin-orbit scattering and spin-flip scattering can be seen by considering, as done by Price [13], the small spin rotations caused by these two types of scattering along a trajectory. In the case of spin-flip scattering, the rotation is independent of the velocity direction. In spin-orbit scattering, the angle by which a time-reversed electron turns is opposite to the angle by which the direct electron turned, because of the change of sign in velocity. The consequence of this is seen by computing the loss of coherence during the sequence pictured in Fig. 7.8.
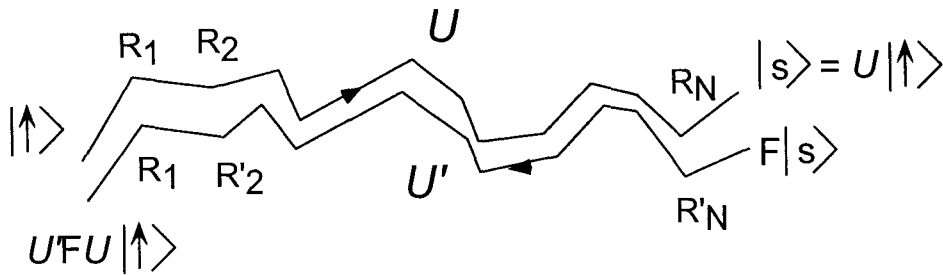
Fig. 7.8.

A sequence $U = R_1 R_2 .... R_N$ of small rotations transforms an initial spin-up state $|\uparrow\rangle$ into a final state $|s\rangle$, an operator F flips the spin of this state, which then follows the reverse trajectories in a reverse sequence of scattering events $U' = R'_N .... R'_2 R'_1$. The loss of coherence is given by the product $\langle\uparrow| FU'FU |\uparrow\rangle$. Following Price, we decompose each spin rotation operator in a product of spin-flip and spin-orbit rotations:

$$R_i = e^{-if_i\frac{\sigma}{2}} e^{-io_i\frac{\sigma}{2}}$$

$$R'_i = e^{-if_i\frac{\sigma}{2}} e^{+io_i\frac{\sigma}{2}}.$$

In addition, the different rotation events $i \neq j$ are uncorrelated, and the spin-flip and spin-orbit rotation operators f_i and o_i commute. This leads to the cancelling of the spin-orbit terms, and only the spin-flip contribution remains:

$$\langle\uparrow| FU'FU |\uparrow\rangle = \langle\downarrow| R'_N .... R'_2 R'_1 R_1 R_2 .... R_N |\downarrow\rangle = e^{-3/2Nf_i^2} = e^{-2t/\tau_{sf}}.$$

Therefore spin-orbit scattering should play no role in the loss of coherence of the time-conjugated trajectories responsible for the Andreev current.

7.6 Conclusion

To second order in tunnel conductances, we have shown that both the theory of the weak proximity effect and the perturbative calculation of the two electron tunneling rate yield the same expression for the Andreev current through an NS system, showing that proximity effect and Andreev reflections are two descriptions of the same phenomenon. In the perturbative regime, the Andreev current involves the probability to diffuse from a point of a tunnel barrier to another. In this description, the trajectories emanating from the tunnel barriers carry the phase of the superconducting electrode of that barrier, and therefore can interfere. The total current through a device containing several NS tunnel junctions is then expected to be modulated by the phase difference between the superconducting electrodes. In the quasi-classical picture, the importance of the modulation is determined not only by the tunnel conductances of the junctions, but also by the elastic scattering, geometrical confinement, and phase coherence time of the electrons in the normal electrode, for all these factors enhance the constructive interference responsible for the subgap current.

REFERENCES

[1] See for instance *Proceedings of the NATO Advanced Research Workshop on Mesoscopic Superconductivity*, F. W. J. Hekking, G. Schön, and D. V. Averin, eds. (Elsevier, Amsterdam, 1994).

[2] G. E. Blonder, M. Tinkham, and T. M. Klapwijk, Phys. Rev. B **25**, 4515 (1982).

[3] H. Pothier, S. Guéron, D. Esteve, M. H. Devoret, Phys. Rev. Lett. **73**, 2488 (1994), reprinted in the next chapter.

[4] B. J. van Wees, P. de Vries, P. Magnée, and T. M. Klapwijk, Phys. Rev. Lett. **69**, 510 (1992).

[5] I. K. Marmorkos and C. W. J. Beenakker, R. A. Jalabert, Phys. Rev. B **48**, 2811 (1993).

[6] F. W. J. Hekking and Yu. V. Nazarov, Phys. Rev. Lett. **71**, 1625 (1993); F. W. J. Hekking and Yu. V. Nazarov, Phys. Rev. B **49**, 6847 (1994).

[7] H. Pothier, S. Guéron, D. Esteve, M. H. Devoret, Physica B **203**, 226 (1994).

[8] A. F. Volkov, A. V. Zaitsev, Phys. Rev. B **53**, 9267 (1996).

[9] T. M. Eiles, J. M. Martinis and M. H. Devoret, Physica B **189**, 210, (1993).

[10] J. R. Schrieffer and J. W. Wilkins, Phys. Rev. Lett. **10**, 14 (1963).

[11] W. L. McMillan, Phys. Rev. B **24**, 2739 (1981).

[12] G. Montambaux, in *Quantum Fluctuations*, S. Reynaud, E. Giacobino and J. Zinn-Justin, eds. (Elsevier, Amsterdam, 1997), p. 387.

[13] John C. Price, Phys. Rev. B **44**, 8997 (1991).

Chapter 8
Experimental investigation of NS-QUIDs

We have seen in the previous chapter that the conductance of an NS-QUID is predicted to be modulated by the phase difference between the two superconducting electrodes. In this chapter, we first present the experiment which has demonstrated this modulation. Both the measured total current and modulated current through the device are compared to the theoretical predictions. This comparison depends on the one hand on measured parameters, such as the tunnel conductance and sample dimensions, and on the other hand on two sample-dependent fit parameters which are the elastic mean free path l_e and the spin-flip scattering time τ_{sf}. In order to perform a more stringent test of the theory, we have fabricated in a single process three NS-QUIDs which therefore have the same parameters τ_{sf} and l_e, but which differ by the distance between the two NS tunnel junctions. We present in the second part of the chapter experimental results on two such samples.

8.1   First experimental demonstration of the current modulation in an NS-QUID (article)

We reprint the article originally published as:

H. Pothier, S. Guéron, D. Esteve, and M. H. Devoret, *Flux-Modulated Andreev Current caused by Electronic Interferences*, Phys. Rev. Lett **73**, 2488 (1994).

See also H. Pothier, S. Guéron, D. Esteve, M. H. Devoret, *Influence of electronic interferences on the Andreev conductance*, Physica B 3604, 226-232 (1994), in which the derivation of the modulated current is given in greater detail.

Note: The scaling factor which must be applied to the theory in order to recover the measured modulated current is actually 1.8, and not 4.7 as wrongly reported in the article.

Also, the spin-flip scattering time used in the article as the exponential cut-off is half the one which we have used in the theoretical description of the proximity effect. To avoid any confusion, in this chapter we will call τ_0 the exponential cut-off used as a fit parameter to reproduce the experimental curves. This time is related to the spin-flip scattering time τ_{sf} of the theories presented in the previous chapters through $\tau_0 = \tau_{\mathrm{sf}}/2$.

Flux-Modulated Andreev Current Caused by Electronic Interference

H. Pothier, S. Guéron, D. Esteve, and M. H. Devoret

Service de Physique de l'Etat Condensé, Commissariat á l'Energie Atomique, Saclay, F-91191 Gif-sur-Yvette, France

We have performed an interference experiment with two tunnel junctions between a thin normal metal wire and a superconducting fork. We have found that the subgap current is strongly modulated by the flux through the resulting normal-superconducting loop. Our results agree with the recent prediction that multiple tunnel attempts of electron pairs, which occur when electrons are confined near the junction, can add coherently if the pair consists of nearly time-reversed states.

Electron tunneling between two normal metal electrodes through an insulating barrier is a basic quantum mechanical phenomenon displaying the wavelike nature of electrons [1]. Interestingly, however, the wave properties of electrons usually manifest themselves in a minimal way: the conductance of such a so-called NN tunnel junction depends only on the area of the barrier, on its transparency, and on the electron densities of both electrodes, as if electrons were classical particles having a certain probability of traversing the barrier each time they collide against it. In particular, the conductance does not depend on the partial confinement of electron wave functions near the barrier [2]. For example, an electron attempting tunneling n times by zigzagging between impurities in the metal and the tunnel barrier contributes exactly to the conductance, on the average, like n electrons colliding against the barrier only once. This insensitivity to confinement occurs because the successive tunnel amplitudes in this iterative tunneling do not interfere constructively. On the contrary, constructive interferences in the case of two-electron tunneling at a normal metal-superconductor tunnel junction (NS junction) are robust to phase randomization induced by disorder. Confinement can thus enhance the two-electron conductance, also known as the Andreev conductance [3,4], by a large factor [5]. Consider two nearly conjugated wave functions on the N side corresponding to nearly time-reversed scattering electron trajectories (Fig. 1). The phase of the two-electron tunnel amplitude at each collision point is the algebraic sum of the phases of the two electrons and of the phase of the superconductor on the other side of the barrier. Therefore, the successive tunneling attempts will add constructively if the phase of the superconductor is constant. If, on the other hand, the iterative tunneling involves two different parts of the barrier with superconducting phases differing by π, destructive interferences will occur [6–8]. We report in this Letter measurements of the two-electron tunnel current as a function of the phase difference imposed between the two halves of a split barrier [7].

We have fabricated "NS-QUIDs" (normal metal-superconductor quantum interference devices) consisting of a normal wire forming two neighboring junctions with

a superconducting fork electrode (see Fig. 2), a design close to one recently proposed by Hekking and Nazarov [8]. The normal wire was made as narrow as possible in order to confine the electrons near the junctions. The difference δ between the superconducting phases at the two junctions is controlled by applying a magnetic field perpendicular to the plane of the fork: $\delta = 2\pi\Phi/\Phi_0$, where Φ is the magnetic flux threading the loop formed by the fork and the wire and $\Phi_0 = h/2e$.

Our samples were fabricated using electron beam lithography and shadow-mask evaporation [9]. A 20 nm thick aluminum film was deposited using electron beam evaporation, then oxidized in a 0.15 Torr O_2 (10%) Ar (90%) mixture for 3 minutes. The 30 nm thick copper counterelectrode was then deposited. The samples were mounted in a copper box which was thermally anchored to the mixing chamber of a dilution refrigerator. Current-voltage (I-V) measurements were performed using properly filtered coaxial lines [10]. We concentrate here on the results obtained on the sample whose I-V characteristic was most strongly flux-dependent. From the large scale normal state I-V characteristic (dashed line in the top-left inset of Fig. 3), measured by applying a field of 0.1 T perpendicular to the films, we obtain $G_T = 641$ μS. The large
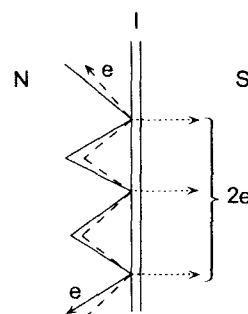

FIG. 1. Semiclassical representation of the mechanism responsible for constructive interferences in iterative tunneling of electron pairs. Two confined electrons in the normal electrode, with nearly time-reversed wave functions, tunnel together through the barrier at different points with the same total phase. If the order parameter of the superconductor is uniform, the tunnel amplitudes at these different points contribute constructively to the total current.
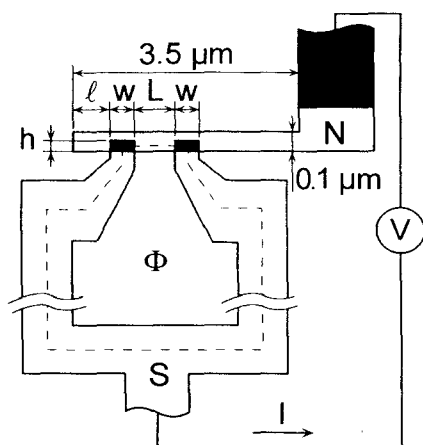
FIG. 2. NS-QUID layout: a normal metal wire overlaps an oxidized superconducting fork electrode to form a split tunnel junction. The effective area of the loop (enclosed by the dotted line) is 13 μm^2. The superconducting bottom electrode (aluminum) and the normal top electrode (copper) were 20 and 30 nm thick, respectively. Regions where the normal electrode overlaps the superconducting electrode are dark. The parameters of the sample whose data are shown in Figs. 3 and 4 were $w = 230$ nm, $h = l = 100$ nm, and $L = 60$ nm. For clarity, we have not represented the normal metal replica of the loop shifted down by 260 nm.

scale I-V characteristic at zero field is shown in the same inset as a solid line. As the temperature is decreased below 300 mK, the subgap current becomes strongly field modulated, as shown in the bottom right inset of Fig. 3 for $V = 20$ μV and $T = 27$ mK. The magnetic field dependence of the current follows a sine function (solid line). Assuming a Φ_0-periodicity for the modulation as a func-
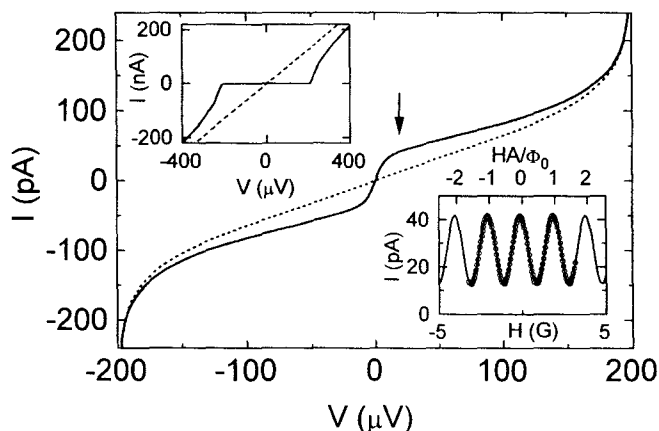
FIG. 3. Extremal subgap I-V characteristic measured at $T = 27$ mK. The solid and the dotted lines correspond to maxima ($\Phi = k\Phi_0$) and minima [$\Phi = (k + 1/2)\Phi_0$] of the modulation of the current with the magnetic field H shown in the bottom-right inset, respectively. The arrow indicates the bias voltage at which the modulation pattern was measured (circles: data; solid line: sine function fit). The top-left inset represents the large scale characteristics of the NS-QUID at $H = 0$ (solid line) and $H = 0.1$ T (dashed line).

tion of the flux threading the loop, we deduce an effective field capturing area A of the loop which agrees within 20% with the area defined in Fig. 2. Note that the positions of the maxima with respect to the external field H do not correspond exactly with integer multiples of Φ_0, an offset which we attribute to the residual field in the cryostat. We show in the main plot of Fig. 3 the two extremal I-V characteristics (solid and dashed lines). At $\Phi = k\Phi_0$, the conductance exhibits a peak at zero voltage, as observed in several experiments [11–13]. The maximal ($\Phi = k\Phi_0$) and minimal [$\Phi = (k + 1/2)\Phi_0$] conductances at $V = 0$ are $G_{max} = 4.6$ μS and $G_{min} = 0.66$ μS, which are much larger than the ballistic value [14] $G_{bal} = (h/4e^2)G_T^2/N_{eff} \approx 25$ nS, where $N_{eff} = S/4\pi\lambda^2$ is the effective number of channels calculated with the upper bound estimate $\lambda = 0.2$ nm for the barrier wavelength cutoff [15]. Such a large discrepancy with the ballistic model was already pointed out in Refs. [16] and [17]. The flux dependence of the conductance indicates that this discrepancy originates from phase-coherent processes in the normal electrode and not, for example, from leaks in the tunnel barrier.

Figure 4 shows the variations of the peak-to-peak amplitude I_{mod} of the current modulation, such as the one shown in the bottom-right inset of Fig. 3, as a function of the bias voltage V, at temperatures ranging from 27 to 233 mK. TThe data show that the zero-voltage conductance decreases with temperature, whereas, up to
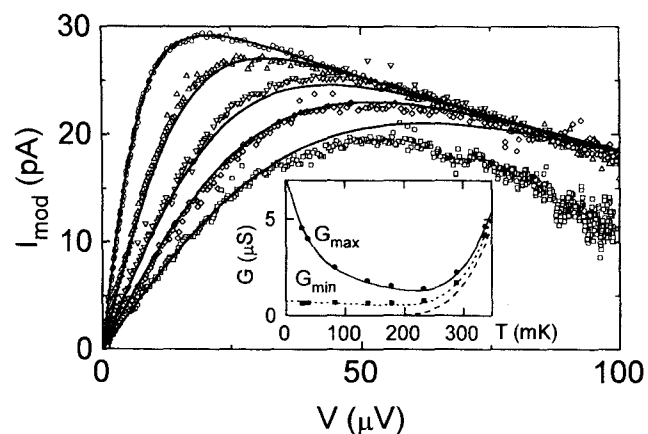

FIG. 4. Comparison between the measured (open symbols) and predicted (solid lines) bias voltage dependence of the peak to peak modulation I_{mod} of the current with the magnetic field at different temperatures (top to bottom: $T = 27$, 82, 137, 177, and 233 mK). The experimental data were obtained by numerical substraction of the extremal I-Vs; predicted curves are calculated using formulas (4) and (6), with $D = 59 \times 10^{-4}$ m^{2}s^{-1} and $\tau_\Phi = 120$ ps. We used $\Delta = 205$ μeV for the gap in aluminum and $\nu = 1.5 \times 10^{47}$ J^{-1}m^{-3} for the density of states of copper. Inset: comparison between the measured (symbols) and predicted (lines) temperature dependences of the maximal and minimal zero-voltage conductances G_{max} and G_{min}. The dashed line shows the quasiparticle conductance contribution G_{qp} to G.

180 mK, the current becomes temperature independent at voltages of the order of 0.1 mV. In the following, we show that the precise voltage and temperature dependence of I_{mod} is qualitatively understood.

The influence of disorder in the normal electrode on the conductance of NS junctions has been treated by several authors [5,14,18]. More recently, Hekking and Nazarov have established the link between the Andreev current and the dynamics of the electrons in the normal electrode and derived an expression for the I-V characteristic at $eV \ll \Delta - k_B T$, where Δ is the gap of the superconductor [8,15]. We find that their expression (4) in Ref. [8] can be recast in the form [19]

$$ I = \frac{1}{\nu e^2} \int_0^\infty dt\, K(t) e^{-t/\tau_\Phi} \frac{\pi k_B T \sin(2eVt/\hbar)}{e \sinh(2\pi k_B Tt/\hbar)} \quad (1) $$

with the kernel $K(t)$ given by

$$ K(t) = \int\int_{(\text{barrier})^2} d^2r\, d^2r'\, g(r)g(r') e^{i[\varphi(r)-\varphi(r')]} p(r,r',t), \quad (2) $$

where $p(r,r',t)\,d^3r'$ coincides for $t \gg \hbar/E_F$ with the conditional probability density that an electron in the normal metal prepared at time $t = 0$ at point r on the barrier is found at time t in a volume d^3r' around point r'. The symbol $g(r)$ denotes the conductance per unit area of the tunnel barrier at point r. The phase $\varphi(r)$ of the superconductor is taken at the point across the barrier from point r. The parameters τ_Φ and ν denote the phase-breaking time and the density of states per unit volume at the Fermi energy, including both spin directions, respectively. The phenomenological factor e^{-t/τ_Φ} was added to the original expression of Hekking and Nazarov in order to account for the loss of coherence due to phase-breaking processes. For an NS-QUID, the phase difference $\varphi(r) - \varphi(r')$ vanishes if r and r' are on the same junction and takes the value $\pm 2\pi\Phi/\Phi_0$ otherwise (for the low fields considered here, the phase along each junction can be taken constant). Therefore,

$$ K(t) = K_{11}(t) + K_{22}(t) + 2K_{12}(t)\cos(2\pi\Phi/\Phi_0), \quad (3) $$

where $K_{ij}(t)$ characterizes electrons going from junction i to junction j. Expression (1) thus predicts a sine-modulated component for the NS-QUID current, which we observe in our experiment (see bottom right inset of Fig. 3). We have focused here on the amplitude I_{mod} of the current modulation rather than its absolute value since the cross-kernel $K_{12}(t)$ is more amenable to quantitative calculations than $K_{11}(t)$ and $K_{22}(t)$ [$K_{12}(t)$ is nonzero only for times greater than the electron transit time from one junction to the other]. We have calculated $K_{12}(t)$ assum-

ing that $p(r,r',t)$ obeys a diffusion equation with diffusion constant D inside a flat slab-shaped normal electrode, taking into account the bending of the normal wire over the superconductor through an effective junction width $w_{eff} = w + 2d$. By inserting the result into (1), we find

$$ I_{mod} = \frac{4(h/e^2)G_T^2}{\pi^2 dSe\nu} \int_0^\infty du\, f(u)h(u), \quad (4) $$

where

$$ f(u) = \left[\frac{\sin(u/2)}{u}\right]^2 \cos\left(\frac{x_1 u}{w_{eff}}\right) \cos\left(\frac{x_2 u}{w_{eff}}\right) $$

and

$$ h(u) = \text{Im}\Psi\left\{\frac{1}{2} + \frac{T_0}{T}\left[1 + \eta\left(u^2 + i\frac{V}{V_0}\right)\right]\right\}, $$

with $x_1 = l + w_{eff}/2$, $x_2 = l + L + 3w_{eff}/2$, $T_0 = \hbar/4\pi k_B\tau_\Phi$, $V_0 = \hbar D/2ew_{eff}^2$, and $\eta = D\tau_\Phi/w_{eff}^2$. At zero temperature, it is possible to improve (1) by taking into account the finite eV/Δ ratio, and one obtains

$$ I = \frac{1}{\nu e^2} \int_0^\infty dt\, K(t) e^{-t/\tau_\Phi} \int_0^V dv\, \frac{\cos(2evt/\hbar)}{1 - (ev/\Delta)^2}, \quad (5) $$

which differs from (1) only near the gap. We can apply this equation to get $I_{mod}(\Delta, T = 0)$ and evaluate $I_{mod}(\Delta, T)$, at temperature such that $k_B T \ll \Delta$, from

$$ I_{mod}(\Delta, T) \approx I_{mod}(\Delta = \infty, T) \frac{I_{mod}(\Delta, T = 0)}{I_{mod}(\Delta = \infty, T = 0)}, \quad (6) $$

which gives a 5% correction to expression (4) at $V = 0.1$ mV. In Fig. 4, we compare the predictions of formula (4) corrected by (6) (solid lines) with the data, using $\nu = 1.5 \times 10^{47}\,\text{J}^{-1}\text{m}^{-3}$. The fit parameters are $D = (60 \pm 5)10^{-4}\,\text{m}^2\text{s}^{-1}$ and $\tau_\Phi = 120 \pm 10$ ps, which are compatible with previous measurements [20]. However, we had to scale the calculated I_{mod} up by a factor 4.7, which is not understood at present. Allowing for this adjustment, we find a quantitative agreement between experiment and theory at temperatures between 27 mK (top curve) and 180 mK (fourth curve from the top). Only at 230 mK is the modulation smaller than predicted for voltages above 50 μV. This is possibly due to the failure of the approximation (6) at high temperatures.

An expression similar to (4) gives the nonmodulated contribution to the current, which corresponds to the functions $K_{11}(t)$ and $K_{22}(t)$. Scaled with the same factor 4.7, the amplitude of the nonmodulated current fits the measurements at low voltages (comparison not shown), but underestimates the current at voltages above 20 μV. We estimate that the expected extra contribution to the current arising from phase-coherent diffusion of quasipar-

ticles in the superconducting electrode [15,21] is, however, too small to resolve the discrepancy, and we rather believe that the diffusion model itself does not adequately describe the spread-out of electrons at short times. In the inset of Fig. 4, we compare the temperature dependence of the maximal ($\Phi = k\Phi_0$) and minimal [$\Phi = (k + 1/2)\Phi_0$] zero-voltage conductances G_{max} and G_{min} with theory, also scaled up by the factor 4.7. Above 200 mK, the contribution G_{qp} of thermally activated quasiparticle tunneling to the conductance (dashed line) is no longer negligible, and we have added it to the Andreev conductance. The calculated conductances agree with experimental data over the whole temperature range.

We have performed the same analysis on two other samples. The values of the fit parameters were $D = 53 \times 10^{-4}$ m^2 s^{-1} and $\tau_\Phi = 25$ ps for the first one and $D = 133 \times 10^{-4}$ m^2 s^{-1} and $\tau_\Phi = 16$ ps for the second one. This dispersion might be explained by the fact that the samples were evaporated separately and had different impurity contents. The scaling factors were 2.5 and 3.0, respectively. For these samples, the amplitude of the nonmodulated current was underestimated by theory already near zero voltage.

An alternative interpretation of the data would be to consider that a small superconducting gap develops in the normal metal side of the junctions, because of the proximity effect, and that our NS-QUID can be considered as a SQUID with one superconductor having a small superconducting gap. The current in such a SQUID is indeed expected to have the same flux dependence as in our experiments. However, even with unrealistic parameters, the best fit obtained using the relevant theory [22,23] is very poor.

In conclusion, we have observed that the Andreev conductance of NS-QUIDs in which the normal electrode confines the electrons near the junctions is much larger than predicted by the ballistic model and is strongly modulated by the flux. The model of constructive interferences in iterative Andreev tunneling provides a quantitative explanation of the voltage and temperatures dependence of the flux-modulated current.

We have benefited from many discussions with F. Hekking and Yu. Nazarov. We are grateful to T. M. Klapwijk for useful comments on our results and to G.-L. Ingold for help in the preparation of the manuscript.

---

[1] L. Solymar, *Superconductive Tunnelling and Applications* (Chapman and Hall, London, 1972), Chap. 1.

[2] Fluctuations of the differential conductance as a function of the bias voltage could, however, be influenced by confinement: see Yu. Nazarov, Zh. Eksp. Teor. Fiz. **98**, 306 (1990) [Sov. Phys. JETP **71**, 171 (1990)].

[3] A. F. Andreev, Zh. Eksp. Teor. Fiz. **46**, 1823 (1964) [Sov. Phys. JETP **19**, 1228 (1964)].

[4] G. E. Blonder, M. Tinkham, and T. M. Klapwijk, Phys. Rev. B **25**, 4515 (1982).

[5] B. J. van Wees, P. de Vries, P. Magnée, and T. M. Klapwijk, Phys. Rev. Lett. **69**, 510 (1992).

[6] Different effects involving the phase difference between two superconductors have already been considered in B. Z. Spivak and D. E. Khmel'nitskii, Pis'ma Zh. Eksp. Teor. Fiz. **35**, 334 (1982) [JETP Lett. **35**, 412 (1982)] and in B. L. Al'tshuler and B. L. Spivak, Zh. Eksp. Teor. Fiz. **92**, 609 (1987) [Sov. Phys. JETP **65**, 343 (1987)].

[7] H. Nakano and H. Takayanagi, Solid State Commun. **80**, 997 (1991).

[8] F. W. Hekking and Yu. Nazarov, Phys. Rev. Lett. **71**, 1625 (1993).

[9] G. J. Dolan and J. H. Dunsmuir, Physica (Amsterdam) **152B**, 7 (1988).

[10] J. M. Martinis, M. H. Devoret, and J. Clarke, Phys. Rev. B **35**, 4682 (1987).

[11] A. Kastalsky, L. H. Greene, J. B. Barner, and R. Bhat, Phys. Rev. Lett. **64**, 958 (1990); A. W. Kleinsasser, T. N. Jackson, D. McInturff, F. Rammo, G. D. Petit, and J. M. Woodall, Appl. Phys. Lett. **57**, 1811 (1990); A. Kastalsky, A. W. Kleinsasser, L. H. Greene, R. Bhat, F. P. Milliken, and J. P. Harbison, Phys. Rev. Lett. **67**, 3026 (1991).

[12] C. Nguyen, H. Kroemer, and E. L. Hu, Phys. Rev. Lett. **69**, 2847 (1992).

[13] P. Xiong, G. Xiao, and R. B. Laibowitz, Phys. Rev. Lett. **71**, 1907 (1993).

[14] C. W. J. Beenakker, Phys. Rev. B **46**, 12 841 (1992).

[15] F. W. Hekking and Yu. Nazarov, Phys. Rev. B **49**, 6847 (1994).

[16] T. M. Eiles, J. M. Martinis, and M. H. Devoret, Phys. Rev. Lett. **70**, 1862 (1993).

[17] J. M. Hergenrother, M. T. Tuominen, and M. Tinkham, Phys. Rev. Lett. **72**, 1742 (1994).

[18] A. F. Volkov, A. V. Zaitsev, and T. M. Klapwijk, Physica (Amsterdam) **210C**, 21 (1993).

[19] We have corrected a factor $1/4\pi^2$ missing in Ref. [8] [Yu. Nazarov (private communication)].

[20] B. Pannetier, J. Chaussy, and R. Rammal, Physica Scripta **T13**, 245 (1986).

[21] D. V. Averin and Yu. Nazarov, Phys. Rev. Lett. **69**, 1993 (1992).

[22] A. Barone and G. Paternò, *Physics and Applications of the Josephson Effect* (Wiley-Interscience, New York, 1982).

[23] G.-L. Ingold, H. Grabert, and U. Eberhardt, Phys. Rev. B **50**, 395 (1994).

8.2   Three NS-QUIDs fabricated simultaneously

In the article reprinted above, it is shown that the measured modulated current agrees with the theoretical predictions, provided that an overall scaling factor of the order of 2 (instead of the factor 4.7 originally published) is included, and that the elastic mean free path l_e in the normal metal and the spin-flip scattering time τ_0 are adequately adjusted.

We have therefore fabricated samples consisting of three NS-QUIDs which differ only by the distance between the two NS tunnel junctions. Since the material-dependent constants are therefore expected to be identical, the measured curves for all three devices should be described with the same parameters l_e and τ_0. We hereafter present experiments on two such samples.

8.2.1   Characteristics of the measured samples

A SEM micrograph of a typical sample is shown in Fig. 8.1. Like the one presented in
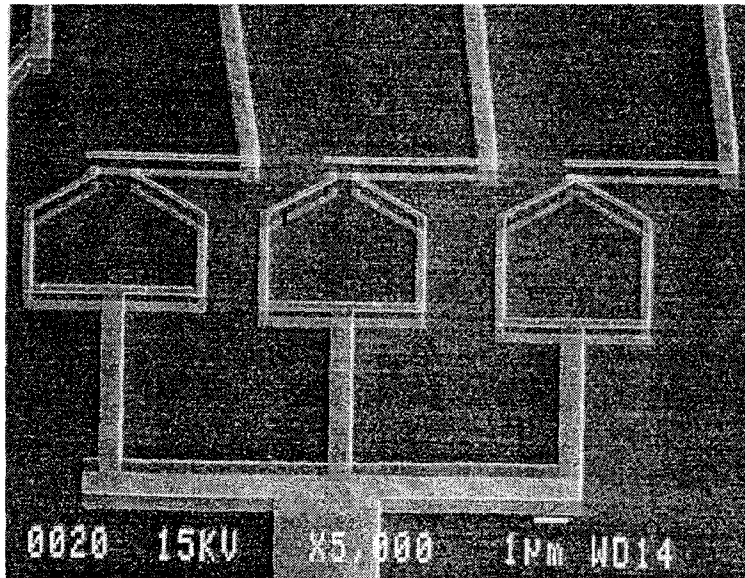
Fig. 8.1.

the previous section, each NS-QUID is made of a 20 nm-thick aluminum loop deposited at an angle, oxidized and covered with a 30 nm-thick copper wire deposited with an opposite angle. The areas of the three superconducting loops are identical. And indeed the current through all three devices was modulated with the same periodicity in magnetic field. The characteristics of the samples 1 and 2 are given in the table below, along with the parameters of the sample

presented in the article. The significance of the symbols is indicated on Fig. 8.2. The bending
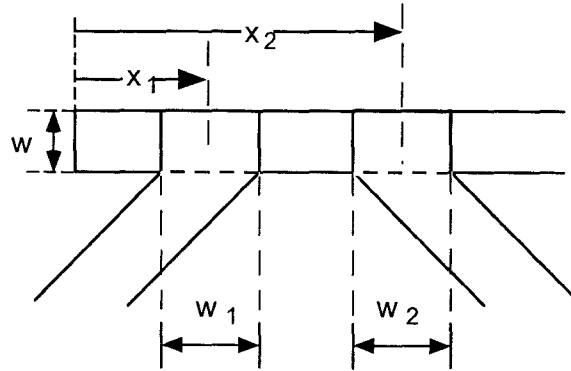
Fig. 8.2.

of the normal wire over the superconductor is accounted for by including the thickness of the film, yielding the effective values given in the table.

	sample article	sample 1a	sample 1b	sample 1c	sample 2a	sample 2b	sample 2c
$r_{leads} + R_T$	1.6 kΩ	1.8 kΩ	1.6 kΩ	1.7 kΩ	910 Ω	870 Ω	870 Ω
x_{1eff}	235 nm	250 nm	265 nm	270 nm	240 nm	265 nm	265 nm
x_{2eff}	565 nm	650 nm	770 nm	1050 nm	650 nm	885 nm	1050 nm
w_{1eff}	270 nm	320 nm	305 nm	290 nm	325 nm	350 nm	330 nm
w_{2eff}	270 nm	280 nm	300 nm	295 nm	335 nm	380 nm	325 nm
Δx_{eff}	330 nm	400 nm	505 nm	780 nm	410 nm	620 nm	785 nm
w	100 nm	205 nm			135 nm	160 nm	180 nm
l_e (fit)	11 nm	12 nm			12 nm		
τ_0 (fit)	120 ps	19 ps			55 ps		
scaling factor	1.8	2.4	2.7	2.7	1.9	2.1	2.4

From the table it is seen that the two samples mainly differ by their tunnel resistances, intentionally decreased in sample 2 in order to enhance the Andreev conductance.

An atomic force microscope picture of the junction region of the three NS-QUIDs of sample 2 is given in the figure on the next page.
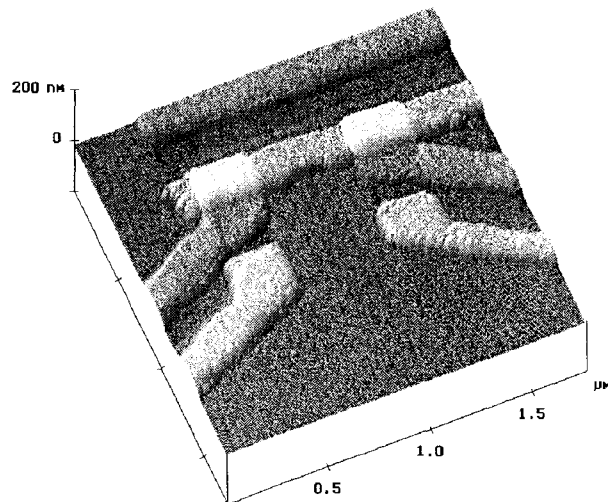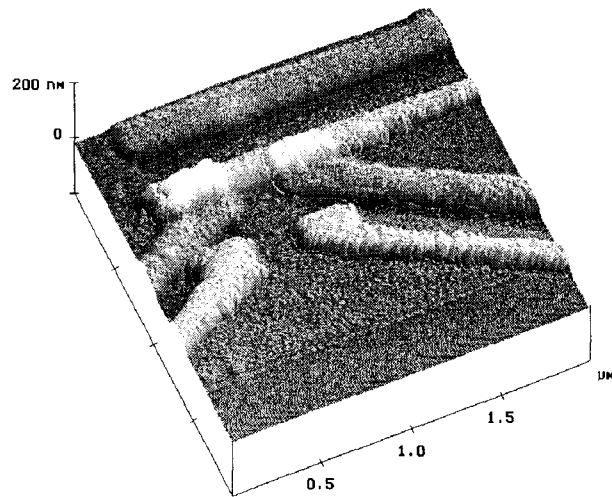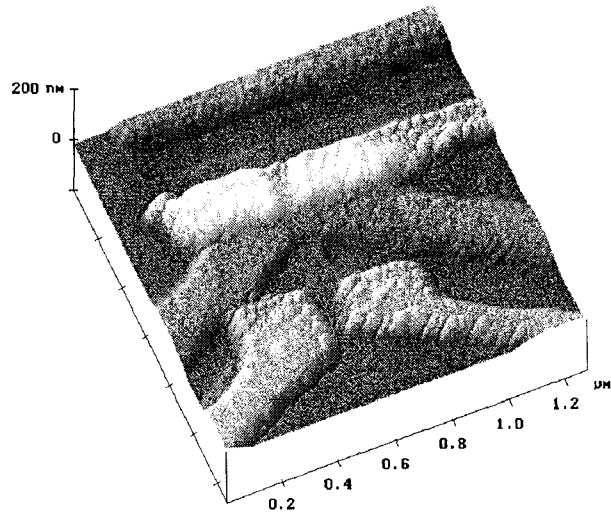
AFM micrographs of the junction regions of the three NS-QUIDs of Sample 2

8.2.2   Measured modulated current in the two samples and comparison with theory

The comparison between the measured and predicted modulated current is shown in Fig. 8.3 for the NS-QUIDs of samples 1 (top) and 2 (bottom). Each curve is labeled by the separation Δx_{eff} between the middle positions of the two junctions. As expected, in both samples the modulated subgap current is greatest for the NS-QUID with the closest junctions: during the dephasing time τ_0, a pair of electrons diffusing in the normal wire hits the barriers a greater number of times if the junctions are closer together. In the insets of the figure, the maximum (0 flux in the loop) and minimum (one half flux quantum Φ_0) subgap current of the three NS-QUIDs are plotted as a function of voltage, with a vertical offset for clarity. The I-V curves of sample 1 exhibit features at given subgap voltages. We attribute them to multiple particle tunneling processes [2] , which can be non negligible if a few channels are well transmitted because of inhomogeneities in the barrier.

The theoretical curves plotted as continuous lines have been computed with the geometrical parameters given in the table above. When fitting each experimental curve separately, we found that several combinations of the elastic mean free path l_e and the spin-flip scattering time τ_0 can reproduce the data quite satisfactorily. However, only one set of parameters succeeds in accounting for the three curves of a given sample. For both samples, we find an elastic mean free path $l_e = 12$ nm. This value is consistent with the empirical rule that the elastic mean free paths in thin evaporated films is of the order of half the film thickness [1] . The spin-flip scattering time τ_0 was found to be 19 ps in sample 1 and 55 ps in sample 2. These two values can be compared to the spin-flip time $\tau_0 = 120$ ps found in the experiment described in the article. The difference in spin-flip times and therefore in magnetic impurity concentration can be explained by various factors, ranging from the sequence of metals evaporated in the evaporation chambers, the composition of the crucible containing the copper (purity 99.999%), to the time of exposure to air of the sample after deposition and before mounting on the refrigerator (copper oxide is magnetic). It is not yet clear how this spin-flip scattering time could be controllably monitored. The agreement between the experimental curves and the theoretical curves is quite good, at least for voltages up to roughly two thirds of the gap. This proves that the geometrical parameters are correctly taken into account by the theory. The discrepancy at high voltage is due to the fact that the theory was computed in the low energy

limit. As in the first experiment, we find that the theoretical curves must be multiplied by a global factor of the order of two in order to match the measured ones. The origin of this factor is presently not understood. Finally, the total current through the NS-QUIDs of sample 2 is roughly five times greater than the current through the NS-QUIDs of sample 1, as expected from the greater conductance of the junctions of sample 2.

8.2.3 Non-modulated current

As in the first experiment, we find a non modulated current greater than the one obtained according to Eq. (7.30), by integrating the probability to return to the same tunnel barrier. This discrepancy might be resolved by taking into account the modification induced in the superconductor by the presence of the normal metal. As was mentioned in the previous chapter, the fact that the pairing angle in the superconductor is not the BCS pairing angle (see Eq. 7.1a) translates into a non negligeable quasiparticle current, even at zero temperature. In terms of the second order perturbation treatment of the subgap current of Hekking and Nazarov [3] , this excess current is viewed as resulting from interference between quasiparticles diffusing in the superconductor.
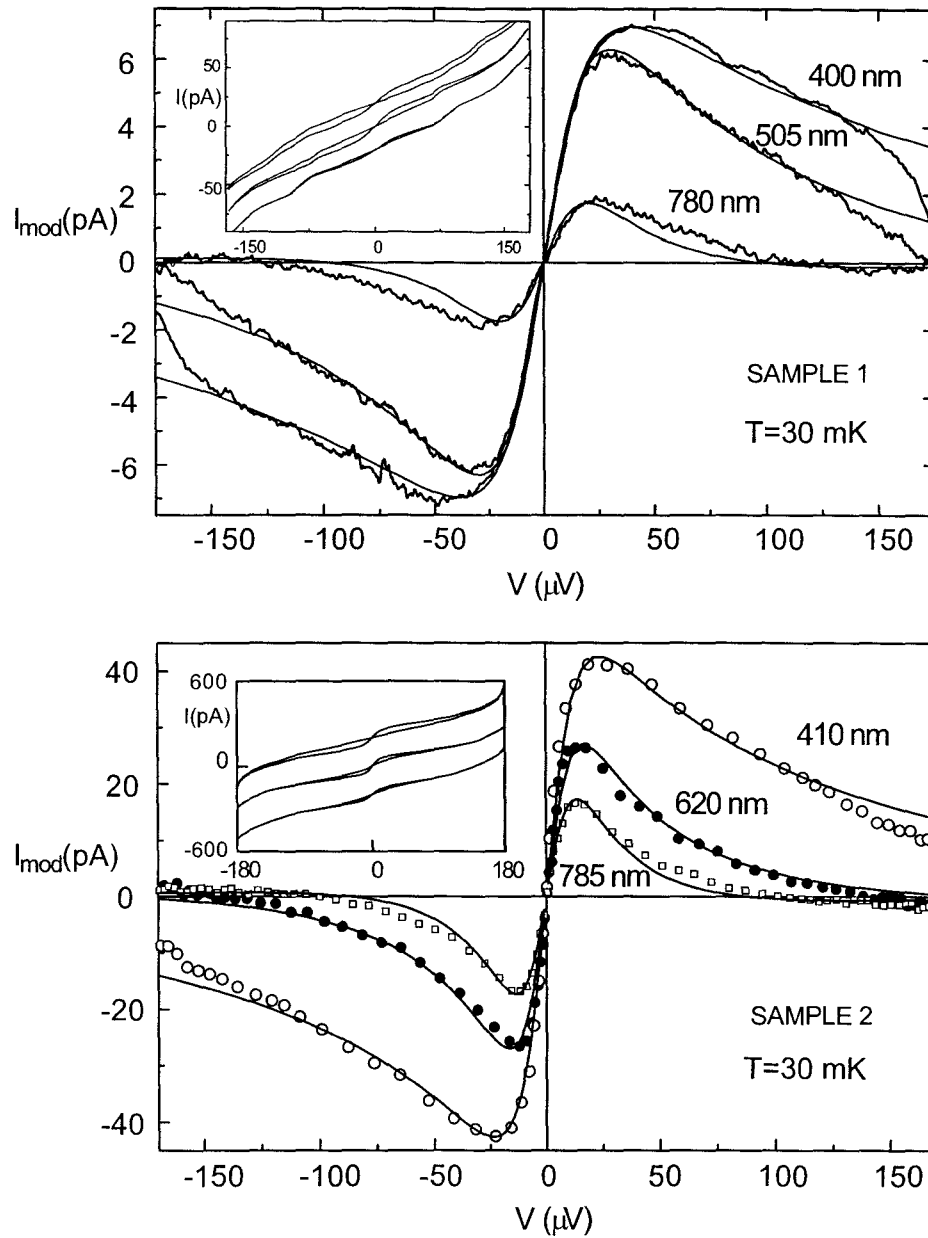
Fig. 8.3. Main panels: comparison between the measured modulated current and the theoretical predictions (continuous curves) for the three NS-QUIDs of each sample. The curves are labeled by the average separation between junctions. Insets: extremal I-V curves. All experimental curves were measured at T=30 mK.

8.3 Conclusion

We have observed a large modulation of the Andreev current in several NS-QUIDs with different geometries and tunnel conductances. The detailed voltage and temperature dependences of this modulation are well accounted for by the theory of the weak proximity effect, even though some features, such as the global scaling factor and the excess non modulated current, remain unexplained.

Given our understanding of the NS-QUID, could one envisage building a flux-sensitive device based on it?

8.3.1 Comparison with the DC-SQUID

Let us first compare the NS-QUID to its better known parent, the DC-SQUID. This device, which presently is an unrivaled flux-sensitive device, similarly consists of two junctions in a loop geometry. In the case of the DC-SQUID, the tunnel junctions are Josephson junctions, *i.e.* tunnel junctions between superconducting electrodes. The magnetic flux modulates the maximum supercurrent that can flow through the device. Normal metal resistive shunts are placed across the junctions in order to suppress the hysteretic switching out of the zero voltage branch. The IV characteristic is continuously modulated by the applied flux in a sine-like way. Typically, the working point of a DC-SQUID is chosen well below the gap voltage, with a current of the order of a few μA. The flux sensitivity of the DC-SQUID is limited by the noise produced by the resistors, and is $S_\Phi \simeq 10^{-6}\Phi_0/\sqrt{Hz}$ for an optimized DC-SQUID [4] .

The NS-QUID operating principle is simpler since the flux directly modulates the conductance of the device. In addition, the NS-QUID cannot trap flux, and is not sensitive to high frequency resonances in the biasing circuitry. However, there are a few drawbacks to the NS-QUID. The first is its low operating temperature. The second drawback is intimately related to its basic principle: the coherent electrons must be confined in the normal electrode close to the junctions. The junctions must therefore be closer to one another than the phase coherence length. Obviously, the design of the NS-QUIDs we have operated is not optimal because the junctions are placed side-to-side, and because electrons are not efficiently confined close to the junctions. Even with a better design, it is not known how well a device would age, since the parameters which determine the coherence time are not well controlled. Finally, an additional constraint on the NS-QUID is that the supercurrent in the loop be kept small.
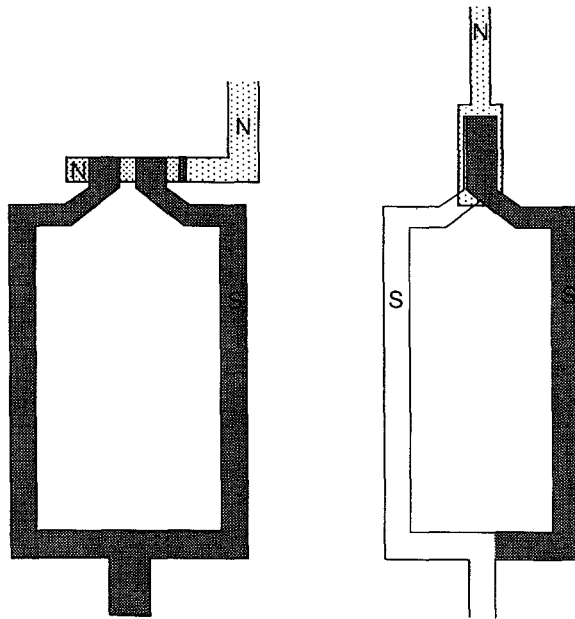
Fig. 8.4. Two possible designs which could enhance the Andreev conductance. In the first design (left), the electrons are confined to the junction region by a tunnel barrier between the normal wire forming the NS junctions and the normal lead. In the second design (right), the normal region where interference occurs is sandwiched between the two superconducting branches. In this way, the junctions can be at the same time large and close to one another, so that numerous collisions against the barriers can occur in the spin-flip scattering time. The simplest implementation of both these designs, requires to build an insulating layer on top of a normal metal. Magnesium would be a possible candidate.

8.3.2 The ultimate NS-QUID

How should one design an optimal NS-QUID, and what would be its sensitivity? More efficient confinement schemes can be obtained either by closing off the normal electrode by a tunnel junction, or by sandwiching it between the NS junctions, or, even better, by combining both tricks. The two basic types of designs are sketched in Fig. 8.4.

The performance of both designs is easily discussed in terms of the effective confinement time τ_c during which the electrons are confined in the normal electrode near the junction region. If the volume of the normal electrode in which the electrons are efficiently confined is noted $\mathcal{V}$, the modulation of the conductance is

$$G_{\max} - G_{\min} \simeq R_K G_T^2 \frac{\tau_{\text{eff}}}{\hbar n_0 \mathcal{V}},$$

with

$$\tau_{\text{eff}} = \min\left\{\tau_c, \tau_{\text{sf}}, \hbar/k_B T\right\}.$$

For a given τ_{sf}, the effect of electron confinement saturates when $\tau_c \simeq \tau_{\mathrm{sf}}$. The conductance modulation cannot however exceed the junction conductance G_T. The largest current modulation $I_{\mathrm{mod}}^{\mathrm{max}} \simeq R_K G_T^2 \frac{1}{en_0\mathcal{V}}$ corresponds, at low enough temperature, to a voltage $V \simeq \hbar/e\tau_{\mathrm{eff}}$. Assuming that the NS-QUID is only limited by the shot noise of the Andreev current, the flux sensitivity of the NS-QUID is $S_\Phi \simeq \sqrt{e/I_{\mathrm{mod}}^{\mathrm{max}}}\Phi_0/\sqrt{\mathrm{Hz}}$. An NS-QUID with tunnel junctions with an area of a few square microns, tunnel barriers similar to those of the devices we have operated, and a normal electrode thickness ~ 10 nm would have a modulated current $I_{\mathrm{mod}}^{\mathrm{max}} \sim 1$ μA and a sensitivity $S_\Phi \sim 10^{-6}\Phi_0/\sqrt{\mathrm{Hz}}$. Its performance level would then match that of a DC-SQUID. Apart from providing evidence for the interferential nature of the Andreev current, the NS-QUID is thus also a device with an appealing potential for flux measurements.

REFERENCES

[1] C. van Haesendonck, private communication.

[2] J. R. Schrieffer and J. W. Wilkins, Phys. Rev. Lett. **10**, 17 (1963).

[3] F. W. Hekking and Yu. V. Nazarov, Phys. Rev. B, **49** 6847 (1994).

[4] John Clarke, in *Advances in superconductivity,* edited by B. Deaver and John Ruvalds (Plenum Press, New York, 1983).

Chapter 9
Present understanding of the proximity effect

The experiments realized in the past five years and their contemporaneous interpretation within the theory of non-equilibrium superconductivity now provide a general understanding of the proximity effect in diffusive metals.

An essential feature of the proximity effect is that pair correlations at energy E propagate up to a distance

$$L = \min\{L_T = \sqrt{\hbar D/k_B T}, L_E = \sqrt{\hbar D/E}, L_{\text{sf}} = \sqrt{D\tau_{sf}}, L_{ee} = \sqrt{D\tau_{ee}}\}, \qquad (9.1)$$

and that the properties are non-local at this scale. Only the first length-scale was clearly identified in the Ginzburg-Landau formalism.

Another essential feature is that the measured properties of a system depend on the electrodes between which the measurement is performed. For instance, a normal wire measured with superconducting electrodes can display a supercurrent, but is found to be resistive if measured with normal electrodes. In this chapter, we summarize the main characteristics of the proximity effect, deduced in part from experiments done by others.

9.1   Equilibrium proximity effect

9.1.1   Modification of the density of states

As observed experimentally (chapter 6) and explained theoretically (chapter 5), the quasiparticle spectrum in a normal electrode in good contact with a superconductor is gapless when the normal electrode is also in contact with a normal reservoir, or when it extends to distances larger than the phase coherence length from the superconductor. In this regime, the spectrum at a distance x from the interface departs from the normal-state spectrum up to the characteristic Thouless energy $E_C(x) = \hbar D/x^2$. The spectrum contains a true gap only when all normal parts are close enough to a large enough superconducting electrode, as observed in NS bilayers [1].

9.1.2   Supercurrent

The second equilibrium characteristic is the ability of the normal metal to sustain a supercurrent when connected to two superconductors, or, if it has the form of a loop which can enclose a magnetic flux, when connected to a single superconductor.

In the simplest case of a short normal wire of length L and normal resistance R in good contact with two superconducting electrodes at its ends, the predicted critical current I_C, *i.e.* the maximum supercurrent that can be sustained by the wire, is:

$$I_C\left(T = 0\right) = \frac{E_C\left(L\right)}{eR},$$

where the Thouless energy $E_C(L)$ replaces the gap energy Δ of the Ambegaokar-Baratoff formula for the critical current of a Josephson junction [2]. The predicted temperature dependence of I_C [3,4] is also qualitatively different from the de Gennes prediction [5]. Fig. 9.1 shows the variations with temperature of the critical current of a silver wire regularly covered by narrow aluminum strips [8], compared to the predictions of [3,4]. The agreement is satisfactory if one assumes a 1.2 μm spacing between the superconducting strips instead of the measured 0.8 μm. Note that the Ginzburg-Landau theory would not reproduce the flattening of the curve at low temperature, nor would it predict the magnitude of the zero temperature critical current.
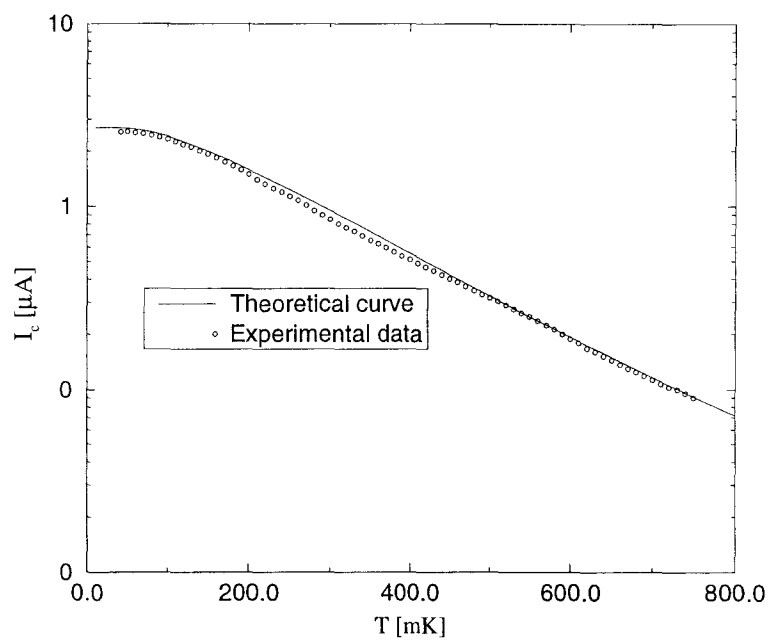
Fig. 9.1. Comparison between the measured and predicted temperature dependences of a silver bar periodically covered by aluminum strips (taken from ref. [3]).

9.2   Non-equilibrium proximity effect

The proximity effect affects very differently the transport properties of diffusive conductors, in which the proximity effect pairing angles (see chapter 5) vary continuously, and of tunnel junctions, where these angles are discontinuous. Both cases are now discussed.

9.2.1   Resistance of normal wires

We have seen that the resistance of a normal wire placed between a superconducting reservoir and a normal reservoir is, at zero temperature, the same as in the normal state. However, it is modified at finite temperature with an unusual reentrant behavior fully understood only recently [6, 7] .

9.2.1.1   Temperature-dependence of the resistance

From the expression of the quasiparticle current through a wire and the equation obeyed by the even part $f_1(E)$ of the distribution function (see chapter 5), one deduces the resistance of a wire of length L between a normal and a superconducting reservoir [6, 7] :

$$R\left(T\right) = R\left[\int_0^\infty \frac{dE}{2k_BT\cosh^2\frac{E}{2k_BT}} \frac{L}{\int_0^L \cosh^{-2}\left[\operatorname{Im}\theta\left(x',E\right)\right]dx'}\right]^{-1} \tag{9.2}$$

This expression predicts a slight decrease in resistance as the temperature is increased, starting from the normal state value at zero temperature. A minimum in resistance is reached when $L_T \simeq L$, then, at higher temperatures, the resistance behaves as if a length of the order of L_T had effectively zero resistance.

Charlat *et al.* [9] have measured the four-wire resistance of a 400 nm-long copper wire, in good contact through a 200 nm-long lateral branch with a single aluminum superconducting reservoir. (This side-branch geometry has the advantage of avoiding any change of resistance due to a shunt of the normal wire by an overlapping superconducting electrode). The measured temperature dependence of the resistance shown in Fig 9.2 exhibits a reentrant behavior in good agreement with the theoretical predictions for the precise geometry of the sample. At the resistance minimum, which occurs at a temperature of about 500 mK, corresponding to $L_T \simeq L/2$, the resistance is reduced by 2.5 %.
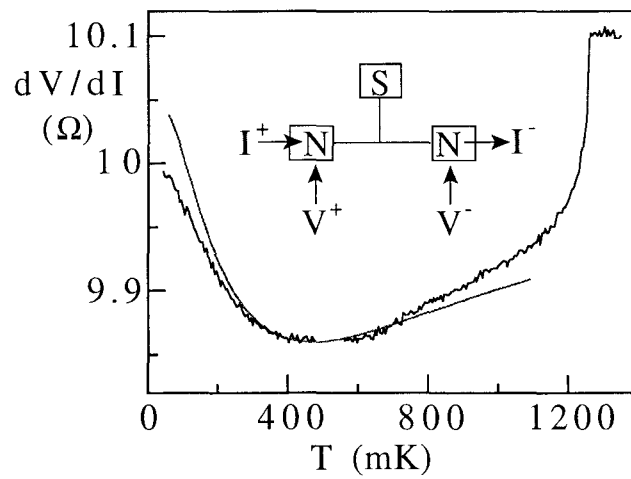
Fig. 9.2. Comparison between the measured temperature dependence of the longitudinal resistance of a normal metal wire side-connected to a superconductor [9] , and the theoretical prediction (smooth curve). The calculation is based on an approximate solution of the Usadel equations (P. Charlat, private communication).

9.2.1.2   Modulation of the resistance of a normal wire

The case of a wire connected to two or more superconductors and to at least one normal reservoir illustrates well the variety of situations. The resistance measured between any pair of superconducting reservoirs distant by less than $L_\varphi = \min\{L_{sf}, L_{ee}\}$ is zero, as long as the probe current is smaller than the maximum supercurrent that can be sustained. The resistance measured between a normal reservoir and any other reservoir is always of the order of the normal state resistance, and displays a reentrant behavior with temperature. This reentrant behavior furthermore varies with the phase differences between the superconducting electrodes which modulate the proximity effect.

Various transport experiments have been carried out on NS structures in which the proximity effect was modulated either by threading a magnetic field through a loop or by phase biasing the sample at two different points [8,11] . All the resistance modulation patterns found in these experiments are now attributed to the modulation of the modification of the resistance at finite temperature discussed above. In particular, Petrashov et al. [11] measured the four-wire resistance of a silver wire in good contact with two superconducting reservoirs S and S' with a phase difference ϕ (see Fig. 9.3). They have observed a 2π-periodic modu-
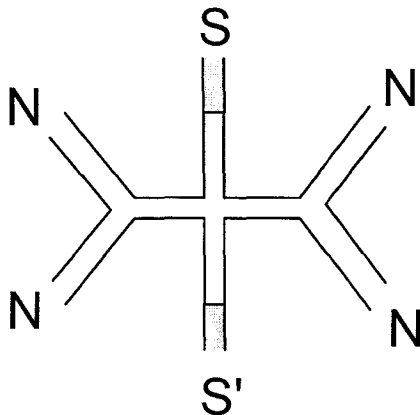
Fig. 9.3. Schematics of the mesoscopic NS structure measured by Petrashov et al. [11] . The proximity effect induced in the normal metal wire is modulated by the phase difference between the superconductors S and S'.

lation of the resistance which is in quantitative agreement with the theoretical prediction [7] taking into account the detailed geometry of their sample, as shown in Fig. 9.4. The mod-

ulation of the resistance variations by the field at a given temperature is explained in the following way: with zero phase difference between the superconductors, the resistance is reduced as much as possible given the actual layout ($\sim 10\%$) with respect to its normal value (full "thermal" effect). A phase difference of π between the superconductors annuls the proximity effect (because the superconductors are disposed symmetrically about the wire), so that the normal state resistance is recovered.
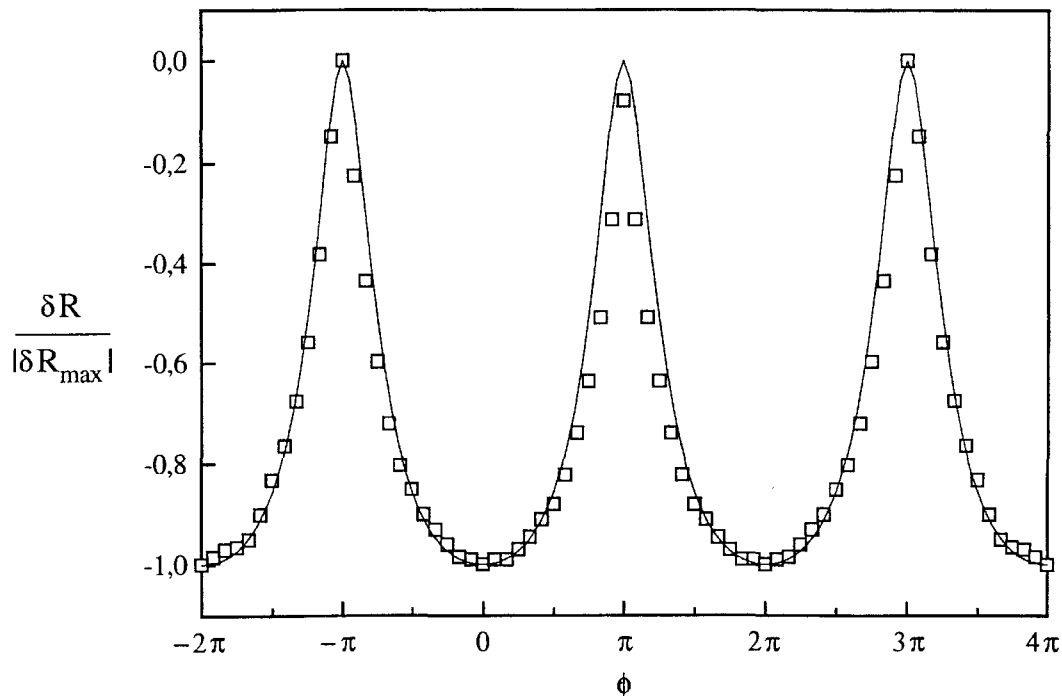
Fig. 9.4. Comparison between the measured (Open squares taken from ref. [11]) and the predicted variations (continuous line) of the resistance of the circuit sketched in Fig. 12, as a function of the phase difference ϕ between the superconducting electrodes (taken from ref. [7]). The maximum effect corresponds to a change of the resistance by 9.7%. The theoretical prediction has been calculated at the temperature for which the effect is maximum.

9.2.2 Resistance of tunnel junctions

At zero temperature, the resistance of tunnel junctions is strongly affected by the proximity effect. The circuit theory of Nazarov (see chapter 5), in which each point of a circuit is represented by a point on the unit sphere, enables an easy determination of the renormalized value of the tunnel junctions resistances, even in complex layouts. The general prediction is $\tilde{R}_T = R_T / \cos \mathcal{L}$, where $\mathcal{L}$ is the length of the arc between the representative points of both

junction electrodes. Two limits are particularly simple:

i) When one electrode is not affected by the proximity effect, $\mathcal{L}$ is just the value of the pairing angle in the modified electrode, so that the renormalized tunnel resistance is the resistance R_T divided by the density of quasiparticle states at the Fermi energy in the other electrode. This simple result allowed us to deduce the density of states modified by the proximity effect (chapter 6).

ii) When one electrode is a BCS superconductor, if there is no other superconductor in the circuit, and if the normal electrode is longer than L_φ, the conductance of the NS tunnel junctions is $R = R_T^2/R\left(L_\varphi\right)$, where $R\left(L_\varphi\right)$ is the normal state resistance of a length L_φ of the N electrode. At finite temperature or finite voltage, L_φ should simply be replaced in this formula by expression (9.1) (see NS-QUID experiment, chapter 8).

9.2.3   Arbitrary NS structures

Finally, the circuit theory of Nazarov allows to calculate at zero temperature the resistance of any NS structure which combines diffusive resistors and tunnel junctions. At finite temperature, it is necessary to solve the Usadel equations to find the pairing angle and filling functions at finite energies, and then deduce the resistance from formula (5.61).

REFERENCES

[1] C. J. Adkins and B. W. Kington, Phys. Rev. **177**, 777 (1969); J. R. Toplicar and D. K. Finnemore, Phys. Rev. B **16**, 2072 (1977); A. Kastalsky, L. H. Greene, J. B. Barner, and R. Bhat, Phys. Rev. Lett. **64**, 958 (1990).

[2] M. Tinkham, *Introduction to Superconductivity* (Mc Graw Hill, 1985).

[3] F. Whilhem, A. Zaikin and G. Schön, Czech. J. Phys. **46**, Supplement S4, 2395 (1996) and J. Low. Temp. Phys. **106**, 305 (1997).

[4] A. Volkov and H. Takayanagi, Phys. Rev. Lett. **76**, 4026 (1996).

[5] G. Deutscher and P. G. de Gennes, in *"Superconductivity"*, ed. by R. Parks (1969)

[6] S. N. Artemenko, A. F. Volkov, and A. V. Zaitsev, Solid State Comm. **30**, 771 (1979).

[7] Yu. V. Nazarov and T. H. Stoof, Phys. Rev. Lett. **76**, 823 (1996); T. H. Stoof and Yu. Nazarov Phys. Rev. **B53**, 14496 (1996).

[8] H. Courtois, Ph. Gandit, and B. Pannetier, Phys. Rev. **B52**, 1162 (1995); Phys. Rev. Lett. **76**, 130 (1996). P. Charlat, H. Courtois, B. Pannetier, Phys. Rev. Lett. **77**, 4950 (1996)

[9] P. Charlat, H. Courtois, Ph. Gandit, D. Mailly, A. F. Volkov and B. Pannetier, Czech. J. Phys. **46**, Supplement S6, 3107 (1996).

[10] T. H. Stoof and Yu. Nazarov Phys. Rev. **B54**, R772 (1996).

[11] V. T. Petrashov, Czech. J. Phys. **46**, 3303 (1996); V. T. Petrashov, V. N. Antonov, P. Delsing and T. Claeson, Phys. Rev. Lett. **74**, 5268 (1995).

Chapter 10
Conclusion

10.1 What ultimately limits the coherence of mesoscopic samples?

From the experiments on the proximity effect, we have found that the quantum coherence time of quasiparticles in our copper films is in the range $\tau_\varphi \sim 10 - 100$ ps. On the other hand, we have seen that electron-electron interactions lead to a redistribution of the energy between quasiparticles with a typical time of $\tau_0 \sim 1$ ns. The corresponding estimated phase-coherence time τ_{ee} is of order τ_0. We therefore attribute the shorter, temperature-independent phase-breaking time invoked to interpret quantitatively our proximity-effect experiments to spin-flip scattering, and not to electron-electron interaction (we have seen in part 7.5 than spin-orbit has no effect). One could try to reach the regime where electron-electron interaction is dominant. What would then be the largest phase coherence time? This issue is presently controversial [1,2], and further investigation of diffusive metals is required in order to clarify the question.

10.2 Open questions about the proximity effect

The experiments presented in this thesis, along with the experiments performed contemporaneously by others, have provided a good understanding of the proximity effect in disordered metals. However, some predictions remain to be tested.

- Non-equilibrium situations remain non-intuitive: the different types of currents predicted
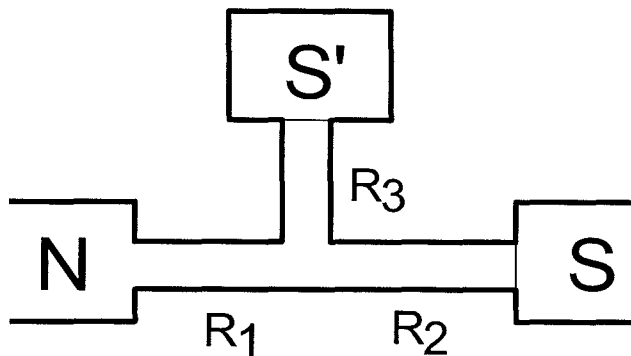
Fig. 10.1. Example of diffusive NS structure in which the resistance is strongly modified by the proximity effect. The resistance R between the N and S reservoirs $R = R_1 + \left(R_2^{-1} + R_3^{-1}\right)^{-1}$ depends on the resistance R_3 of the dangling arm.

by the theory can coexist. This can lead to strange situations, as illustrated by the example of the circuit of Fig. 10.1. When a voltage is applied between the left (normal) and the right (superconducting) electrode, no net current would of course flow in the dangling arm. But surprisingly, according to the theory, both an Andreev current and a supercurrent flow in opposite directions in this arm, and cancel one another. Because the lateral superconductor is able to convert quasiparticles into pairs, which can super-flow to the other superconductor, this is equivalent to having the two superconductors connected, and the resistance is expected to be $R_1 + R_2 // R_3$. Such conversion would show up in the increase of the resistance to $R_1 + R_2$ when the supercurrent current in the dangling arm exceeds the critical current.

- Another surprising prediction concerns the electric field: even though the resistance of a diffusive metal in is only slightly modified by proximity effect, the electric field is predicted to be expelled from the normal wire close to a good NS contact [3]. Direct experimental confirmation of this prediction is difficult, however, because electrical contacts are sensitive to the distribution function and not to the electrostatic potential.

- Finally, fully out-of-equilibrium situations, with voltage differences between superconducting electrodes, lie beyond the scope of the present theory.

REFERENCES

[1] P. Mohanty and R. A. Webb, Phys. Rev. Lett. 78, 3366 (1997).

[2] M. Vavilov, V. Ambegaokar, cond-mat. 9709241.

[3] F. Zhou, B. Spivak, and A. Zyuzin, Phys. Rev. B **54**, 9443 (1996).

Appendix A
Scattering approach to conductivity: from N to NS circuits

In the scattering approach, a whole coherent conductor is treated as a single scatterer. Electron waves are guided to and from the conductor by semi-infinite leads of finite section. Due to the quantization of transverse momentum, there is a finite number of propagating channels or modes in each lead (the number of modes is of the order of S/λ_F^2, where S is the section of the lead and λ_F the wavelength at the Fermi energy). The conductor is characterized by a transmission amplitude matrix $\mathbf{t}$, the coefficients of which are the projections of each mode of the incoming lead onto each mode of the outgoing lead. The importance of the scattering method comes from the fact that quantities such as normal state conductance, shot noise, and Andreev conductance can be expressed in terms of the eigenvalues of the transmission matrix $\mathbf{T} = \mathbf{tt}^\dagger$. The corresponding eigenmodes can be considered as the independent conduction channels through which electrical conduction proceeds. Depending on the value of its
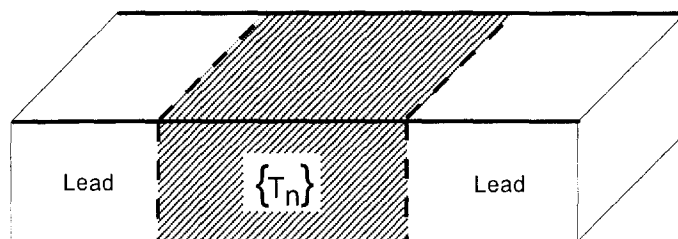
Fig. A.1.

transmission eigenvalue T_n, channel n will be considered open ($T_n \lesssim 1$), closed ($T_n \approx 0$), or

anything in between. In order to determine a given property of a conductor, one must know

(i) the expression of that quantity in terms of a sum over transmission eigenvalues, and

(ii) the distribution of the transmissions T_n of the conductor

In the following paragraphs, we will apply these principles along the lines of Beenakker [2] and Nazarov [3] .

A.1   Expression of the conductance in the scattering formalism

The scattering formalism [1] can be represented graphically as shown in Fig. A.2. The conductor, represented as a block, is entirely characterized by the set of reflection and transmission coefficients r_n and t_n, which give the probability amplitude for an electron of channel n to be reflected by the conductor or transmitted through it. The conductor is connected to semi-infinite incoming and outgoing leads.

A.1.1   Landauer formula for the normal state conductance of a scatterer

The Landauer formula relates the conductance to the channel transmissions T_n through

$$G = 2G_K \sum_{n=1}^{\mathcal{N}} T_n, \qquad (A.1)$$

where $G_K = e^2/h$. The conductance is simply proportional to the trace of the transmission matrix $\mathbf{T}$. This formula is valid for any scatterer between normal leads. However, the distribution of transmissions T_n differs strongly according to the system considered.

In a tunnel junction, all the transmissions are small, whereas in a diffusive resistor the transmission distribution is:

$$\rho_0\left(T\right) = \frac{G_N}{2G_K}\frac{1}{T\sqrt{1-T}}. \qquad (A.2)$$

This result is valid whatever the shape and resistivity distribution of the conductor, as long as there are no discontinuities in the voltage distribution. The transmission distribution is plotted in Fig. A.3. The great majority of transmission channels in a diffusive conductor are either almost completely closed or extremely well transmitted, so that the conduction through a diffusive conductor is due to a very small number of extremely well transmitted channels.
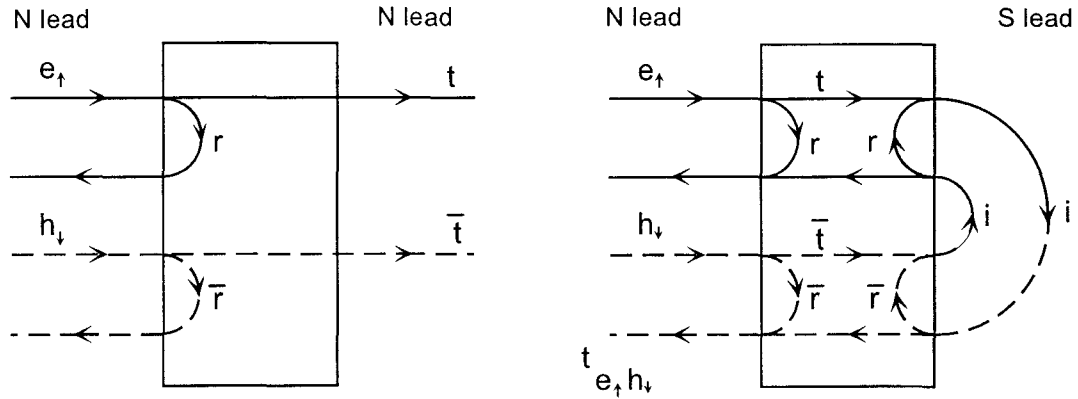
Fig. A.2. The reflection and transmission coefficients r and t of a scatterer suffice to compute the conductance of this scatterer connected between normal leads (left) or, when the additional process of Andreev reflection of an electron into a hole is taken into account, the conductance between a normal and superconducting lead (right).
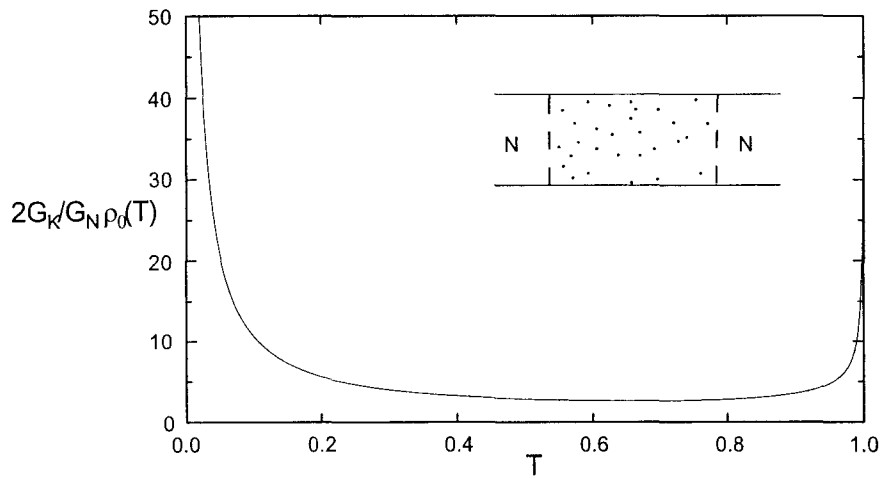
Fig. A.3.

A.1.2   Andreev conductance of an NS system

A similar approach has been developed for NS systems [1]. In such systems, the zero voltage conductance is due to the Andreev reflection. Therefore the conductance is proportional to the total probability to reflect an electron into a hole:

$$G_{NS} = 2 \times 2G_K \sum_{n=1}^{\mathcal{N}} |r_{eh}|^2 \,,$$

where r_{eh} is the electron-hole reflection amplitude.. The extra factor of two is due to the charge $2e$ transferred in the Andreev process.

Figure A.2 illustrates how r_{eh} is computed from the reflection and transmission coefficients of the scatterer in its normal state, by summing all possible trajectories participating in this process. For a given channel, the amplitude t_{eh} is the product of the amplitude t for transmission of a spin up electron, the Andreev reflection factor at zero energy i, and $\bar{t}$ for transmission through the conductor, multiplied by the geometrical series of ratio $i^2 r\bar{r}$ corresponding to the sum of all loops describing the multiple reflections between the scatterer and the interface with the superconductor:

$$t_{eh_n} = \frac{it_n \bar{t}_n}{1 + r_n \bar{r}_n} = \frac{iT_n}{2 - T_n}. \tag{A.3}$$

Consequently, the Andreev conductance is:

$$G_{NS} = 4G_K \sum_{n=1}^{\mathcal{N}} \frac{T_n^2}{(2 - T_n)^2}. \tag{A.4}$$

In the case of an NS tunnel junction, one gets $G_{NS} \cong \frac{R_K}{4\mathcal{N}} G_T^2$, where $\mathcal{N}$ is the number of channels. Therefore, in the limit of a large number of channels, the Andreev conductance is negligible (in a metallic junction of area 100 nm$\times$ 100 nm, there are approximately one million channels). We will see that the situation changes dramatically if a diffusive resistor R is added in series with the tunnel junction. To calculate G_{NS} in this case, one needs first the transmission distribution of a tunnel junction in series with a resistor.

A.2 Distribution of transmissions of complex circuits

Nazarov [3] has devised a way to compute the transmission distribution of any combination of conducting elements, of which we give the outline, without justification.

A.2.1 Generating function for the transmission distribution

Nazarov defines the transmission distribution generating function $F(\Phi)$ as

$$F(\Phi) \equiv \sum_{n=1}^{\mathcal{N}} \frac{T_n}{1 - T_n \sin^2 \frac{\Phi}{2}}. \tag{A.5}$$

The angle Φ can be interpreted an effective voltage drop across the conductor. The effective current $I(\Phi)$ corresponding to this effective voltage drop is defined in terms of the function F as

$$I(\Phi) \equiv 2G_K F(\Phi) \sin \Phi. \tag{A.6}$$

The probability to have transmission T is then

$$\rho(T) \equiv \sum_n \langle \delta(T - T_n) \rangle = \frac{\rho_0(T)}{\pi G_N} \operatorname{Re}\left[I\left(\pi + i \arg \cosh \frac{1}{\sqrt{T}}\right) \right], \tag{A.7}$$

where $\rho_0(T)$ is the transmission distribution (A.2) of a diffusive resistor.

A.2.2 Transmission distributions of simple elements

For a tunnel junction, one gets:

$$F(\Phi) = \sum_n T_n = \frac{G_T}{2G_K},$$

$$I(\Phi) = G_T \sin \Phi, \tag{A.8}$$

and for a diffusive conductor:

$$F(\Phi) = \frac{G_N}{2G_K} \frac{\Phi}{\sin \Phi},$$

$$I(\Phi) = G_N \Phi.$$

A.2.3 Combination rules and examples

Nazarov has shown that the effective current I and effective potential drop Φ obey the
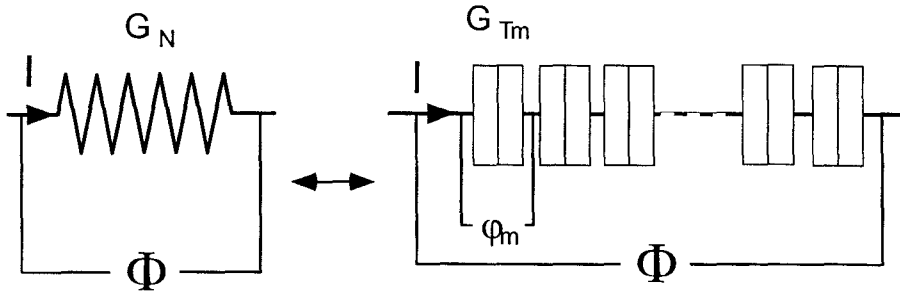
Fig. A.4.

same conservation laws as regular currents and voltages, thereby enabling the elaboration of a circuit theory for these quantities. To find the transmission distribution of any two terminal circuit, one uses to following rules:

(i) one first assigns an effective potential Φ_n to each node n of the network of elements;

(ii) each element is characterized by its $I_n - \Phi_n$ characteristic (relations A.6 and A.8);

(iii) from the conservation of effective current in each node, one determines the effective potential distribution. The total current is then obtained as a function of the total potential difference Φ.

(iv) The transmission distribution is then given by (A.7).

A.2.3.1   Example 1: Transmission distribution of a diffusive resistor recovered by combining several tunnel junctions in series

The characteristics of a diffusive conductor can be deduced from those of a tunnel junction if one considers the diffusive conductor to be constituted of a number M of tunnel junctions in series, with M tending towards infinity [5] (see Fig. A.4). The small effective voltage drop across each junction is $\varphi_m = \Phi/M$, where Φ is the effective voltage drop across the resistor. Consequently the current through each tunnel junction is equal to the current I through the entire structure:

$$I\left(\Phi\right) = G_{Tm}\varphi_m = G_T \frac{\Phi}{M} = G_N\Phi,$$

and the generating function is

$$F\left(\Phi\right) = \frac{G_N}{2G_K} \frac{\Phi}{\sin\Phi}.$$

From there one immediately recovers the transmission distribution (A.2) through (A.7).

A.2.3.2   Example 2: Diffusive conductor in series with a tunnel junction

Let $X(\Phi)$ be the effective potential at the node between the diffusive resistor and the tunnel junction. Conservation of current writes
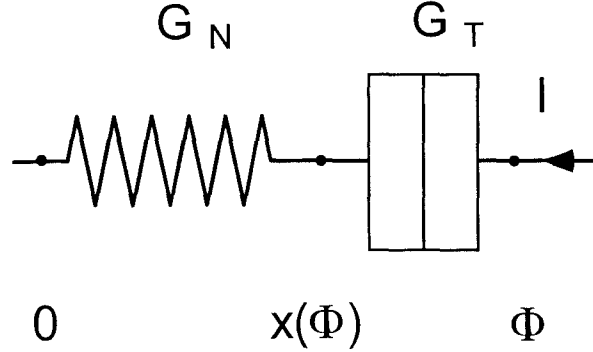
Fig. A.5.

$$I = G_N X(\Phi) = G_T \sin[X(\Phi) - \Phi] \tag{A.9}$$

so that

$$F(\Phi) = \frac{G_N}{2G_K} \frac{X(\Phi)}{\sin\Phi} \tag{A.10}$$

From there the transmission distribution, given by Eq. (A.7), can be determined. Nazarov finds

$$\rho(T) = \rho_0(T) \times f,$$

where the function f is given as a function of the parameter μ which parametrizes the transmission T :

$$\left\{ \begin{array}{l} T = \frac{1}{\cosh^2\mu} \\ \mu = \frac{1}{2}\left[\operatorname{arg cosh}\left(\frac{\pi f}{G_T/G_N \sin\pi f}\right) - \frac{G_T}{G_N}(\cos\pi f)\sqrt{\left(\frac{\pi f}{G_T/G_N \sin\pi f}\right)^2 - 1}\right] \end{array} \right.$$

The resulting transmission distribution is plotted in Fig. A.6, for ratios of diffusive conductance over tunnel conductance of 100, 20, 10, 2, and 1. When the tunnel resistance dominates $(G_T/G_N \ll 1)$, the transmission distribution is strongly peaked around transmissions below $T_{\max} \approx 4G_T/G_N$. As the ratio G_T/G_N increases but remains below 1, channels of higher transmission open up, but there are no channels perfectly transmitted. Channels with transmission
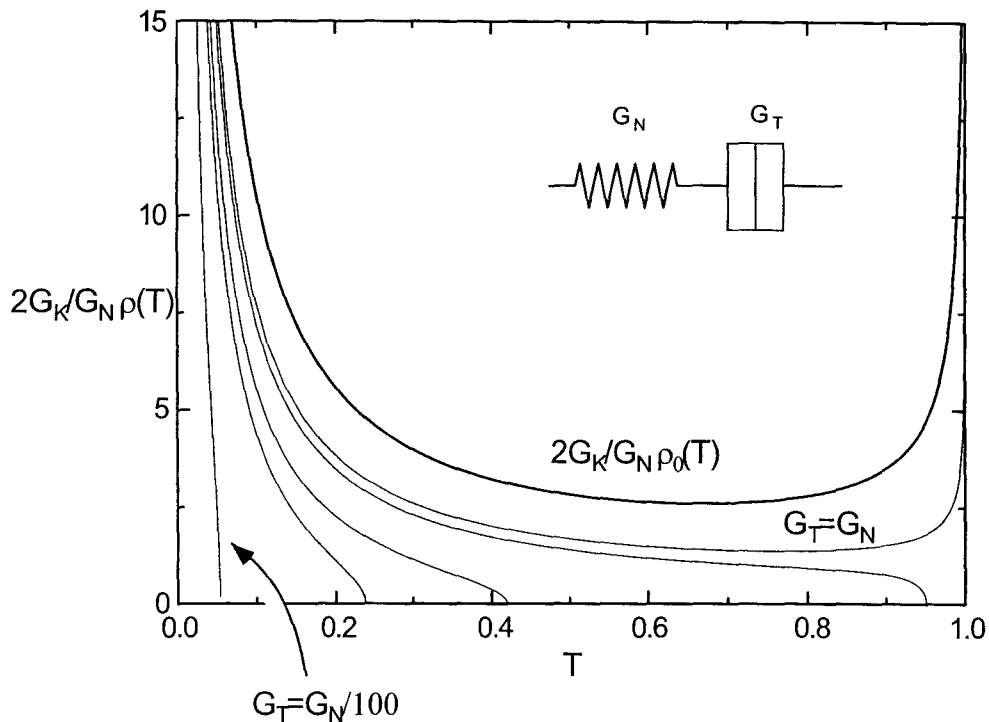
Fig. A.6. Transmission distribution of a circuit consisting of a diffusive conductor of conductance G_N in series with a tunnel junction of conductance G_T. The different curves are plotted for ratios G_N/G_T of 100, 20, 10, 2, and 1. The top curve is the transmision distribution of a diffusive conductor alone.

1 are only found when $G_T/G_N \geq 1$. The transmission distribution then resembles, but stays below, the distribution ρ_0 of a single diffusive conductor.

A.2.4   From the transmission distribution to Andreev conductance

From Eq. (A.4), and the definition (A.5) of $F(\Phi)$, the Andreev conductance is simply given by:

$$G_{NS} = \frac{\partial I}{\partial \Phi}\bigg|_{\Phi=\pi/2} = 2G_K \frac{\partial F}{\partial \Phi}\bigg|_{\Phi=\pi/2} \qquad (A.11)$$

For a diffusive conductor we immediately find that $G_{NS} = G_N$, and for an NS tunnel junction with many weakly transmitted channels $G_{NS} = G_T$. This contrasts with the ballistic result of a scatterer containing only one perfectly transmitted channel $G_{NS_{bal}} = 2G_{N_{bal}}$ (formula (A.4)). The presence of disorder reduces the Andreev conductance by exactly one half.

The Andreev conductance of the resistance in series with the tunnel junction previously

considered is given by equations (A.9) and (A.10):

$$\begin{cases} G_{NS} = G_N X' \left(\frac{\pi}{2}\right) = \frac{G_N}{1 + 1/(X \tan X)} \\ \frac{\cos X}{X} = \frac{G_N}{G_T} \end{cases}.$$

In the limit $G_T \ll G_N$, $X \simeq \frac{G_T}{G_N}$, and the Andreev conductance is $G_{NS} = R_N G_T^2$, as also found with the theory of the proximity effect. This contrasts with the conductance $\frac{R_K}{4N} G_T^2$ of a sole NS tunnel junction between ballistic leads.

REFERENCES

[1] C. Beenakker, Rev. Mod. Phys. **69**, 3, p. 731 (1997), and references therein.

[2] C. W. J. Beenakker, in *Mesoscopic Quantum Physics*, ed. by E. Akkermans, G. Montambaux, and J.-L. Pichard, North-Holland (Amsterdam).

[3] Yu. V. Nazarov, Phys. Rev. Lett. **73**, 134 (1994); Yu. V. Nazarov, in *Quantum Dynamics of Submicron Structures*, ed. by H. A. Cerdeira, B. Kramer and G. Schön, Kluwer, (Dordrecht), 687-704 (1995).

[4] M. Büttiker, Phys. Rev. Lett. **65**, 2901 (1990).

[5] M. de Jong, Ph.D. thesis .

REFERENCES OF CHAPTER 1

[1] D. Pines, P. Nozières, *The theory of quantum liquids* (W.A. Benjamin, New York, 1966).

[2] M. Tinkham, *Introduction to Superconductivity* (Mc Graw Hill, New York, 1985), chapter 3.

[3] P. G. de Gennes, *Superconductivity of metals and alloys* (W. A. Benjamin, New York, 1966).

[4] V. T. Petrashov, V. N. Antonov, P. Delsing, and T. Claeson, Phys. Rev. Lett. **70**, 347 (1993); See also *Procedings of the NATO Advanced Research Workshop on Mesoscopic Superconductivity*, F. W. J. Hekking, G. Schön, and D. V. Averin, Editors (Elsevier, Amsterdam, 1994).

REFERENCES OF CHAPTER 2

[1] V. Bouchiat, Ph.D. thesis, Université Paris 6 (1997).

[2] D. Vion, P. F. Orfila, P. Joyez, D. Esteve, and M. H. Devoret, *J. Appl. Phys.* **77**, 2519 (1994).

[3] D. C. Glattli, P. Jacques, A. Kumar, P. Pari and L. Saminadayar, *J. Appl. Phys.* **81**, 7350 (1997).

REFERENCES OF CHAPTER 3

[1] N.W. Ashcroft and N.D. Mermin, *Solid State Physics*, CBS Publishing (1975).

[2] D. Pines and P. Nozière, *The Theory of Quantum Liquids. 1: Normal Fermi Liquids,* W.A. Benjamin (1966).

[3] B. L. Altshuler and A. G. Aronov, in *Electron-Electron interactions in Disordered Systems,* Ed. by A. L. Efros and M. Pollak, Elsevier, (1985).

[4] R. Landauer, IBM J. Res. Develop. **1**, 223 (1957); **32**, 306 (1988).

[5] K.E. Nagaev, Phys. Lett. A **169**, 103 (1992); Phys. Rev. B **52**, 4740 (1995).

[6] V.I. Kozub and A. M. Rudin, Phys. Rev. B **52**, 7853 (1995).

[7] M.J.M. de Jong and C.W.J. Beenakker, Physica A **230**, 219 (1996).

[8] See for example, F. C. Wellstood, C. Urbina, and John Clarke, Phys. Rev. B **49**, 5942 (1994).

[9] D.E. Prober, M.N. Wybourne, and M. Kansakar, Phys. Rev. Lett. **75**, 3964 (1995).

[10] A.H. Steinbach, J.M. Martinis, and M.H. Devoret, Phys. Rev. Lett. **76**, 3806 (1996).

[11] Numerical recipes, Cambridge University Press (Cambridge), Chapter 10.

REFERENCES OF CHAPTER 4

[1] A. Schmid, Z. Phys. **271**, 251 (1974).

[2] B. L. Altshuler and A. G. Aronov, in *Electron-Electron Interactions in Disordered Systems*, Ed. A. L. Efros and M. Pollak, Elsevier Science Publishers B.V. (1985), p. 29.

[3] W. L. McMillan, Phys. Rev. B **24**, 2739 (1981).

[4] G. Montambaux, in *Quantum Fluctuations*, S. Reynaud, E. Giacobino and J. Zinn-Justin, eds. (Elsevier, Amsterdam, 1997), p. 387.

[5] B. L. Altshuler, A. G. Aronov, and D. E. Khmelnitskii, J. Phys. **C15**, 7367 (1982).

[6] Note that the polarizability of an out-of-equilibrium fermionic system, such as the one created in our experiment, might have a different form (M. Combescot, C. Caroli, private communication).

[7] B. L. Altshuler and A. G. Aronov, in *Electron-Electron Interactions in Disordered Systems*, Ed. A. L. Efros and M. Pollak, Elsevier Science Publishers B.V. (1985), formula (4.4).

[8] Ya. Blanter, private communication.

[9] H. Pothier, S. Guéron, Norman O. Birge, D. Esteve, and M. H. Devoret, Z. Phys. B **104**, 178 (1997).

[10] M. Büttiker, Phys. Rev. B **45**, 3807 (1992); S.-R. Eric Yang, Solid State Comm. **81**, 375 (1992).

[11] R. Kubo, M. Toda, N. Hashitsume, *Statistical Physics II* (Springer Verlag, Berlin, 1991), p. 170.

[12] S. Chakravarty and A. Schmid, Phys. Rep. **140**, 193 (1986).

[13] K. E. Nagaev, Phys. Lett. A **169**, 103 (1992).

[14] R. Landauer, IBM J. Res. Develop. **1**, 223 (1957); **32**, 306 (1988).

REFERENCES OF CHAPTER 5

[1] H. Courtois, Ph. Gandit, and B. Pannetier, Phys. Rev. B **52**, 1162 (1995); Phys. Rev. Lett. **76**, 130 (1996).

[2] P. Charlat, H. Courtois, Ph. Gandit, D. Mailly, A. F. Volkov and B. Pannetier, Czech. J. Phys. **46**, Supplement S6, 3107 (1996).

[3] M. Tinkham, *Introduction to Superconductivity* (Mc Graw Hill, 1985), chapter 4.

[4] M. Tinkham, *Introduction to Superconductivity* (Mc Graw Hill, 1985).

[5] P. G. de Gennes, Rev.Mod. Phys **36**, 225 (1964).

[6] A. Barone and G. Paterno, *Physics and Applications of the Josephson Effect* (Wiley,1982).

[7] G. Deutscher and P. G. de Gennes, in *Superconductivity*, edited by R. D. Parks (Marcel Dekker, New York, 1969), p. 1005.

[8] A. I. Larkin and Yu. N. Ovchinnikov, in *Nonequilibrium Superconductivity*, edited by D. N. Langenberg and A. I. Larkin (North Holland, Amsterdam, 1986), p. 531; A. I. Larkin and Yu. N. Ovchinnikov, Sov. Phys.-JETP **41**, 960 (1975).

[9] A. Schmid, in *Nonequilibrium Superconductivity, Phonons, and Kapitza Boundaries*, edited by K. E. Gray (Plenum Press, New York, 1981), p. 423.

[10] J. Rammer and H. Smith, Rev. Mod. Phys. **58**, 323 (1986).

[11] K. D. Usadel, Phys. Rev. Lett. **25**, 507 (1970).

[12] A. F. Volkov, A. V. Zaitsev, and T. M. Klapwijk, Physica (Amsterdam) **210C**, 21 (1993); A. F. Volkov, Phys. Rev. Lett. **74**, 4730 (1995).

[13] W. L. McMillan, Phys. Rev. **175,** 537 (1968).

[14] These results can be found in A. A. Golubov, in *Superconducting Superlattices and Multilayers*, edited by I. Bozovic, SPIE proceedings Vol. 215 (SPIE, Bellingham, WA, 1994), p.353.

[15] G. Eilenberger, Z. Phys. **214**, 195 (1968).

[16] Yu. V. Nazarov, Phys. Rev. Lett. **73**, 1420 (1994).

[17] D. Esteve, H. Pothier, S. Guéron, N. O. Birge, and M. H. Devoret in *Correlated fermions and transport in mesoscopic systems*, edited by T. Martin, G. Montambaux et J. Trân Thanh Vân (Editions Frontières, Paris, 1996).

[18] T. H. Stoof and Yu. Nazarov Phys. Rev. B **54**, R772 (1996).

[19] P. G. de Gennes, *Superconductivity of Metals and Alloys* (W. A. Benjamin, New York, 1966), (7-64) p. 232.

[20] W. Belzig and C. Bruder, Phys. Rev. B **54**, 9443 (1996).

[21] F. Zhou, B. Spivak, and A. Zyuzin, Phys. Rev. B 52, 4467 (1995).

[22] S. Yip, Phys. Rev. B **52**, 15504 (1995).

[23] W. J. Hekking and Yu. V. Nazarov, Phys. Rev. Lett. **71**, 1625 (1993) and Phys. Rev. B **49** 6847 (1994).

[24] A. Kastalsky, A. W. Kleinsasser, L. H. Greene, R. Bhat, F. P. Milliken, and J. P. Harbison, Phys. Rev. Lett. **67**, 3026 (1991).

[25] A. F. Volkov, Physica B **203**, 267 (1994) and refs. therein to earlier work.

[26] C. W. J. Beenakker, Phys. Rev. B **46**, 12841 (1992) and in *Mesoscopic Quantum Physics*, edited by A. Akkermans et al., (Elsevier, Amsterdam, 1995), course 5.

[27] S. Guéron, H. Pothier, N. O. Birge, D. Esteve, and M. H. Devoret, Phys. Rev. Lett. **77**, 3025 (1996).

[28] H. Pothier, S. Guéron, D. Esteve, and M. H. Devoret, Phys. Rev. Lett. **73**, 2488 (1994) and Physica B **203**, 226 (1994).

[29] J. R. Toplicar and D. K. Finnemore, Phys. Rev. B **16**, 2072 (1977).

REFERENCES OF CHAPTER 6

[1] J. J. Hauser and H. C. Theuerer, Phys. Letters **14**, 270 (1965). See also references in G. Deutscher and P.G. de Gennes, in *Superconductivity*, edited by R. D. Parks (Marcel Dekker, New York, 1969), p. 1005.

[2] T. Claeson and S. Gygax, Solid State Comm. 4:385 (1966); see also references in T. Claeson, in *Tunneling Phenomena in Solids*, edited by E. Burnstein and S. Lundqvist (Plenum, New York,1969), p. 443.

[3] W. Belzig and C. Bruder, Phys. Rev. **B54**, 9443 (1996).

[4] V. T. Petrashov, V.N. Antonov, P. Delsing and T. Claeson, Phys. Rev. Lett. **74**, 5268 (1995); V. T. Petrashov, R. Sh. Shaikhaidarov, I. A. Sosnin, Czech. J. Phys. **46**, 3303 (1996).

[5] H. Courtois, Ph. Gandit, and B. Pannetier, Phys. Rev. B **51**, 9360 (1995); Phys. Rev. B **52**, 1162 (1995).

[6] G.-L. Ingold and Yu. Nazarov, in *Single Charge Tunneling*, edited by H. Grabert and M. H. Devoret (Plenum Press, New York, 1992), p. 21; H. Pothier, Ph.D. Thesis, Université Paris 6 (1991).

[7] P. Charlat, H. Courtois, Ph. Gandit, D. Mailly, A.F. Volkov, and B. Pannetier, Phys. Rev.

Lett. **77**, 4950 (1996).

[8] P. Lafarge, P. Joyez, D. Esteve, C. Urbina, and M. H. Devoret, Nature **365**, 422 (1993).

[9] F. C. Wellstood, C. Urbina, and John Clarke, Phys. Rev. B **49**, 5942 (1994).

[10] J. J. Hauser, H. C. Theuerer, and N. R. Werthamer, Phys. Rev. **136**, A637 (1964).

REFERENCES OF CHAPTER 7

[1] See for instance *Proceedings of the NATO Advanced Research Workshop on Mesoscopic Superconductivity*, F. W. J. Hekking, G. Schön, and D. V. Averin, eds. (Elsevier, Amsterdam, 1994).

[2] G. E. Blonder, M. Tinkham, and T. M. Klapwijk, Phys. Rev. B **25**, 4515 (1982).

[3] H. Pothier, S. Guéron, D. Esteve, M. H. Devoret, Phys. Rev. Lett. **73**, 2488 (1994), reprinted in the next chapter.

[4] B. J. van Wees, P. de Vries, P. Magnée, and T. M. Klapwijk, Phys. Rev. Lett. **69**, 510 (1992).

[5] I. K. Marmorkos and C. W. J. Beenakker, R. A. Jalabert, Phys. Rev. B **48**, 2811 (1993).

[6] F. W. J. Hekking and Yu. V. Nazarov, Phys. Rev. Lett. **71**, 1625 (1993); F. W. J. Hekking and Yu. V. Nazarov, Phys. Rev. B **49**, 6847 (1994).

[7] H. Pothier, S. Guéron, D. Esteve, M. H. Devoret, Physica B **203**, 226 (1994).

[8] A. F. Volkov, A. V. Zaitsev, Phys. Rev. B **53**, 9267 (1996).

[9] T. M. Eiles, J. M. Martinis and M. H. Devoret, Physica B **189**, 210, (1993).

[10] J. R. Schrieffer and J. W. Wilkins, Phys. Rev. Lett. **10**, 14 (1963).

[11] W. L. McMillan, Phys. Rev. B **24**, 2739 (1981).

[12] G. Montambaux, in *Quantum Fluctuations*, S. Reynaud, E. Giacobino and J. Zinn-Justin, eds. (Elsevier, Amsterdam, 1997), p. 387.

[13] John C. Price, Phys. Rev. B **44**, 8997 (1991).

REFERENCES OF CHAPTER 8

[1] C. van Haesendonck, private communication.

[2] J. R. Schrieffer and J. W. Wilkins, Phys. Rev. Lett. **10**, 17 (1963).

[3] F. W. Hekking and Yu. V. Nazarov, Phys. Rev. B, **49** 6847 (1994).

[4] John Clarke, in *Advances in superconductivity,* edited by B. Deaver and John Ruvalds (Plenum Press, New York, 1983).

REFERENCES OF CHAPTER 9

[1] C. J. Adkins and B. W. Kington, Phys. Rev. **177**, 777 (1969); J. R. Toplicar and D. K. Finnemore, Phys. Rev. B **16**, 2072 (1977); A. Kastalsky, L. H. Greene, J. B. Barner, and R. Bhat, Phys. Rev. Lett. **64**, 958 (1990).

[2] M. Tinkham, *Introduction to Superconductivity* (Mc Graw Hill, 1985).

[3] F. Whilhem, A. Zaikin and G. Schön, Czech. J. Phys. **46**, Supplement S4, 2395 (1996) and J. Low. Temp. Phys. **106**, 305 (1997).

[4] A. Volkov and H. Takayanagi, Phys. Rev. Lett. **76**, 4026 (1996).

[5] G. Deutscher and P. G. de Gennes, in *"Superconductivity"*, ed. by R. Parks (1969)

[6] S. N. Artemenko, A. F. Volkov, and A. V. Zaitsev, Solid State Comm. **30**, 771 (1979).

[7] Yu. V. Nazarov and T. H. Stoof, Phys. Rev. Lett. **76**, 823 (1996); T. H. Stoof and Yu. Nazarov Phys. Rev. **B53**, 14496 (1996).

[8] H. Courtois, Ph. Gandit, and B. Pannetier, Phys. Rev. **B52**, 1162 (1995); Phys. Rev. Lett. **76**, 130 (1996). P. Charlat, H. Courtois, B. Pannetier, Phys. Rev. Lett. **77**, 4950 (1996)

[9] P. Charlat, H. Courtois, Ph. Gandit, D. Mailly, A. F. Volkov and B. Pannetier, Czech. J. Phys. **46**, Supplement S6, 3107 (1996).

[10] T. H. Stoof and Yu. Nazarov Phys. Rev. **B54**, R772 (1996).

[11] V. T. Petrashov, Czech. J. Phys. **46**, 3303 (1996); V. T. Petrashov, V. N. Antonov, P. Delsing and T. Claeson, Phys. Rev. Lett. **74**, 5268 (1995).

REFERENCES OF CHAPTER 10

[1] P. Mohanty and R. A. Webb, Phys. Rev. Lett. 78, 3366 (1997).

[2] M. Vavilov, V. Ambegaokar, cond-mat. 9709241.

[3] F. Zhou, B. Spivak, and A. Zyuzin, Phys. Rev. B **54**, 9443 (1996).

INDEX